Extreme Events in Turbulent Combustion

by

Malik Hassanaly

A dissertation submitted in partial fulfillment
of the requirements for the degree of
Doctor of Philosophy
(Aerospace Engineering)
in The University of Michigan
2019

Doctoral Committee:

Professor Venkat Raman, Chair
Associate Professor Karthik Duraisamy
Associate Professor Mirko Gamba
Professor Krishna Garikipati

Malik Hassanaly
malihass@umich.edu
ORCID iD: 0000-0002-0425-9090

Pour Anar et pour Dim Smak!

ACKNOWLEDGEMENTS

First and foremost, I would like to thank my advisor, Venkat Raman, who gave me the opportunity to join the master's program in UT Austin and the doctoral program at the University of Michigan. I learned not only technical skills but also equally important "soft" skills that I probably lacked at the beginning of my Ph.D.! Venkat made me discover many facets of research from executing it to organizing it, and I will always be grateful for his efforts.

I also would like to thank my doctoral committee, Karthik Duraisamy, Krishna Garikipati and Mirko Gamba, for reviewing my thesis and providing constructive remarks along the way. Those are genuinely appreciated, and I look forward to many future collaborations!

My grad student colleagues were also an instrumental part of this thesis. They shared their experiences, their thoughts, and politely laughed at my terrible jokes. In particular, Heeseok has always made himself available to help me get up to speed from day 1 in Austin; Damien has remarkably been able to cheer me up every single day; Alex, Yihao, Taku, Shivam and Supraj were my late night fellas at the lab; Romain and Negin were always ready for political conversations; Chris showed me the best hiding spots; Stephen introduced me (maybe too brutally) to the American lifestyle! Special thanks to Negin, Shivam and Supraj for reviewing the thesis!

Along the way, I also met incredible friends, Aaron, Akin, Amy, David, Greg, Juan, Lakshay, Morgan, Nati, Vira, Wendy, Will and others. These people were my surrogate family thousands of kilometers away from home, and I can't wait for new

adventures with them.

Pour mes potes en France, et en particulier Sam et Alex, merci pour votre éternel soutien.

I want to thank my non-surrogate family and in particular my sister and my parents for always pretending that I was the best person on earth. I know it is a lie, but I'll take it!

Finally, thank you, Kristin, from the bottom of my heart! You coped with me for three years already. You commuted with me, you listened to all my presentations, you made me talk through my problems (you pretend not understanding, but I suspect you secretly do!), you listened to my science fun facts, you made me look outside my bubble, you made me think about who I wanted to become, you prevented my hermit-transformation. I became a better person with you, and I can never thank you enough for your role in this grad school journey.

TABLE OF CONTENTS

LIST OF FIGURES

Figure

LIST OF TABLES

Table

LIST OF ALGORITHMS

Algorithm

LIST OF APPENDICES

Appendix

LIST OF ABBREVIATIONS

QoI quantities of interest

LES large eddy simulation

DNS direct numerical simulation

LE Lyapunov exponent

FTLE finite-time Lyapunov exponent

LV Lyapunov vector

LS Lyapunov spectrum

FLV forward Lyapunov vector

BLV backward Lyapunov vector

MET Multiplicative Ergodic Theorem

OLV orthogonal Lyapunov vector

GSV Gram-Schmidt vector

CLV covariant/characteristic Lyapunov vector

BV bred Vector

LWD Lyapunov weighted dynamics

MRO maintenance, repair and overhaul

RANS Reynolds Averaged Navier-Stokes

SV singular vector

LCS large coherent structures

KY Kaplan-Yorke

NLSE non-linear Schrödinger equation

ECMWF European Center for Medium-Range Weather Forecasts

NCEP National Center for Environmental Prediction

CFL Courant-Friedrichs-Lewy

OS Orr-Sommerfeld

HIT Homogeneous isotropic turbulence

OTD optimally time-dependent

ABSTRACT

The design of reliable combustors is a crucial aspect of propulsion and energy production applications: a faulty engine could cost human lives and millions (if not billions) of dollars. In practice, it is unreasonable to expect all devices to be extensively tested for all operating conditions that they will experience. The set of possible conditions is large, and the state of the device itself can evolve during its lifetime. Yet, deviations from normal behavior, or *extreme events*, should be appropriately accounted for during the design and the operation of the combustor.

In this work, a theoretical approach for the prediction of extreme events is presented. A classification of failures is proposed, and predictive questions that pertain to the failures are identified. This framework guides the work done in this thesis and is tailored to pave the way of future developments that are not addressed here. Two different routes for the prediction of extreme events are explored: one which attempts to characterize the dynamics of a system, and one which attempts to quantify the statistics of a failure.

The target of the first route (dynamical system approach) is to provide an understanding of the process through which a failure occurs so that the design can be adjusted to inhibit a failure. To this end, the Lyapunov analysis is examined in the context of turbulent reacting and inert flows from different angles. The convergence of the Lyapunov exponents with respect to the numerical discretization is examined. Lyapunov exponents are used to quantify the complexity of the attractor and the Lyapunov vectors are used to characterize the response of the flow to perturbations.

The objective of the second route (statistical approach) is to quantify the statistics

of the failure. In particular, the main focus is on obtaining the probability of a rare extreme event. This is achieved by estimating the trajectory leading to a rare event.

The uniqueness of this work lies in the comprehensive approach to extreme event prediction that is developed. While the work is mostly illustrated with target problems relevant for turbulent combustion, it has applications in other complex and high-dimensional problems.

CHAPTER I

Approaching the problem of extreme events

In all industrial applications where some form of combustion is used, the combustor is arguably one of the most critical components. Not only does it allow the device to function since it provides the necessary source of energy, but it also operates in fragile conditions. Consider an aircraft engine illustrated in Fig. 1.1. Here, the air intake enters the jet engine at conditions that are not favorable for combustion (around 0.4 atm and 265 K [17]). Before entering the combustion chamber, the air intake needs to be pressurized in order to lead to stable combustion, which is the role of the compressor. However, flight conditions may vary over time, while the compressor is designed for some range of conditions only. Changes of the airflow at the inlet of the engine can end up generating unstable conditions for the combustor. They can be due to an external agent entering the combustor (for instance, a bird or ice), or simply because the airplane flies into turbulent air [18]. In case an engine does not behave as it should, damage can occur inside the engine (when equipment is exposed to high temperatures) and outside the engine. The latter situation occurred, for example, in the Southwest Airlines Flight 1380 in 2018, when debris from the engine cracked open a cabin window [19].

One should bear in mind that no device is perfectly designed, and sooner or later, failures do occur. In aerospace more than in many other fields, a single failure can

have unacceptable human and financial consequences. It is, therefore, necessary to design engines so that such extreme events can be efficiently handled.

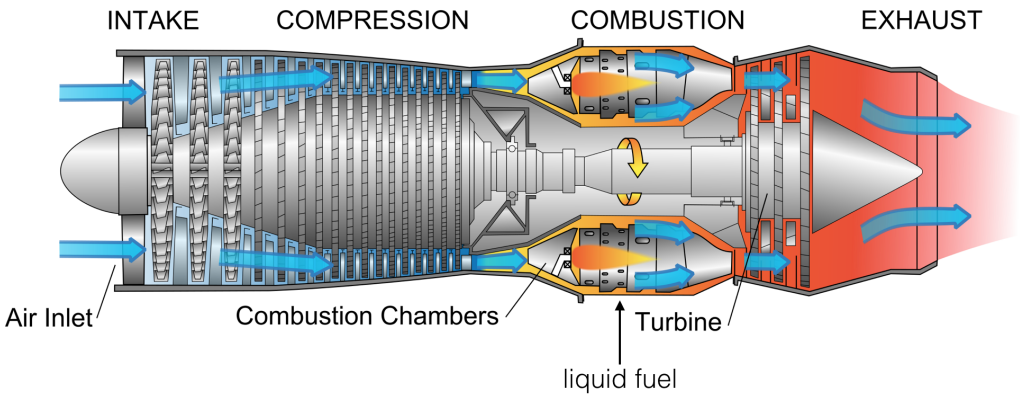

Figure 1.1: Schematic of a jet-engine typically used in commercial aircraft [1].

1.1 Motivation: relevance of extreme events

Extreme events in engineering are marked by excursions of a device away from its design point. The outcome of extreme events is the potential loss of the combustor and of its load. Despite significant advances in the design of combustors, extreme events can occur. The purpose of this section is to provide illustrative examples that will be used throughout the dissertation. Consider the following cases:

- In cruise conditions, aircraft engines can experience flame blow-out. In that case, the combustor temperature and pressure gradually decrease as the burnt gas exits the combustor, and the compressor stops. Within a finite amount of time, the combustor needs to be able to reignite: the longer the combustor remains extinguished, the more difficult the reignition process. A flame blow-out is rare but occurs often enough that it is required for aircraft to be equipped with auto-relight systems [20]. Here, failure to reignite the engine is an extreme event. The ignition is done by introducing a pocket of high energy (a spark) in the engine while injecting liquid fuel [21, 5.11]. Depending on the flow properties

next to the spark (the level of turbulence and the fuel-air mixing), the engine can either reignite or remain extinguished. In Fig. 1.2, these two scenarios (ignition success/failure) are illustrated. The time-sequence of the temperature field in a lab-scale combustor during a relight process is generated using a numerical simulation [3]. A pocket of high energy is introduced at the bottom left of the combustor into two different initial turbulent flow fields. In one case, the spark leads to an ignition (bottom row), while in the other it fails to ignite (top row).

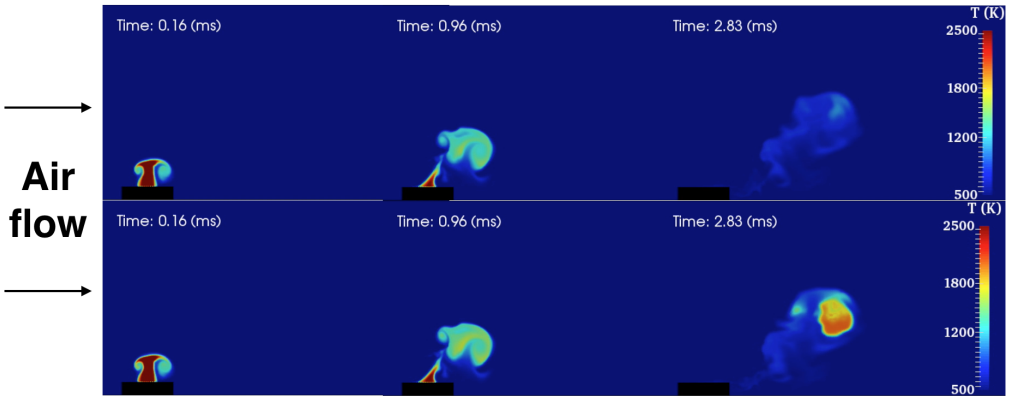

Figure 1.2: Temperature contour in a lab-scale combustor that replicates the relight process obtained through numerical simulations. Top: example of an ignition failure. Bottom: example of an ignition success (see [2] and [3] for additional information about the simulations).

- In stationary gas turbines used on the ground for energy production, fuel is sometimes diluted with hydrogen. For example, syngas is a fuel used in integrated gasification combined cycle (IGCC) and is made of a blend carbon monoxide and hydrogen. While it decreases pollutant emissions and facilitates carbon capture and storage [22], this dilution has a negative impact on the stability properties of the flame [23]. In particular, the flame can be so reactive that it may not remain in the combustion chamber but instead, propagate upstream. In swirl combustors, for example, the flame can take advantage of the low near-wall velocity to creep upstream. This process is called boundary-layer

flashback. An investigation of this phenomenon in the context of swirl combustors was carried out experimentally in [24] and numerically in [4]. Figure 1.3 illustrates the flashback process using numerical simulation data. There, the flame front illustrated as the red contour takes advantage of the presence of a central rod in the mixing tube to propagate upstream. This process can be triggered when the gas turbine needs to generate more energy, and the operator increases the ratio of fuel to air, thereby increasing the reactivity of the mixture. If this situation occurs, severe damages can incur in the gas turbine.

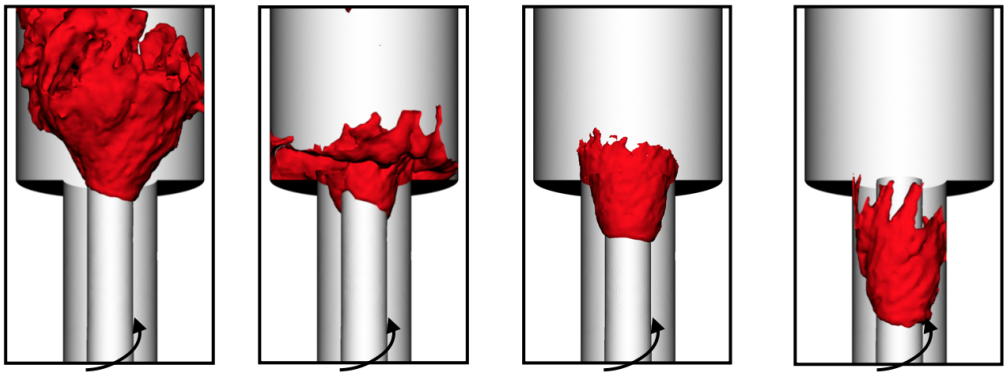

Figure 1.3: Illustration of the boundary-layer flashback process in a labscale swirl combustor obtained with numerical simulations (see [4] for additional information about the simulations). Time advances from left to right. The red iso-surface represents the flame front. The arrow denotes the swirling motion of the flow.

To ensure safe operations, it is crucial to prevent such extreme events from happening. One should also note that these extreme events encourage the use of large safety margins that can significantly affect the efficiency of the combustor. For example, in the case of an aircraft engine, while premixed combustion is more efficient and emits fewer pollutants, non-premixed combustion is preferred for ensuring the stability of the combustion zone and avoid a blow-out. A better understanding of extreme events not only helps designing more reliable combustors but also allows reducing these safety margins, thereby enabling the design of more efficient combustors.

1.2 Definition of extreme events

Extreme events or anomalies are not only relevant in aerospace engineering but also in different contexts, such as oceanic engineering [25, 26], weather forecasting [27, 28], finance [29–31], mechanical engineering [32] and geophysics [33]. Anomalies that are studied in these fields originate from different causes and are governed by different mechanisms, but are commonly referred to as extreme events. The goal of this section is to provide a unifying mathematical definition.

1.2.1 Theoretical description of extreme events

Broadly speaking, extreme events are characterized by the unusual behavior of a system. Since extreme events deviate from normal behavior, they are also referred to as anomalous events. A system can be defined as a set of variables $\boldsymbol{\xi} \in E$, where E is the space of all states of the systems. In continuous mechanics, E is infinite dimensional but will be approximated with an appropriate discretization throughout this work. Typically $E = \mathbb{R}^n$ and $n >> 1$. The systems of interest here are unsteady and their time evolution is described by a governing equation

$$\frac{d\boldsymbol{\xi}}{dt} = \mathcal{F}(\boldsymbol{\xi}, \boldsymbol{\zeta});\ \boldsymbol{\xi}(t=0) = \boldsymbol{\xi}^0, \tag{1.1}$$

where $\boldsymbol{\xi}^0$ is the set of initial conditions for the state-vector, and $\mathcal{F}$ is the operator that describes the time-evolution of the system. Typically, the operator $\mathcal{F}$ is obtained from physics principles. In the present work, the focus is on fluid systems, and the functional form of $\mathcal{F}$ may be derived from the conservation of momentum. Note that the operator $\mathcal{F}$ can depend on variables $\boldsymbol{\zeta}$ that are independent of $\boldsymbol{\xi}$. For example, $\boldsymbol{\zeta}$ can refer to boundary conditions or an external body force. From a practical point of view, $\boldsymbol{\zeta}$ also contains the operating conditions noted $\boldsymbol{\mathcal{I}}$. In general, $\boldsymbol{\mathcal{I}}$ is a set of macroscopic input or such as pressure, mass flow rate, or fuel-split in multi-injection

combustors. The set $\boldsymbol{\mathcal{I}}$ is precisely known since it constitutes the theoretical set of operating conditions (i.e., the set of conditions the operator wants to enforce). Throughout this dissertation, systems with open or extended boundaries are of interest. In practical applications, the only information available about the system is a subset of $\boldsymbol{\xi}$, which constitutes the observables.

$$\begin{aligned} \mathcal{Q}\colon E &\to \mathbb{R}^p \\ \boldsymbol{\xi} &\mapsto q = \mathcal{Q}(\boldsymbol{\xi}). \end{aligned} \tag{1.2}$$

This equation defines p observables obtained for the system, where $\mathcal{Q}$ is an operator that could be non-linear. In particular, the observables can be local or non-local in physical space, i.e., they can be constructed with values of $\boldsymbol{\xi}$ corresponding to one or multiple physical space locations. Typical examples of spatially distributed observables are spatial averages. The observables can also be local or non-local in time, i.e., they can be constructed with instantaneous or past values of $\boldsymbol{\xi}$. Typically, running time-averages are observables non-local in time. In such a case, the inverse of the operator $\mathcal{F}$ is involved in the functional form of $\mathcal{Q}$. An essential subset of the observables is the set of quantities of interest (QoI), used to quantify the performances induced by a particular design. Consider the example of an aircraft engine in Fig. 1.1. There, $\boldsymbol{\xi}$ is made of the field of flow velocity, the field of species mass fractions and energy, and $\boldsymbol{\zeta}$ are the inlet and outlet boundary conditions for all the fields. In this case, one is primarily concerned with the thrust of the engine, which is the QoI in this case. The outputs of the sensors available are the observables of the system. In the case where a thrust sensor is available, the thrust is both a QoI and an observable. The definition of an extreme event has to do with the values taken by observables.

When the system is not subject to extreme events, the values of the observables are confined to $\mathcal{D} \in \mathbb{R}^p$, which defines acceptable values. These acceptable values are arbitrarily defined by the system designer or user. The boundaries of $\mathcal{D}$ are essential to the definition of an extreme event, and without it, extreme events are simply nonexistent. A typical example are extreme dissipation events that were observed in HIT [34]. In HIT flows, the turbulent dissipation rate ϵ normally oscillates over time. However, it was found that the magnitude of oscillations could become intermittently large, which was defined as an extreme event. Without a threshold for the magnitude of the oscillation of ϵ, the extreme event would not exist. The definition of an extreme event is therefore subjective as it requires to properly define the set of acceptable observables.

1.2.2 Definition of rare events in relation to extreme events

It is noted that extreme events can be rare but do not need to be. If the focus is an engineering application where the design of the product is final or close to final, it can be expected that the frequency of an extreme event will be low. However, in the early stages of design, it is not unreasonable to expect a non-rare extreme event. The precise definition of a rare event is again subject to interpretation as it depends on some probability range of a chosen observable.

The lower bound of this probability range depends on the severity of this extreme event. Below this lower bound, the extreme event is considered a non-relevant as part of the design. For example, if an extreme event causes cabin turbulence with a probability lower than once every ten flights, it is irrelevant for the design. However, if an extreme event leads to an engine explosion, it is relevant if it occurs more than once every 10^9 flights. Labeling an extreme event as too rare is important to ensure that only relevant problems are addressed by the design, but is not straightforward as it requires to compute the probability of an event that is rarely observed. Techniques

that accelerate the observations of rare events are crucial to this end, and will be the object of Chap. VI.

The upper bound of this probability range does not depend on the severity of the extreme event but on its observability. If using random observations to analyze the extreme event is possible for a given extreme event, then the extreme event is non-rare. In turn, if too little data for the analysis can be gathered about the extreme event through random observations, the extreme event is a rare event, in the sense that it needs specific treatment. The definition of the upper bound depends on the type of analysis that is conducted (a different number of observations is needed to estimate averages and higher order moments), and the cost of an observation (limits the total number of observations allowed).

Figure 1.4 schematically illustrates the labels of rare and extreme events in relation to the probability that an observable q exceeds specific threshold values a. The red line is the lower bound of the probability range that defines a rare event, and the blue line is the upper bound.

1.2.3 Causality of extreme events as a classifier of extreme events

The definition of extreme events provided in Sec. 1.2.1 is general enough to describe different scenarios. However, it does not simplify the approach to extreme events. It is instead preferred here to classify extreme events based on their causality. Further, the definition is theoretical, and a more illustrative approach is preferred in this section. Three main types of extreme events are isolated based on their causality and illustrated using turbulent combustion problems in order to better address the goals of the dissertation.

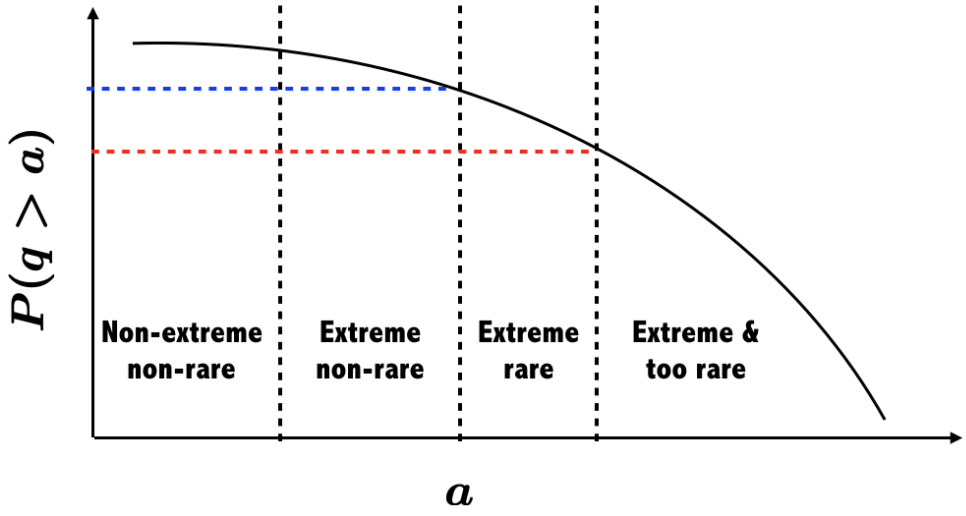

Figure 1.4: Illustration of the relation between rare and extreme events. The probability that an observable q exceeds a threshold a is plotted (—) along with thresholds for the probability upper bound (--) and lower bound (--) that define an extreme rare event. The limits between extreme and non-extreme event (defined a), non-rare and rare events, and rare event and too rare events (defined by the probability thresholds) are also indicated (--).

1.2.3.1 Type I: Extreme events associated with a controllable state

The Type I events represent reliable behavior of complex devices. Here, for any given macroscopic operating condition $\mathcal{I}$, the output is precisely known. In other words, there is a direct connection between the input state and the output state. When such behavior is observed, it is possible to develop a map that relates input to output variables, either through experimental or computational procedures. Once this map is known, the device can be operated within boundaries such that unwanted output states are not observed. For instance, when thermoacoustic instabilities are noted for particular operating conditions, the device can be operated away from these conditions. For most combustion systems, such an operating map is devised in order to understand the limits of stability.

In the sense of the above definition, Type I events are extreme but non-rare events.

Here, operating conditions $\boldsymbol{\mathcal{I}}$ themselves could lead to unwanted regimes, where potentially catastrophic behavior is possible. Most studies of combustion instabilities and transient phenomena in combustion devices have focused on Type I events due to their easy reproducibility. In particular, Type I events can be readily studied using experiments, since the outcomes are directly dictated by the operating or boundary conditions at a macroscopic scale (such as pressure, inflow velocity, boundary layer thickness, etc.), and can be precisely controlled and/or measured. Type I events are also leveraged to collect data about a particular phenomenon with a limited number of observations. For example, the experimental work related to the problem of boundary layer flashback that was mentioned in Sec. 1.1 falls in the category of the Type I problems [24]. There, the flashback (the extreme event) is triggered with a probability equal to 1 by increasing the global equivalence ratio (one of the macroscopic input of the system). Other experimental studies of scramjet unstart fall in the same category [35]. There, an unstart (the extreme event) is triggered with a probability 1 by a sudden change in the flow outlet condition.

The dimension of $\boldsymbol{\mathcal{I}}$ is typically much smaller than that of the dynamical system. The fact that these inputs are sufficient to guarantee the output state shows that either a) there occurs a drastic reduction is the true dimensionality of the system, or b) the output variables are insensitive to much of the state-space of the dynamical system.

Although relevant for the validation of tools able to capture extreme events, Type I events are not the object of the analysis conducted in this dissertation. Other types of events (Type II and III) pose new problems that are related to the dynamics of the system and that require a new approach.

1.2.3.2 Type II: Extreme events associated with a non-controllable state

Type II events are related to the imprecise control of the state of the system using the limited set of input parameters $\boldsymbol{\mathcal{I}}$ available. In other terms, for a fixed set of input parameters, the system can adopt many different states among which, some can lead to extreme events.

First, an anomalous behavior can stem from imprecise knowledge of the initial conditions of the system. Turbulence is a typical context in which this uncertainty would arise. Only macroscopic features of the flow are precisely controlled, while small scale turbulent fluctuations of the flow field are not. In initial conditions-driven anomalous events, a finite time horizon is considered. In other words, the short time evolution of the system matters. More formally, let Q be some threshold for the observable, and T be some time threshold. During normal operations, $q > Q$ for $t = T$. During an anomaly, $q \leq Q$ for $t = T$. Such behavior is illustrated in Fig. 1.5. Most initial conditions lead to normal operating conditions, but at times, an extreme event can be encountered with a low-probability (highlighted in blue in the figure).

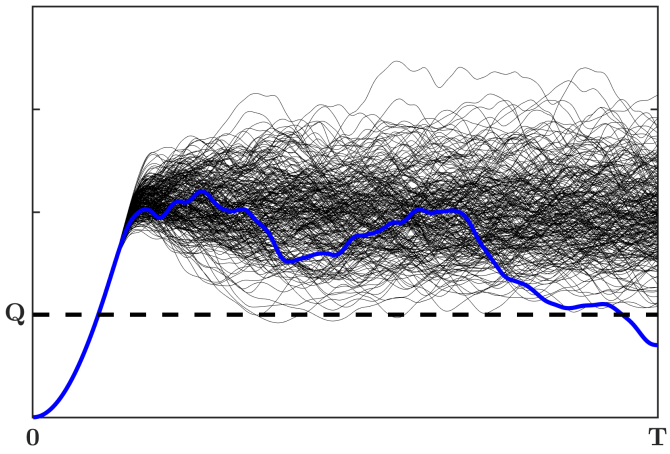

Figure 1.5: Illustration of the an anomaly driven by initial conditions. Most of the initial conditions lead to a quantity of interest in the normal operating range $q > Q$ for $t = T$ (—). Some initial conditions with low-probability can lead to an extreme event (—).

A practical turbulent combustion example is the relight problem mentioned in Sec. 1.1. Here, the flame blows out at some operating condition, typically at high-altitude, and a relight procedure is initiated. Fuel is pumped into the combustor, and an igniter is used to send in high-enthalpy gases that can ignite and stabilize a flame. Both experimental [36] and simulation studies [2, 37] show that uncertainty in igniter output, turbulence state, and fuel-air mixing can lead to failed ignition events. Figure 1.6 shows the ignition outcome in a lab-scale experiment at fixed operating conditions. Variations in initial conditions lead to ignition success (top) or ignition failure (bottom). In other terms, the output cannot be solely controlled with the input parameters. Here, an anomalous event occurs when too many successive ignition failures occur, and the engine is too cold to relight.

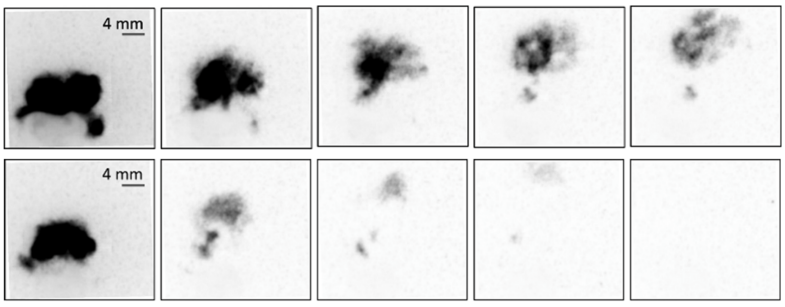

Figure 1.6: Sequence of line of sight measurement of OH^* during successful ignition (top) and ignition failure (bottom). Time advances from left to right. Reproduced from [5].

Second, an anomalous behavior can stem from imprecise knowledge of the boundary conditions of the system. This aspect is particularly important for open systems with turbulent boundary conditions. Typically, the mass flow rate of a burner would be known, but the exact boundary conditions would not be. This imprecision could leave room for extreme events to occur.

In swirl premixed burners, it was for example observed that at lean equivalence ratios, a flame could oscillate between two states: one attached to the nozzle and another detached from the nozzle. This process is illustrated in Fig. 1.7. At the

moment, it is not entirely clear why the transition from attached to detached flame occurs, but experimental investigations have hypothesized that it could be due to a perturbation coming from the inflow [38]. In this scenario, the perturbation would break the symmetry of the flow field, and subsequently cause the flame detachment. This explanation suggests that imprecise boundary condition are the cause of this anomalous behavior.

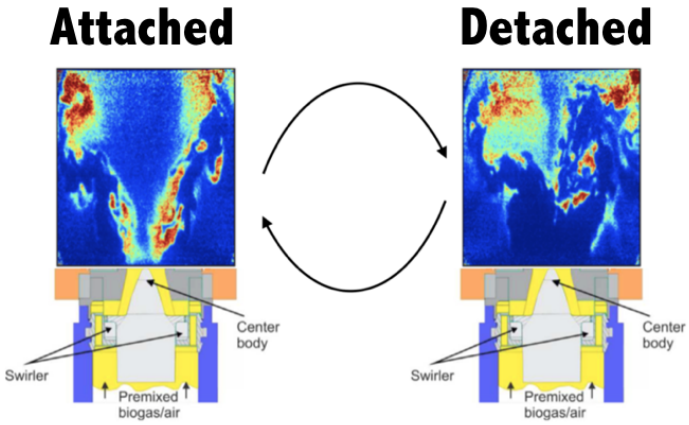

Figure 1.7: Illustration of the flame transition in a swirl premixed burner with OH PLIF contours taken at the combustor mid-plane. The OH contour denotes the flame location. Left: flame attached to the combustor nozzle. Right: flame detached from the combustor nozzle. Based on experiments of [6] and visualization of [7].

1.2.3.3 Type III: Extreme events associated with the nature of the system dynamics

Extreme events can also occur because the dynamical behavior of the system itself allows for the existence of such extreme events. Different "pathologies" for the system dynamics can be identified and are listed below.

Type III-A: Spontaneous bursts

Here, the QoI q exhibits intermittent bursts that constitute extreme events. These events are periodically encountered, with a non-fixed period, and characterize the long-term behavior of the system [39]. In other terms, these extreme events are

naturally encountered by the system as they are part of the underlying dynamics. Note the frequency of such events can be extremely low and can, therefore, qualify as a rare event.

In the turbulent combustion parlance, such events are termed intermittent behavior. For instance, soot formation in gas turbine combustors can be highly intermittent. An illustration of this behavior is provided in Fig. 1.8. The instantaneous contour of soot volume fraction in a swirl combustor at different times is shown and highlights this intermittent behavior, i.e., the spatial and temporal localization of soot concentration. The production of soot can be considered an extreme event as the system is required to locally encounter specific conditions over extended periods of time [8, 40, 41]. Experiments of practical combustors showed that such behavior is central to the production and transport of soot [42].

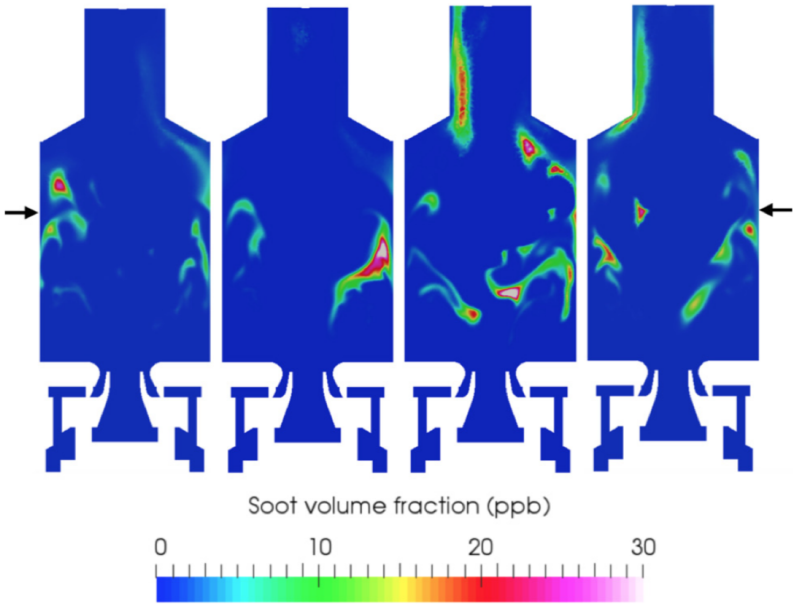

Figure 1.8: Instantaneous soot volume fraction snapshots at the center plane of a swirl combustor every at different times. Reproduced from [8].

Similarly, premixed combustors can exhibit macroscopic transitions that can be categorized as spontaneous bursts. At fuel-lean conditions, the flame front can, for example, oscillate between "V"- and "M"-shapes [9, 43] (Fig. 1.9). Such transitions

can be detrimental for the efficiency and the durability of the combustor [44]. For example, the flame topology controls the spatial distribution of heat flux to the walls, and these transitions may expose walls to large heat loads. Numerical simulations conducted in non-swirling flames by Huang and Yang [45] suggested that this behavior is a spontaneous process that occurs due to the interaction between the flame and the outer walls of the combustor.

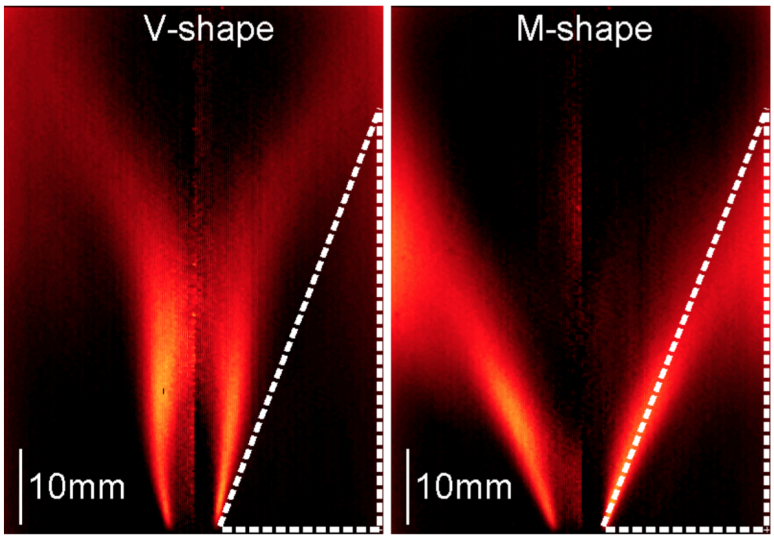

Figure 1.9: Variation of flame topology that can be encountered in a swirl combustor. The flow goes from the bottom to top. The flame can alternatively stabilize in a V-shape (left) or M-shape (right). Images are captured using flame chemiluminescence. Reproduced from [9].

Outside the field of turbulent combustion, this type of events has received considerable attention. In oceanic engineering, the formation of rogue waves has been studied [26] and was shown to be a spontaneous event using an analogy with the nonlinear Schrödinger equation (NLSE). Other examples of such spontaneous transition in turbulent flows are extensively discussed in Ref. [46].

Type III-B: Sensitivity to external shocks

In some cases, a system is allowed to adopt multiple irreversible stable states. Once the system is in a stable macroscopic state, it cannot move to another macro-

scopic stable state, unless it is subject to an external shock with the proper magnitude and orientation. Here, a shock is defined as a perturbation of significant amplitude and localized in time. In principle, an engineering device is designed to remain in one macroscopic state only. If the device transitions to an undesired state, the consequences can be disastrous. For Type III-B events, the transition may never be reverted unless another external shock is applied. For aerospace applications, combustor can be expected to operate in a hostile environment where external shocks may occur. In a more general setting, external shocks can also refer to the modification of input parameters $\boldsymbol{\mathcal{I}}$ of the system, which can be interpreted as a variation of initial conditions. Systems that lead to different macroscopic behavior depending on their initial conditions have been reported in many fields (including turbulent combustion), and are said to exhibit *hysteresis*.

In turbulent combustion, hysteresis has been reported in swirl combustors. Depending on the fuel-air volume ratio (equivalence ratio) at which a swirl combustor is operated, thermoacoustic instabilities can be observed [47]. In short, thermoacoustic instabilities are large pressure oscillations, typically encountered in a closed combustor, that can damage it in the long run [48]. As a flame front propagates, it emits acoustic waves that can affect the flame front propagation. Under certain conditions, the pressure oscillations can amplify or fail to damp, eventually destroying the combustor [48, 49]. In swirl combustors, it was found that if the equivalence ratio is increased or decreased towards the same end-value, the system can stabilize in a state where the pressure wave resonate (thermoacoustic instabilities) or are damped. Examples of such behavior are provided in Ref. [50] and references therein. One of such hysteresis plots is shown in Fig. 1.10.

This hysteresis phenomenon can be explained by the fact that for specific equivalence ratios, there exist two irreversible stable conditions: one where thermoacoustic instabilities occur and one where they do not. Depending on the initial conditions

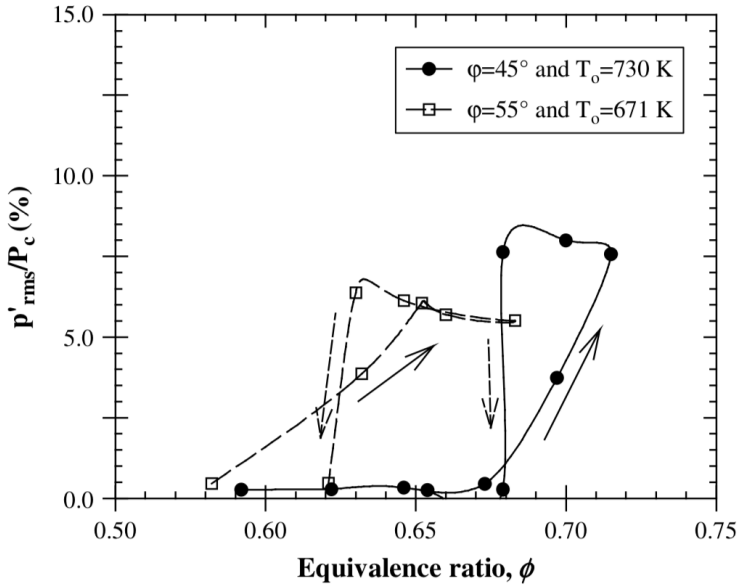

Figure 1.10: Stability maps of a swirl combustor as a function of the equivalence ratio for two different swirl angles. Arrows indicate the chronological order of measurements. Reproduced from [10].

(the direction along which equivalence ratio is varied), the system stabilizes in either one of these states. In combustion problems, hysteresis is not only limited to swirl combustors and has also been observed numerically for droplet vaporization. Figure 1.11 illustrates this effect with the map of the evaporation rate of a droplet as a function of the Reynolds number of a crossflow. It was found that two different vaporization rates can be observed depending on the direction along which the Reynolds number is varied [11]. Again, this suggests that for the same Reynolds number, two stable states for the system are realizable, and each one can be attained depending on the direction along which the Reynolds number is varied.

Type III-C: Sensitivity to continuous perturbations

On the same note as the previous category, other external perturbations can lead to extreme events. This time, the case of continuous perturbations is considered, and refers to perturbations applied to the system, that are typically small and distributed over time. In this case, the dynamical behavior of the system is not only determined by

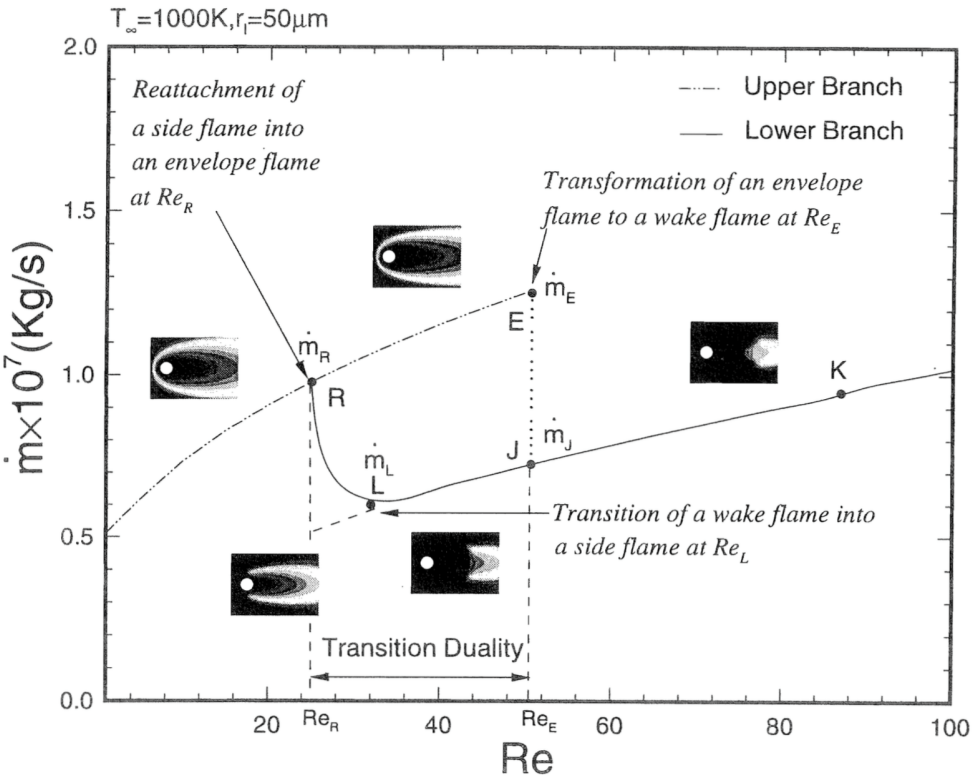

Figure 1.11: Illustration of the multistability phenomenon for droplet vaporization. In the transition regime, two different vaporization rates are possible at fixed operating conditions. Reproduced from [11].

the governing equations, but also by the continuous perturbations. This case arises due to a modeling problem that can never be overcome. The physics of external perturbations cannot be reasonably incorporated in the model, but without external perturbations, no extreme event occurs. More formally, Type III-C events occur due to the imprecise definition of the functional form of the governing equations $\mathcal{F}$.

For instance, Popov et al. [12] studied the onset of thermoacoustic instabilities due to variability in the acceleration of a rocket. Stable and unstable behaviors of this system are shown in Fig. 1.12, along with the spectrum of the rocket acceleration leading to this behavior. The system used there was not deterministic as the perturbations could be neither reasonably assumed to be known a priori, nor functions of the solution.

In other studies unrelated to combustion applications, the effect of external perturbation was also investigated for the stall of rotorcraft [51]. Similar to the thermoacoustic instability due to the acceleration of a rocket, the rotorcraft is exposed to the wind, which contains some level of variation. These variations act as external perturbations and can eventually lead to the stall of the rotorcraft (the extreme event). Modeling the physics of the wind, on top of that of the rotorcraft would be impractical. Instead, the system's dynamics are assumed to be continuously affected by external perturbations. These examples illustrate how perturbations in the dynamics of the system (the functional form of the governing equation $\mathcal{F}$) can lead to an extreme event.

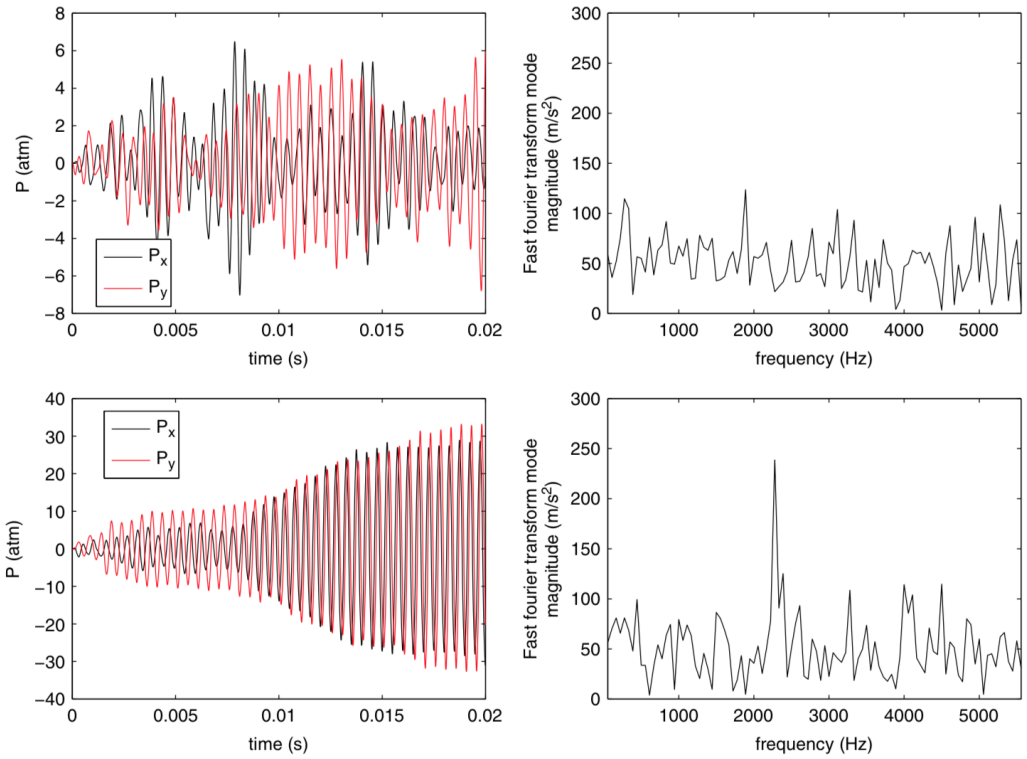

Figure 1.12: Pressure history of stable (top) and unstable (bottom) configuration in a model rocket engine exposed to different accelerations. The acceleration acts as an external perturbation that can drive the system to an unstable behavior (here, an acoustic instability). Reproduced from [12].

As a final remark, it is noted that the system dynamics can evolve over time

depending on wear or damages incurred during operations. The changes induced on the dynamics of the system can lead to an extreme event when the long-term behavior of the device is different from the one for which it was initially designed. A system that was not prone to extreme events at the beginning of operation can be exposed to all Type III events after.

1.3 Definition of prediction

Extreme events pose unique modeling challenges and require to precisely define the notion "prediction" in this context. In fact, the predictive questions that are posed determine not only the algorithms used but the level of expert input needed. These questions constitute the grand challenges of extreme events prediction. Below, a nominal set of prediction targets are discussed. These predictions questions are relevant for Type II and III events, which are the main focus.

1. Predict for real-time control:

   In practical systems, actuation could be used to push the system away from an anomalous event, if it could be predicted sufficiently ahead of time. Doing so requires to identify precursors for such events using some of the observables, and devise an actuation mechanism that could annihilate the extreme event.

2. Estimate the probability of an event:

   For design purposes, it is useful to determine the probability of encountering a pre-determined anomalous event. For instance, if for safety reasons the ignition time for high-altitude relights T_{ig} should not exceed T, then estimating the probability $P(T_{ig} > T)$ is a useful design metric. Here again, the models and techniques used to compute these probabilities should reflect the underlying reasons for the variability in the ignition.

3. Predict unencountered events:

A remarkable use of computational tools will be the ability to predict unencountered anomalous events. In other words, if q is not adequately defined, is there a way to determine events that fall outside the normal range of their values? Such tools will be ultimately useful in prognosis of devices in the context of maintenance, repair and overhaul (MRO), where decisions are informed primarily through the use of device-generated data [52].

4. Bound quantities of interest:

   Safeguarding against failure is one of the primary design constraints. In this sense, being able to predict the worst outcomes possible, or more precisely, provide bounds on quantities of interest would be a valuable tool.

5. Understand how an extreme event occurs:

   In order to design devices for which some extreme events do not occur, it is necessary to understand the root cause of a particular anomaly. Understanding the process leading to the extreme event can also guide the modeling procedure, the search of precursors, or help generate more observational data when the extreme event is rare.

1.4 The importance of computations in the study of extreme events

Each of the examples provided in Sec. 1.2.3 can result in a complete failure of the propulsion system. The obvious solution in design is to consider choices that remove such events. However, this is not a fail-proof solution for two main reasons. First, turbulent systems are chaotic, which means that small perturbations can exponentially amplify over time. Understanding the onset of bursting events in statistically stationary systems requires to identify what infinitesimal perturbation could lead to an extreme event, and be able to track its evolution. Such an approach is not feasible

using experimental approaches as it requires small temporal and spatial resolution of the flow field. Second, turbulent combustion systems exhibit a broad range of scales (typically from molecular scales to meters) and are coupled with a multitude of other devices. Therefore, a system can fail or reach a catastrophic state in a myriad of ways. All such paths cannot be exhaustively accounted for during design. More critically, it may not be possible to thoroughly search all such possibilities, since certain events may be catalyzed by conditions that are present only during operation. For instance, the effect of operational cycles on the combustor or particular changes to fuel composition may not have been anticipated during the design phase. As a result, even a conservative design based on known failure modes cannot completely guarantee that other paths to failure have been considered.

In the case where the existence of catastrophic failures is known based on practical observations, there exists minimal data that can be used to derive a reasonable estimation of the underlying physics. Engineering systems are in general not designed to fail, and if a failure occurs, it is usually a rare event. Unlike in statistically stationary processes, experiments that can produce a significant statistical ensemble for practical systems are not a valuable option. As a result, very limited experiments exist for the problems mentioned in Sec. 1.1 for instance ([24, 35] for the boundary layer flashback, and [36] for the relight problem).

Computational tools are indispensable in a way that is fundamentally different from other conventional uses. Without models, certain quantities of interest for addressing such failure events are just not accessible. However, models and their outputs also have to be fundamentally different since the targets of simulations are now different.

1.5 Summary

In this chapter, extreme events were mathematically defined and illustrated with practical examples. An important contribution of the present work is the classification of extreme events, which is meant to be a practical tool for the analysis of an extreme event in engineering systems. It is advocated against trying to unify the definition of extreme events, and it is instead encouraged to distinguish different types of extreme events. A causality-based classification of extreme events is formulated for the first time, and is illustrated using examples drawn from turbulent combustion applications. It is also emphasized that the definition of prediction should be revisited as the predictive questions that pertain to extreme events of Type II an III significantly differ from the ones corresponding to more traditional design problems. The new predictive questions require to develop and deploy new tools, which is the object of the rest of the dissertation.

1.6 Scope of the dissertation

With this background, the dissertation is organized around two main approaches to tackle the problem of extreme event prediction. First, the dynamical approach is presented to gain knowledge about the process through which a bursting event might occur in a statistically stationary flow. Second, a statistical approach is presented to extract a probabilistic description of the extreme event. The dissertation is organized as follows:

Chapter II: In the next chapter, the use of the dynamical systems approach for studying extreme events is introduced. In particular, the subtle link between numerical simulations of turbulent combustion systems and dynamical systems is described. The classification of extreme events presented in Chapter I is revisited from a dynamical system perspective. Existing methods to answer the predictive

question presented in Chapter I are briefly described. In particular, the concept of Lyapunov analysis is introduced, and it is shown how it can provide a route for answering most of the questions posed.

Chapter III: Given the potential of Lyapunov analysis for studying extreme events, the computation of Lyapunov exponents is examined more closely. The convergence properties of the Lyapunov exponents in the context of turbulent flows is precisely assessed for the first time using a new convergence procedure. A suite of numerical tests from 1D problems to 3D turbulent flows is conducted. The convergence properties of Lyapunov exponents are obtained for the first time in this section. Furthermore, a method to bypass numerical issues in the computation of Lyapunov exponents is introduced in this chapter.

Chapter IV: The dynamical properties of turbulent flows are examined by applying the Lyapunov analysis on a triply periodic homogeneous isotropic turbulent case that is artificially sustained by an external body force. For the first time, enough Lyapunov exponents are computed so that complexity of the turbulent flow dynamics (dimensionality) can be quantified. The scaling of the dimension with respect to the level of turbulence is also estimated for the first time. The spatial distribution of the chaotic response of the turbulent flow field is characterized and correlated to various turbulent quantities. Different forcing schemes are used to sustain the turbulence in the domain, and the Lyapunov analysis is conducted for each one of these cases. This chapter illustrates how the Lyapunov analysis can be used to compare the dynamical properties of different models, rather than only focusing on their statistical properties.

Chapter V: The Lyapunov analysis is applied to a lab-scale turbulent combustion problem. The Lyapunov exponents are used to estimate the complexity of the turbulent flame dynamics, which can provide a route for creating reduced order models able to capture extreme events. The origin of chaos in turbulent flames is also identified and discussed.

Chapter VI: The method for the computation of rare event probability is investigated. Through the concept of importance splitting, which will be presented in the section, rare event probability in the context of turbulent combustion can be estimated. A new method for efficiently applying importance splitting for oscillatory quantities is proposed and tested on a canonical problem. A priori tests are also conducted on a turbulent reacting flow.

Chapter VII: The main findings of the dissertation are summarized, and an outlook on the problem of extreme event prediction is provided. Directions for future work in this emerging field are also outlined.

CHAPTER II

Dynamical system perspective of extreme events

The prediction of extreme events involves a range of questions that require a corresponding range of tools that can be grouped into methods based on either the dynamical or the statistical approach. In the dynamical approach, the goal is to characterize the dynamical behavior of the system, such as its response to perturbations or its stability properties. There, the goal is to understand the root cause of an extreme event so that real-time prediction and actuation can be used. In the case of a man-made system, this approach can help design new devices that are more resilient to excursions away from normal behavior. In the statistical approach, the goal is to obtain a statistical description of an extreme event. For example, one can ask what the probability of a rare event is in order to design a system that is resilient enough to this rare event during its lifetime. Another application could be to understand the average behavior of the system close to a rare event, in which case, one could also create indicators for real-time prediction. Chapter III-V are dedicated to the dynamical approach and Chapter VI discusses a statistical approach.

In this chapter, the main purpose is to introduce tools that can be used for characterizing the dynamics of a system. Section 2.1 describes more formally what is meant by a dynamical system approach and why it is peculiar in the context of turbulent combustion. In Sec. 2.2, the classification of extreme events is revisited from a dy-

namical system perspective. Section 2.3 introduces the Lyapunov analysis as a tool to characterize the dynamics of a system. Applications of the Lyapunov analysis in the context of extreme events are reviewed in Sec. 2.4.

2.1 The dynamical system perspective in turbulence

Traditionally, numerical simulations of turbulent flows adopt a statistical perspective as opposed to the dynamical system perspective. This is justified by a number of reasons related to the modeling and predictive needs of turbulent combustion that are detailed here.

2.1.1 Definitions

A statistical approach describes a system using an ensemble of observations that are, in some sense, equivalent. As opposed to this, a dynamical system approach focuses on the description of individual observations of the system. In the context of extreme events, adopting a statistical approach is useful to quantify how often it occurs and to design systems resilient to them. With a dynamical approach, one can obtain an understanding of the process through which an extreme event occurs, which can help formulate a design that decreases the extreme event frequency or eliminate it.

The evolution of a single realization of the system is called a trajectory. The state of the system $\boldsymbol{\xi}$ evolves in a high-dimensional space E called phase space. The long-time behavior of the system can be described by a closed subset of the phase space [53, 54] that is called an attracting set. Starting from an initial condition within the basin of attraction of this subset, the trajectory of the system ends up being trapped indefinitely in the attracting set. The attracting set can be made of disjoint subsets called attractors. The nature of an attractor $\mathcal{A}$ and its properties depend on the governing equations ($\mathcal{F}$ in Eq. 1.1), the boundary conditions and the

operating conditions represented by the variable $\boldsymbol{\zeta}$ introduced in Eq. 1.1. Schematic visualization of these three concepts is shown in Fig. 2.1.

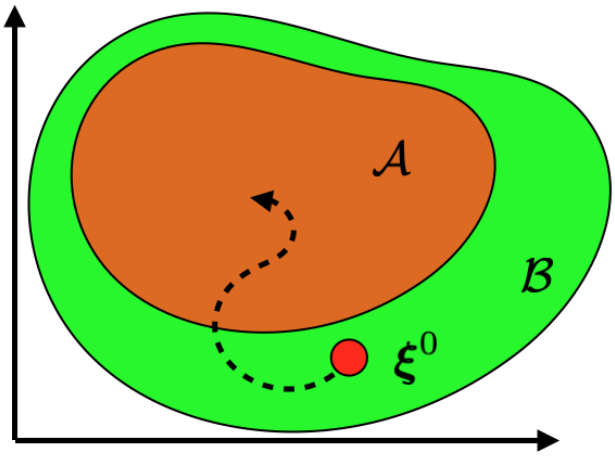

Figure 2.1: Schematic of the phase space representation of a dynamical system. The plane represents the phase space. The initial condition is represented by the red dot. The trajectory is shown as a dashed black line. The red subspace is the attractor $\mathcal{A}$ and its basin of attraction is represented in green and called $\mathcal{B}$.

2.1.2 The multi-scale problem

Before describing further the advantages of both the dynamical and statistical approaches, the systems of interest are briefly presented. In this dissertation, the focus in on turbulent combustion. The flow physics is described using the Navier-Stokes equations that govern the evolution of a velocity field over time. These equations take the following form

$$\frac{\partial \rho \boldsymbol{u}}{\partial t} + \nabla \cdot (\rho \boldsymbol{u}\boldsymbol{u}) = -\nabla p + \nabla \cdot \overline{\boldsymbol{\sigma}}, \tag{2.1}$$

where $\boldsymbol{u}$ denotes the velocity vector, ρ denotes the flow density, p the pressure, $\overline{\boldsymbol{\sigma}} = \mu(\nabla \boldsymbol{u} + {}^t\nabla \boldsymbol{u}) - \frac{2}{3}\mu(\nabla \cdot \boldsymbol{u})\overline{\boldsymbol{I}}$ is the viscous stress tensor, μ is the dynamic viscosity and $\overline{\boldsymbol{I}}$ is the identity tensor. An additional constraint of mass conservation links the

velocity and the density field and is expressed as

$$\frac{\partial \rho}{\partial t} + \nabla \cdot (\rho \boldsymbol{u}) = 0, \tag{2.2}$$

Energy conservation equation may also be of interest but is not important here since the low Mach number approximation will be used. Additional justification will be provided in Sec. 3.2.2. For systems where combustion occurs, it is also advantageous to describe the mixing processes of fuel, oxidizer, and products of the chemical reaction. The set of governing equations can then be augmented with transport equations of species mass fraction or other equations (e.g., mixture fraction, progress variables, etc.) that take the form

$$\frac{\partial \rho \boldsymbol{\phi}}{\partial t} + \nabla \cdot (\rho \boldsymbol{\phi} \boldsymbol{u}) = \nabla \cdot (D_{\boldsymbol{\phi}} \nabla \boldsymbol{\phi}) + \dot{\omega}_{\boldsymbol{\phi}}, \tag{2.3}$$

where $\boldsymbol{\phi}$ denotes the transported scalar, $D_{\boldsymbol{\phi}}$ denotes mass diffusivity and $\dot{\omega}_{\boldsymbol{\phi}}$ is a volumetric source term. Note that the discrete form of these equations can be recast in the form of Eq. 1.1.

These equations are in part challenging because they involve the interaction of many different length scales. The multi-scale interaction can be understood by considering the incompressible version of the Navier-Stokes equation in a $2\pi \times 2\pi \times 2\pi$ periodic domain:

$$\frac{\partial \boldsymbol{u}}{\partial t} + \nabla \cdot (\boldsymbol{u}\boldsymbol{u}) = -\nabla \frac{p}{\rho} + \nu \nabla^2 \boldsymbol{u}, \tag{2.4}$$

where ν denotes the kinematic viscosity. Note that this equation will be the main focus of Chap. IV. Using the Fourier decomposition, one can represent the velocity field as $\boldsymbol{u} = \sum_{\boldsymbol{\kappa}} \widehat{\boldsymbol{u}}(\boldsymbol{\kappa}, t) e^{i\boldsymbol{\kappa} \cdot \boldsymbol{x}}$, where $\boldsymbol{\kappa}$ is the three-dimensional wavenumber, and $\widehat{\boldsymbol{u}}(\boldsymbol{\kappa}, t)$ is the velocity mode amplitude. Writing the Galerkin projection of Eq. 2.4, one obtains

$$\frac{\partial}{\partial t}\widehat{\boldsymbol{u}}(\boldsymbol{\kappa},t)+\nu|\boldsymbol{\kappa}|^2\widehat{\boldsymbol{u}}(\boldsymbol{\kappa},t)=\boldsymbol{\kappa}\frac{\boldsymbol{NL}\cdot\boldsymbol{\kappa}}{|\boldsymbol{\kappa}|^2}-\boldsymbol{NL}, \tag{2.5}$$

where $\boldsymbol{NL}$ is a the non-linear convective term taking the form of a triadic interaction as $\sum_{\boldsymbol{\kappa_1}+\boldsymbol{\kappa_2}=\boldsymbol{\kappa}} i\boldsymbol{\kappa}\cdot\widehat{\boldsymbol{u}}(\boldsymbol{\kappa_1},t)\widehat{\boldsymbol{u}}(\boldsymbol{\kappa_2},t)$. This equation is useful since it explicitly shows the multi-scale coupling.

Besides turbulence, combustion processes also lead to multi-scale phenomena. For example, the chemical reactions can occur at much shorter timescales than turbulence, while the production of pollutants (e.g., soot) can occur over timescales much larger than that of the flow field [40].

Numerically integrating the equations aforementioned would, therefore, require resolving a broad range of timescales and spatial scales and would quickly become intractable. Instead, it is often desired to integrate only specific scales (typically the largest ones) that can be assumed to be weakly coupled with other ones, or for which the dependence with other scales can be modeled. This is the idea of large eddy simulation (LES) which has been particularly successful in the field of turbulent combustion (see Ref. [52] and references therein).

2.1.3 Coarse-graining problem and the statistical approach

When only certain degrees of freedom of a system can be numerically integrated (large scales, for example), one refers to this approach as coarse-graining. More formally, using the notations of Chap. I, one would write the state of the system as

$$\boldsymbol{\xi}=\boldsymbol{\xi}_p+\boldsymbol{\xi}_q, \tag{2.6}$$

where $\boldsymbol{\xi}_p$ denotes the degrees of freedom that are resolved, and $\boldsymbol{\xi}_q$ denotes the degrees of freedom that are not resolved. In the case of LES, $\boldsymbol{\xi}_p=\overline{\boldsymbol{\xi}}$, where $\overline{(.)}$ denotes a filtering operation.

Whenever any coarse-graining of the system of equation is involved, the individual realizations of the unresolved scales are not accessible. Since the dynamics of the resolved variables depend on the unresolved ones, it is not theoretically possible to follow the evolution of one individual realization. At best, one can only hope to approximate the dynamics of the resolved scales averaged over all the possible unresolved scales. More formally, this corresponds to estimating

$$\widetilde{\mathcal{F}}(\boldsymbol{\xi}_p) \triangleq \langle \frac{d\boldsymbol{\xi}_p}{dt} | \overline{\boldsymbol{\xi}} = \boldsymbol{\xi}_p \rangle. \tag{2.7}$$

This facet of LES has been recognized by several authors [55–58] who showed that coarse-graining was rooted in a statistical approach. In part, it justified using LES for statistically stationary flows and designing models to capture statistical moments of turbulent combustion fields [59, 60].

However, the statistical definition of LES need not constrain its use for statistically stationary flows. In fact, LES was originally introduced in the field of weather forecasting [61, 62] where it was seen that the dynamics of the larges scales could reasonably approximate the future state of atmospheric flows (over a finite time horizon). Here, the evolution of the flow field needs to be approximated over a finite amount of time (say several hours). Over this finite amount of time, it is considered that LES reasonably approximates the dynamics of the original flow-field, for the purposes that it serves [63, 64]. This is a typical example of a dynamical system approach to numerical simulations. In turbulent combustion, similar approximations have been introduced recently and proved to be informative of the physics at stake. For example, for the problem of boundary layer flashback mentioned in Chap. I, simulation using direct numerical simulation (DNS) [65] and LES [66] models showed surprising agreement in terms of the flame shape and speed. For the problem of high-altitude relight, using LES was sufficient to capture the ignition probability of a wide variety of fuels [3, 37].

To summarize, any coarse-graining theoretically prevents one from capturing the dynamics of individual realizations of the system. In part, it explains why few studies attempt to characterize the dynamics of turbulent flames. In this work, it is argued that the ability of LES to reasonably approximate the dynamics of the large scales suggest that it could be used to characterize the dynamics of turbulent combustion systems and help understand the formation of extreme events.

2.1.4 Dynamical or statistical prediction

The prominent statistical approach in numerical simulations is not only justified by the range applicability of existing numerical tools, but also by the needs of design itself. Many design questions are concerned with the efficiency of the device over long periods of time. In these cases, the QoI is often a time-average of flow quantities (e.g., mean thrust, mean temperature at a location, etc.). If the purpose of a simulation is to inform about the variation of these QoI when the design is changed, then techniques such as Reynolds Averaged Navier-Stokes (RANS), where the statistics of the flow field are directly transported, are sufficient. However, if the goal is to understand the behavior of the flow field in the presence of a transient process that needs to be encouraged or mitigated, the statistical approach is not sufficient. Even though coarse-grained models provide a statistical prediction of the system (Sec. 2.1.3), they could also play a role in characterizing the dynamics.

Recently, it appeared that coarse-graining approaches could be useful to understand the dynamical behavior of the system. For example, it has been found that LES was able to capture the onset of thermoacoustic instabilities in combustors and accurately predict what design could lead to pressure wave resonance [48]. In itself, this achievement is surprising, given the approximation error between the actual realization and the coarse-grained model exponentially increases over time [62].

While the coarse-grained models do not allow to follow the dynamics of an indi-

vidual realization exactly, they still provide a useful approximation of the dynamics of the system. This opens a path to using numerical simulations for purposes different than design optimization, such as failure prediction and deviation from nominal behavior. In the rest of the thesis, the dynamical system point of view will be central when drawing conclusions about the true dynamics of the system using either DNS or LES.

2.2 Classification of extreme events from a dynamical systems approach

In this section, the different classes of extreme events introduced in Chap. I are revisited and described from a dynamical system perspective. In particular, an interpretation of the behavior of the system in phase space is provided. Note that Type I events (controllable extreme event) are not reexamined here since the trajectory of the system is not relevant to the occurrence of an extreme event. No matter what succession of states is taken by the system, the extreme event only occurs depending on the input parameters $\boldsymbol{\mathcal{I}}$.

2.2.1 Type II: Extreme events associated with a non-controllable state

In the case where the input parameters $\boldsymbol{\mathcal{I}}$ are not sufficient to guarantee that an extreme event will occur or not, one can illustrate the configuration of phase space using a ball of uncertainty. Within this ball of uncertainty, some trajectories can lead to an extreme event. In other terms, a pathological solution in phase space can be reached by some trajectories that exist within the uncertainty range. This is illustrated in the case of initial conditions uncertainty in Fig. 2.2.

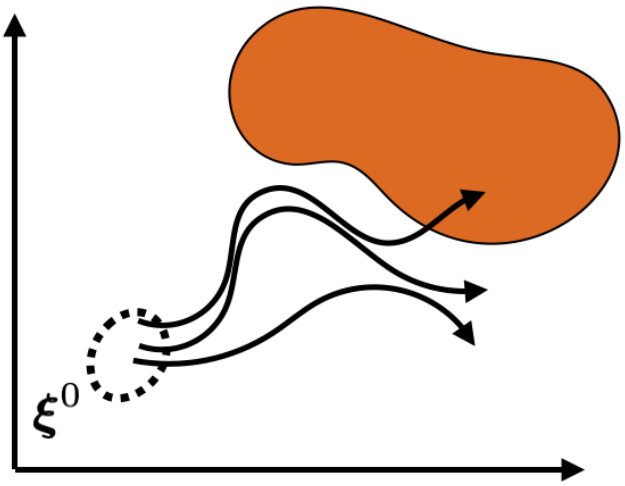

Figure 2.2: Illustration of an extreme event driven by imprecise initial conditions. The dashed area is the range of initial conditions. When a trajectory intersects the red area, an extreme event occurs. Three trajectories are illustrated, one leads to an extreme event.

2.2.2 Type III-A: Spontaneous bursts

Spontaneous bursts are experienced intermittently by the system, and occur unpredictably. Here the extreme event happens during the long-time behavior of the system and therefore is part of its attractor. In other terms, there exists a pathological part of the attractor that leads to these spontaneous bursts. The fact that these bursts repeatedly occur is compatible with their presence on the attractor and is a consequence of the Poincaré recurrence theorem [67, 68].

This theorem states that for dynamical systems that preserve the measure of the phase space (see Sec. 2.3.3 for a discussion on this point), for almost all initial conditions, the dynamical system eventually returns infinitely close to its initial conditions. By shifting the time $t = 0$ to the time of the first observed burst, the theorem ensures that the same burst will be observed at later times. A schematic illustration of the phase-space configuration is provided in Fig. 2.3.

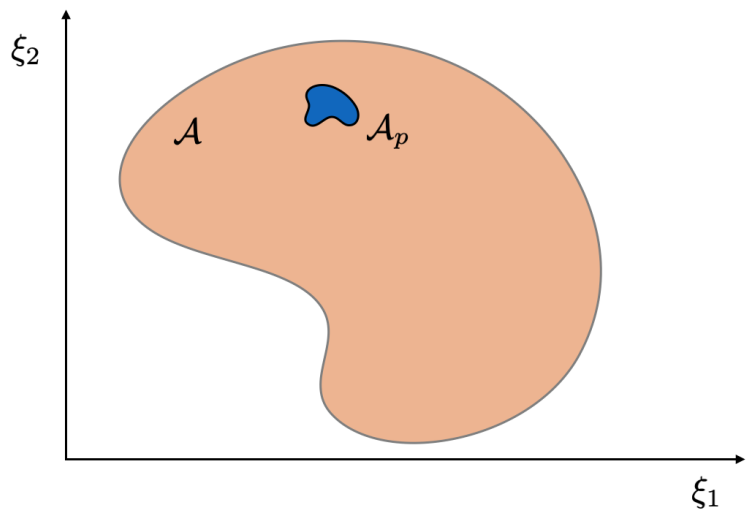

Figure 2.3: Illustration of an attractor $\mathcal{A}$ of a dynamical system that exposes the system to spontaneous bursts. When a trajectory encounters the blue region $\mathcal{A}_p$, an extreme burst occurs. Because this region is part of the attractor, this burst occurs periodically during the life time of the system.

2.2.3 Type III-B: Sensitivity to external shocks

Extreme events driven by external shocks can also be described more intuitively using a dynamical system approach. These events occur because of the existence of two disjoint attractors within the attracting set. Depending on which basin of attraction the initial conditions belong to, the system can be driven to one attractor or another. This situation is illustrated in Fig. 2.4.

Alternatively, if the system is exposed to external perturbation localized in time, these external perturbations can drive it towards one basin of attraction or another. The configuration in phase space would look the same as in the case of variation of initial conditions.

2.2.4 Type III-C: Sensitivity to continuous perturbations

The last class of event involves an uncertainty on the dynamics of the system itself. In this case, there is an imprecision on the geometry of the attractor and on the motion of the system on the attractor. In this case, an extreme event occurs

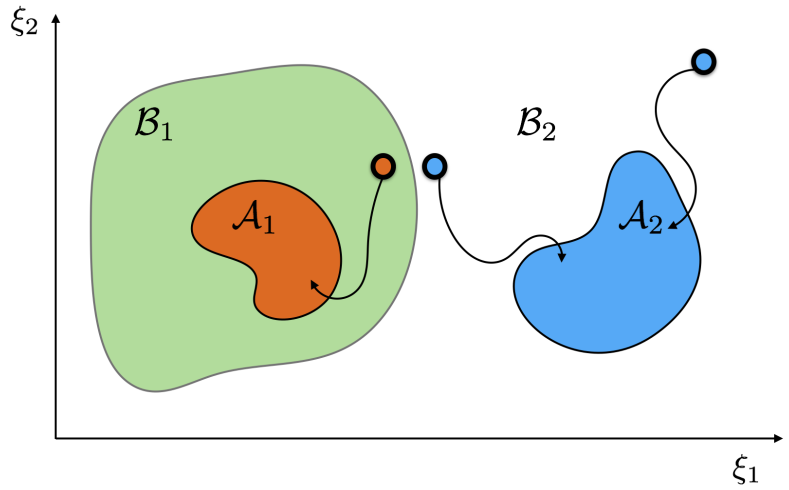

Figure 2.4: Illustration of the phase space in which a dynamical system evolves. The space is partitioned between two attractors $\mathcal{A}_1$ and $\mathcal{A}_2$ of basins of attraction $\mathcal{B}_1$ and $\mathcal{B}_2$. The arrows denote the time evolution of the dynamical system. Initial conditions are denoted by red dots when they are attracted by $\mathcal{A}_1$ and blue dots when attracted by $\mathcal{A}_2$.

	Type I	Type II	Type III-A	Type III-B	Type III-C
Trigger	$\boldsymbol{\mathcal{I}}$	$\delta\boldsymbol{\xi}^0$ or $\delta\boldsymbol{\zeta}$	none	external shock	$\delta\mathcal{F}$
Attracting set	non-relevant	non-relevant	existence of pathology	disjoint attractors	$\lvert\frac{\delta\mathcal{A}}{\delta\mathcal{F}}\rvert \gg 1$,
Output sensitivity	$\boldsymbol{\mathcal{Q}}(\boldsymbol{\xi},\mathcal{I}) \approx \boldsymbol{\mathcal{Q}}(\boldsymbol{\mathcal{I}})$	$\lvert\frac{\delta q}{\delta\boldsymbol{\xi}^0}\rvert \gg 1$ or $\lvert\frac{\delta q}{\delta\boldsymbol{\zeta}}\rvert \gg 1$	$\exists\boldsymbol{\xi}_c \in \mathcal{A}$, $\lvert\frac{\delta q}{\delta\boldsymbol{\xi}}\rvert_{\boldsymbol{\xi}_c}\rvert \gg 1$	$\lvert\frac{\Delta q}{\Delta\mathcal{A}_i}\rvert \gg 1$	$\lvert\frac{\delta q}{\delta\mathcal{A}}\rvert \gg 1$

Table 2.1: Classification of extreme events.

because the outcome is sensitive to small variations in the geometry of the attractor and in the governing equations.

All the different types of extreme events mentioned here are summarized in Tab. 2.1. The events are classified based on their triggering mechanism and are enables by the properties of the attracting set and the sensitivity of the output.

For all of these situations, if the goal is to predict or understand how the extreme event occurs, it is necessary to use an objective approach to characterize the dynamics of the system. For statistically stationary systems, this is equivalent to characterizing its attractor. Characterizing the dynamics of a high-dimensional system is however

not easy, as the system's dynamical behavior changes over time as the system travels through phase space. Therefore, the goal is to find a global metric that describes the dynamics of the system over its entire trajectory. For this purpose, it is proposed in this dissertation to use the Lyapunov analysis as a global quantifier of the dynamics of the system.

2.3 Lyapunov analysis: a tool for characterizing the dynamics of turbulent flows

2.3.1 Characterizing the dynamics with a global approach

Characterizing the dynamics of a system implies describing the way a system evolves over time, from one point of phase space to another. The first approach is to determine this behavior over short time scales: starting from one point in phase space, the goal is to understand the way the system will evolve over a finite time. For example, this is the main goal of the weather forecasting problem. In this context, the description of the dynamics is local in the sense that the system starts from one particular set of initial conditions. Besides its applicability for a finite time only, this analysis typically requires to perform an ensemble of simulations starting from many different possible initial conditions [3, 63, 64] as the true initial conditions of the system are not exactly known (see Sec. 2.2.1). Another approach describes the dynamics from a global point of view irrespective of the initial conditions. Global dynamics can be characterized by identifying, for example, bifurcations [69]. In short, the system of equation is parameterized, and one looks for the evolution of the long-time behavior of the system (its attracting set) as the parameters change. Alternatively, the global stability properties of equilibrium points can be sought. There, the goal is to understand the dynamics of the system near equilibrium points by evaluating the impact of any arbitrary perturbation on the system. These two global points of view

are at the origin of the Lyapunov analysis.

2.3.2 History of Lyapunov exponents

Among many other contributions, Aleksandr Mikhailovich Lyapunov has had a profound impact on ways to characterize the global dynamics of a dynamical system. The field of dynamical systems theory was particularly fertile when Lyapunov worked on his doctorate thesis. One of his contemporaries being Henri Poincaré who was at the origin of the Poincaré recurrence theorem mentioned in Sec. 2.2.2. Lyapunov was particularly interested in characterizing the stability properties of dynamical systems near equilibrium points. In particular, he introduced different definitions of stability, including the exponential stability that asserts that some equilibrium points can attract perturbed solutions of the system at least as fast as some exponential rate. This exponential rate has commonly been named the Lyapunov exponent (LE).

Lyapunov's goal was to obtain the stability properties of the system without integrating its governing equations. This motivation led him to introduce the concept of Lyapunov function [70]. Several decades later, it was found by Oseledet [71] that the LEs can, in fact, characterize the global dynamics of the system, and not only equilibrium points. Interestingly, the practical computation of these exponents requires integrating the governing equations of the dynamical system, contrary to the initial motivation of Lyapunov. The numerical algorithms for the computations of the LEs are extensively discussed in Chap. III.

2.3.3 Oseledet's theorem

Formally, Oseledet's theorem [71, 72] states the following

Theorem II.1 (Multiplicative Ergodic Theorem (MET))**.** *Let E be a subset of the phase space and F be a smooth measurable map or flow that preserves the measure ρ. Let $T_{\boldsymbol{\xi}}$ denote the tangent linear operator of the map F at the point $\boldsymbol{\xi}$ and note*

$T^n_{\boldsymbol{\xi}} = T_{F^{n-1}\boldsymbol{\xi}} \cdot ... \cdot T_{F\boldsymbol{\xi}} \cdot T_{F^0\boldsymbol{\xi}}$,

then

$$\lim_{n\to\infty} (T^{n*}_{\boldsymbol{\xi}} T^n_{\boldsymbol{\xi}})^{1/2n}$$

exists, depends on $\boldsymbol{\xi}$ *and is written* $\Lambda_{\boldsymbol{\xi}}$.

In particular, the eigenvalues of $\Lambda_{\boldsymbol{\xi}}$ *exist, are noted* $exp(\lambda^1_{\boldsymbol{\xi}}) < ... < exp(\lambda^p_{\boldsymbol{\xi}})$ *and correspond to eigenspaces* $U^1_{\boldsymbol{\xi}}, ..., U^p_{\boldsymbol{\xi}}$.

Let $V^r_{\boldsymbol{\xi}} = U^1_{\boldsymbol{\xi}} + ... + U^r_{\boldsymbol{\xi}}$,

then $\forall \delta\boldsymbol{\xi} \in V^r_{\boldsymbol{\xi}} \backslash V^{r-1}_{\boldsymbol{\xi}}$

$$\lim_{n\to\infty} \frac{1}{n} log \left\| T^n_{\boldsymbol{\xi}} \delta\boldsymbol{\xi} \right\| = \lambda^r_{\boldsymbol{\xi}}.$$

In the theorem, the measurable map in the theorem is the dynamical system, and the tangent linear operator is its Jacobian. The notation $(.)^*$ denotes the adjoint of an operator. A measure preserving map is such that the image of any subspace of the phase space by the map does not change the measure of the subspace. This property is valid for statistically stationary flows and is a consequence of the Liouville theorem. The power of this theorem lies in the fact that very few assumptions about the dynamical system are required.

The logarithm of the eigenvalues of $\Lambda_{\boldsymbol{\xi}}$ can be interpreted as the exponential rate (expressed in s^{-1}) at which a perturbation would evolve. For a chaotic system, at least one strictly positive exponential rate can be found. The largest exponential rate provides a horizon time over which prediction can be made before an exponentially growing uncertainty takes over.

2.3.4 The ergodic assumption

Proposition II.2. *If the measure* ρ *is an ergodic measure with respect to the map, the eigenvalues of* $\Lambda_{\boldsymbol{\xi}}$ *do not depend on* $\boldsymbol{\xi}$.

Under the hypothesis of ergodicity, any orbital average in phase space is equal to its time average (see for example Ref. [68]). Therefore, each $\lambda^r_{\boldsymbol{\xi}}$ is constant along a trajectory. This result can be shown by recognizing that the temporal average used to construct the Lyapunov exponents is independent of the starting time. By invoking the fact that $\lambda^r_{\boldsymbol{\xi}}$ are continuous functions in phase space and using the Poincaré recurrence theorem, it can be obtained that the exponents are constant everywhere. [73].

Note, however, that this property does not guarantee that the eigenvectors are independent on $\boldsymbol{\xi}$. In fact, the evolution of the eigenvectors with $\boldsymbol{\xi}$ can help characterize the dynamics of the system [73].

The question of the applicability of the ergodic assumption to turbulent flows is examined next. Proving the ergodicity of the system requires to prove that the orbital average of any function is equal to its temporal average. It is, therefore, easier to disprove ergodicity than to prove it [68]. Up to now, it is still unclear whether turbulent flows can be considered ergodic. Nevertheless, some encouraging findings indicate that it is not unreasonable to assume ergodicity for the systems of interest [74].

A system that is on its attractor is statistically stationary and will be assumed to be ergodic. As a result, the eigenvalues of the matrix $\Lambda_{\boldsymbol{\xi}}$ are global quantifiers of the dynamics of the system. These eigenvalues quantify the growth rate of perturbations in the long-time limit, and are used in this dissertation to characterize the attractor.

2.3.5 Lyapunov exponents

For a dynamical system given by

$$\boldsymbol{\xi}^{n+1} = F(\boldsymbol{\xi})\boldsymbol{\xi}^n, \tag{2.8}$$

where n denotes the timestep, the $r-th$ Lyapunov exponent is given by

$$\lim_{n\to\infty} \frac{1}{n} \log \left\| T^n_{\boldsymbol{\xi}} \boldsymbol{u} \right\|$$

where $\boldsymbol{u} \in V^r_{\boldsymbol{\xi}} \backslash V^{r-1}_{\boldsymbol{\xi}}$. The LE is defined as a long time limit, and its finite time counterpart is called a finite-time Lyapunov exponent (FTLE). As opposed to the LE, which is a global quantity, the FTLE depends on $\boldsymbol{\xi}$ and measures the local expansion rate of perturbations. Thus, the FTLE are time-varying, and the LE are not.

In this dissertation, the vector $\boldsymbol{u}$ is a field, and in that case, one typically refers to the associated LEs as quantifiers of Eulerian chaos. There also exists a large body of literature in fluid mechanics [75, 76], where LEs refer to Lagrangian chaos, i.e., the deformation rate of fluid particles. From a numerical standpoint, these LEs are constructed by seeding inert particles that move with the local flow velocity and measuring their rate of separation in the three spatial directions. The latter definition of LEs has been popularized by their ability to identify large coherent structures (LCS), which has important applications in oceanic flows. For example, it can help tracking the spread of oceanic pollutants and mitigate their impact on the coast [77]. There exist different ways of computing the Lagrangian LEs, namely the finite-size method [78, 79] and the finite-time method [80]. An illustration of the capability of the finite-time method to identify the ridges of the LCS in a turbulent flow is illustrated in Fig. 2.5. Here, fictional particles are seeded in a periodic box filled with a turbulent flow with a $Re_\lambda = 22$, where Re_λ represents the Taylor microscale of the flow. The rate at which particles move away from each other during one eddy turnover time gives the field of the Lagrangian LE, and the large values of the Lagrangian LE delineate the ridges of the LCS. Additional details about the computational methods can be found in Ref. [81].

It is stressed here that while it is tempting to link Lagrangian and Eulerian LEs, there exists no mathematical equivalence between them. In particular, a chaotic Eulerian field may not lead to chaotic behavior of particles seeded in it [82]. In

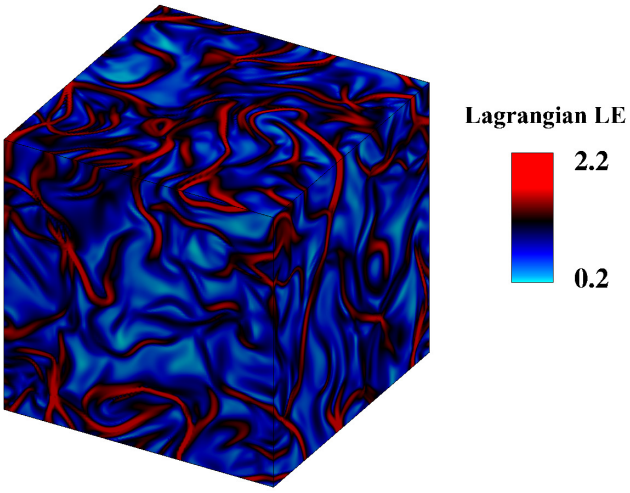

Figure 2.5: Example of the calculation of the Lagrangian LE for a turbulent flow in a box with $Re_\lambda = 22$.

this dissertation, only the Eulerian LEs are considered. Here and in the rest of the chapters, the set of all the Eulerian LEs is called the Lyapunov spectrum (LS) or the LE spectrum, unless specified otherwise.

2.3.6 Orthogonal Lyapunov vectors

It can be shown that by defining the matrix $\Lambda_{\boldsymbol{\xi}}$ (also called the Oseledet matrix [73]) using the inverse of the dynamical system, the same Lyapunov exponents can be recovered. The Lyapunov vectors (the eigenvectors of the Oseledet matrix) can then be defined in two ways: using the forward or the backward dynamics, respectively leading to the forward Lyapunov vector (FLV) and the backward Lyapunov vector (BLV). These two sets of vectors are orthogonal since the Oseledet matrices are symmetric. However, they do not necessarily coincide [73]. An illustration of this problem is provided in Ref. [83] for a simple system. Intuitively, the first few positive FLVs describe the perturbations to which the dynamical system is the most sensitive. The first few positive BLVs describe the chaotic response of the system to

perturbations.

For reference, these LVs receive a variety of names in the literature. The nomenclature orthogonal Lyapunov vector (OLV) [84] is used typically for the backward Lyapunov vector to distinguish them from other LVs that are not necessarily orthogonal. The name Gram-Schmidt vector (GSV) is used [73, 85] in reference to the numerical method used to compute them (more details in Chap. III).

Overall, the construction of the forward and backward Oseledet matrix adds a layer of complexity in the definition of the LVs. Since the forward and backward LVs do not coincide, they cannot, separately from each other, uniquely characterize the dynamics of the system. Further, the constraint of orthogonality introduces a dependency of these vectors on the definition of the scalar-product used. A more robust definition of Lyapunov vectors was provided with the introduction of the concept of the covariant/characteristic Lyapunov vector (CLV) [72].

Proposition II.3. *Let v^n be a CLV defined at the point $\boldsymbol{\xi}$ in phase space, encountered at the n-th step.*

Then $T^n v^n = \Lambda v^{n+1}$,

where Λ is the local expansion rate of the perturbation. The CLVs are said to be covariant with the dynamics of the system. By construction, the CLVs are defined as a linear combination of the BLVs in the following way [73, 85]

Proposition II.4. *Let $v_r(\boldsymbol{\xi})$ be the r-th CLV and $g_i(\boldsymbol{\xi})$ be the first r BLVs,*

then

$$v_r = \sum_{i=1}^{r} \alpha_i g_i,$$

where $\alpha_i \in \mathbb{R}$.

The BLVs are therefore particularly interesting since they are closely related to the covariant vectors of the system. This property will be used in Chap. IV to derive

properties about the CLVs from the BLVs. Further, the BLVs are physically relevant for the analysis of the system since they belong to the attractor of the system as opposed to the FLVs [83]. It is, therefore, possible to interpret the BLVs to gain some understanding of the dynamics of the system when it reaches its attractor. In the rest of the dissertation, the BLVs will be the main focus of the analysis conducted. Finally, it is emphasized that unlike LEs, the BLVs are instantaneous quantities and are not global quantifiers of the system dynamics. Therefore, time averages of the BLV are necessary to interpret them with a global point of view. This approach is used in Chap. IV and Chap. V.

2.3.7 Variants of the Lyapunov analysis

Some variants of the Lyapunov analysis are routinely used, mainly to evaluate the propagation of uncertainties. For example, in weather forecasting problems, most of the uncertainty about future predictions stems from the imprecise definition of initial conditions. With time, uncertainties accumulate and need to be quantified.

2.3.7.1 Singular vector method

Starting from the best guess of initial conditions, one can typically estimate the range of magnitude of error without knowing the distribution of error. The goal is to find the worst impact of an initial error $\boldsymbol{\epsilon}^0$ on a certain metric for the system at a later time (after n timesteps). The evolution of any perturbation $\boldsymbol{\epsilon}$ can be described by the following equation

$$\boldsymbol{\epsilon}^n = L\boldsymbol{\epsilon}^0, \tag{2.9}$$

where L is the product of the tangent linear model at the first n timesteps. It can be shown that the initial perturbation $\boldsymbol{\epsilon}^0$ that maximizes $\frac{\|\boldsymbol{\epsilon}^n\|}{\boldsymbol{\epsilon}^0}$, is nothing else than the first singular vector (SV) of the matrix $L^T L$ [86]. This SV is closely related to the

first FLV but is defined over a finite time interval. In the infinite time limit, the SVs can be shown to converge to the FLVs [87]. This approach is routinely used by the European Center for Medium-Range Weather Forecasts (ECMWF) [63] to provide uncertainty estimates on weather forecasts.

2.3.7.2 Bred vector method

The breeding method is another derivative of the Lyapunov analysis, also used in the field of weather forecasting. The practical need is the same as mentioned above (evaluate the uncertainty of future predictions), but the mathematical problem is different. Instead of trying to find the initial perturbation that would lead to the largest possible future error, the goal is to find an approximation of the difference between the true initial conditions and the best initial guess [64]. This is achieved by using a derivative of the BLV, called the bred Vector (BV). Using the best initial guess and several possible approximated differences, the forward model is run to approximate the distribution of the prediction at a later time.

In terms of dynamical system vocabulary, one wants to sample elements of the attractor that correspond to the sparse measurements available for the initial conditions. For this purpose, the first BLV is a natural choice, since, by definition, it lies on the attractor. In fact, the calculation of the BVs follows closely that of the BLVs. This approach is routinely used by the National Center for Environmental Prediction (NCEP).

2.3.8 Physical interpretation of Lyapunov exponents and vectors

To be of any practical use, the relation between the outcome of the Lyapunov analysis and physical quantities need to be precisely established. In this section, the goal is to explain how and to what extent the LE and BLV can be used to illuminate the dynamics of a physical process.

The LE (time average of the FTLE) are properties of the system itself (as opposed to being local properties of the phase-space). The LE can be understood as the inverse of a timescale over which a perturbation amplifies. When considering the largest LE, it provides an estimation of the time-horizon over which state predictions can be done. However, the LE is only an estimate of this horizon time since it characterizes the growth rate of a perturbation over a long period of time. In practice, perturbations amplify at different rates depending on the underlying state of a system. For example, perturbations might amplify faster when a macroscopic transition occurs in the system [88]. In this work, the focus is solely on the LE since it can indicate how to appropriately model the dynamics of the system (See Sec. 2.4.1).

The main advantage of BLV is that it allows extracting the unstable and stable manifold of the system considered. Typically, turbulent flows rely on scale separation to be representative of stability separation. However, there can be a more clear separation between unstable and stable modes that can lead to a more clear description of the dynamics of the system. From a physics point of view, the Lyapunov vectors can be related to the stability properties of a flow. They allow identifying the parts of the flow (in physical space) that lead to instability. When the flow experiences a macroscopic change, the BLV indicate the path that the system follows during the transition. If the BLV can be related to physical quantities, the cause of the transition can be explained [88, 89]. The BLV associated with the positive exponents span the unstable manifold while the ones associated with negative exponents span the dissipative manifold. It is not a priori possible to assign a particular physical role to each one of the BLV, just like it is not possible to assign a role to each one of Fourier modes, or other types of modes.

2.4 Benefit of Lyapunov analysis for extreme events

The Lyapunov analysis described in the previous section provides tools that can help characterize the dynamical behavior of the system. These tools are useful for different aspects of the prediction of extreme events. It is stressed that other tools could also be useful (the reader is referred to Ref. [90] for an extensive review), but that the Lyapunov analysis can already cover many different topics. This section describes how the Lyapunov analysis can be used to answer the five prediction questions listed in Chap. I.

2.4.1 Predict for real-time control

First, as mentioned earlier, the first LE is related to the growth of initial perturbation over time. It allows quantifying the horizon time over which any prediction can be made without having initial errors contaminate the result. Therefore the first LE indicates to what extent predictions can be made about the future state of the system.

Second, predicting an upcoming extreme event requires to execute a model that captures the dynamics of the extreme event. As discussed in Sec. 2.1, the coarse-graining approach is not suited for capturing the full dynamics of the system. Nevertheless, it is necessary to coarse-grain the system in order to make any modeling approach computationally tractable. A natural question ensues: what is the minimum amount of coarse-graining necessary to capture reasonably well the dynamics of the system? For a statistically stationary problem, the goal is to find the number of degrees of freedom that compose the attractor, i.e., the geometric dimension of the attractor. Incidentally, the Lyapunov exponents can also be used for this purpose, using the Kaplan-Yorke (KY) conjecture [91].

Formally, the KY conjecture defines

$$D_{KY} = i + \frac{\sum_1^i \lambda_j}{|\lambda_{i+1}|}, \tag{2.10}$$

where D_{KY} is the Kaplan-Yorke dimension, λ_j denotes the j^{th} LE, and i is the last index such that $\sum_1^i \lambda_j \geq 0$. The conjecture states state $D_{KY} = D_I$, where D_I is the information dimension of the attractor. Precise definitions for the information dimension can be found in Ref. [92]. Intuitively, the information dimension is the amount of information necessary to locate a point on an ensemble. In the context of attractors, it is therefore related to the number of degrees of freedom of the system [93, 94]. This conjecture has proven to be wrong for some systems [95] which have later been argued to be only pathological. The KY formula can thus provide guidelines in the design of reduced-order models that still capture the dynamics of the system. This property of the LE will be exploited in Chap. IV and V.

2.4.2 Predict unobserved events

Ideally, a numerical simulation tailored to capture extreme events should be able to inform about the existence of an extreme event before it is encountered. While it is not the focus of this work, it has been demonstrated that the FTLEs can be used to explore the phase space, in search of extreme events. The technique relies on using the FTLE as an indicator of the local (in phase space) degree of chaoticity that is associated with the propensity of an extreme event. Many pairs of walker/crawler are seeded in phase space and look for the most chaotic part of the attractor until they isolate outliers. This method is commonly called Lyapunov weighted dynamics (LWD) and is illustrated for a two-dimensional system in Fig. 2.6. Although this technique could be used for systems with arbitrarily high dimensions, it has been used only with smaller systems so far.

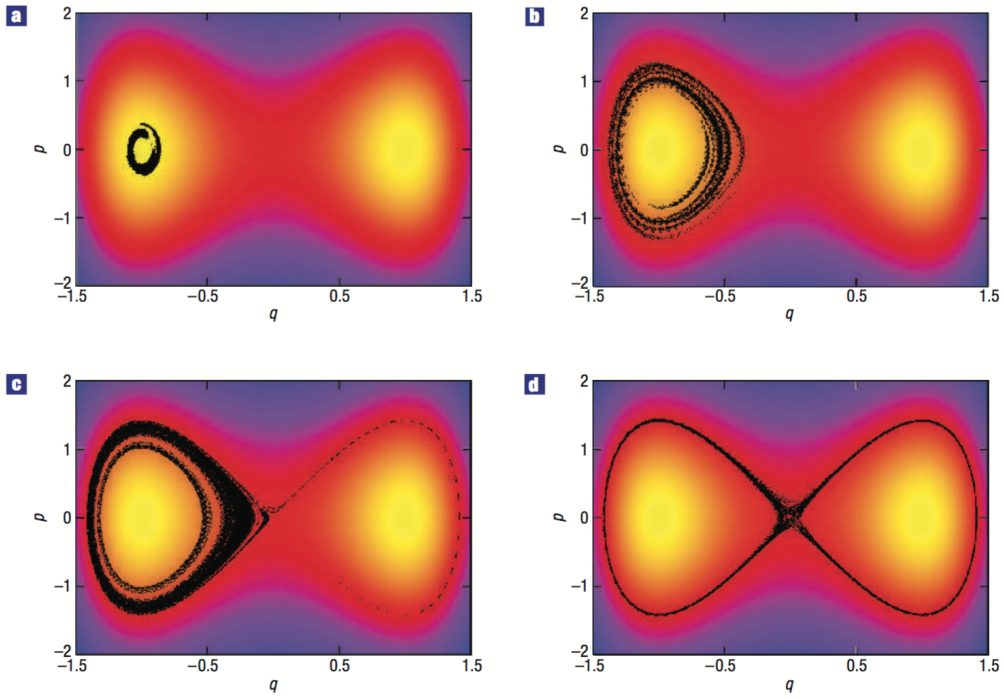

Figure 2.6: Contours denote a potential surface used to construct a dynamical system. The dots are walkers that explore the phase space in search of the most chaotic trajectories. Such trajectories are obtained by searching for large values of short-time Lyapunov exponents. Reproduced from [13].

2.4.3 Bound quantities of interest

If the goal of the extreme event analysis is to find the most extreme scenario at the final time, the SV analysis (Sec. 2.3.7.1) can, for example, be used. A finite-time version of the first FLV is computed to find the maximal propagation of uncertainty for a certain metric. This method is suited for transient problems such as weather prediction, or the high-altitude relight problem introduced in Chap. I.

2.4.4 Understand how the extreme event occurs

From the LVs, one can extract the response of the system to perturbations (BLVs) and find the perturbations to which the system is the most sensitive (FLVs). The CLVs can be extracted from the BLVs and are the directions that expand or contract under the dynamics. They allow to probe the stability properties of the attractor at

different points of the phase space and understand how perturbations grow during the lifetime of the system.

The LVs are particularly powerful to describe the growth of instabilities in flow fields. For example, using the first BLV, Vastano and Moser [88] found that the chaotic behavior in a Taylor-Couette flow occurred due to a Kelvin-Helmholtz instability. Inubushi et al. [89] identified that streamwise vortices were at the origin of streak regeneration in Couette turbulence. Xu et al. [96] pinpointed the crucial role of walls in the generation of instabilities in Rayleigh-Bénard convection with side walls.

2.4.5 Estimate the probability of an extreme event

There is at the moment no existing application of the Lyapunov analysis for predicting the probability of an extreme event. The main issue for probability estimation of rare events is to sample the phase space efficiently. Additional details and context will be provided extensively in Chap. VI. It can be noted that the work on BV explained in Sec. 2.3.7.2 can, in fact, serve as a basis for sampling realizations of turbulent flows. This topic will not be covered in the thesis and is left for future work, but illustrates other capabilities of the Lyapunov analysis.

2.5 Other approaches for the analysis of extreme events

As explained above, the Lyapunov analysis has applications that range over the whole spectrum of predictive questions relevant for extreme events (See Chap. I, Sec. 1.3). Other noteworthy approaches have been introduced in other fields, and their relevance for turbulent combustion application is evaluated below.

2.5.1 Predict for real-time control

Prediction for real-time control is one of the target questions that has received the most attention in the past. The main strategy consists in finding a *precursor*,

that is, a variable that one can track and which variations inform about an imminent extreme event. Different types of precursors have been derived.

The first type of precursor is obtained from the underlying mechanism of an extreme event, when it is well-understood. As an example, Cousins and Sapsis [97] derived precursors for the occurrence of rogue waves by separating each wave group and performing the so-called "Gabor transform" which quantifies the rate of change of the energy of waves. For turbulent combustion applications, similar precursors have been defined, for example in the case of the swirling flame detachment already mentioned in Chap. I. Several experimental investigations [6, 38] found that the flame detachment event was correlated with the existence of a precessing vortex core (PVC). To predict ahead of time the detachment, it was proposed to track the asymmetry of the flow field. This kind of precursor could only be obtained because prior knowledge about the flame detachment mechanism existed. Ad-hoc precursors can be valuable for turbulent combustion, however only to tackle extreme events that are already well-characterized.

For problems where little is known about the onset of the extreme events, the ad-hoc strategy is not suitable and should be replaced by a more systematic procedure. Using the so-called optimally time-dependent (OTD) modes [98], precursors of extreme dissipation events could be predicted for Kolmogorov flows [99]. Incidentally, OTD modes have also been shown to be intimately related to the BLV [100]. This opens the path to using the outcome of the Lyapunov analysis as a precursor of extreme events. More recently, Farazmand and Sapsis [101] formulated an optimization problem to find the optimal system state that grows the fastest over a short period of time. In particular, this rate was constrained to trajectories that lie on the attractor, which allows for the prediction of spontaneous bursts. This methodology was applied by Blonigan et al. [102] to predict extreme dissipation in turbulent channel flows. There, a precursor based on the distance to the optimum was shown to

be successful at predicting the occurrence of the spontaneous extreme event. These high-dimensional examples are encouraging for applications to turbulent combustion. It is, however, unclear whether the precursors provide an optimal horizon time and are worth the computational investment required.

More practical precursors have been identified in realistic systems using measurement data. In particular, the extreme and non-extreme trajectory of the system in phase-space can be constructed using experimental measurement and classification techniques such as clustering [7, 103] or symbolic dynamics [104]. These techniques can then be useful to detect anomalies ahead of time in realistic systems. However, the precursors inherently depend on the availability of data, which is not guaranteed in the case where the extreme event is also rare.

2.5.2 Predict unobserved events

Engineering applications fundamentally differ from geophysics with regard to the parameters of the system. Operating conditions can be changed depending on the desired output of the device and can lead to the emergence of extreme events. Unlike extreme events mentioned in Chap. I Sec. 1.2.3, the extreme behavior here is controllable and is only a function of the macroscopic parameters of the problem. In the case where many parameters can be adjusted, it can be tedious to explore the space of operating conditions in search of the limit between stable and unstable states. Some approaches, including the identification of critical states based on growth rates on the attractors, have been developed [105]. These methods are directly applicable to combustion problems, as long as the model used is capable of capturing such extreme events.

2.5.3 Understand how the extreme event occurs

Anomaly detection techniques that extract the trajectory of the system in its normal and anomalous operation can also be used to understand how an extreme event occurs, by simply analyzing its phase-space trajectory. For example, using clustering techniques [7, 103], it is possible to extract the behavior of a system around the emergence of an extreme event. The limitation is the same as for the precursors: enough data needs to be collected. These techniques are therefore applicable for extreme non-rare events. The applicability of data-driven tools is limited to lab experiments that can reproduce an extreme event with a high frequency. The knowledge gained about the process that leads to the extreme event can then be hopefully used in a practical system, where the extreme event is likely rare.

2.6 Summary

In this chapter, the benefit of adopting a dynamical system point of view when studying extreme events was described. It allows to gain an understanding of the dynamical behavior of the system and describe the growth of instabilities. The set of Lyapunov exponents obtained from the Lyapunov analysis can help characterize the global dynamics of the system and has applications over all the predictive questions for extreme events that were listed in Sec. 1.3. The Lyapunov vectors characterize only the local dynamics, and their statistics will need to be extracted in order to derive global dynamical properties. Unless the finite-time counterpart of LE and LV is used, this analysis can only be conducted in the context of statistically stationary flows. By using it on canonical configurations that are relevant for turbulent combustion, it is hoped that the conclusions about the emergence of extreme events will hold in non-statistically stationary flows. The rest of the thesis describes how the Lyapunov analysis can be deployed for statistically stationary turbulent inert and reacting flows.

CHAPTER III

Numerical convergence of the Lyapunov spectrum

In Chap. II, the importance of the dynamical system analysis for the prediction of extreme events was discussed. In particular, the Lyapunov analysis was shown to be a powerful tool for characterizing the dynamics of a system. In this Chapter, numerical methods for computing the Lyapunov exponents and Lyapunov vectors are reviewed. The numerical convergence of the procedure for the problems of interest is also examined. This chapter is partially based on the work [106].

3.1 Numerical methods for the Lyapunov analysis

The Lyapunov exponents and vectors are defined with respect to the Oseledet matrix that was introduced in Sec. 2.3.6. Direct construction of this matrix is not practically feasible since it contains exponentially diverging terms [73, 83]. Instead, the Lyapunov exponents and vectors should be constructed by resorting to alternative numerical strategies.

3.1.1 Computing the Lyapunov exponents

The computation of the LEs received most of the attention early on, mainly because there is less ambiguity in the definition of the LEs compared to the LVs. The simultaneous seminal work of Benettin et al. [107, 108] and Shimada et al. [109] led to

the development of a numerical method able to provide the LEs of chaotic dynamical systems. This method is used throughout the dissertation and is therefore described in detail below.

Instead of assembling the Oseledet matrix, this method consists of running multiple realizations of the system, each one being a slightly perturbed copy of the reference simulation. Since the system of interest here is chaotic, any perturbation, no matter how small initially, will exponentially expand until reaching saturation (see Ref. [110] for characterization of saturation in the context of Lyapunov analysis). When reaching saturation, no matter its orientation, the perturbation cannot grow because of the physical constraints of the system. Therefore, it is not possible to compute the LEs of the system if perturbations reach the saturation state. To avoid saturation of the perturbations, they are intermittently renormalized. Furthermore, irrespective of their initial orientations, perturbations tend to align in the direction along which the system responds the most to them. As a result, numerical problems arise when distinguishing the growth rates of different initial perturbations. This problem can be again circumvented by periodically orthonormalizing the perturbations, instead of simply normalizing them. The orthonormalization procedure is carried out using a Gram-Schmidt algorithm [111, 112], which led to the naming of Gram-Schmidt vectors introduced in Sec. 2.3.6. Algorithm 3.1 summarizes and formalizes the procedure explained above. To compute the first m LEs, $m+1$ simulations are evolved simultaneously, where m of them are perturbed by $\delta\boldsymbol{\xi}$ about an unperturbed baseline solution which is also evolved. All simulations are advanced for k_s timesteps after which the m finite-time estimates are computed. The perturbations are then orthonormalized. After each orthonormalization, m FTLEs are obtained. The LEs are then obtained by repeating this procedure N_s times and averaging the FTLEs over the N_s cycles. In the following, $\mathcal{F}_k$ is the non-linear operator that advances a solution vector for k timesteps of size Δt:

Algorithm 3.1: Benettin's algorithm

Randomly initialize $\{\delta\boldsymbol{\xi}_j\}_{1,m}$, orthogonal with norm $\left\|\delta\boldsymbol{\xi}_j\right\| = \varepsilon$
for $i = 1, N_s$ **do**
    for $j = 1, m$ **do**
        $\delta\boldsymbol{\xi}_j = \mathcal{F}_{k_s}(\boldsymbol{\xi} + \delta\boldsymbol{\xi}_j) - \mathcal{F}_{k_s}(\boldsymbol{\xi})$
    end for
    Orthogonalize $[\delta\boldsymbol{\xi}_1, ..., \delta\boldsymbol{\xi}_m]$.
    for $j = 1, m$ **do**
        $\Lambda_j = \frac{1}{k_s \Delta t} log(\frac{\left\|\delta\boldsymbol{\xi}_j\right\|}{\varepsilon})$
        $\lambda_j = \lambda_j + \frac{1}{N_s}\Lambda_j$
    end for
    Normalize $[\delta\boldsymbol{\xi}_1, ..., \delta\boldsymbol{\xi}_m]$, with norm ε
    $\boldsymbol{\xi} = \mathcal{F}_{k_s}(\boldsymbol{\xi})$
end for

$$\mathcal{F}_k \colon \boldsymbol{\xi}(t = t_0) \mapsto \boldsymbol{\xi}(t = t_0 + k\Delta t) \ \forall t_0 \tag{3.1}$$

As a side note, the algorithm described above relies on periodically applying artificial perturbations to copies of the system. Therefore, this algorithm can only be used when numerical computations are conducted. An approximation of this method can be formulated for long time-series that can be observed experimentally [113]. Experimental estimates of the LEs are useful if one wants to validate the LE calculation or characterize the dynamics of a system without resorting to multiple expensive numerical simulations. In short, the method considers that points on a trajectory that are close to one another can be interpreted as perturbed states. The deviations of these two points over time provides an estimate of the local FTLE.

3.1.2 Computing the Lyapunov vectors

Despite containing valuable information about the dynamics of the system (Sec. 2.3), computations of LVs have received significantly less attention. In fact, the method outlined in Sec. 3.1.1 was primarily designed to compute the LEs, but also provides directions for perturbations that correspond to each LE. These directions are used

to compute the next value of the local FTLE. It was shown decades later [114], that these perturbations converge in the sense that they are independent of the initial perturbation, and characterize the phase space at the location $\boldsymbol{\xi}$. Furthermore, the perturbations converge to nothing else than the BLVs for the scalar product chosen.

As explained in Sec. 2.3.6, the definition of BLVs is ambiguous as they are not invariant under time-reversal of the dynamics and they are not uniquely defined: they are dependent on the scalar product adopted. Recent advances have focused on methods that could provide the CLVs, which are not as ambiguously defined. These methods use the SVs [115] or the BLVs themselves, along with the by-products of the periodic orthogonalization [85]. In this dissertation, the method of Benettin and Shimada [107–109] will be used for all the cases investigated, and the BLVs are computed for each one of the cases. When possible, conclusions about the CLVs are also provided (see Chap. IV).

3.2 Applications of interest

In this section, the numerical procedure used to advance each one of the forward simulations involved in the calculation of each LE is detailed. In particular, the low Mach number assumption is used and justified with regard to the end application of interest.

3.2.1 Low Mach number regime

Many gas turbine applications, especially related to the combustor section, operate in the low Mach number regime, characterized by velocities smaller than 0.3 Ma, where the Mach number is defined based on local fluid properties. Even in aircraft engines, the flow speed close to the flame front is slowed down using recirculation zones, so that the flame can be stabilized inside the combustor. There, the combustion also occurs in a low Mach regime.

In the low Mach regime, the acoustic component of the Navier-Stokes equations is decoupled from the basic flow physics. Consequently, by reformulating the governing equations for this low Mach regime, it is possible to go beyond the Courant-Friedrichs-Lewy (CFL) restriction imposed by the acoustic wave speed (i.e., the local speed of sound). In many applications, this can amount an order of magnitude increase in the timestep used.

The method used here for obtaining the LEs requires multiple detailed simulations. Therefore, it is advantageous to leverage the low Mach regime and decrease the cost of each simulation. In this work, the Navier-Stokes equations are solved with a low Mach number solver that suppresses the link between the pressure and other thermodynamic variables (density, temperature, etc.). In the low Mach assumption, the pressure is decomposed as $p = p_{th} + p'$, where p is the pressure, p_{th} is the thermodynamic pressure (which has an influence on the thermodynamic variables and is held constant), p' is the non-constant hydrodynamic pressure and $p' << p_{th}$.

Note that if an extreme event involves the dynamics of pressure waves, then a low Mach solver is not suited for the analysis. Typically, in the case of thermoacoustic instabilities, the interaction between acoustic waves and the flame front should be accurately captured. Here, the low Mach solver is only used for problems that do not require to resolve the dynamics of pressure waves.

3.2.2 Low Mach number solver

Several versions of low Mach number solvers [116–120] have been formulated in past. The main differences amongst these methods lie in the formulation of pressure correction, in the arrangement of variables (staggered or collocated), the time advancement of variables (staggered or not), and discretizations that satisfy secondary conservation properties (kinetic energy, enstrophy, etc.). Here, the general framework is described. For variable density flows, the Navier-Stokes equations are written as

Eq. 2.1 and Eq. 2.2. In many reacting flow applications, energy release from these chemical reactions is assumed to affect only the internal energy, leading to a change in density and temperature of the fluid. An important corollary is that in low Mach number solvers, the density variations are assumed to be entirely decoupled from pressure fluctuations. For such applications, some techniques parameterize density changes based on a transported scalar, which describes the thermochemical state (see, for instance, references within [52, 121]). Here, additional transport equations of scalar quantities are solved (Eq. 2.3).

The right-hand side of the scalar transport equation is written as $RHS_{\boldsymbol{\phi}}$. The momentum transport equations are advanced such that continuity is enforced at each timestep through a projection algorithm. In low Mach number solvers, this projection is done using the computed pressure field. One such projection algorithm (semi-implicit fractional timestep [122]) is shown in Algo. 3.2 with Euler time discretization with a timestep Δt. Continuous derivatives are used when the details of the discretization are not relevant to the low Mach procedure. The momentum equation is advanced in two separate steps: first, an intermediate momentum (also called fractional momentum) $\rho\boldsymbol{u}^*$, is advanced using the best guess of the right-hand-side of the momentum equation $RHS_{\rho\boldsymbol{u}^*}$:

$$\rho\boldsymbol{u}^* = \rho\boldsymbol{u}^n + \Delta t(RHS_{\rho\boldsymbol{u}^*}). \tag{3.2}$$

The field $\rho\boldsymbol{u}^*$ is then corrected with pressure gradient to ensure that mass conservation is enforced. With Euler-type discretization, the correction step takes the form

$$\rho\boldsymbol{u}^{n+1} = \rho\boldsymbol{u}^* - \Delta t\nabla p. \tag{3.3}$$

The pressure field that is used to correct $\rho\boldsymbol{u}^*$ is constructed such that $\rho\boldsymbol{u}^{n+1}$

Algorithm 3.2: Variable density low Mach number solver

At every grid point, initialize $\rho\boldsymbol{u}$, $\boldsymbol{\phi}$
for $n = 1, end$ **do**
    $\boldsymbol{u}^{n+1} = \boldsymbol{u}^n$, $\boldsymbol{\phi}^{n+3/2} = \boldsymbol{\phi}^{n+1/2}$
    for $k = 1, N_{outer}$ **do**
        $\boldsymbol{\phi}^{n+3/2} = \boldsymbol{\phi}^{n+1/2} + \Delta t RHS_{\boldsymbol{\phi}}$
        From $\boldsymbol{\phi}^{n+3/2}$ get $\rho^{n+3/2}$, $D^{n+3/2}$, ...
        $\rho\boldsymbol{u}^* = \rho\boldsymbol{u}^n + \Delta t(RHS_{\rho\boldsymbol{u}^*})$
        Solve $\nabla^2 p = \frac{1}{\Delta t}(\frac{\partial \rho}{\partial t} + \nabla \cdot (\rho\boldsymbol{u}^*))$
        $\rho\boldsymbol{u}^{n+1} = \rho\boldsymbol{u}^* - \Delta t \nabla p$
    end for
end for

satisfies the mass conservation constraint. The following Poisson equation for the pressure can be obtained by taking the divergence of the correction step (Eq. 3.3)

$$\nabla^2 p = \frac{1}{\Delta t}(\frac{\partial \rho}{\partial t} + \nabla \cdot (\rho\boldsymbol{u}^*)). \tag{3.4}$$

Note that inverting Eq. 3.4 is not possible in general without an additional constraint as a pressure field shifted by any arbitrary constant satisfies the Poisson equation. Various strategies are used to ensure that Eq. 3.4 is well-posed. The spatial average of the pressure can be required to be null [118] or the value of the pressure at a particular point can be fixed [117].

The low Mach number solver algorithm used here follows a time-staggered procedure: at each step, $\boldsymbol{u}$ is advanced from time n to time $n+1$ and $\boldsymbol{\phi}$ is advanced from $n+1/2$ to time $n+3/2$. Within each timestep, N_{outer} outer-iterations (typically 3) are used to couple the momentum and scalar equations [117, 119].

Because the pressure fluctuations are computed using a Poisson equation, the pressure adjusts everywhere within a single timestep to satisfy locally and globally the constraint of mass conservation. The propagation of pressure waves is not considered in the low Mach number solver. As a result, the CFL number does not depend on the speed of sound. An illustration of the contribution of pressure waves on the

flow field with and without the low Mach assumption is provided in Fig. 3.1. In the compressible solver, density evolves following the continuity equation, then the scalar fields (typically species mass fraction) evolve and affect the energy transport equation. Through the equation of state, the pressure is updated and affects the velocity. The effect of pressure on velocity is the result of a gradual transport of information at a finite rate (the acoustic speed). In the low Mach number solver, this cycle is reversed, and the energy transport equation is bypassed, thereby removing the acoustic waves.

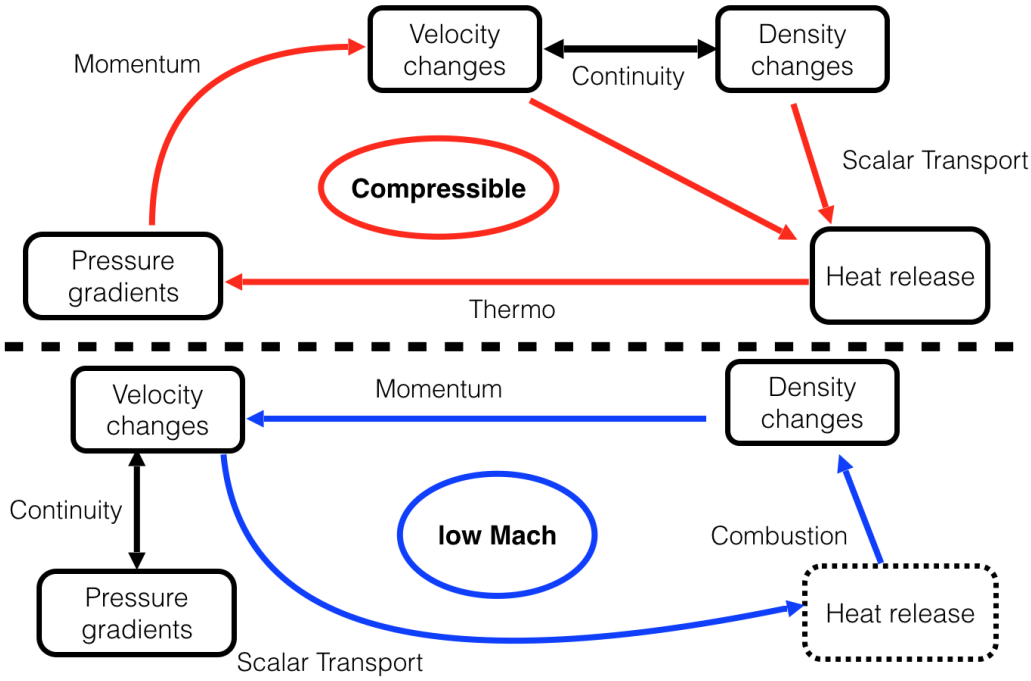

Figure 3.1: Schematic illustration of the algorithmic sequence between a compressible solver (top) and a low Mach number solver (bottom).

In the end, the timestep can be at least an order of magnitude larger than in a compressible problem which decreases the computational cost of the simulation [123]. Note that the computational gain is not exactly proportional to the ratio of timesteps between the compressible and the low Mach number solvers since the cost per timestep of the low Mach number solver is typically larger than that of the compressible solver, due to the Poisson equation solver.

3.3 Lyapunov analysis with low Mach solver

Before using the Lyapunov analysis in the context of turbulent reacting flows solved with low Mach number solvers, it is necessary to establish the convergence properties of the Lyapunov exponents, so that reliable conclusions can be obtained. In particular, the problem here is to determine how the LEs converge with the grid size and the timestep size. Keefe et al. [124] showed that refining the computational domain led to changes in the LE spectrum, even when highly accurate pseudo-spectral simulations were performed. Further, the orthonormalization procedure used to obtain the Gram-Schmidt vectors is also subject to errors [125]. Finally, the timestepping procedure was found to introduce another error in the final LE spectrum, with the conclusion that a finer temporal discretization is needed to obtain converged solutions [124]. Recently, Fernandez et al. [126] conducted a systematic study to determine the role of mesh size and order of numerical scheme on the Lyapunov exponents. While the study showed that LEs depend on the grid size and the numerical order, a clear convergence could not be established, precisely because the underlying forward solution was highly sensitive to the grid resolution.

The problem of numerical convergence of the Lyapunov spectrum is not straightforward to solve as there is no general way of obtaining a "true" LE, not affected by numerical errors. Furthermore, since the LEs are dependent on the underlying flow fields, the flow should not be affected by successive grid refinements. Finally, since the LEs are obtained from long-time averages, statistical uncertainty should be carefully be taken into account. In the next sections, a procedure to precisely evaluate the convergence properties of the LEs is developed and tested using increasingly complex test cases.

Section 3.3.1 explains how to use the Lyapunov analysis with low Mach number solvers. In Sec. 3.4, the convergence properties of the LEs are examined for a steady flow problem using a low Mach number solver. Next, the convergence properties found

are tested on a one-dimensional transient chaotic flow in order to separate numerical errors due to discretization and the approximations due to the low Mach assumption (Sec. 3.5.1). Finally, the convergence of the LE is investigated for a three-dimensional turbulent flow in Sec. 3.5.2.

3.3.1 Definition of the state vector

Establishing an analogy between a dynamical system and a low Mach solution approach for Navier-Stokes equations requires precise knowledge of the numerical procedure. In general, the state vector should be defined such that its elements at the current timestep n, are necessary and sufficient to determine the state vector at the next timestep $n+1$. To see the importance of the definition of the state vector on the computed LEs, consider an N-dimensional dynamical system. In an ideal case, perturbations of the state vector can be expressed as

$$\delta\boldsymbol{\xi} = \begin{bmatrix} \delta\xi_1^0 \\ \vdots \\ \delta\xi_N^0 \end{bmatrix},$$

where the components of $\delta\boldsymbol{\xi}$ are necessary and sufficient to express any perturbation. The "true" growth rate of a perturbation between the timestep 0 and the timestep n takes the form shown in Eq. 3.5.

$$\tau_{true} = \frac{||\delta\boldsymbol{\xi}^n||}{||\delta\boldsymbol{\xi}^0||}. \tag{3.5}$$

Now suppose that the definition of the perturbation vector is altered, for example by adding N_{alt} components in the perturbation vector $\delta\boldsymbol{\xi}$. The added components are noted $\delta\boldsymbol{\zeta}$ which is a N_{alt}-dimensional vector. Using the L_2-norm, the "altered"

growth rate of the perturbation becomes:

$$\tau_{alt} = \sqrt{\frac{||\delta\boldsymbol{\xi}^n||^2 + ||\delta\boldsymbol{\zeta}^n||^2}{||\delta\boldsymbol{\xi}^0||^2 + ||\delta\boldsymbol{\zeta}^0||^2}}. \tag{3.6}$$

A similar expression can be obtained if components are removed from the "ideal" perturbation vector definition. Assuming that $||\delta\boldsymbol{\zeta}^n|| << ||\delta\boldsymbol{\xi}^n||$ and $||\delta\boldsymbol{\zeta}^0|| << ||\delta\boldsymbol{\xi}^0||$, one can obtain that $\tau_{alt} \approx \tau_{true}$. In many flow solvers, ghost cells are used to impose boundary conditions. The above conditions are satisfied even when these cells are not imposed in the state vector. In such cases, the condition $N_{alt} << N$, and the ghost cells are not expected to exhibit sensitivity to perturbations larger than other interior cells. However, these assumptions are in general not valid if an entire field is removed ad-hoc from the state vector. For instance, the entire determination cannot be based on only one component of velocity. In such cases, $N_{alt} \approx N$. While this may seem obvious, it is important to recognize that such choices are not self-evident in timestepping algorithms that use outer-iterations within each time iteration to satisfy physical constraints. Beside the computation of the growth rates, the convergence properties of the algorithm described in Sec. 3.1.1 also depend on the orientation of the initial perturbation in the state space. With omission of variables, the orientations of the perturbation may be substantially modified, and may not guarantee convergence of the procedure.

3.3.2 State vector for low Mach number solver

At the very least, the state vector should contain all the transported variables that are independent of each other. Even if the variables are not defined at the same time locations, they are used together to define the next numerical step. Hence, the state vector should contain at least the fields $\{\rho\boldsymbol{u}, \boldsymbol{\phi}\}$. The remaining set of discrete variables to be included in the state vector needed at each timestep depends

on additional choices of the algorithm. In particular, the focus is here on the way the variables are used to form the guessed fractional momentum equation (see Algo. 3.2).

In the original formulation of the fractional timestep method [127], the fractional momentum equation contained a pressure gradient obtained from the previous timestep. In other terms, while the pressure term is solely dependent on the $\{\rho\boldsymbol{u}^*, \boldsymbol{\phi}\}$, its contribution is accumulated over time. It is then necessary to include p^n in the state vector in order to be able to write the relation between $\boldsymbol{\xi}^{n+1}$ and $\boldsymbol{\xi}^n$. Alternatively, the pressure can be left out of the state vector by setting it to zero at the beginning of each timestep. Instead of using an initial guessed pressure, one relies on outer-iterations to recover it. Here, this alternative approach is chosen in order to minimize the number of variables in the state vector. Note that in the case of variable density low Mach number solvers such as the case studied in Chap. V, the definition of the state vector needs to be slightly modified.

3.4 Convergence of LE for laminar planar Couette flow

The issue of numerical convergence of the LS was recently investigated by Fernandez et al. [126]. While they were able to conjecture the convergence with spatial discretization, conclusive results were not obtained. It was noted that as spatial discretization was refined, the flow features were changed, thereby affecting the LEs. Since LEs are obtained from a time average of expansion rates, statistical errors could also contaminate LE computations. To overcome these issues, a laminar planar Couette flow is studied here. Because the flow is laminar, no uncertainty due to time averaging is introduced, and since the attractor is a single point, the flow features are unaffected by spatial refinement. Furthermore, as noted by Keefe et al. [124], this particular test case offers the possibility to estimate analytically the true set of LEs $\boldsymbol{\lambda}$ and its associated true set of LVs $\boldsymbol{\psi}$. The rigorous link between the stability analysis and the Lyapunov theory is detailed below, and the procedure to test the

convergence of the LEs is then described.

Following Keefe et al. [124], the domain size in the streamwise (x direction), height (y direction) and spanwise directions (z direction) is [0,8π] $\times$ [-1,1] $\times$ [0, 2π]. The domain is periodic in the x and z direction. At the conditions described in Ref. [124], the viscosity is $\nu = \frac{1}{Re_\tau}$ and the streamwise velocity profile can be expressed as $U(y) = \frac{Re_\tau}{2}(y^2 - 1)$, where $Re_\tau = 34$. The analytical value of the pressure gradient can be obtained from the laminar channel flow equations. It is used for the forcing the laminar flow, as opposed to a more classical forcing term using the wall integral of the friction coefficient.

3.4.1 Orr-Sommerfeld (OS) equations

The OS equations have been formulated for several types of flows in the past [128, 129]. The OS approach uses linearized governing equations to describe the evolution of small perturbations around the base flow. The main purpose here is to extract the stability properties of a given flow. Similar to the Lyapunov-related quantities, the OS approach describes the asymptotic behavior of the system subject to infinitesimal perturbation. The OS equations take the form of a reduced set of ODEs that can be solved with a high degree of accuracy [130, 131]. Intuitively, the results of the OS analysis should be tightly linked to the results of the Lyapunov analysis. In Ref. [124], it is, in fact, argued that the LEs should match the OS temporal eigenvalues up to a certain factor. In this section, this assertion is clarified further and used to determine convergence of LEs with grid refinement.

For Couette flows, the OS equations have been formulated for two or three physical dimensions [132, 133]. Here, the three dimensional version is used. The full derivation of the three-dimensional OS equation can be found in Ref. [129, Chap 3.1]. The perturbation to the flow field can be expressed in terms of wall normal velocity and

vorticity perturbations as follows:

$$\begin{aligned}\widehat{v}(x,y,z,t) &= \widetilde{v}(y)e^{i(\alpha x+\beta z-\omega t)} + c.c.,\\ \widehat{\eta}(x,y,z,t) &= \widetilde{\eta}(y)e^{i(\alpha x+\beta z-\omega t)} + c.c.,\end{aligned} \tag{3.7}$$

where $\widehat{(.)}$ is a real field that satisfies the OS equation, $\widetilde{(.)}$ is the complex amplitude of $\widehat{(.)}$, and α, β, c are complex coefficients, and $c.c.$ denotes the complex conjugate. The governing equations for the complex amplitudes $\widetilde{v}$ and $\widetilde{\eta}$ is then obtained as

$$\begin{aligned}\Big\{(-i\omega + i\alpha U)(\boldsymbol{D}^2 - (\alpha^2+\beta^2)) - i\alpha U'' - \frac{1}{Re_\tau}(\boldsymbol{D}^2 - (\alpha^2+\beta^2))^2\Big\}\widetilde{v} = 0\\ \Big\{(-i\omega + i\alpha U) - \frac{1}{Re_\tau}(\boldsymbol{D}^2 - (\alpha^2+\beta^2))^2\Big\}\widetilde{\eta} = -i\beta U'\widetilde{v},\end{aligned} \tag{3.8}$$

where $\boldsymbol{D}$ is the derivative operator with respect to y.

The OS solution vectors are noted $\boldsymbol{\theta} \equiv \{\widehat{v}, \widehat{\eta}\}$ and are entirely defined by $\{\widetilde{v}(y), \widetilde{\eta}(y), \alpha, \beta, \omega\}$. It should be noted that α and β can hold only restricted values in order to satisfy constraints regarding periodicity in the streamwise and spanwise directions. As an illustration, let $\alpha = \alpha_1 + i\alpha_2$, where α_1 and α_2 are real numbers. Since the configuration is periodic in the x direction, with spatial period L_x, and α is uniform and constant,

$$\forall\ y,\ t,\ \widehat{v}(x=0,y,z=0,t) = \widehat{v}(x=L_x,y,z=0,t).$$

Consider a y coordinate for which the amplitude $\widetilde{v}(y) \neq 0$, then using Eq. 3.7

$$\forall\ t,\ e^{-i\omega t} = e^{-\alpha_2 L_x}e^{i(\alpha_1 L_x - \omega t)}.$$

Therefore α_2 is necessarily zero and the set of realizable values of α_1 can be restricted to $\alpha_1 = \alpha = n\frac{2\pi}{L_x}$, where n is an integer. Reproducing the same analysis in the spanwise direction, it can be shown that $\beta = m\frac{2\pi}{L_z}$ where m is an integer, and L_z is the domain size in the spanwise direction.

3.4.2 Link between Lyapunov exponents and OS eigenvalues

Consider a single LV $\boldsymbol{\psi}$. Since $\boldsymbol{\psi}$ and the real part of the OS eigen solutions satisfy the same linear perturbation equation, the LV can be expressed as a linear combination of OS eigen solutions. More formally, it can be written as

$$\boldsymbol{\psi} = \sum_j \kappa_j \boldsymbol{\theta}_j, \tag{3.9}$$

where κ_j is a real coefficient. Note that the summation is over infinite set of solutions. It is also known that the orientation of the LV $\boldsymbol{\psi}$ is constant over time since the underlying flow field is steady. Eq. 3.9 can therefore be written in the limit of infinite time. Under the assumption that all the OS eigenvalues ω are different, the RHS of Eq. 3.9 align with the direction of the OS eigenfunction that decays the least, i.e. for which $\mathrm{Im}(\omega)$ is the largest. In the limit of infinite time,

$$\boldsymbol{\psi} = A\boldsymbol{\theta}_1, \tag{3.10}$$

where A is a normalization factor taking into account the decay of the vector norms, and $\boldsymbol{\theta}_1$ is the least decaying OS eigenfunction out of the set involved in the sum in Eq. 3.9. Therefore, each Lyapunov vector $\boldsymbol{\psi}$ is oriented in the direction of one OS eigenfunction. Additionally, the norm of the LV must decay at the rate at which the OS eigenfunction decays, since these two vectors are aligned. The relation between the LEs and the OS eigenvalues is

$$\lambda = \mathrm{Im}(\omega). \tag{3.11}$$

This equivalence allows to cross-validate the computed value of the LE obtained with the low Mach number solver and the OS equation. Keefe et al. [124] used this equivalence between OS solutions and LVs but did not explicitly derive the relations shown

in this section. The above derivation clarifies the equivalence invoked in Ref. [124].

3.4.3 Convergence of LEs

3.4.3.1 Convergence procedure

The equivalence between OS solutions and LVs was used by Keefe et al. [124] to verify LS solutions. However, this approach requires that for each LV, the corresponding streamwise (α) and spanwise wavenumbers (β) be manually identified from the computed LVs. Here instead, one takes advantage of the knowledge of the full solution of the OS eigenvalue problem. The main observation is that when the perturbation for the full system is introduced based on the eigensolution for a given $\{\alpha, \beta\}$, the evolution in time retains this vector direction. As a result, the decay rate of the perturbation can be directly obtained and compared with the corresponding OS eigenvalue.

The full procedure is as follows:

- Choose a set of wavenumbers $\{\alpha, \beta\}$, and obtain the eigensolution to the OS problem. This will provide an eigenvalue that characterizes the Lyapunov exponent as shown in Eq. 3.11.
- Using the definition of η and mass conservation equations, obtain $\widetilde{u(y)}$ and $\widetilde{w(y)}$. Together with $\widetilde{v(y)}$, a full vector of perturbations of dimension equal to that of the system can obtained.
- Evolve the perturbed simulation in time and obtain the decay rate of the perturbations.

The LE convergence is evaluated in terms of the absolute error of the LEs defined as

$$\lambda_{err} = |\lambda_{computed} - \mathrm{Im}(\omega)|, \tag{3.12}$$

where λ_{err} is the absolute error for LE estimation, $\lambda_{computed}$ is the computed LE. $\mathrm{Im}(\omega)$ is therefore considered to be the best knowledge we have of the LE because it can be computed to a high degree of accuracy using the OS analysis. Using the absolute error of the LE offers the advantage of evaluating the convergence of LE close to zero.

Note that the conventional approach of using random initial perturbations has some notable disadvantages compared to this approach. First, a long transient time will be needed before the solution converges to a particular LV. Second, it is not possible to isolate a single eigensolution but feasible to compute multiple LVs at the same time, and match these with OS solutions in a post-processing step. Such matching might itself be problematic if there are large numerical errors due to the discretized set of equations used. As a result, the above procedure is equivalent to a manufactured solutions approach for verifying an algorithm.

3.4.3.2 Temporal convergence

For the temporal convergence tests, three different sets of parameters α and β are considered: $(\{0.75, 3\}, \{1.25, 2\}, \{1.5, 1\})$. For all the parameters, calculations are conducted with a $16 \times 32 \times 16$ grid. In order to evaluate the relative impact of spatial and temporal discretization, a $32 \times 64 \times 32$ grid and a $64 \times 128 \times 64$ grid are additionally used with $(\alpha, \beta) = (1.5, 1)$. Figure 3.2 shows the impact of the time discretization on the numerical estimate of the LE. One can observe a first-order convergence of the LEs with respect to the time discretization for large timesteps. However, this convergence is quickly stopped and plateaus for a convective CFL number larger than 1. The level of accuracy at which the convergence stops depends on the spatial discretization and will be investigated in greater details in the next section. The minimal effect of the timestep on the convergence of the error at small CFL numbers is consistent with the analysis Fernandez et al. [126], who used a compressible flow solver for an

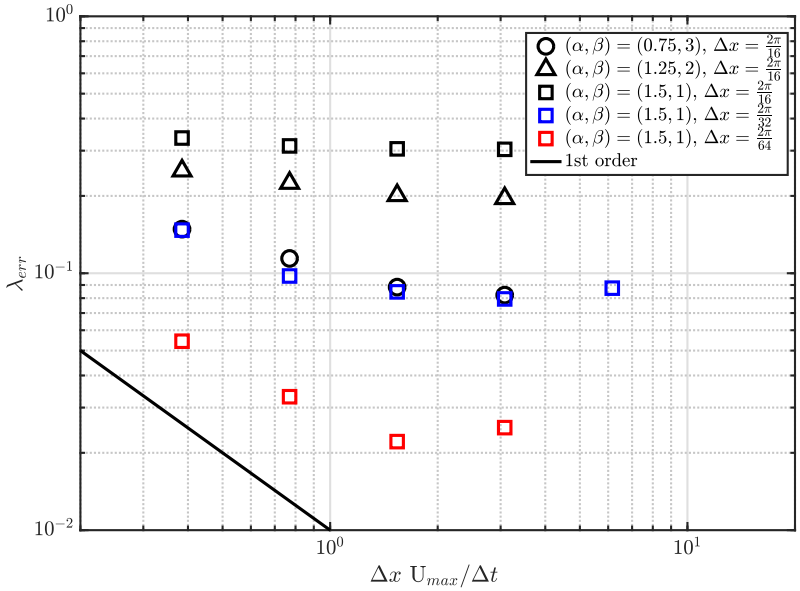

Figure 3.2: Convergence of LE as a function of the timestep. The exponent error is the difference between the observed LE and the Orr-Sommerfeld eigenvalue.

airfoil geometry and an acoustic CFL number ranging from 0.2 to 0.0125. Since the LEs are precisely determined here, there are no statistical errors associated with this evaluation.

3.4.3.3 Spatial convergence

The effect of grid spacing on the LE calculation can be determined similarly to the temporal convergence tests. Here, spatial convergence for different discretization truncation orders is studied. Starting from a grid of $8 \times 16 \times 8$, the grid spacing is progressively decreased by a factor of 2 each time to obtain the results shown in Fig. 3.3. In order to clearly distinguish between the impact of temporal discretization and spatial discretization, the timestep is held fixed. For the 2^{nd} order case, the timestep is set to 7.5ms; for the 4^{th} order case it is set to 1.625ms. At these timesteps, the temporal errors do not dominate the errors in the approximation of LE. It is seen that the LE convergence rate is directly related to the order of numerical scheme used, with the slope of the error nearly matching the order of the scheme. To the

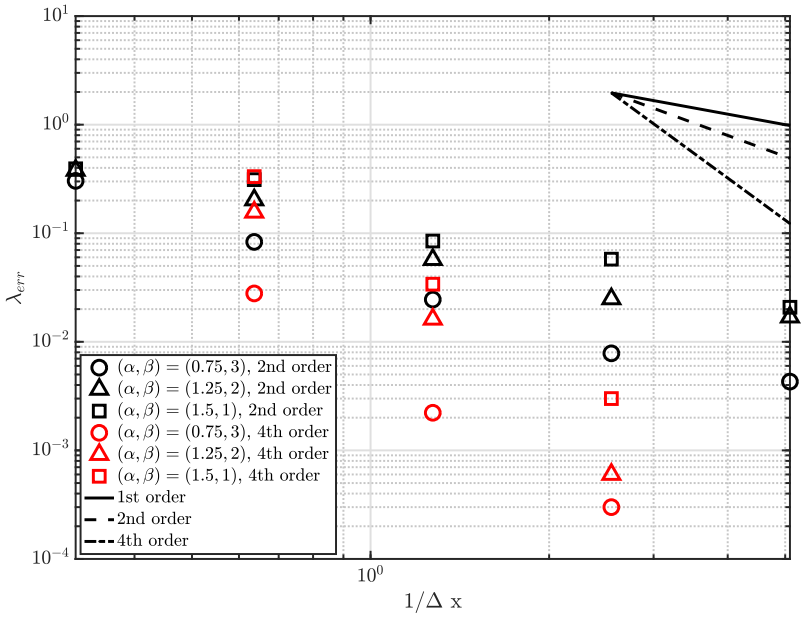

Figure 3.3: Convergence of LE with spatial discretization. The exponent error is the difference between the observed LE and the Orr-Sommerfeld eigenvalue.

authors' knowledge, this is the first such result for convergence for LEs.

3.4.3.4 LV-dependent error

Although the LEs converge with spatial discretization, the absolute errors for individual LEs span a wide range that follows an interesting pattern. Figure 3.4 shows the exponent error for LEs (defined similar to Fig. 3.2 and Fig. 3.3) as a function of the streamwise wavenumber for a single computational grid $16 \times 32 \times 16$. It is seen that there exists a strong dependence on the wavenumber, which is comparable to dispersion errors arising from Taylor series expansion-based discretization schemes [134]. This trend can also be observed in Fig. 3.3. This result was verified using two independent procedures. First, similar to Keefe et al. [124], the LS was computed using Benettin's algorithm. The streamwise and spanwise wavenumbers of the LV were individually extracted, allowing for the comparison of the LEs with the eigenvalues obtained from the OS analysis. Second, similar to the procedure used in Sec. 3.4.3.1,

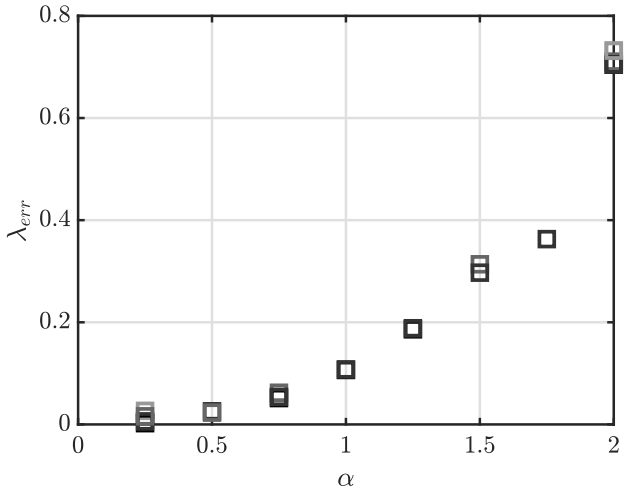

Figure 3.4: Absolute error between the LE and the Orr-Sommerfeld eigenvalue plotted against the streamwise wavenumber of the Orr-Sommerfeld eigenvector. Darker colors indicate smaller spanwise wavenumber and lighter color indicate larger spanwise wavenumber (ranging from 0 to 3).

initial conditions aligned with the eigenvectors obtained from the OS analysis were imposed, and the decay rate of the perturbations was measured. Both procedures showed a similar dependence with respect to the streamwise wavenumber.

3.5 Numerical convergence of Lyapunov spectrum for unsteady problems

Although the laminar Couette flow problem is an interesting unsteady validation case for the LS algorithms, Lyapunov theory is more useful in the context of turbulent flow with strange and multidimensional attractors. In particular, an accurate estimation of the dimension is a first step in obtaining a high fidelity envelope for the attractor. In this section, a suite of test cases is used to determine the convergence properties of the LS for such transient problems.

3.5.1 Kuramoto-Sivashinsky equation (KSE)

In order to investigate whether the spatial and temporal convergence obtained with the low Mach number solver for the Couette flow are just properties of the low Mach number solver, a one-dimensional case is studied using spectral discretization of the spatial derivatives. This case exhibits chaoticity and is, therefore, a natural step towards evaluating the convergence of LEs in turbulent, chaotic flows. The KSE represents a canonical configuration with turbulence-like chaotic behavior [135, 136]. Due to its one-dimensional formulation, it is a computationally efficient model for studying chaotic behavior using the Lyapunov approach. With unity diffusion coefficient, the KSE is written as

$$\frac{\partial u}{\partial t} + \nabla^4 u + \nabla^2 u + \nabla u^2 = 0, \tag{3.13}$$

where $u(x,t)$ is the solution of the KSE, defined on $x = [0, 16\pi]$ and $t = [0, 400]$, with $u(x,0) = \cos(x/16) * (1 + \sin(x/16))$. For this study, a spectral approach is used. As will be discussed below, this method is modified to reflect some of the properties of the low Mach number solver. The PDE is using an exponential time differencing Runge-Kutta method (ETDRK4) [137, 138] with timestep fixed at 0.05s. The non-linear term is treated with a pseudo-spectral approach and 2/3 dealiasing. The simulations were performed using MATLAB, and the code used is provided in [137]. Note that due to the fully explicit nature of this problem (no inversion of Poisson equation is required), the algorithm introduced in Sec. 6.2.2 does not affect the computation of the LE.

Figure 3.5 shows the resulting space-time plots for a spatial discretization using 500 grid points. The first 75 exponents of the LS are computed in the statistically stationary region after $t = 40$ s (shown in Fig. 3.5). The shape of the spectrum is comparable to prior work [139] and thus provides confidence in the results shown here.

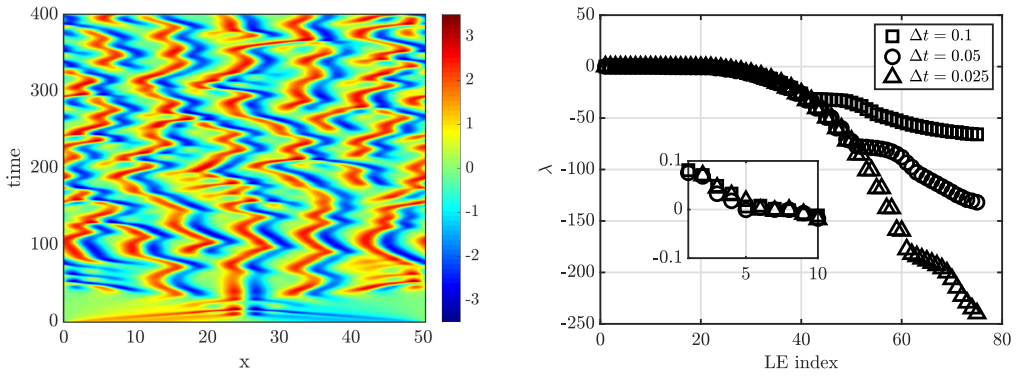

Figure 3.5: Left: time evolution of the solution to the KSE considered here. Right: first 75 LEs obtained using spectral method with 500 modes. Inset shows the first 10 exponents

.

The perturbation norms are averaged over three timesteps before being orthogonalized. As can be seen in Fig. 3.5, the timestep size has a substantial impact on the last exponents of the spectrum. Because of the particular time integration scheme used, the temporal discretization dependence of the LS is not investigated here. Instead, Fig. 3.5 indicates that a timestep 0.05 s is sufficient to study the dependence of the first 45 exponents with the time discretization. The L_2-norm of the perturbations applied was set to 0.1, which ensures that the fastest decaying perturbation does not locally go below machine precision. With a 0.05 s timestep, the perturbations are propagated for 0.3 s before being orthonormalized. Since the $\lambda_{45} \approx -70$, the perturbation norm aligned with the 45^{th} LV would decay to 0.1 exp $(-70 \times 0.3) = \mathcal{O}(10^{-11})$. The average component of the perturbation would, therefore, be $\mathcal{O}(10^{-13})$ which is above machine precision. The KSE for this set of conditions exhibits a chaotic attractor with five strictly positive Lyapunov exponents (shown in Fig. 3.5).

The impact of spatial discretization is assessed in this problem in two ways: a) by changing the number of grid points from 76 to 500 progressively, and b) by altering the truncation order of the spectral solver using a modified wavenumber approach [134]. Here, modified wavenumbers for second and fourth order central difference schemes are used in addition to the spectral derivatives. In order to be consistent with the low

Mach number solver used in the rest of the study, the modified wave number is based on a staggered spatial discretization [118]. Since the FTLEs are time-varying, the statistically averaged global LEs are evaluated using multiple re-orthonormalization steps. To assess the sampling uncertainty resulting from the use of a finite number of such steps, the method outlined in Ref. [140, 141] is used. In all the plots, the LS obtained with the spectral method using 500 points is considered to be the "true" LS.

Figure 3.6 shows the convergence for the 35^{th}, 40^{th} and 45^{th} LEs. Here the errors reported are absolute errors. It is seen that the spatial convergence of this set of LEs is directly related to the discretization order, with very high convergence rates (albeit not exponential) for the LEs computed using spectral derivatives. These results are consistent with the planar Couette flow findings (Sec. 3.4). It is therefore conjectured that the convergence properties of the LEs obtained with the Couette flow are properties of the LEs themselves and are not due to the low Mach number numerical procedure used. This result supports the conclusions obtained by Fernandez et al. [126]. However, it is possible to find other LEs that do not conform to this trend. For instance, Fig. 3.7 shows spatial convergence plots for 1^{st}, 10^{th} and 20^{th} LEs.

The space-time plot for two representative LVs (1^{st} and 35^{th}) are plotted in Fig. 3.8. Interestingly, the 35^{th} LV shows minimal variation with time and very organized structure with nearly periodic wave patterns. The first LV, on the other hand, shows a more chaotic structure that is similar to the solution of KSE itself. We postulate that the difference in convergence properties is due to the associated smoothness of these solutions. The 35^{th} LV (and the other convergent vectors) exhibits a regular spatial structure that is smooth with respect to the grid spacing. On the other hand, the non-converging LVs exhibit a broadband spectrum of fluctuations which may amplify the dispersion errors. It is also worth noting that even when the LVs do not converge with grid spacing, the absolute errors are relatively low (Fig. 3.7).

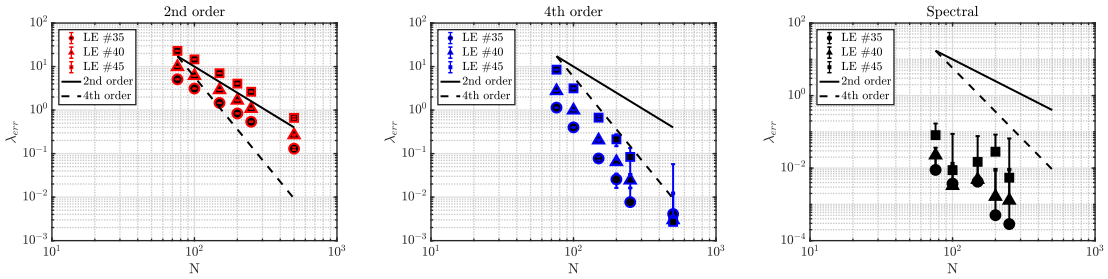

Figure 3.6: Convergence of the 35^{th}, 40^{th}, 45^{th} LEs with discretization level. Left: 2^{nd} order. Middle: 4^{th} order. Right: spectral method.

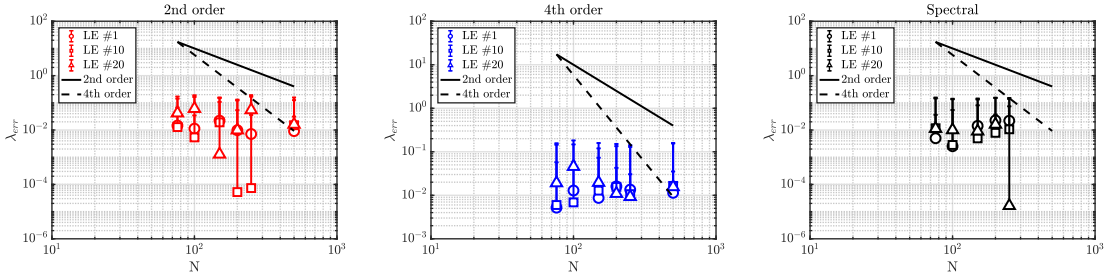

Figure 3.7: Convergence of the 1^{st}, 10^{th}, 20^{th} LEs with discretization level. Left: 2^{nd} order. Middle: 4^{th} order. Right: spectral method.

This study indicates that the LS could have LE-dependent convergence rates, which should be treated as a note of caution when obtaining the spectrum. In particular, the lack of spatial convergence for the first LE is noteworthy.

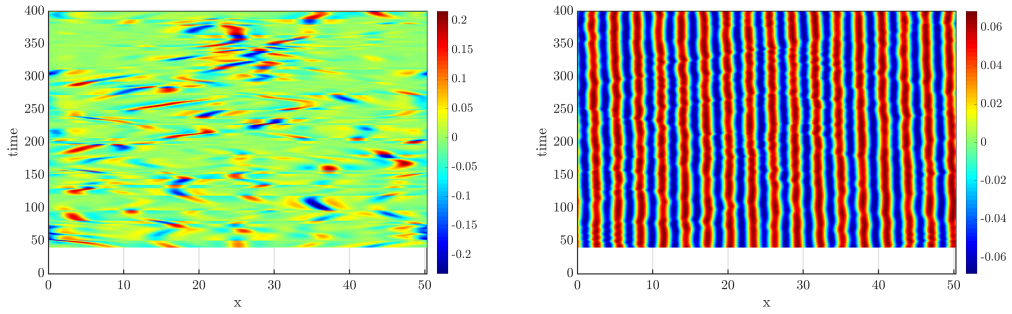

Figure 3.8: Time evolution of the 1st LV (left) and 35th LV (right) of the KS equation computed with 500 modes.

Resolution	Re_λ	$\frac{k_s \Delta t}{\tau_{eddy}}$	m	$\frac{N_s k_s \Delta t}{\tau_{eddy}}$	Δt
32^3	12.9	1.06	100	6707	0.02s
64^3	12.9	1.06	55	7028	0.02s
128^3	12.9	1.06	55	1013	0.02s
256^3	12.9	1.06	55	446	0.02s

Table 3.1: Mesh resolution and simulation parameters for the LS computation for HIT, where τ_{eddy} denotes the eddy turnover time.

3.5.2 HIT

Another typical theoretical configuration for turbulence studies is the HIT flow in a $2\pi^3$ periodic box. This case will be revisited in Chap. IV to obtain a physical interpretation of the LVs. Here, the main concern is the numerical convergence of the LE. Previously, the largest LE (i.e., the first LE) has been computed by Mohan et al. [140], who found that time-scale associated with this LE decreases faster than the Kolmogorov time scale. Here, a partial spectrum of LEs is computed. The HIT simulation is conducted with the low Mach number with 2^{nd} order spatial and temporal accuracy. Other relevant simulation details are summarized in Table. 3.1. The grid resolution is chosen such that the coarsest grid resolves the smallest turbulence length scale. The turbulence is sustained using a linear forcing method [142] with a forcing coefficient of 0.1 and a viscosity of $\nu = 0.05$ m^2.s^{-1}. The resulting Taylor microscale Reynolds number is $Re_\lambda = 12.94$ for all simulations as indicated in Tab. 3.1. For all the spatial resolutions, the timestep was held constant at 0.02s, which is based on the CFL condition for the finest mesh resolution. Here, the flow is fully resolved and and the ratio $\frac{\eta}{\Delta x} \approx 1.7$ on average, where $\eta = (\frac{\nu^3}{\varepsilon})^{1/4}$ is the Kolmogorov length scale, and ε is the turbulence dissipation rate. The turbulence spectrum obtained is plotted against the one obtained by Carroll et al. [14] at a higher Reynolds number. Both spectra are appropriately scaled (see [143, chap 6.5]) in order to be meaningfully compared. As seen in Fig. 3.9, the spectra compare reasonably well, even given the differences in Reynolds numbers.

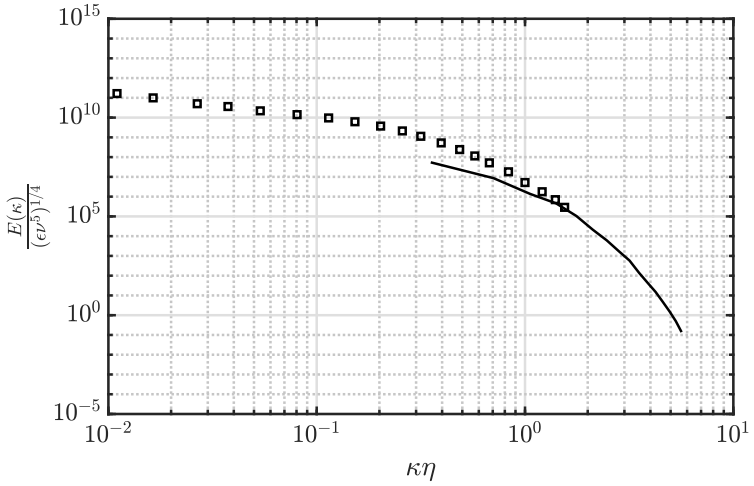

Figure 3.9: Turbulent kinetic energy spectrum averaged over 60 τ_{eddy} for the 32^3 resolution (solid line) plotted against the turbulent energy spectrum obtained with $Re_\lambda = 110$ from [14].

Figure 3.10 shows the spectrum obtained with all four resolutions along with the standard deviation in the estimation of the average LEs. Since the Reynolds number is low, the spectrum is converged for all resolutions considered. The dependence of the LEs with the Reynolds number will be the object of Chap. IV. It is simply noted for now that the structure of the LS is reminiscent of other work conducted in the past [144, 145].

Using the results of the finest-mesh simulation as the "true" spectrum, the convergence properties of various exponents can be examined (Fig. 3.11). It is seen that there is large uncertainty in the estimated errors, primarily due to large fluctuations in the FTLEs. Hence, it is difficult to draw conclusive evidence from these results. Nevertheless, focusing on the mean LE, there are differences in the convergence rates for different regions of the spectrum. In the chaotic regime, a first order convergence is observed, while in the knee and dissipative regimes, second-order convergence is obtained. These findings are consistent with results from the KS study, where LE-dependent convergence rates were also obtained.

Based on the LS, the Kaplan-Yorke dimension of the attractor can be estimated

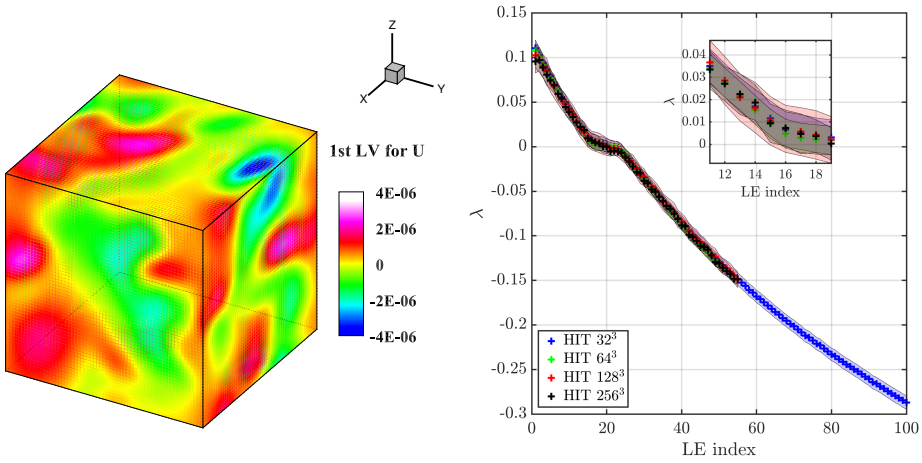

Figure 3.10: Left: instantaneous contour of the first Lyapunov vector projected in the x component of velocity for the 64^3 homogeneous isotropic turbulent simulation. Right: Lyapunov spectrum obtained with different spatial resolutions. Right inset: zoom on the LEs between the 12^{th} and the 18^{th} index.

as [91] through Eq. 2.10. The dimension estimates obtained for all cases are shown in Fig. 3.11. The variations in dimension are relatively small as the grid size is altered, and is roughly 2% of the mean value. First, it appears that the dimension obtained for each resolution vary from each other by as little as 2%. However, the convergence of the dimension with respect to the grid resolution is not directly evident, even if only the upper-bound of the dimension is considered. This result suggests that the flow field has been slightly affected by the increased resolution even at DNS resolution.

3.6 Summary and conclusions

The computation of the Lyapunov spectrum using low Mach number solvers introduces several challenges that are addressed in this work. The definition of state-space depends on the numerical procedure adopted by the solver. Failure to include a variable in the state-vector can lead to errors in the estimation of the Lyapunov exponents. The issue of spatial and temporal convergence of the Lyapunov spectrum was studied using several canonical flow problems. The Orr-Sommerfeld (OS) equations were used

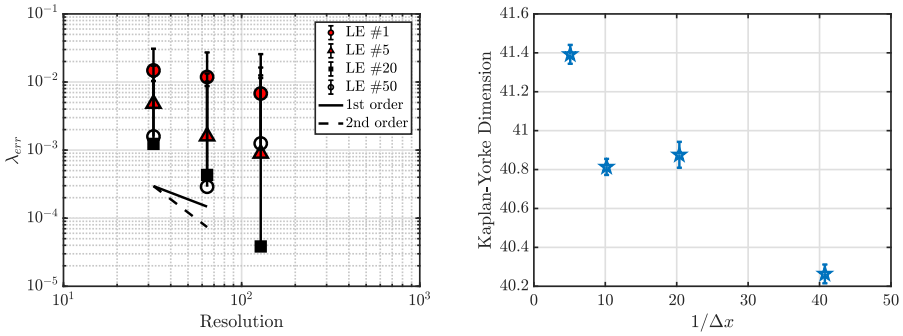

Figure 3.11: Left: dependence of the LEs of the HIT simulation with spatial discretization. Right: dependence of the Kaplan-Yorke dimension of the HIT simulation with the spatial discretization

to derive an analytical relation between the OS eigenvalues and Lyapunov exponents, which provides a highly accurate approach for verifying the numerical algorithms. A sequence of canonical configurations allowed to derive the convergence properties of the Lyapunov exponents. First, the spatial convergence is related to the discretization order, while the temporal convergence weakly related to the timestepping accuracy. The same properties were found without using a low Mach number solver. The convergence of the Lyapunov exponents confirms that conducting the Lyapunov analysis on a discretized problem allows drawing conclusions about the continuous configuration. Second, within a particular configuration, different Lyapunov exponents might exhibit different convergence rates. In the Kuramoto-Sivashinsky Equation (KSE) as well as homogeneous isotropic turbulence (HIT) cases, it was found that select exponents and their associated vectors converged at the rate of the underlying discretization order, while other exponents showed non-convergent behavior.

Finally, the Lyapunov exponents and vectors computed in this work for the different canonical flow problems deserve additional studies. For instance, the LE spectrum for HIT showed three distinctive regions, which to our knowledge, is the first such observation for this problem. For the KSE, certain Lyapunov vectors are highly localized in spectral space, while other vectors show turbulence-like spectrum. These results show an extraordinary richness in the chaotic behavior of these systems that

has yet to be explored.

In light of these findings, the Lyapunov vectors of a canonical turbulent flow are further examined and interpreted in Chap. IV. The origin of the chaotic behavior of a turbulent jet flame using its Lyapunov vectors is discussed in Chap. V.

CHAPTER IV

Lyapunov analysis of homogeneous isotropic turbulence (HIT)

In Chap. III, the numerical tools for computing the LEs and LVs were examined. The convergence properties of the tools with respect to spatial and temporal discretization were evaluated. In this Chapter, the Lyapunov analysis is conducted in the context of a canonical turbulent flow. Using the LEs, the scaling of the attractor dimension with increasing Reynolds number is directly computed for the first time. The structure of the LVs is also analyzed and related to classical turbulent flow quantities. Furthermore, the turbulent flow investigated here requires an external force to sustain a certain level of turbulence. The precise functional form of this force is a modeling choice that has impacts on the dynamics of the flow field. This impact is quantified using the LEs. This chapter is partially based on [146].

4.1 Introduction

The focus here is on the set of Lyapunov exponents and vectors for HIT. While there have been many studies on extracting the spectra for other canonical flows, such as the Kuramoto-Sivashinsky equation (KSE) [147] and the turbulent channel flow [124], the periodic turbulent flow in HIT has not been explored. Even so, the focus

of many of these studies has been on the Lyapunov exponents. Since the computation of each exponent requires one additional forward run of the dynamical system (DS), obtaining a large number of such exponents can quickly become computationally intractable, depending on the complexity of the DS equations. When the DS is not high-dimensional, the entire spectrum can typically be computed [145, 148]. More specifically, all the positive exponents of the system are directly computed, while retaining some of the negative exponents. Since the positive exponents determine the structure of the attractor and the negative exponents track the dissipative behavior, such extensive Lyapunov computations provide detailed information about the chaotic dynamics of the system.

The goal of this work is to compute and study the Lyapunov spectrum for HIT. Section 4.2 treats the numerical approach used for the DS and the computation of the LS. Section 4.3 covers the results obtained by analyzing both the LEs and the LVs. In particular, the effect of different Reynolds numbers on the dimension of the chaotic attractor (Sec. 4.3.2) and the effect of the forcing scheme on the LEs (Sec. 4.3.3) are discussed. The response of the flow field to perturbation is analyzed in Sec. 4.3.4 by examining the backward Lyapunov vectors, or Gram-Schmidt vectors (GSV). Their structure, as well as their dependence on the Reynolds number, is investigated. The findings are summarized and discussed in Sec. 4.4.

4.2 Configuration and computational approach

In this section, the simulation configuration and the numerical procedure are described. While the algorithm used for the computation of the LS is the same as the one described in Chap. III, the forward simulations are conducted differently.

4.2.1 Flow configuration

Forced homogeneous isotropic turbulence in the low Mach number incompressible flow regime is simulated in a 2π-triply periodic box. A constant density of $\rho = 1$ kg.m^{-3} and kinematic viscosity of $\nu = 0.05$ m^2.s^{-1} are used throughout the Chapter. The governing equations of the DS are written as

$$\frac{\partial u_i}{\partial t} + \frac{\partial u_i u_k}{\partial x_k} = -\frac{1}{\rho}\frac{\partial p}{\partial x_i} + \nu \frac{\partial}{\partial x_k}\frac{\partial u_i}{\partial x_k} + f_i,$$

where u_i is the velocity component, f_i is a forcing term in the i-th direction that maintains the turbulence level, and p is the fluid pressure. In the absence of forcing, the turbulent kinetic energy in the domain tends to zero due to viscous dissipation. Therefore, the forcing term ensures statistical stationarity, which is necessary for evaluating the Lyapunov spectrum. The impact of the forcing term will be studied in detail in Sec. 4.3.3. For this reason, the exact form of the forcing term will be discussed later.

4.2.2 Numerical details

Consistently with the notations of Chap. I to III, the discretized governing equations are written as a set of ordinary differential equations that take the form

$$\frac{d\boldsymbol{\xi}}{dt} = \mathcal{F}(\boldsymbol{\xi});\ \boldsymbol{\xi}(t=0) = \boldsymbol{\xi}^0,$$

where $\boldsymbol{\xi}$ is a vector of all the variables, $\mathcal{F}$ are the discrete governing equations and $\boldsymbol{\xi}^0$ are the initial conditions.

The algorithm used for computations of the LEs and LVs is the same as in Chap. III. Here, this procedure is used for all the simulations with an averaging time of one eddy turnover time s (300 to 1300 timestep depending on the resolution).

The set of LVs obtained are the GSV. Since the GSV converge to the backward Lyapunov vectors [114] they describe the response of the system to perturbations that expand or contract and thereby provide interesting information about the dynamical system. Since the CLVs can also be expressed as a linear combination of the GSVs, studying the GSV allows to draw conclusions about the tangent space to the attractor. This aspect is further discussed in Appendix A.3.

As opposed to Chap. III where the governing equations were solved in physical space, in the present work, the incompressible governing equations are solved using a Fourier spectral transformation [149, 150], by decomposing the primitive variables into Fourier modes:

$$u_i = \sum_{\boldsymbol{\kappa}} \widehat{u}_i(\boldsymbol{\kappa}, t) e^{j\boldsymbol{\kappa}\cdot\boldsymbol{x}}$$

where $\boldsymbol{\kappa}$ is the wave vector and $\boldsymbol{x}$ is the vector of the location in physical space. The Galerkin projection of the governing equations is obtained for all the Fourier modes. A pseudo-spectral method with dealiasing is used for the non-linear term and is integrated in time using a second-order Runge-Kutta scheme. The viscous term is integrated analytically. The timestep is chosen to maintain a Courant number of 0.5 for all the simulations. The ratio of the Kolmogorov length scale to grid size is maintained close to unity. Due to round-off numerical errors, it was found that there was a growth of instability in the simulations that contaminated the Lyapunov evaluations. For this reason, the continuity is explicitly forced using a correction procedure at each time step (see Appendix A.1 for details).

As a validation of the implementation, the LS of the HIT case presented in Chap. III which used a spatial discretization is computed this time with the spectral code. A linear forcing [151] with a coefficient $A = 0.1$ is used and the governing equations takes the form

$$\frac{\partial u_i}{\partial t} + \frac{\partial u_i u_k}{\partial x_k} = -\frac{1}{\rho}\frac{\partial p}{\partial x_i} + \nu \frac{\partial}{\partial x_k}\frac{\partial u_i}{\partial x_k} + A u_i.$$

In order to verify the spectral code, four different simulations are run: a) 32^3 and 64^3 simulations with the low-Mach number solver (same as the one presented in Chap. III, b) 32^3 and 64^3 Fourier mode simulations with the spectral solver. Figure 4.1 (left) shows a snapshot of the vorticity magnitude, demonstrating the presence of well-defined vortical structures in the relatively low Reynolds number flow. For all 32^3 calculations, 100 LEs were computed, while 50 LEs were computed for the 64^3 spectral simulation. The Lyapunov spectra from all of these calculations are shown in Fig. 4.1 (right). The good agreement between all four cases indicates that the dynamics of the flow were sufficiently resolved to capture the spectrum. It also shows that both the low-Mach spatial solver and the spectral solver capture similar dynamics of the flow field. Note that there are significant numerical differences between the spectral and the physical space code, which make this result non-trivial. In particular, the pressure in the spectral code is constructed by assuming incompressibility of the velocity field, while it is constructed to ensure incompressibility in the low-Mach number solver.

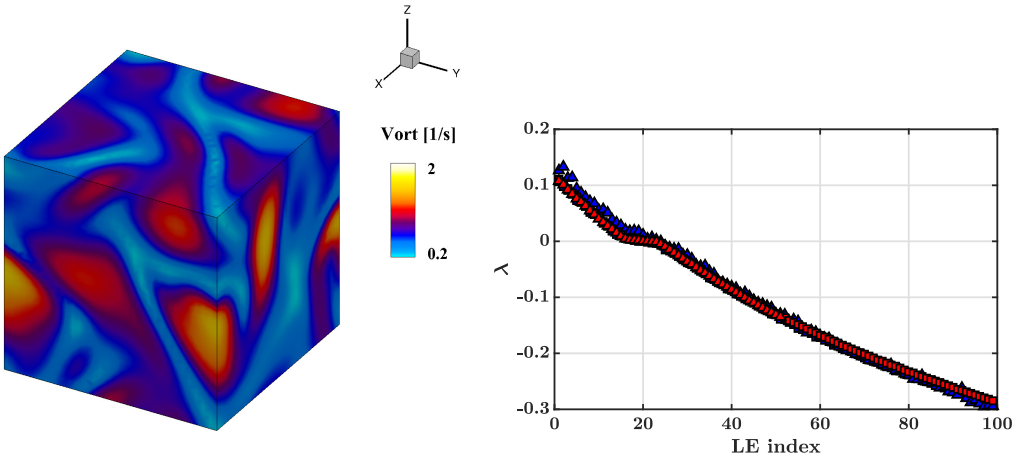

Figure 4.1: Left: contour of vorticity magnitude for the case solved with the spectral code using 32^3 Fourier modes. Right: first 100 LEs obtained with: the spectral code with 32^3 Fourier modes (■) and 64^3 Fourier modes (▲); the physical space code with 32^3 grid points (■) and 64^3 grid points (▲, first 50 exponents only).

4.3 Results

In this section, the LEs are used to directly estimate the dimension of the attractor of the flow field. Using different Reynolds numbers, an estimate of the scaling of the attractor dimension is also obtained. The structure of the LVs is also described, and their localization in physical space are characterized as well as their correlation with classical turbulent flow quantities.

4.3.1 LE spectrum

As mentioned in Chap. II, one of the main uses of the Lyapunov study is the determination of the dimension of the attractor. For this purpose, a set of Lyapunov exponents needs to be computed. In order to obtain an accurate estimate, it is necessary to determine at least all of the positive exponents and some of the negative components. In prior studies [124], a partial set of positive exponents had been used to extract a polynomial fit, from which the entire spectrum was determined. Here, the negative components are directly evaluated in order to increase the accuracy of the results. The main disadvantage of this procedure is that the range of Reynolds numbers which could be studied is limited since the number of positive exponents grows exponentially with the Reynolds number [152].

As a starting point, the structure of the exponent spectrum can be examined from the validation case investigated in Sec. 4.2.2. Figure 4.1 shows the spectrum of the first 100 exponents. The structure of this plot is similar to that for other systems, such as turbulent channel flow [124] or Rayleigh Bénard flows [153]. It is not clear at the moment why are the shapes of the LE spectrum similar across turbulent flows. An important consequence of the exponential shape of the spectrum is that only a few modes are responsible for most of the chaoticity. Overall, a finite set of positive exponents is observed, followed by a long tail of negative exponents. The magnitude is inversely related to the index, with near-linear scaling, as opposed to

the K-S system, where negative exponents were found to scale as the fourth power of the Lyapunov index [147]. This difference is likely due to the stronger dissipation term (fourth derivative) in the K-S system as opposed to the second-order viscous term in the Navier-Stokes equations. Further, the near-zero LEs show a knee-like structure, where the values do not follow the linear trend observed for the lower and higher LE indices. This structure has also been observed in Kolmogorov flows [154] and with a Hamiltonian description of the motion of a collection of two-dimensional discs [155].

4.3.2 Scaling of the dimension of the attractor

From a physical point of view, the dimension of the attractor is expected to increase with the Reynolds number of the flow. As the Reynolds number increases, the range of scales available for the turbulent flow extends. The number of states that the system can occupy increases, i.e. the dimension of the attractor increases. The LEs are also expected to depend on the level of turbulence through the Kolmogorov quantities [156]. Consider the rate of change induced by an eddy of size l. The time over which a perturbation amplifies is $l^{2/3}/\varepsilon^{1/3}$, where ε is the turbulent energy dissipation rate. In terms of LE, the inverse of this expression should be considered. This means that the largest LE depend on the smallest eddy, i.e., the Kolmogorov length scale η.

The scaling of the dimension of the attractor of turbulent flows with the Reynolds number has important implications, in particular, about the resolution required to capture the dynamics of the flow field [157, 158]. To estimate this scaling relation, a series of calculations with varying Reynolds numbers is conducted. Through the Kaplan-Yorke (KY) conjecture [91], the geometric dimension of the system's attractor

Case	1	2	3	4
Re_λ	15.55	21.26	25.57	37.67
ϵ [m^2/s^3]	0.07	0.26	0.68	8.8
l_{int} [m]	0.47	0.53	0.55	0.52
k [m^2/s^2]	0.35	0.93	1.8	9.7
N	32	64	64	128
m	99	199	299	49
A	0.137	0.215	0.3	0.75
D_{KY}	57.67	128.67	232.54	1430.7

Table 4.1: Turbulent statistics of the simulations conducted with various Re_λ using the linear forcing scheme. Re_λ denotes the Reynolds number based on the Taylor microscale; ϵ is the energy dissipation rate; l_{int} is integral length scale based on the turbulent kinetic energy and the energy dissipation rate; k is the turbulent kinetic energy; N is the number of modes in one direction. m is the number of LEs computed; A is the linear forcing coefficient; D_{KY} is the computed Kaplan-Yorke dimension.

can be related to its LEs. The KY dimension is expressed as

$$D_{KY} = i + \frac{\sum_1^i \lambda_j}{|\lambda_{i+1}|},$$

where λ_j denotes the j^{th} LE, and i is the last index such that $\sum_1^i \lambda_j \geq 0$. The dimension of the attractor of the system can inform about the complexity of the dynamics considered as well as serve as an indicator that determines the minimal number of degrees of freedom required to capture all the dynamics on the attractor [158]. All calculations use the linear forcing techniques discussed in Sec. 4.2.2. The statistics of these cases are provided in Tab. 4.1.

The LEs computed for each one of these cases are shown in Fig. 4.2. For cases 1-3, a sufficient number of exponents are obtained to estimate the dimension from the above relation directly. In practice, the exponents are obtained from long-time averages. Therefore, these values are subject to statistical errors, which may be estimated from the time-series of the exponents. The approach used here is based on the technique proposed in [141] for turbulence statistics. For the average turbulence

quantities (Re_λ, Kolmogorov length scale η), uncertainty estimates are obtained following the same procedure. An uncertainty estimate for the attractor dimension of Cases 1, 2 and 3 can then be derived by computing D_{KY} using the mean LE shifted by one standard deviation up or down. For Case 4, the number of computed exponents is not sufficient to estimate the dimension of the attractor (the first 49 exponents are all positive). Since it is computationally expensive to obtain more exponents, D_{KY} must be estimated using an extrapolation method for the LEs. For this purpose, it is recognized that the shape of the Lyapunov spectrum is similar in all the cases considered and can be approximated as an exponentially decaying function of the Lyapunov index (similar to what is done in Chap. V). Since the extrapolation procedure can now affect the D_{KY}, it is necessary to estimate the uncertainty that it generates for the estimation of the attractor dimension. Note that the functional form of the spectrum can reasonably be assumed to be the same, but cannot be expected to use the same exponential decay rate as can be seen in Fig. 4.2. The uncertainty quantification procedure is explained in detail in Appendix A.2.

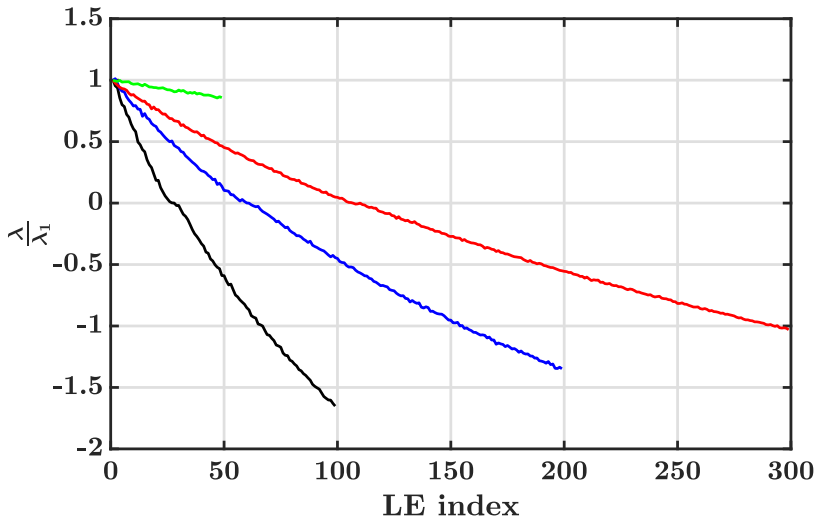

Figure 4.2: LEs rescaled by the first LE computed for Case 1 (—), Case 2 (—), Case 3 (—), Case 4 (—).

Prior estimates [159] show that the attractor dimension scales as $(\frac{L}{\eta})^3$, where L de-

notes the length of the domain in one direction, and η is the Kolmogorov length scale. Other refinements of the estimate have been mathematically derived [152, 160], but involve the scaling with the upper bound rather than average turbulent flow quantities. Here, the scaling of the dimension with the length scale ratio is shown in Fig. 4.3. It is seen that $D_{KY} \approx (L/\eta)^{2.8\pm0.095}$, which is close to the theoretical estimate. The procedure to obtain the uncertainty estimate is described in Appendix A.2. The fact that the theoretical scaling is based on fully developed high Reynolds number turbulence, where the underlying assumptions regarding the separation of scales are valid, indicates that the attractor properties are only weakly dependent on these assumptions.

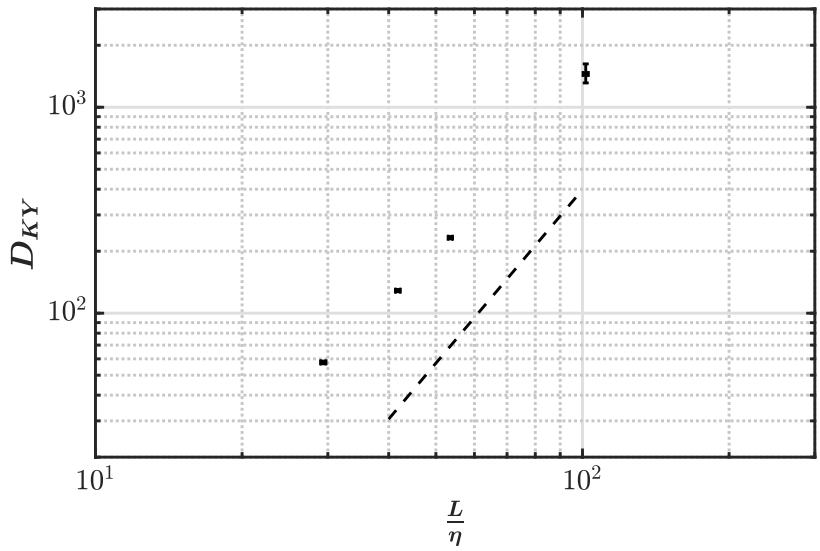

Figure 4.3: Kaplan Yorke dimension obtained from Case 1, 2, 3 and 4 (variable Re_λ and linear forcing scheme) plotted against the ratio $\frac{L}{\eta}$, along with a $(\frac{L}{\eta})^{2.8}$ slope (--). The error bars denote uncertainty estimate for both the x and y-axis due to statistical convergence and extrapolation uncertainty.

4.3.3 Effect of forcing scheme

In the case of forced HIT, despite the ability to run detailed simulations (resolve the smallest length scales), the turbulence needs to be sustained using an external

volumetric force that compensates for the dissipation. The functional form of this forcing term is a modeling choice that can have an impact on the turbulent flow field. Many forcing schemes have been proposed over the past decades with various objectives [14, 161–164]; more recent techniques have focused on minimizing the time to statistical stationarity [14]. As a result, the forcing functions might, on purpose, alter the dynamics of the flow. The Lyapunov analysis can be a valuable tool to quantify how the dynamics of the flow are affected by different forcing schemes.

Four different forcing schemes are considered. All of the cases are run using the spectral method described in Sec. 4.2 and with 32^3 modes. The following forcing methods are used :

- Case 1 uses a linear forcing technique for all the wavenumbers, similar to [142] and [151] with a linear forcing coefficient of $A = 0.137$.

- Case 5 uses a linear forcing technique for only the lowest wavenumbers, similar to [165]. The linear forcing coefficient applied is $A = 0.14$ for all wavenumbers with $|\kappa| \leq 3$.

- Case 6 uses a stochastic forcing technique [162]. The forcing functional form is based on an Ornstein-Uhlenbeck process. The parameters used are $T_L = 0.92$, $K_f = 2\sqrt{2}$ and $\varepsilon^* = 0.0015$. Since the forcing term is not solely dependent on the position of the system in phase space, the Lyapunov calculation is conducted by communicating, at every timestep, the same forcing term to all the forward realizations. The LEs are computed by using the "same noise realization" technique in the sense of "noise on the particle" (see [166] for a detailed discussion).

- Case 7 is not a realistic forcing method but rather a numerical experiment used to compare Case 1, 5 and 6 in a fair manner. It consists of using a classical linear forcing technique with linear forcing coefficient $A = 0.137$ for the unperturbed

Case	1	5	6	7
Re_λ	15.55	16.09	15.79	15.55
ϵ [m^2/s^3]	0.07	0.069	0.1802	0.07
l_{int} [m]	0.47	0.488	0.37	0.47
k [m^2/s^2]	0.35	0.37	0.58	0.35

Table 4.2: Turbulent statistics of the simulations conducted with various forcing schemes.

simulation (similar to Case 1) and communicating the same forcing to all the other perturbed simulations. This procedure is similar to the one used for Case 6.

The Reynolds number and statistics of all the cases are provided in Tab. 4.2, where Re_λ is the averaged Reynolds number based on the Taylor microscales, ϵ is averaged the turbulent dissipation rate, k is the averaged turbulent kinetic energy (k) and l_{int} is the integral length scale. As can be seen, the statistics of the cases are similar for all forcing techniques except Case 6, which shows higher kinetic energy.

The first 100 Lyapunov exponents of all the forcing schemes for HIT are shown in Fig. 4.4. Case 1 and 5 share similar values of the LEs implying similar chaotic behavior of the flow field. However, Case 6 shows significantly lower LEs despite turbulent statistics that suggest a higher turbulence intensity. This feature can be understood by considering the last case. Cases 1 and 7 lead to the same statistics as they use the same forcing for the unperturbed simulation, but again the LEs of Case 7 are significantly lower than Case 1. The level of chaoticity is therefore significantly reduced when all the realizations are forced in the same manner, which explains the results found in Case 6. This example shows that the Reynolds number alone is not enough to characterize the dynamics of a turbulent flow field and that the level of chaoticity is strongly dependent on the functional form of the forcing, and the dependence of the forcing on the perturbation. In the present case, it appears that a forcing insensitive to perturbations annihilates chaos in the flow field. More broadly, this study illustrates the potential of the Lyapunov analysis in comparing different

models by assessing their effect on the dynamics of the flow field.

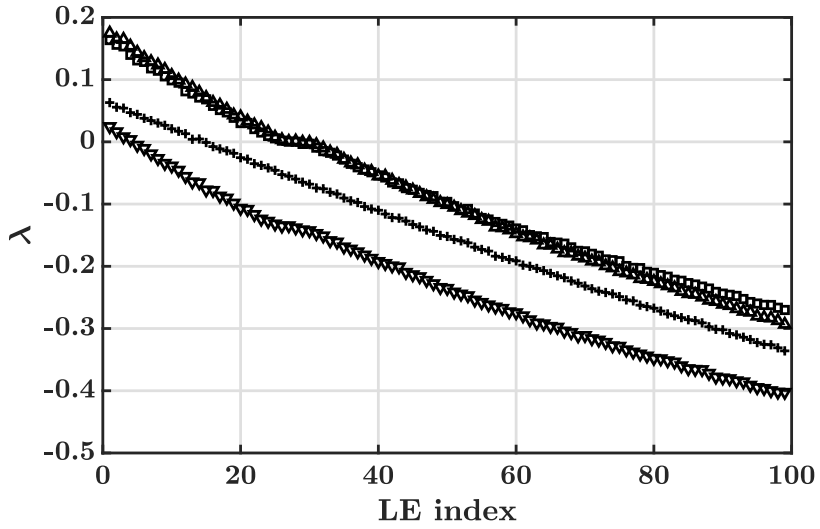

Figure 4.4: First 100 LEs for the linear forcing technique (Case 1, □), the linear forcing applied to the large scales only (Case 5, △), the stochastic forcing technique (Case 6, +), the linear forcing techniques with the same force across simulations (Case 7, ▽).

4.3.4 The response of the flow to perturbations

So far, the discussion has centered on the Lyapunov exponents. In order to assess the correlation between the flow field and the Lyapunov perturbations, the Lyapunov vectors have to be studied. Each LV is a three-dimensional flow field made of three variables (one for each velocity component) at every grid point. To identify where perturbations grow the most, the energy of the LV $\delta\boldsymbol{\xi}^2$ can be computed as the sum of squares of the velocity components that compose the normalized LV and rescaled by a factor $1/N^3$, where N^3 is the total number of grid points. In Fig. 4.5, the first, 27th and the 100th LVs obtained for Case 1 are plotted alongside the turbulent kinetic energy of the flow field k, its helicity H and its enstrophy ζ. Noting $\boldsymbol{x}$ the physical space location, $\boldsymbol{u}$ the velocity field, the turbulent kinetic energy is defined as $k(\boldsymbol{x}) = \frac{1}{2}\boldsymbol{u}\cdot\boldsymbol{u}$, enstrophy is defined as $\zeta(\boldsymbol{x}) = (\nabla\times\boldsymbol{u})\cdot(\nabla\times\boldsymbol{u})$, and the helicity is defined as $H(\boldsymbol{x}) = (\nabla\times\boldsymbol{u})\cdot\boldsymbol{u}$. From these plots, it is seen that the LV itself is a highly

chaotic field, containing structures similar to the original velocity field. A detailed statistical analysis of the correlation between the LVs and the flow field quantities considered is performed and discussed below. To understand the correlation between the flow and the LVs, statistical analysis is performed and is discussed below.

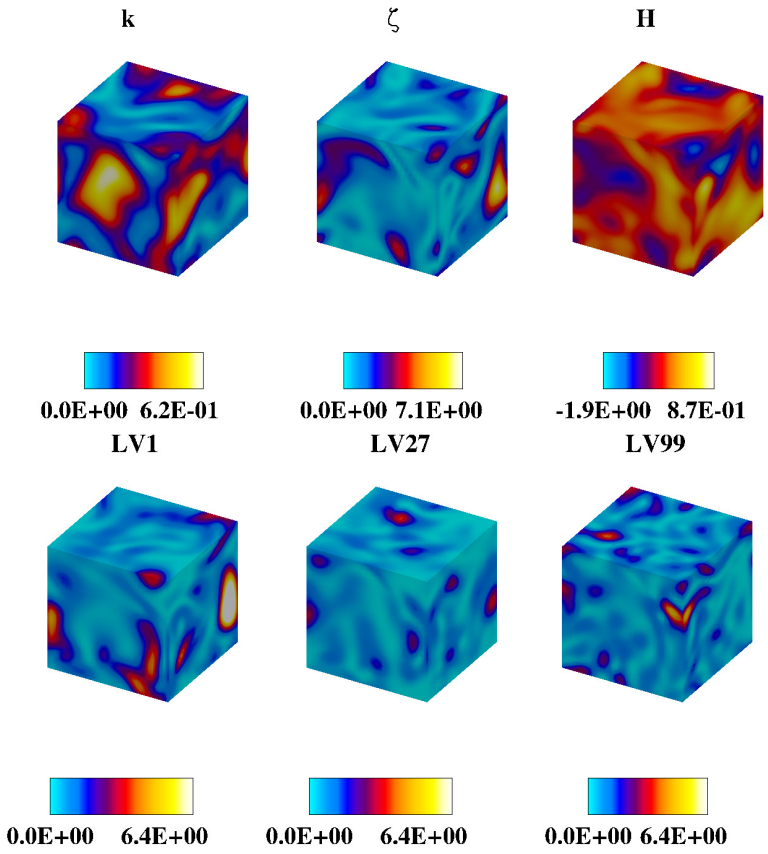

Figure 4.5: Contours of Case 1 taken at the same instant. Left: instantaneous contour of turbulent kinetic energy k (left), enstrophy ζ (middle) and helicity H (right). Right: contour of $\delta\boldsymbol{\xi}^2$ for the most chaotic first LV (left), the 27th LV corresponding to near-zero LE (middle), and the 100th LV (right).

4.3.4.1 Localization of chaotic response

It has been reported [153, 167] in different chaotic systems that only a small part of the physical space was responsible for most of the perturbation growth in chaotic systems. This property is called the localization. In the case of hard-disc systems, it

has been found that the number of particles that contribute to perturbation growth decreased as the total number of particles in the system was increased [167]. This finding led to speculations about the convergence of the LS in the thermodynamic limit (with a large number of particles). In fluid systems, it has also been found that the most chaotic LV could be highly localized in physical space and that the least chaotic LV could be more spatially distributed [168]. As a side note, the localization has been mostly investigated with GSVs but has also been recently examined using CLVs [169], where it was observed that while the spatial distribution of the least chaotic LV was less pronounced for the CLVs than the GSVs, these were still more distributed than the most chaotic CLV. In this section, the localization of the LVs is the main focus. Here, the variation of the localization with respect to the turbulence level, the Lyapunov index, and other macroscopic properties such as local kinetic energy are investigated.

The first mathematical definition of the LV localization is inspired by Ref. [167]. Here, the parameter C_θ is defined by counting the number of vector entries of $\delta\boldsymbol{\xi}^2$ that contribute to a certain fraction θ of its total L_2-norm. More formally, let $\delta\boldsymbol{\Gamma}^2$ be defined as $\delta\boldsymbol{\xi}^2$ with entries sorted in descending order. Then $C_\theta = j$, where j is such that $\sum_{i=1}^{j} \delta\boldsymbol{\Gamma}_i^2 \geq \theta \left\|\delta\boldsymbol{\xi}\right\|^2$ and $\sum_{i=1}^{j-1} \delta\boldsymbol{\Gamma}_i^2 < \theta \left\|\delta\boldsymbol{\xi}\right\|^2$. In Fig. 4.6 (left), the localization of the most chaotic LV is shown as a function of Re_λ for different thresholds θ. It appears that the fraction of the domain that contributes to the perturbation growth gets smaller and smaller as the Re_λ increases. This result suggests that tracking the evolution of perturbations over time using measurement techniques to anticipate their chaotic build-up would get more and more difficult as the Reynolds number increases. In turn, if one wants to exploit the chaoticity of the flow field for flow control purposes, the localized response of the flow field could facilitate targeted control for high-Re flows. At the moment, it is unclear whether this trend would continue for higher levels of turbulence.

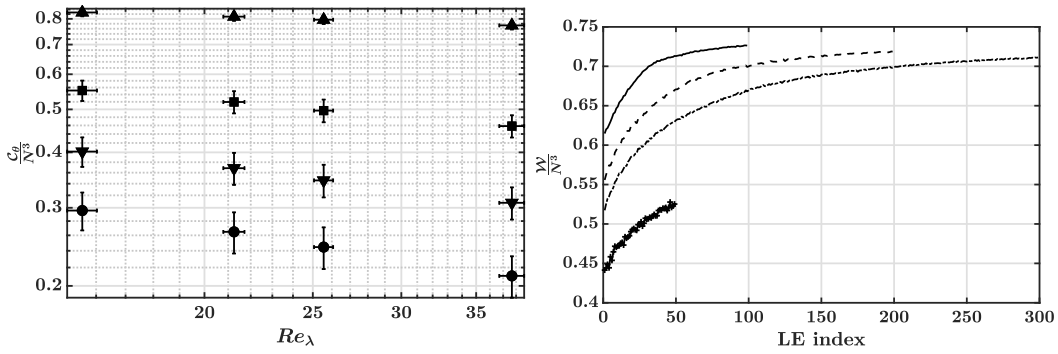

Figure 4.6: Physical space localization of the LV. Left: time average localization C_θ obtained from Cases 1, 2, 3 and 4 with different threshold $\theta = 0.98$ (▲), $\theta = 0.88$ (■), $\theta = 0.78$ (▼), $\theta = 0.68$ (●). The vertical error bars denote the RMS fluctuations around the mean (as opposed to statistical uncertainty). The horizontal error bars denote statistical uncertainty in the average value of Re_λ. Right: localization width plotted against the LE index obtained from Case 1, 2, 3 and 4.

The variation of the localization as a function of the LE index is now examined. To do so, the entropy-like metric of localization introduced in Ref. [170] is used. This metric $\frac{\mathcal{W}}{N^3}$, called the localization width, where N^3 is the number of entries in $\delta\boldsymbol{\xi}^2$ and is defined as $\mathcal{W} = exp(S)$, where $S = -\langle\sum_{j=1}^{N^3} \delta\xi_j^2 \log \delta\xi_j^2\rangle$, and $\delta\xi_j^2$ is the j-th entry of $\delta\boldsymbol{\xi}^2$ normalized by the L_2-norm of $\delta\boldsymbol{\xi}^2$. This metric is advantageous since it can be easily computed as it does not require sorting the entries of $\delta\boldsymbol{\xi}^2$, and it does not depend on the value of a particular threshold. However, this metric is bounded between $\frac{1}{N^3}$ and 1, and its value depends on the total number of vector entries (number of grid points): the same value of $\frac{\mathcal{W}}{N^3}$ for cases discretized with different number of modes can mean that a field is localized in one case and distributed in the other. As opposed to C_θ, this metric is not suited for comparing fields discretized with a different number of grid points which explains why it was not used to compare different Re_λ simulated with different numbers of Fourier modes. Figure 4.6 (right) shows the localization width obtained for Cases 1, 2, 3 and 4. Here, the statistical uncertainty of the quantity is not indicated for clarity. Similar to previous results mentioned at the beginning of this section, the LVs are increasingly distributed in physical space as the LE index

increases, although the range of variation is narrower than in other systems [170].

The metrics used above characterize the level of localization of the perturbations but do not indicate the location where perturbations grow the most. To answer this question, the conditional averages of $\delta\boldsymbol{\xi}^2$ with turbulent flow quantities are examined. Below, only the results from the linear forcing technique-based simulations are used, since the results were found to be consistent across different forcing schemes (see Appendix A.4).

First the conditional average of $\delta\boldsymbol{\xi}^2$ conditioned on the helicity H is examined (Fig. 4.7) for Case 1. It is seen that large values of $\delta\boldsymbol{\xi}^2$ are correlated with large absolute values of helicity for the most chaotic LV only. This suggests that perturbations grow where helicity is the largest. In turn, large values of $\delta\boldsymbol{\xi}^2$ for the dissipative LVs appear uncorrelated with helicity. Figure 4.7 also shows the conditional root mean square (RMS) of $\delta\boldsymbol{\xi}^2$. This data shows that at high helicity values, the variation in the LV energy is also high. This suggests that although high helicity regions are associated with increased perturbation growth, this feature is not persistent and there are times when the growth is small. In fact, the range of variation exceeds the conditional average.

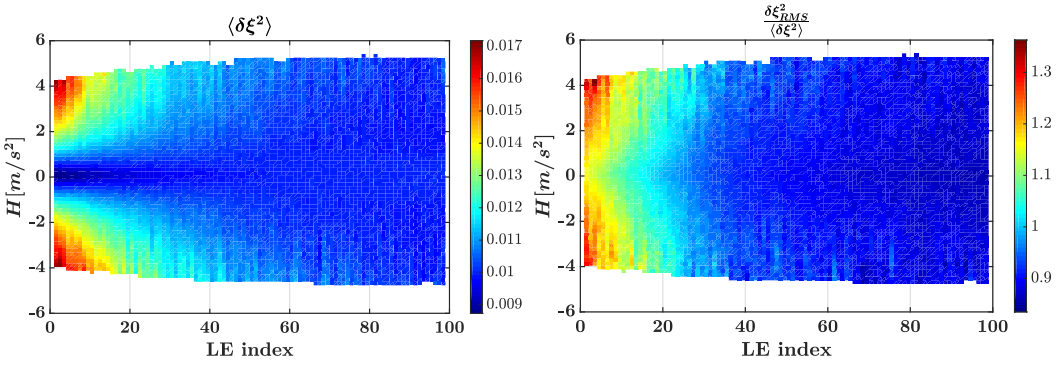

Figure 4.7: (Left) conditional average of $\delta\boldsymbol{\xi}^2$ conditioned on helicity values H, for each LV. (Right) conditional RMS of $\delta\boldsymbol{\xi}^2$ conditioned on helicity values H, for each LV, rescaled by the conditional average of $\delta\boldsymbol{\xi}^2$.

The local helicity can be intuitively understood as containing a contribution stem-

ming from the local kinetic energy and the local enstrophy. It is then natural to investigate the conditional averages with both fields to identify the importance of each component on the localization of the LV. Figure 4.8 (left) shows the conditional averages of $\delta\boldsymbol{\xi}^2$ with k. As opposed to the findings obtained with helicity, the first GSV (which is the first CLV) suggests that perturbations grow where the local kinetic energy is low. In turn, the conditional averages with enstrophy (right) are similar to the ones observed with helicity with slightly higher conditional averages. In this sense, enstrophy is a better marker for isolating the most chaotic locations in the domain.

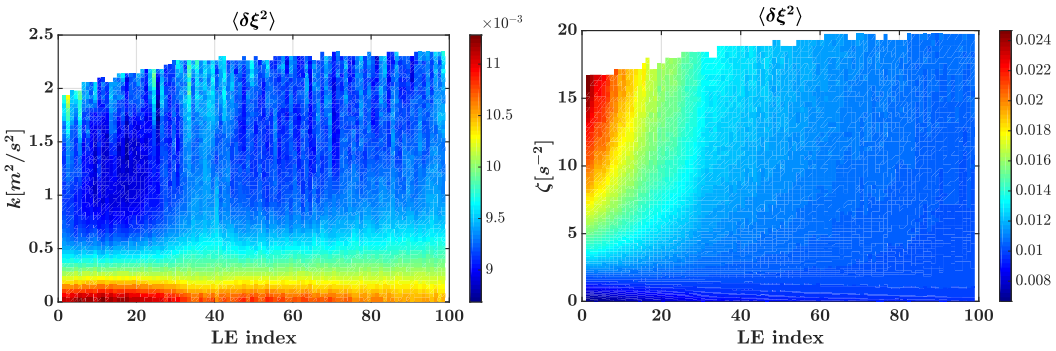

Figure 4.8: Left: conditional average of $\delta\boldsymbol{\xi}^2$ conditioned on turbulent kinetic energy values k, for each LV. Right: conditional average of $\delta\boldsymbol{\xi}^2$ conditioned on enstrophy values ζ, for each LV.

The average values of $\delta\boldsymbol{\xi}^2$ for the first LE index, conditioned on enstrophy can also be compared across different Reynolds numbers to investigate its effect on the findings listed above, by considering a normalized enstrophy $\zeta_n = \zeta/\tau_\eta^2$, where τ_η is the Kolmogorov time scale. Note that microscale scaling is adopted given than ζ is a gradient-based quantity. Figure 4.9 shows the obtained conditional average results, along with the statistical uncertainties. The trends noted in Fig. 4.8 hold across the Reynolds number considered. Overall, the large values of ζ_n are a better marker for the chaotic response of the flow to perturbations as the Reynolds number increases. Furthermore, an asymptotic limit for the conditional average seems to exist in the

limit of large Reynolds number.

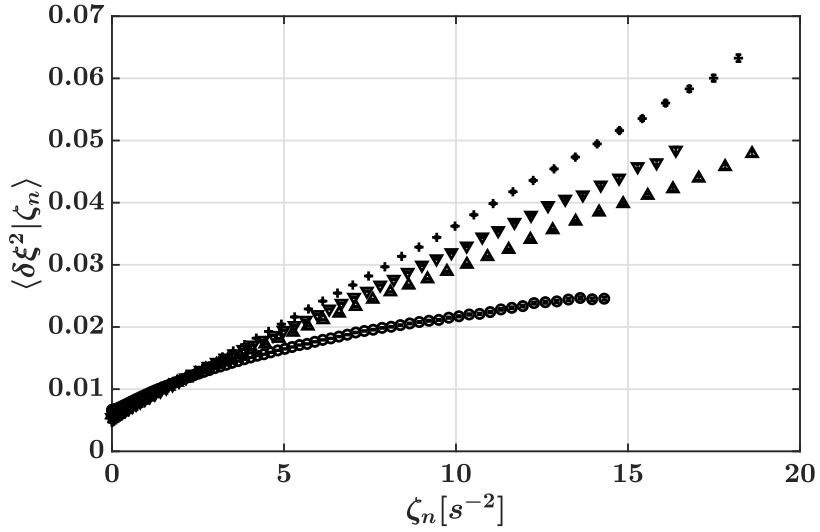

Figure 4.9: Conditional average of $\delta\boldsymbol{\xi}^2$ at different rescaled enstrophy ζ_n for Case 1 (○), Case 2 (△), Case 3 (▽), Case 4 (+). Error bars show the statistical uncertainty.

To further characterize the spatial structure of the perturbation growth, statistical correlations between different variables are used. The correlation of two fields ϕ and ψ is defined as

$$\rho_{\phi,\psi} = \frac{(\phi - \langle\phi\rangle) \cdot (\psi - \langle\psi\rangle)}{\|\phi - \langle\phi\rangle\| \, \|\psi - \langle\psi\rangle\|}, \tag{4.1}$$

where the norm considered is the L_2-norm and $\langle\cdot\rangle$ denotes a spatial average. Figure 4.10 shows the field correlation of $\delta\boldsymbol{\xi}^2$ with enstrophy, helicity, and turbulent kinetic energy. In line with the findings of Sec. 4.3.4.1, the LV appears slightly anticorrelated with the turbulent kinetic energy, where low values of kinetic energy provide high localized energy. Since helicity is symmetric about the zero value, the correlation with $\delta\boldsymbol{\xi}^2$ is close to zero. Enstrophy is positive valued, which picks the direct correlation with $\delta\boldsymbol{\xi}^2$.

The two-point correlation for the flow field and the LVs are shown in Fig. 4.11.

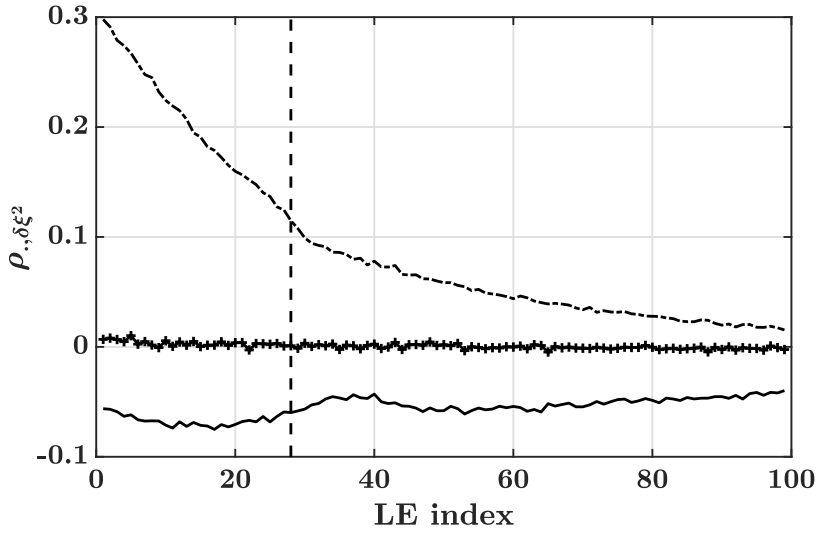

Figure 4.10: Field correlation of $\delta\boldsymbol{\xi}^2$ and ζ (···), $\delta\boldsymbol{\xi}^2$ and H (+), $\delta\boldsymbol{\xi}^2$ and k (—). The curves are plotted alongside the index where the LS crosses zero (- -).

Here, the spatial correlation of $\boldsymbol{\xi}$ in the x direction is given by

$$\rho_{ij}(r) = \frac{\langle \boldsymbol{\xi}_i(\boldsymbol{x})\boldsymbol{\xi}_j(\boldsymbol{x}+(r,0,0))\rangle}{\|\boldsymbol{\xi}\|^2}, \tag{4.2}$$

and is defined similarly for the underlying flow field. As expected, the integral length scale of the LV is smaller than that of the underlying flow field. However, there is slight reduction of integral length scale as a function of LE index, seen from the more rapid decorrelation at higher LE indices.

The two-point correlation may be expressed in the spectral domain as the energy spectrum, which is shown in Fig. 4.12. It is seen that there is a significant difference in the structure of the LVs and the flow field spectra, with more energy at small scales observed for the Lyapunov fields. Further, the peak of the spectrum is located at larger wavenumbers, which is consistent with the two-point correlation (Fig 4.11). It is noted that this result differs from previous findings for the Kuramoto-Sivashinsky Equation (KSE) in several aspects (see [147] and Chap. III). For the KSE, the spectra of the chaotic and dissipative LVs were found to differ significantly. Further, the

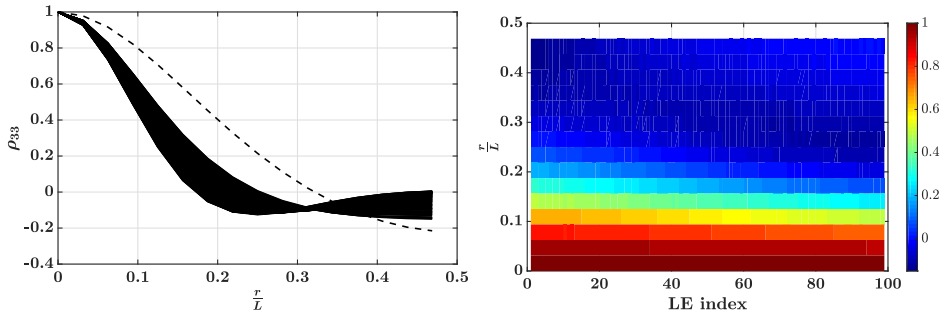

Figure 4.11: Left: spatial correlation $\rho_{33}(r)$ of the LV (—) and of the underlying flow-field (--). Right: spatial correlation $\rho_{33}(r)$ of the LV plotted against the LE index and the distance. Both plots are generated with the data of Case 1. L denotes the box length (2π).

spectra of dissipative LVs were found to be localized in Fourier space. Other work with the Rayleigh-Bénard convection showed that the energy spectra of the CLVs were not independent of the Lyapunov indices [153]. Given the present result, it can be expected that the first few CLVs also have a non-localized energy spectrum. This analysis is presented in Appendix A.3.

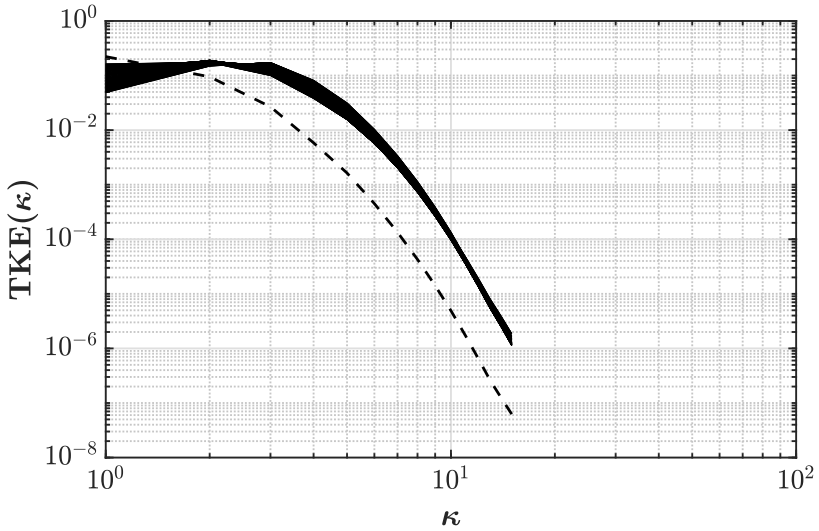

Figure 4.12: Time-averaged energy spectrum of the computed LVs for Case 1 (—) and time-averaged energy spectrum of the underlying flow field (--).

4.4 Summary and conclusions

For the first time, all the positive LEs and LVs of forced HIT flows were computed for several Reynolds numbers Re_λ. The analysis of the LVs revealed that the fraction of the spatial volume where the perturbations grow decreases as Re_λ increases. It was found that there exists a strong correlation between the chaotic parts of the domain and the field of enstrophy. This relation was found be even stronger at higher Reynolds number and seemed to tend to a universal law in the limit of large Reynolds numbers. From this observation, it can be concluded that an extreme event that emerges in a turbulent flow will strive where enstrophy is large. A model that aims at capturing extreme events should therefore capture the time-history of intense vortical structures. The precise reason behind the location of perturbation is regions of high enstrophy remains unclear. We postulate that since regions of high enstrophy are regions where fluid particles change direction the most, the continuous change of direction could be at the origin of the amplification of perturbations. This interpretation would require further investigations.

It was also found that the dimension of the attractor scales as $(\frac{L}{\eta})^{2.8}$ where L is the domain size and η is the Kolmogorov length scale, which is close to other estimates predicted by prior theoretical work. However, the actual dimension is much smaller than the full dimension of the phase space, indicating that reduced order models that capture the dynamics of the flow field with fewer modes than what is usually considered, could be developed.

The results indicate that the evolution of perturbations in a turbulent flow is considerably different than in other canonical systems, such as those studied using the Kuramoto Sivashinsky Equation (KSE). In particular, the Lyapunov vectors do not show significant localization in Fourier space with an increase in the index. This difference is likely due to the very strong diffusion term in the KSE (fourth order derivative) as opposed to the second order viscous dissipation in fluid flow. Addi-

tionally, the forcing scheme used to sustain the turbulent was found to only mildly affect the results obtained about the LVs (see Appendix A.4). However, the values of LEs were found to differ depending on the forcing scheme adopted suggesting that the Lyapunov analysis could be a powerful method for discriminating between models, especially in the context of capturing the flow dynamics rather than spatial or temporal statistics. Ultimately, the Lyapunov analysis could be used to better guide the design of models able to capture extreme and rare events.

In the next Chapter, the Lyapunov analysis is applied to a flow closer to the problems of interest: a turbulent jet flame. Similar questions to the ones posed and answered in this Chapter will be examined. In particular, the dimension of the attractor will be estimated, and the LVs will be interpreted by examining their conditional average with respect to other flow quantities.

CHAPTER V

Lyapunov spectrum of a partially premixed jet flame

In Chap. IV, the Lyapunov analysis of a canonical turbulent flow case was conducted. It was found that the distribution of the most chaotic BLVs was different from the distribution of less chaotic BLVs. In particular, the chaotic response of the turbulent flow field is aligned with the field of enstrophy. In this section, a similar question is asked about the canonical turbulent flame configuration. Moreover, the Lyapunov analysis conducted is used to estimate dynamical characteristics of the system's attractor such as its geometric dimension. This chapter is partially based on [171].

5.1 Description of the configuration

Turbulent jet flames are omnipresent in the combustion applications. They are particularly important for non-premixed and partially premixed configurations that are used in reciprocal internal combustion engines, aircraft engines or even scramjet applications. For this reason, turbulent jet flames have been the object of intense modeling activities within the combustion community. The ultimate goal of these models is typically to replicate the first or second-order statistics of temperature or

species mass fractions different distances away from the injection nozzle. In this Chapter, the Lyapunov analysis is applied to two well-known turbulent jet flames in order to reveal details about their dynamics that are not usually part of the modeling target.

5.1.1 Sandia flame series

The Sandia flames series [15, 172, 173] uses a partially-premixed CH_4/Air mixture as fuel, and air as oxidizer. Figure 5.1 shows a schematic of the piloted flow configuration. The different flames in the series contain different inflow velocities for the central jet and the pilot, which change the local strain rates and the level of extinction. In this study, the D and E configurations with central jet bulk velocities of 49.6 m/s and 74.4 m/s and pilot bulk velocity of 11.4 m/s and 17.1 m/s, respectively, are considered. The D flame exhibits very limited extinction, while flame E exhibits significant local extinction phenomena especially for $x/d < 20$, where d is the fuel jet diameter. It will be shown that the level of extinction and reignition play a crucial role in the structure of the LVs computed. Unless specified otherwise the LVs refer to the BLVs, just like in Chap. III and Chap. IV.

5.1.2 LES/Flamelet approach

The Sandia D and E flames have been simulated with a wide range of combustion models over the past decade [174–178]. The LES approach has been widely used to simulate turbulent jet flames [174, 175] and will be utilized here. As for the combustion model, the flamelet/progress variable approach (FPVA) [179] will be used. Therem the thermodynamic state is parameterized with the mixture fraction Z_{mix}, the progress variable C and the mixture fraction variance Z''^2. The mixture fraction describes the level of mixing between the central jet and the other streams, the progress variable describes the advancement of the reaction and the mixture fraction

variance describes the subgrid scale mixing. The progress variable is defined as the sum of the mass fraction of water and carbon dioxide, $Y_{H_2O} + Y_{CO_2}$. The flamelet solutions are obtained using 1D-counterflow diffusion flames computed with FlameMaster [180] and the GRI-2.11 chemical mechanism [181], and are stored in a look-up table. The set of transport equations can be found in [179]. The filtered density ($\overline{\rho}$) and transport properties are obtained from the look-up table. The LES computations use a low Mach number structured code with a staggered arrangement of variables [118] that was already used in Chap. III. Transport equations for velocity, mixture fraction and progress variable are solved, and the mixture fraction variance is obtained using an algebraic closure model with dynamic coefficient [182]. Similar to Ref. [174], the cylindrical computational grid spans $80d$ in the axial direction, and $20d$ in the radial direction. For the Lyapunov analysis, two different grids will be used to evaluate the impact of the spatial resolution on the results. A fine grid $256 \times 128 \times 32$ and a coarse grid $172 \times 90 \times 32$ will be used.

Figure 5.1 also demonstrates the solver's capability at capturing local extinction. The conditional scatter plots highlight the presence of low-temperature zones near stoichiometric conditions for the E flame, indicating local extinction events. The contour plot shows that even when such local extinction is present, there are re-ignition events downstream due to mixing with hot fluid pockets that prevent global extinction.

Similar to the other LES/FPVA results, these simulations also capture unconditional statistics accurately. Additional cases with different grid spacing are used. The different grid sizes used are $128 \times 64 \times 16$, $172 \times 86 \times 24$, $256 \times 128 \times 32$, $384 \times 192 \times 48$ and $512 \times 256 \times 64$. For all the cases, the timestep is kept constant equal to 1.5 μs, which is based on the finest resolution case. The flow field simulated is compared to experimental measurements [15] in Fig. 5.2 for the Sandia E flame. Similar results can be obtained with the Sandia D flame. It can be seen that the mixture fraction

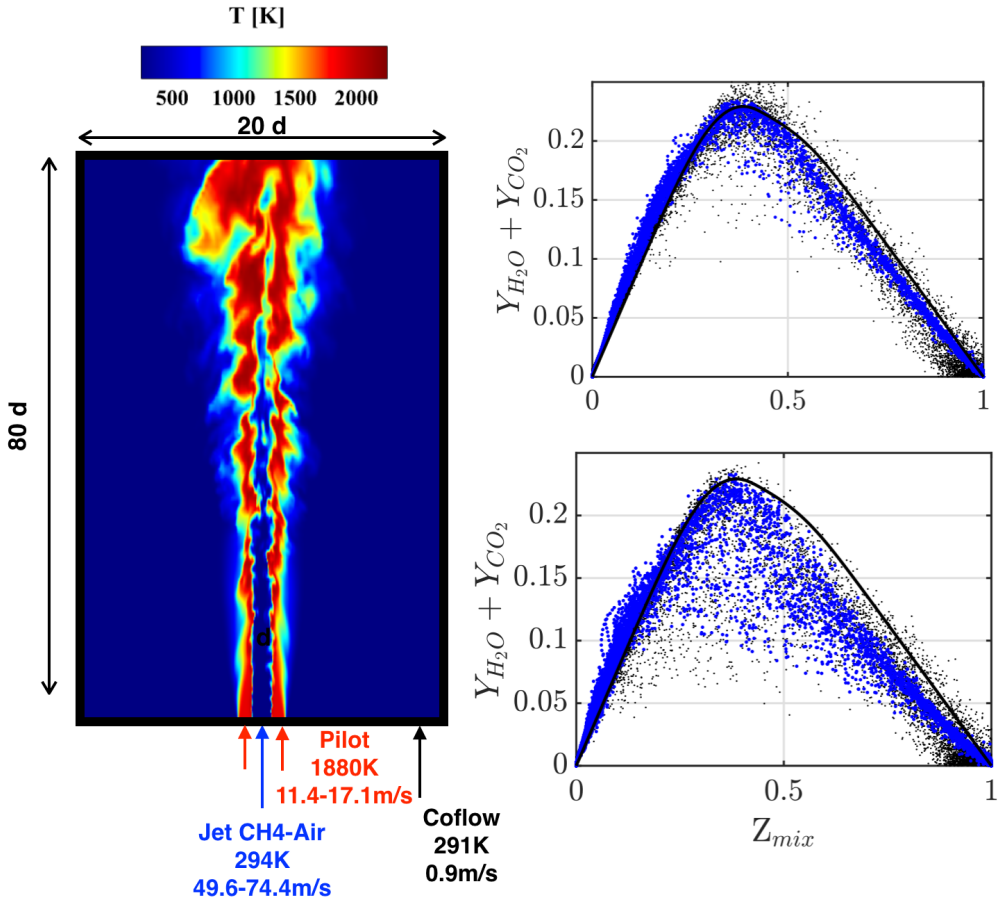

Figure 5.1: Left: schematic of the simulated configuration. The contour does not show the entire domain. Right: scatter data of progress variable conditioned on the mixture fraction for the $256 \times 128 \times 32$ simulation (blue dots) and the experiments (black dots), for the D flame (top) and the E flame (bottom) at $x/d = 7.5$. The plots are overlayed with a burning flamelet obtained at a strain rate $a = 87s^{-1}$.

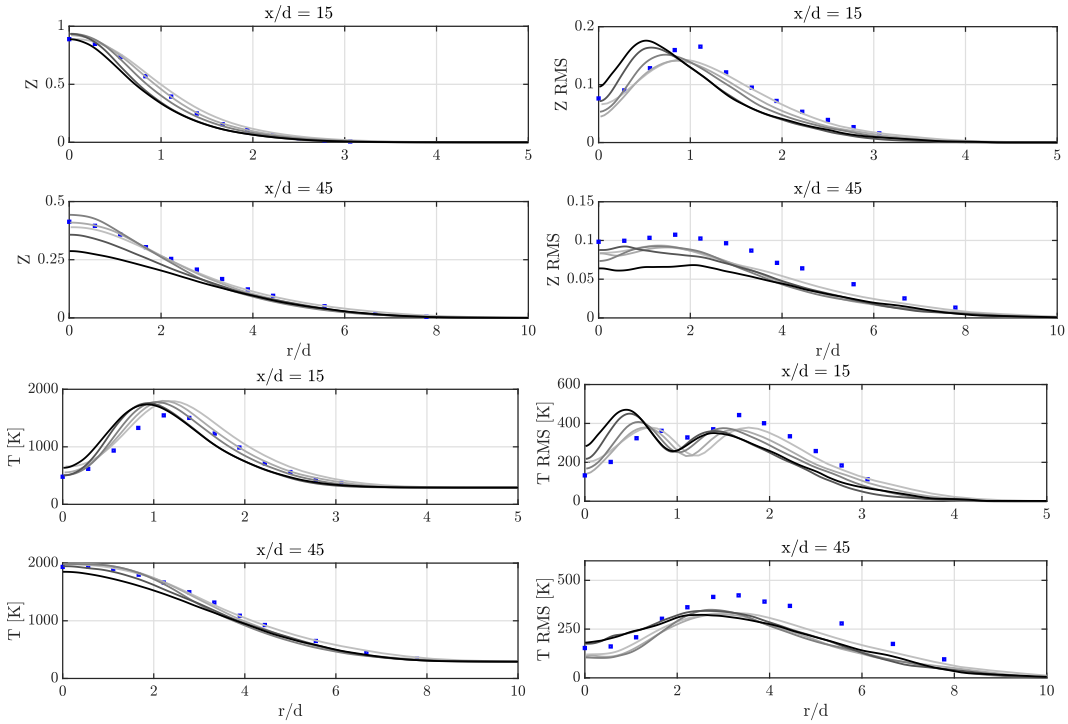

Figure 5.2: Comparison of simulated and experimental measurements [15] of the radial distribution at different axial sections of mean mixture fraction (top left), root mean square mixture fraction (top right), mean temperature (bottom left), and root mean square temperature (bottom right). The blue squares denote the experimental measurements. The darker the line, the finer the grid resolution. The resolutions are $128 \times 64 \times 16$, $172 \times 86 \times 24$, $256 \times 128 \times 32$, $384 \times 192 \times 48$, $512 \times 256 \times 64$.

and temperature fields reasonably approximate the experimental measurements. The fluctuation quantities are also fairly accurate even though they are overall slightly underestimated compared to experimental data. Note that this difference could be due to modeling or experimental errors [52, 121]. It can also be seen that no grid convergence can be obtained at the resolutions considered. This is due to the fact that DNS resolution is not achieved here and means that as the grid is refined, the underlying flow field keeps changing. While the LVs obtained are not converged, the structure of the LVs will be shown to be only mildly affected by the grid resolution. A more involved discussion about the convergence of the LEs will be provided in Sec. 5.3.1.

5.2 Lyapunov analysis with variable density low Ma solvers

In this section, the application of the Lyapunov analysis is revisited for the turbulent flame case. First, the definition of the state vectors is adapted to variable density cases. Second, the numerical procedure for the computation of the LE is modified since instabilities can occur in the limit of small perturbations. These instabilities were in particular observed for variable density cases and are therefore presented in this section.

5.2.1 Definition of state-vector

The same solver as the one used throughout Chap. III is used here. The time-staggered representation creates variables at time stations $n+1/2$ and $n+3/2$ for the scalars, while momentum-related variables are advanced from n to $n+1$. Hence, within each timestep, a set of variables that are necessary for advancing the state vector is $\{\rho\boldsymbol{u}^n, \boldsymbol{\phi}^{n+1/2}\}$. However, writing the momentum equation requires obtaining $\boldsymbol{u}$ at timestep n. In the current implementation, this is achieved by approximating ρ^n as $\frac{\rho^{n+1/2}+\rho^{n-1/2}}{2}$. Hence, for complete determination of the state vector, it needs to be augmented to include information about $\rho^{n-1/2}$. Here, this variable is introduced as $\Delta\rho^n = \rho^{n+1/2} - \rho^{n-1/2}$, although other choices could have just easily been made. With the present formulation, the set of variables necessary and sufficient is $\boldsymbol{\xi}^n = \{\rho\boldsymbol{u}^n, \boldsymbol{\phi}^{n+1/2}, \Delta\rho^n\}$.

5.2.2 A modified algorithm for the computation of the LEs

The Lyapunov analysis of variable density flows does not only require to change the definition of the state vector but also to be careful with issues related to machine precision. In this section, it is shown that numerical difficulties can arise when Algo. 3.1 is used for the computation of the LEs with arbitrarily small perturbation. Consider the coarsest resolution case for which the first LE is computed. For this pur-

pose, a baseline simulation and another simulation perturbed from this baseline at the initial time are run. Since only the leading Lyapunov exponent is sought, no orthogonalization is necessary, but the perturbations are normalized at fixed timesteps to maintain boundedness. For the algorithm to probe the tangent space of the attractor at the state of the unperturbed simulation, the perturbation magnitude needs to be infinitesimally small. Therefore, it is expected that the LEs will converge as the magnitude of the initial perturbation is reduced. Here, the averaging time used to record the perturbation growth is set to 2×10^{-4} s which is on the order of 130 timesteps. Figure 5.3 (left) shows the evolution of the perturbation norm over time for different initial norms. The plot shows the time history of the perturbation norm averaged over 440 normalization cycles (88 ms). It is seen that when the initial magnitude is small, the time history of perturbation norm experiences a rapid jump before stabilizing at an exponential rate with a constant exponent. As a result, the LE does not converge monotonically with the reduction in perturbation magnitude. This observation can be explained by analyzing the precision accuracy of the computational platform used. Define p as the proportion of entries of the perturbation vector falling below a specific threshold value. In Fig. 5.3, p is averaged over time and normalized by the values obtained with the smallest initial perturbation norm. For reference, the initial jump disappeared for initial perturbation norm $\sim 5 \times 10^{-4}$ which is indicated as a dashed line. As expected, as the perturbation magnitude increases, the proportion of entries below each threshold decreases. However, the proportion of entries close to machine precision plateaus when the initial perturbation norm is close to 5×10^{-4}. The jump in the perturbation norm is therefore attributed to machine precision errors. In the low Mach solver, a Poisson equation is inverted at every step but is only inverted up to a certain numerical accuracy. If the difference between the two simulations is too small, the errors introduced by the Poisson solver might dominate leading to the observed trends.

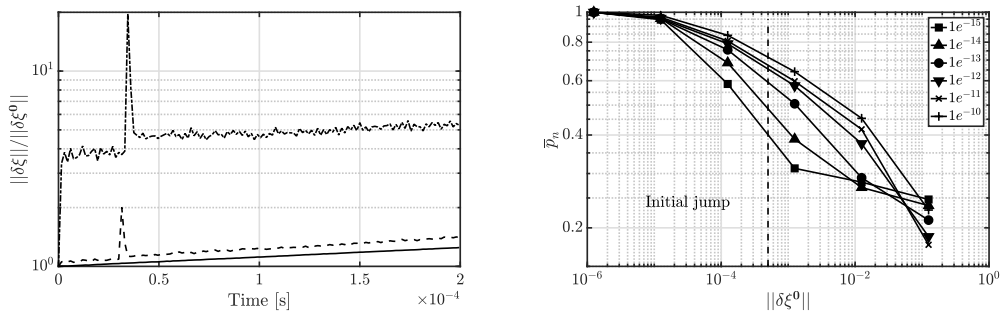

Figure 5.3: (Left) Time evolution of the perturbation norm normalized by initial perturbation norm for $||\delta\boldsymbol{\xi}^0|| = 0.125$ (solid line); $||\delta\boldsymbol{\xi}^0|| = 1.25 \times 10^{-4}$ (dashed line); $||\delta\boldsymbol{\xi}^0|| = 1.25 \times 10^{-6}$ (dot-dashed line). (Right) Proportion of state vector entries that are below stipulated thresholds plotted against initial perturbation norm. The different lines correspond to threshold levels shown in legend. The dashed line shows the smallest initial perturbation norm for which the perturbation jump is not observed.

From Fig. 5.3, it can be seen that after the transient jump in perturbation norm, the norm follows an exponential growth similar to the cases where no jumps were observed. A method that can be used to bypass the machine precision issue is to wait for a few timesteps before recording the growth of the perturbation norm. The perturbations are evolved for k_w timesteps, to provide a buffer time for the system to stabilize. An orthogonalization process takes place only to record the initial norm of orthogonal perturbation vectors, but the simulations are continued without any change in the state vector at this step. The simulations evolve, and the perturbation norms are then recorded a second and last time to compute the expansion rates of each perturbation. Currently, it is not feasible to determine a priori the buffer time needed to reach stability. Instead, a sensitivity analysis is used to determine the optimal buffer time. This modified procedure is detailed in Algo. 5.1.

Figure 5.4 shows the impact of the algorithm on the value of the first LE for the Sandia E calculation with the $128 \times 32 \times 16$ grid and the $172 \times 86 \times 24$ grid. The value obtained for the LE is plotted against different initial perturbation norms. The error bars indicate the statistical uncertainty obtained using the method outlined

Algorithm 5.1: Modified algorithm

Randomly initialize $\{\delta\boldsymbol{\xi}_j\}_{1,m}$, orthogonal with norm $\left\|\delta\boldsymbol{\xi}_j\right\| = \varepsilon$
for $i = 1, N_s$ **do**
    for $j = 1, m$ **do**
        $\delta\boldsymbol{\xi}_j = \mathcal{F}_{k_w}(\boldsymbol{\xi} + \delta\boldsymbol{\xi}_j) - \mathcal{F}_{k_w}(\boldsymbol{\xi})$
    end for
    Orthogonalize $[\delta\boldsymbol{\xi}_1, ..., \delta\boldsymbol{\xi}_m]$ and store the result as $[\delta\boldsymbol{\zeta}_1, ..., \delta\boldsymbol{\zeta}_m]$.
    for $j = 1, m$ **do**
        $\delta\boldsymbol{\xi}_j = \mathcal{F}_{k_s-k_w}(\mathcal{F}_{k_w}(\boldsymbol{\xi}) + \delta\boldsymbol{\xi}_j) - \mathcal{F}_{k_s-k_w}(\mathcal{F}_{k_w}(\boldsymbol{\xi}))$
    end for
    Orthogonalize $[\delta\boldsymbol{\xi}_1, ..., \delta\boldsymbol{\xi}_m]$.
    for $j = 1, m$ **do**
        $\Lambda_j = \frac{1}{(k_s-k_w)\Delta t} log(\frac{\left\|\delta\boldsymbol{\xi}_j\right\|}{\left\|\delta\boldsymbol{\zeta}_j\right\|})$
        $\lambda_j = \lambda_j + \frac{1}{N_s}\Lambda_j$
    end for
    Normalize $[\delta\boldsymbol{\xi}_1, ..., \delta\boldsymbol{\xi}_m]$, with norm ε
    $\boldsymbol{\xi} = \mathcal{F}_{k_s}(\boldsymbol{\xi})$
end for

in Ref. [141]. For both resolutions, it can be seen that for a low initial norm, the LE computed with the original algorithm grows as the initial perturbation norm decreases. This growth is purely due to numerical effects as explained above. It can be seen that the modified algorithm helps damp this effect and stabilizes the value of the first LE. For larger perturbations, the modified algorithm recovers the same LE as the original algorithm.

The algorithm used here is schematically shown in Fig. 5.5, and involves the simultaneous evolution of several LES computations, which interact at regular intervals to alter individual fields.

Throughout the dissertation, the modified algorithm was used in all computations of the LE since it only has an impact on cases where an initial jump in the magnitude of the perturbations is observed. For instance, in the case of the HIT run in Chap. III, the modified algorithm does not affect the value of the LE. As can be seen in Fig. 5.6, the initial jump in the perturbation magnitude is not observed here. Therefore, the modified algorithm has no particular effect on the computation of the LEs in the HIT

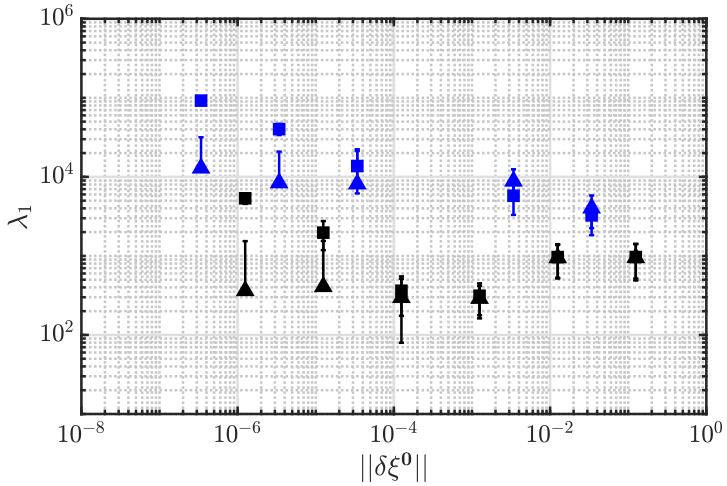

Figure 5.4: First LE plotted against the initial perturbation norm. The results of the original algorithm are denoted by squares and the results of the modified algorithm are denoted by the triangles. Black symbols show results from a resolution of $128 \times 32 \times 16$ while blue symbols are from a resolution of $172 \times 86 \times 24$.

case.

5.3 Results of the Lyapunov analysis

5.3.1 Dimension of attractor

As the Reynolds number is increased, the range of scales associated with a turbulent flow increases. Hence, the number of states that can be occupied by the system increase which means that its dimensionality increases. However, it is not guaranteed that the dimension of the attractor will exactly follow the trend found in Chap. IV, since thermodynamics could impose strict relations that might constrain the chaoticity of the flow. At the same time, the dimension of the attractor may be affected by other factors than turbulence only. Intuitively, the Sandia E flame can occupy more states in phase space due to the presence of extinction events. For instance, consider the conditional plots shown in Fig. 5.1, which are projections of the entire phase space into a two-dimensional sub-space. The presence of local extinction events

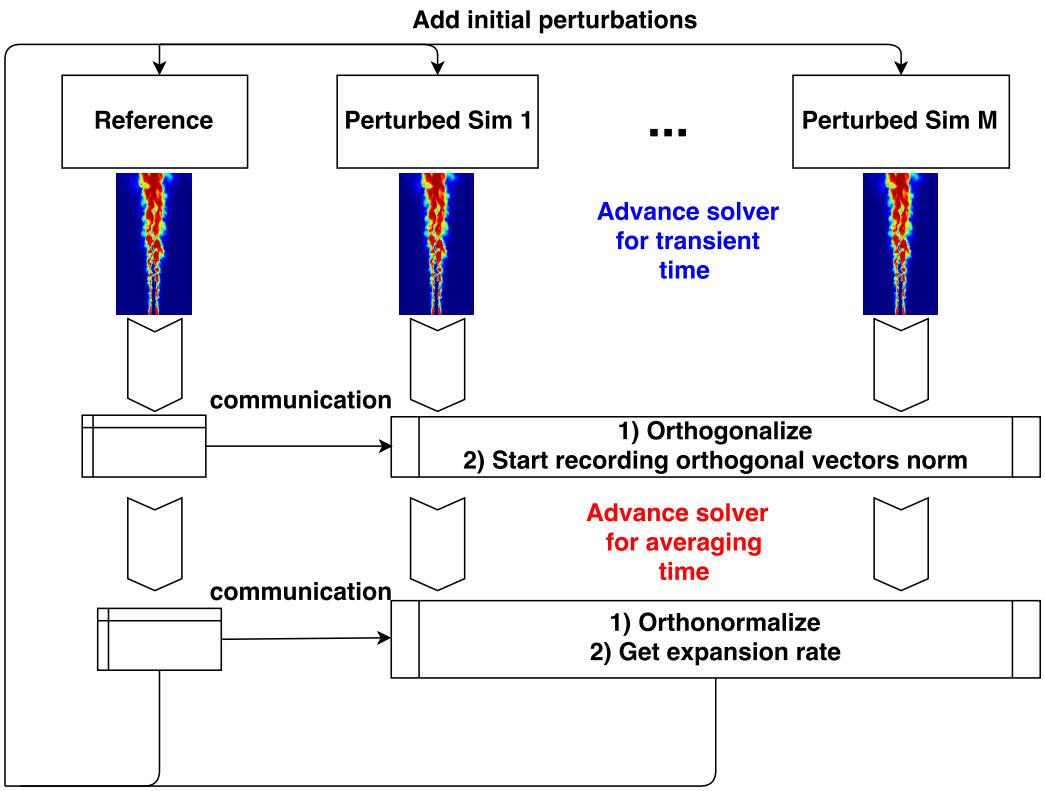

Figure 5.5: Flow chart of the modified algorithm used to compute the Lyapunov spectrum of the D and E flames.

leads to scattering near the stoichiometric mixture fraction with suppressed values for progress variable in the flame E simulations. Hence, the dimension of the attractor, which is the effective number of dimensions that dictate the evolution of the turbulent flame, is a crucial metric. Here, the Lyapunov spectrum of exponents is computed using the algorithm described in the previous section. The LEs are obtained over a total simulation time of 0.2s for the D flame and 0.12s for the E flame. The coarse grid results are averaged over twice this amount of time. In the end, 300 exponents were computed for both the D and the E flame.

Figure 5.7 shows the LE spectrum for both flames. For each exponent, an error estimate is defined by considering the time series of LEs and applying the central limit theorem while compensating for the lack of independence of the samples [141]. The spectra exhibit interesting trends. First, there is a clear decay in the values of

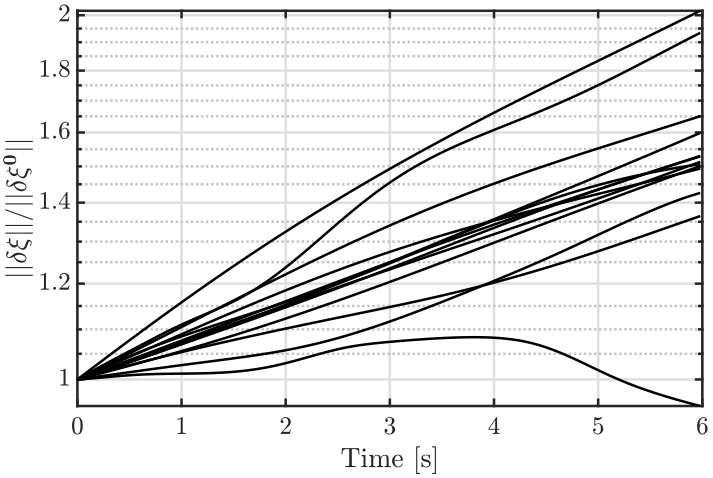

Figure 5.6: Time evolution of the perturbation norm used to compute the first LE scaled by the initial perturbation norm for the HIT solved with 128^3 points. The perturbation norm is plotted over 15 cycles. Each line is a particular cycle.

the LEs with an increase in the LE index, that follow a power-law-like shape, in line with the findings of Chap. IV. The first negative LE can be expected to be obtained at much higher LE indices. Using an extrapolation procedure for the value of the LEs for both flames, based on a power fit (similar to Chap. IV), the attractor dimension can be obtained using the Kaplan-Yorke definition as:

$$D = i + \frac{\sum_1^i \lambda_j}{|\lambda_{i+1}|}, \tag{5.1}$$

where λ_j denote the j^{th} LE, and i is the last index such that $\sum_1^i \lambda_j \geq 0$. The estimation yields an attractor dimension of roughly 5000 for flame D and roughly 10500 for flame E. This estimate is obtained using the filtered solution and is expected to be lower than the dimension that would be obtained with fully resolved simulations. As an illustration, the spectrum obtained with the coarser resolution is shown in Fig. 5.7 would lead to lower estimates of the attractor dimension. It shows that the dimension obtained here can be considered as a lower bound of the dimension of the fully resolved attractor. Despite the large level of uncertainty, the dimension of the

attractor can be approximated to be of order $\mathcal{O}(10^4)$ and should be compared to the number of degrees of freedom that is necessary to perform a DNS of the D flame $\mathcal{O}(10^{10})$ [183].

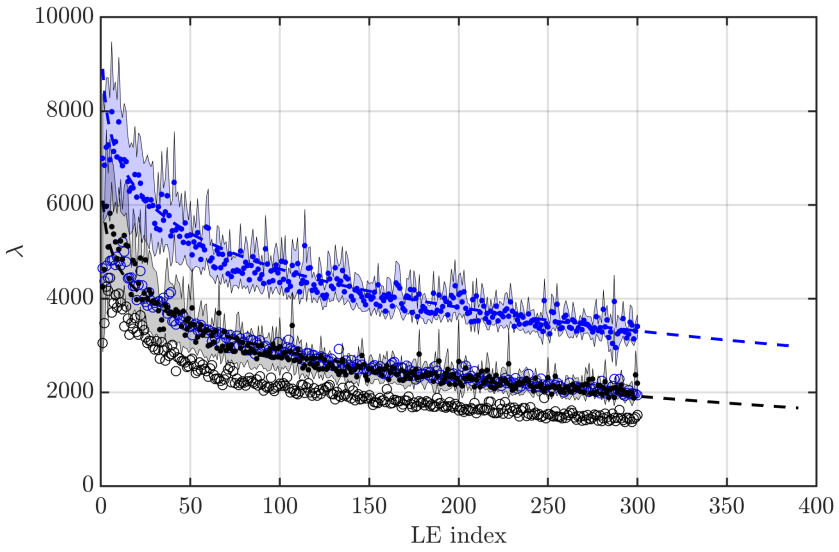

Figure 5.7: Lyapunov exponents of the D flame (black symbols) and the E flame (blue symbols). Filled symbols are obtained with resolution $256 \times 128 \times 32$, empty symbols are obtained with resolution $172 \times 90 \times 32$. The shaded region denotes the uncertainty associated with the sampling errors for the exponents of the D flame (black shade) and the E flame (blue shade). The dashed lines (black for D flame and blue for E flame) are the inverse power law fit used to determine the attractor dimension.

Second, the LEs for the flame E are larger than the corresponding LEs for the flame D. The inverse of LE can be understood as a time-scale over which perturbations grow. Here, this indicates that perturbations expand faster in the flame E than the flame D. Given the same perturbation, the growth in these perturbations will be larger for the flame E compared to the flame D. The largest strain rates for flames D and E are roughly 2×10^5 s^{-1} and 2.5×10^5 s^{-1}, respectively. The LEs are much lower than the peak strain values, indicating that perturbation dynamics are controlled by length and time scales that lie in the inertial range of the turbulence cascade.

Finally, it is important to note that the larger LEs tend to have higher scatter in

values, indicating that the local expansion rates in phase space change significantly. However, the scatter reduces at lower values of LEs (especially for the flame D), which is an indication that there are stable sub-spaces where the perturbation expansion is dictated by flow properties that are location independent.

5.3.2 Characterization of the response of the system to perturbations

The second component of the Lyapunov computations is the set of Lyapunov vectors, which are N_l fields of the corresponding primary variables N_s. Each vector is orthogonal to every other vector by definition. Figure 5.8 shows the progress variable component of the first and 300^{th} LVs of the D flame (in the following, this quantity is called LVP). Note that the magnitude range ($\pm 1 \times 10^{-10}$) is a function of the number of variables in the LVs since the vector is normalized. While both fields have similar magnitudes, there is a clear difference in their spatial distribution. The first LVP is clustered at particular locations of the jet. Further, this LV is highly unsteady (not shown here) and changes locations with time. The 300^{th} LVP is spread along the shear layer that separates the fuel jet and the pilot. This suggests that the first LVP is controlled by an intermittent phenomenon. The LVPs have a structure similar to the strain/dissipation rate, with alternating negative and positive values. Further, the length scale of the structures decreases from the first to the 300^{th} vector.

Since the LVs are mutually orthogonal, it is expected that they identify different instability modes of the system. For the Sandia flame series, the main sources of chaoticity are extinction/re-ignition and turbulence. To determine the relative roles of these physical mechanisms, the extinction process is first defined in terms of a burning index, a quantity that has been modified from the original definition [184] to represent a field:

$$BI(\boldsymbol{x}) = \frac{C(\boldsymbol{x})}{C_b(\boldsymbol{x})_{|Z_{mix}(\boldsymbol{x})}}, \tag{5.2}$$

where $BI(\boldsymbol{x})$ is the burning index field, $C(\boldsymbol{x})$ is the progress variable field and $C_{b_{|Z_{mix}}}$

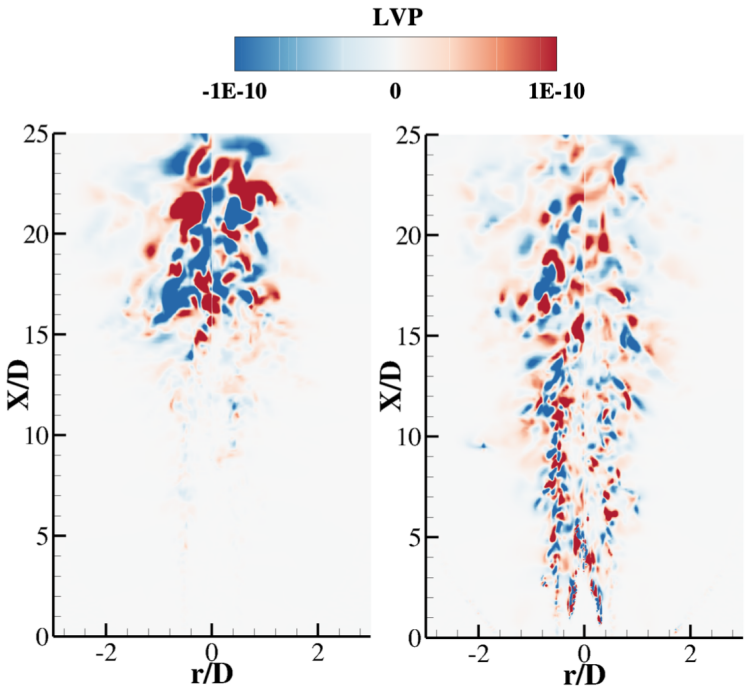

Figure 5.8: Contours of the progress variable component of the first (left) and 300^{th} LV (right) of the D flame.

is the progress variable at the local mixture fraction for a fully burning flamelet. A burning index close to 0 indicates extinction, while 1 denotes a fully burning solution. The maximum progress variable is obtained from the flamelets generated with the smallest strain rates. Figure 5.9 shows the probability of finding the absolute values of LVP components above a particular threshold conditioned on the burning index. For both flames, two different peaks exist: a peak at $BI = 0.85$ (flame D) or 0.8 (flame E), and a peak at $BI = 1$. The first peak is related to partially burning regions of the flame and denotes a direction in phase space along which any additional perturbation can cause the flame to transition to an extinguished or re-ignited state. The second peak is related to turbulence induced jet motion in the fully burning part of the flame. The relative height of the peaks indicates which mode dominates each LV. It appears that the progress variable instabilities captured by the first LV are more related to extinction/reignition effects, while the instabilities captured by the last LV are more related to jet oscillation, i.e., turbulence induced instabilities. Note that the value

of the threshold has little influence on the results, as long as infinitesimal values of LVP are filtered. Similar results were found with the coarser grid simulation (Fig. 5.9 right). This suggests that although the underlying flow field is not grid-converged (see Sec. 5.1.2), the structures of the LVs at different grid resolution are distributed the same way.

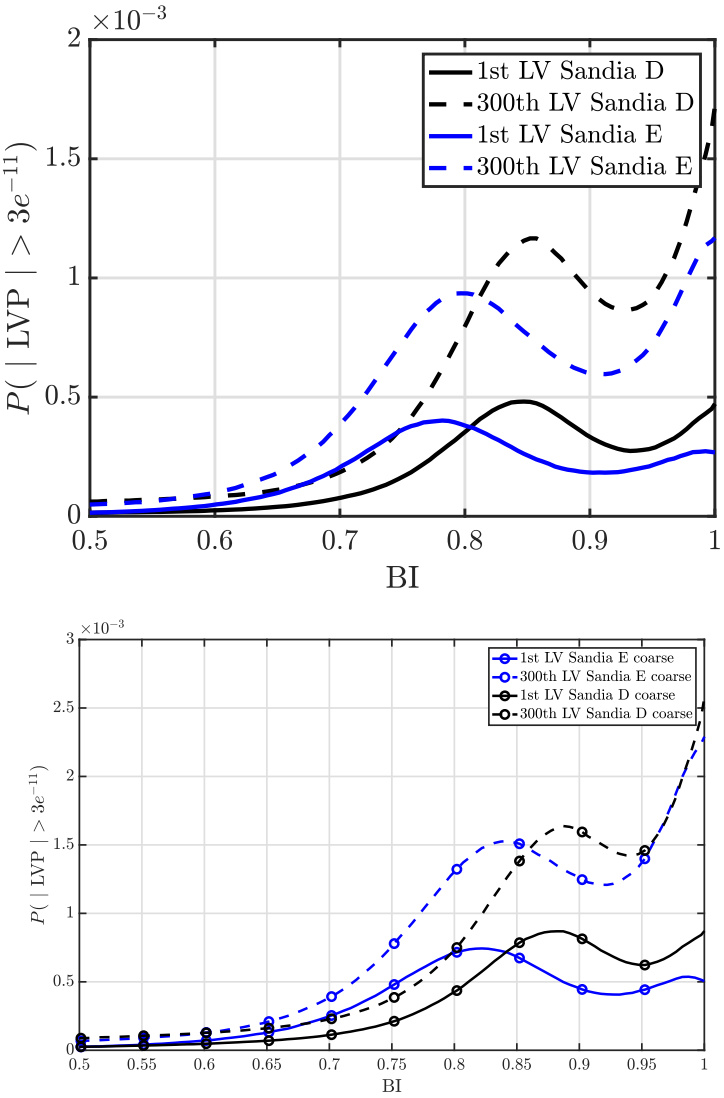

Figure 5.9: Probability of encountering $|\text{LVP}| > 3 \times 10^{-11}$ conditioned on the burning index. Solid lines denote the first LV, dashed lines denote the 300^{th} LV. Black lines denote the Sandia D (obtained over 250 realizations) and blue lines denote the Sandia E (obtained over 160 realizations). Top: fine resolution $256 \times 128 \times 32$. Bottom: coarse resolution $172 \times 90 \times 32$.

Figure 5.10 shows the distribution of the mean of the absolute value of LVP in the (Z_{mix}, C) space. The plot shows results consistent with the BI analysis (Fig. 5.9) as a peak in the LVP is visible for 0.8 of the fully burning flamelet (highlighted in the figure). This implies that the flame is the most responsive to perturbations in the region of phase space between fully burning and extinguished. Physically, the regions of extinction and reignition generate large time derivative of density which strongly affect the flow field. Therefore, it is unsurprising that the response of the flow field is marked the most in these regions. The phase space plot also reveals that most of the perturbations are effective at a mixture fraction of around $Z_{mix} = 0.6$, which corresponds to the shear layer between the inner jet and the pilot jet for $x/d < 25$. It is also seen that the perturbations do not increase as much where the reaction is the most active. For this flame, the reaction acts as a constraint on the chaoticity.

5.4 Summary and conclusions

In this chapter, the Lyapunov analysis was applied to a canonical turbulent flame to understand perturbation dynamics of turbulent flames. It is first highlighted that in variable density problems, the initial perturbation norm cannot be made arbitrarily small; otherwise, machine precision errors may influence the direction of the perturbation. The consequence of this modified perturbation direction is that the flow can be set in a non-mass-conservative state leading to large initial variations in the initial steps of the calculation of the Lyapunov exponents. For this reason, it might be beneficial to increase the initial size of the perturbation to avoid such issues. Alternatively, a numerical procedure has been introduced to bypass this effect and is shown to damp the initial growth of the perturbation vector norm, and recovers the LEs when the initial growth is not observed.

The Lyapunov analysis allows full characterization of the chaotic dynamics associated with turbulent flows, which have broad ramifications for both modeling and

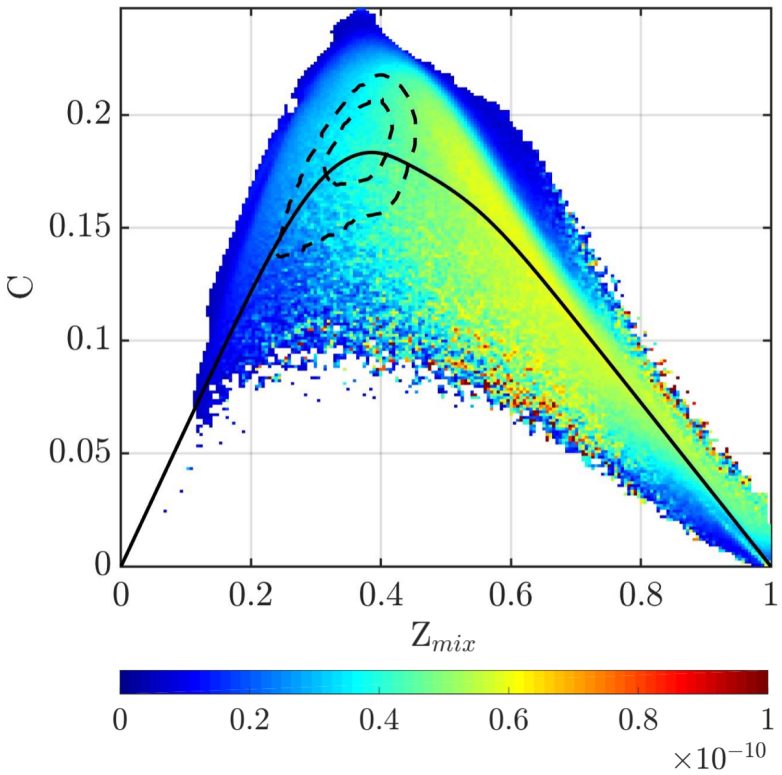

Figure 5.10: Average conditioned on the mixture fraction and progress variables for |LVP| for the 300^{th} LV of the E flame. Average is taken over 160 realizations. Overlaid with 80% of the fully burning flamelet of strain rate $a = 87s^{-1}$ (solid line). Overlaid with 2 iso-contours of progress variable source term (dashed lines).

control of such complex flows. The algorithms can be directly applied to any practical flow, by replacing the computational solver used in the ensemble procedure. The ensemble-LES approach is used to estimate the dimension of the chaotic attractor for Sandia flames D and E. The results indicate that the dimension is at least 5000 (flame D) and 10500 (flame E) which are smaller than the full dimension of the state-space $N = 7.34 \times 10^6$. This is a significant result, which demonstrates that the strong thermodynamic relations imposed by the combustion process combined with the larger viscosity related to the heat-release severely constrain the dynamics of the flow. As a comparison, a recent DNS run for the Sandia D flame required about 10^{10} degrees of freedom [183].

In addition to the Lyapunov exponents, the LVs describe the response of the flow to perturbations. These modes are dictated by the interplay between extinction/re-ignition and the turbulence-induced jet motion. In particular, the strongest growth is related to the jet breakdown process, while other LVs are aligned with the extinction/re-ignition regions in the shear layer. Further, the perturbation growth modes exhibit location-dependent behavior in (Z_{mix}, C) space. The response of the flow to perturbation is dominant in regions of extinction/re-ignition, in the rich side of the shear layer and away from the location of maximum heat release.

In conclusion of Chap. II-V, the Lyapunov theory is a valuable tool to characterize the dynamics of turbulent flow and combustion problem. It allows evaluating how the flow responds to perturbations. This characterization of the dynamics can help understand how deviations from nominal behavior occur which can lead to a better understanding of the process through which extreme events are triggered.

This chapter closes the discussion about applying the Lyapunov analysis to turbulent reacting flows. In Chap. VI, a method that characterizes, in turn, the statistics of extreme events will be described.

CHAPTER VI

Statistical analysis of extreme events

In Chap. II-V, the focus was on providing a global characterization of the dynamics of turbulent inert and reacting flows. This approach was justified by the need to understand how extreme events occur in complex systems. Among the five challenges of extreme events listed in Chap. I, not all the questions were concerned with the dynamics of the system. In particular, the quantification of the probability of an extreme event requires a statistical approach.

Predicting the probability of rare events is particularly important if one wants to design devices resilient to intermittent and spontaneous events. For example, the probability of an extreme event can be used to quantify how many times a device will be exposed to extreme conditions it during its lifetime. The probability may also be used to simply assess the relevance of the extreme event. Typically, extreme events that are too rare may actually be irrelevant (see Sec. 1.2.2).

The prediction of the probability of a rare event using random observations is problematic in general as the uncertainty of a probability estimator scales with the number of observations of the rare event. Computing the probability of a rare event using a Monte-Carlo estimator requires observing many realizations of the system. A remedy to this problem is to observe rare events more often than non-rare events. In this Chapter, a method to accelerate the observation of rare events is proposed. It

relies on the following principle: a phase space trajectory leading to a rare events is close to one leading to less rare events. This chapter is partially based on [185].

6.1 Introduction

Rare excursions of a complex system from its nominal behavior are difficult to predict, since very few observations, if at all any, would exist to reliably characterize the source of this behavior. Although rare events are sparsely encountered, when they are associated with extreme events, their impact can be of tremendous importance. For instance, in propulsion applications, gas turbines and other such energy conversion devices are designed to minimize failure probability, but any failure can have catastrophic consequences [90, 186]. The problem of rare event prediction is also relevant to other fields such as market crashes in financial systems [187], prediction of reaction rates in molecular dynamics [188], the occurrence of rogue waves next to offshore platforms [26], rare and extreme atmospheric heat waves [28], heavy rains [33, 189] or energy grid blackouts [190]. Even though each such event is rare, the presence of this possibility requires an endeavor to develop prediction tools.

Defining prediction in this context is itself a multifaceted issue [90], but much of the prior work in this area can be grouped as following a dynamical systems approach or a statistical approach. In the dynamical approach, the goal is to characterize the dynamical behavior of the system, such as its response to perturbations or its stability properties (See Chap. III-V). One application could be that understanding these aspects could enable real-time control, where some precursor is identified for the purpose of an actuation mechanism. In the statistical approach, the goal is to obtain statistics of a rare event. Estimating the probability of a rare event may enable a more resilient system that is less susceptible to such extreme excursions. Such statistical approaches can also reveal the average behavior close to a rare event, which may also be used to identify precursors. However, developing such a statistically significant

ensemble of rare events is in itself a formidable challenge. This is especially the case in high-dimensional systems, where several paths to such rare events may exist. The focus of this work is to develop a statistical framework for such high-dimensional systems, where features of a rare event trajectory are inferred from less rare (more probable) trajectories.

Rare events occur when there is some uncertainty imposed on the system. For instance, this could be due to uncertainty associated with the initial or boundary conditions. The objective of the numerical approach is to sample realizations that lead to extreme events, as defined by specific regions of phase-space. For this purpose, consider the quantities used to define the rare events as $\boldsymbol{\xi} \in E$, where E is the phase space. The rare event probability is defined as $p = P(\boldsymbol{\xi} \in A)$, where $A \subset E$. In a Monte-Carlo sense, this probability can be estimated by sampling n independent events, with the estimator of p given by

$$p = \frac{1}{n} \sum_{i=1}^{n} 1_A(\boldsymbol{\xi}_i),$$

where $1_A(x) = 1$ if $x \in A$ and 0 otherwise. While the estimator is unbiased, the variance of this estimator can be obtained as $(p - p^2)/n$. The relative uncertainty of the estimator scales as $\sqrt{\frac{1}{np}}$ for $p << 1$. Therefore, the lower the probability to be estimated, the higher relative uncertainty of the estimator. In order to improve this estimation process, a reliable approach to sampling more of the trajectories that lie in A is necessary. The main challenge that makes such an estimator difficult to obtain is that the set of initial/boundary conditions that lead to the rare event is not known a priori.

There are many techniques that exist to improve this estimation procedure. For example, in importance sampling methods [191], a biased distribution is used to draw more samples from certain regions of initial and boundary condition space. However,

the optimal bias needed to obtain extreme events is unknown, which reduces the effectiveness of this method [192]. Typically, a functional form of the biased distribution is assumed, and its parameters are adjusted to approximate the optimal biased distribution [193]. The biased distribution could also be obtained from the direct observation of a rare event with a cheaper low-fidelity model [194]. An alternative technique is the importance splitting (ISP) method, where the rare event region is progressively reached. Suppose that one defines a rare event as $A = \{\boldsymbol{\xi}, Q(\boldsymbol{\xi}) > a\}$, where $\boldsymbol{\xi}$ is the state of the system, $Q(\boldsymbol{\xi})$ is the quantity of interest (QoI) and a is some threshold. Instead of directly finding A, one can sample $A_i = \{\boldsymbol{\xi}, Q(\boldsymbol{\xi}) > a_i\}_{1 \leq i \leq N}$ such that $a_1 < ... < a_N$, and use the fact that $A_1 \supset ... \supset A_N$. Until recently, these methods were limited due to their sensitivity to the definition of the intermediate levels $a_1, ..., a_N$. New adaptive methods that do not require to define these levels explicitly [195] have allowed importance splitting to be used in a variety of fields [196, 197]. Recently, ISP has been shown to be particularly successful at capturing rare events in turbulent flows. For example, it has been used to observe transitions in planetary atmosphere [196, 198]. It has also been successful for computing the time separating two extreme events (return times) in turbulent flows that can be obtained from the probability of the rare event itself [28, 199]

For the specific problem of interest, Wouters et al. [16] introduced a genealogical particle algorithm based on Ref. [200]. The algorithm relies on the simulataneous evolution of several copies of the dynamical system. The copies that are the closest to the rare event of interest are cloned or pruned periodically. At the end of the procedure, the observation of the system are clustered next to rare event of interest and can be used to estimate the desired probability. With this background, the goal here is to use properties of the physical system to improve the convergence of estimators, especially when used with the ISP method. In particular, the approach is inspired by techniques used in computational chemistry. For instance, if the goal is to

capture the probability of transition of a molecular system from one state to another, it can be beneficial to focus calculations around the most likely transition path in order to observe many such transitions [201]. In other areas, including fluid mechanics, the importance of the most likely path leading to a rare event (the instanton) has also been recognized and used to sample rare-events [51, 198, 202]. It was also noted by Wouters et al. [16] that the knowledge of the path to a rare event can help for the convergence of the importance splitting algorithm they introduce. Here, this notion of estimating the most likely path to a rare event is quantified in the case of high-dimensional deterministic dynamics.

The rest of the paper is organized as follows: Section 6.2 briefly describes the algorithm of Wouters et al. and illustrates the benefit of using the average time-history of the observable that correspond to rare events for the statistics of the probability estimator. Section 6.3 introduces a method to estimate the path to a rare event from a simple rationale. The method is tested with an *a priori* and *a posteriori* analysis. In Sec. 6.4, the applicability of the method to more complex systems is investigated and discussed. Concluding remarks are provided in Sec. 6.5.

6.2 Path-to-event based estimation of probability

6.2.1 Definition of the dynamical system and rare event notation

The rare events of interest occur over a finite-time interval, and the quantity of interest (QoI) is defined at the final time. More formally, the dynamical system is defined as

$$\forall t \in [0, T_f],\ \frac{d\boldsymbol{\xi}}{dt} = \mathcal{F}(\boldsymbol{\xi}),\ \boldsymbol{\xi}(t=0) \sim \mathcal{P}, \tag{6.1}$$

where $\mathcal{F}$ represents the governing equations. In the case of turbulent flow or other systems governed by partial differential equations, $\mathcal{F}$ is some finite-dimensional approximation of these equations obtained by, for instance, numerical discretization.

$\mathcal{P}$ is the nominal distribution of initial conditions. The QoI is defined as $QoI = Q(\boldsymbol{\xi}(T_f)) = Q(T_f)$ and the observable is chosen to be $Q(t)$.

6.2.2 Genealogical particle algorithm

The genealogical particle algorithm introduced in Ref. [16] is briefly presented as it will be used as the basis for the proposed method. Since the problem is deterministic, only the uncertainty in initial conditions can lead to a distribution of QoI. The goal is to find the probability with which the QoI exceeds a certain threshold a, $P(Q(T_f) > a)$. The algorithm starts by sampling M initial conditions (also called particles) at $t = 0$ that are evolved over time. The name genealogical is due to the fact that at intermediate times (or selection steps) between $t = 0$ and $t = T_f$, realizations that are deemed likely to lead to the rare event are cloned, while others are pruned. Cloning of particles implies that at time $t = T$, another copy of this particle is initiated. For deterministic dynamics, this copy should be perturbed by a small amount before being evolved. In this work, the selection steps are fixed a priori and occur at fixed time stations. For the numerical tests that are conducted, the number of selection steps is expressed in terms of the timesteps that separate two selections. After every selection step, a special procedure is used to maintain the total number of trajectories to be constant (see [16, Sec. 2.3.3] for the details of this procedure). In order to select the particles that need to be cloned or pruned at every selection step, a weight is attributed to each particle based on the chosen observable. This particle weighting is the focus in this work.

The weight chosen in Ref. [16] is of the form $W = exp(C\Delta Q)$, where C is a constant called the *weighting factor* and ΔQ is the variation of the observable between two selection steps. The value of C determines the aggressiveness of the cloning process expressed as the pruning ratio $\frac{N_{prune}}{M}$, where N_{prune} is the number of particles that are pruned. A large value of C would lead to a large pruning ratio, meaning

that at every selection step, only a few particles are saved. In turn, a large pruning ratio would also prioritize particles that lead to the rarest events. In Ref. [16], it was proposed to choose C such that $C = \frac{\Delta\mu_Q}{\sigma_Q^2}$, where $\Delta\mu_Q$ is the deviation between the expected values of the QoI at the end of the ISP compared to a expected value of QoI without using the ISP, and σ_Q^2 is the variance of the QoI at $t = T_f$ without using the ISP. In practice, the statistics of the QoI can be estimated by running M non-biased simulations prior to using the ISP. If a large deviation from the average behavior is sought, then $\Delta\mu_Q$ will be larger and the value of C will increase as well. Since C controls the pruning process, it is necessary to understand the implications of the choice of this variable.

The influence of the weighting factor C on the ISP is illustrated in Fig. 6.1 for the Lorenz 96 system [203], using parameters based on Ref. [16]. This system will be used throughout the paper as a benchmark for the performances of the modified algorithm. This system is non-linear, can have an arbitrarily high number of dimension and exhibits chaotic dynamics that makes it a good surrogate for turbulent flow problems. The governing equations are written as

$$\forall t \in [0, T_f],\ \forall i \in [1, d], \frac{d\xi_i}{dt} = \xi_{i-1}(\xi_{i+1} - \xi_{i-2}) + f - \xi_i, \tag{6.2}$$

where $f = 256$, $\xi_{d+1} = \xi_1$, $\xi_0 = \xi_d$, $\xi_{-1} = \xi_{d-1}$ and d is the number of degrees of freedom chosen (here, 32). The observable considered here is related to the turbulent energy of the system and is defined by

$$Q = \frac{1}{2d}\sum_{i=1}^{d} \xi_i^2. \tag{6.3}$$

A second-order Runge Kutta scheme is used for the time-integration, and the time step is set to 10^{-3}. In Fig. 6.1 (left), 1000 instantaneous realizations of Q are shown along with the ensemble average. The initial conditions are distributed

following a normal distribution $\mathcal{N}(0,1)$ and quickly diverge from each other due to the chaotic dynamics. In the middle and right plots, the trajectories simulated at the end of the splitting algorithm using $M = 100$ particles are shown for weighting factors $C = 0.0104$ (middle) and $C = 0.0208$ (right). Note that the weighting factor $C = 0.0104$ was used in Ref. [16] to demonstrate the capabilities of the algorithm. At every selection step, the clones are perturbed using a normal distribution $\mathcal{N}(0, 0.871)$. The selection steps are separated by 19 timesteps. Note that the importance splitting algorithm is stochastic due to perturbation introduced during the cloning process. Hence, the algorithm needs to be executed multiple times to obtain statistics about the probability estimator. As can be seen, the largest weighting factor leads to the largest value of QoI at the final time. However, it also quickly discards most of the particles. This effect was also observed in [204]. As a result, the solution space ensemble containing the trajectories that lead to a rare events are not appropriately sampled, which can lead to large variance for the probability estimator, thereby increasing its associated uncertainty.

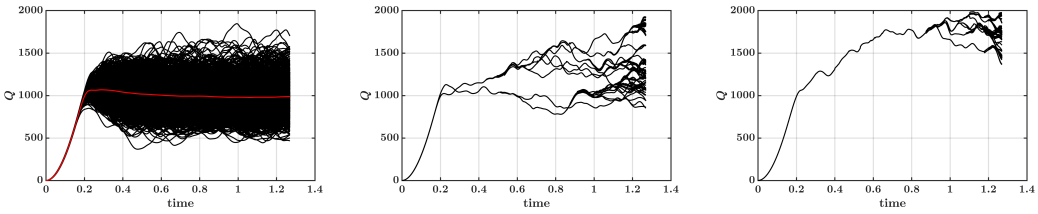

Figure 6.1: Left: instantaneous values of the observable $Q(t)$ plotted over time (—). Ensemble average of Q (—). Middle: time-history of $Q(t)$ obtained with the importance splitting algorithm using a constant weight factor $C = 0.0104$. Right: time-history of Q obtained with the importance splitting algorithm using a constant weight factor $C = 0.0208$. Plots correspond to the Lorenz 96 case with 32 degrees of freedom.

6.2.3 The rare mean path approach

In order to improve the trajectory sampling for estimating probabilities of events significantly removed from the mean behavior, the weighting factor will have to be modified. In fact, the weighting factor could be made time-dependent [16]:

$$C(t) = \frac{\mu_{rare}(t) - \mu_Q(t)}{\sigma_Q(t)^2}, \tag{6.4}$$

where $\mu_{rare}(t)$ is the time-dependent value of the average observable leading to a rare-event, $\mu_Q(t)$ is the time-dependent value of the ensemble average observable and $\sigma_Q(t)^2$ is the time-dependent variance of the observable. In Ref. [16], this method was illustrated for a noise-driven problem for which $C(t)$ could be analytically computed, and it was shown to decrease the pruning ratio while leading to the expected final QoI. Here, the objective is to evaluate this procedure for the Lorenz 96 problem and quantify the impact of the procedure on the statistics of the probability estimator. In all the following discussions, target level refers to the threshold that QoI is designed to exceed at the final time when using the ISP. For the fixed-weight algorithm, target level refers to $\Delta\mu_Q + \mu_Q(T_f)$, and for the time-dependent algorithm, target level refers directly to the threshold a.

The system of interest is defined by Eq. 6.2. While, $\sigma_Q(t)$ and $\mu_Q(t)$ can be approximated using a few observations of the system, estimating $\mu_{rare}(t)$ requires observation of the rare event. The target levels investigated are $Q(T_f) = 1356$ and $Q(T_f) = 1737$, and are located two and four standard deviations away from the mean. In order to get a reasonable approximation of the mean path leading to these values, 10^6 trajectories are simulated. The value of the observables for the trajectories exceeding these levels are stored and averaged at every timestep. More formally, the mean path $R(t)$ that exceeds a threshold a is defined as:

$$\forall t \in [0, T_f],\ R_a(t) = \langle\, Q(t) \mid Q(T_f) > a \,\rangle. \tag{6.5}$$

The mean trajectories of the observable leading to both levels are shown in Fig. 6.2.

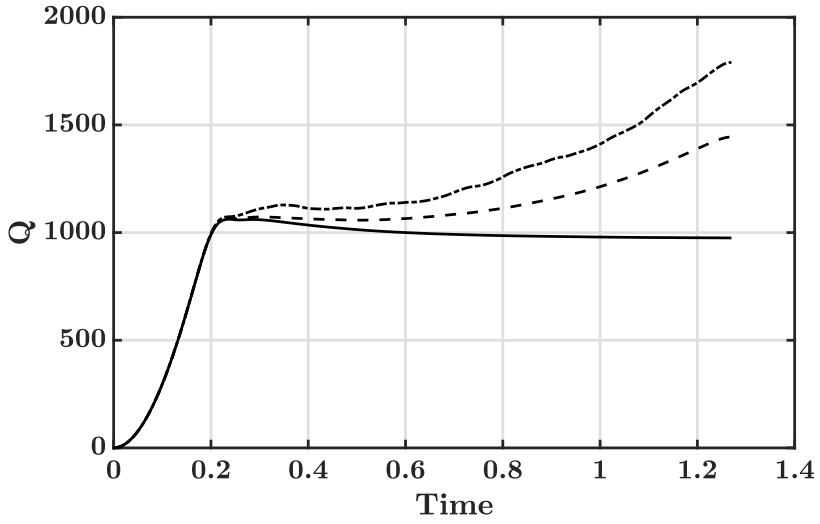

Figure 6.2: Ensemble average time history of the observable (—). Rare mean path of the observable R_{1356} (- -); R_{1737} (-··-). Plots correspond to the Lorenz 96 case with 32 degrees of freedom.

Using the computed rare mean path, the probability $P(Q(T_f) > 1356)$ and $P(Q(T_f) > 1737)$ are computed using the genealogical particle algorithm presented in Sec. 6.2.2 with the fixed and the time-dependent weighting factor. Here, the number of particles is $M = 2500$ and algorithm is run 100,000 times in order to ensure that the statistics of the estimator are converged. In Fig. 6.3, the probability obtained with the fluctuating path approach is compared to a brute force calculation computed with 8×10^8 calculations. Note that although a single level is targeted, it is only used to compute C. The ISP method used does not preclude from estimating probabilities at higher levels. Therefore, the results present probabilities corresponding to different value of the QoI. As can be seen, the estimators obtained are unbiased, and the variance is significantly reduced compared to that of the Monte-Carlo simulation. Furthermore, by targeting larger levels, lower probabilities can be estimated by the

algorithm. For reference, the probability obtained in Ref. [16] through Monte-Carlo run are also indicated to show consistency between the cases run.

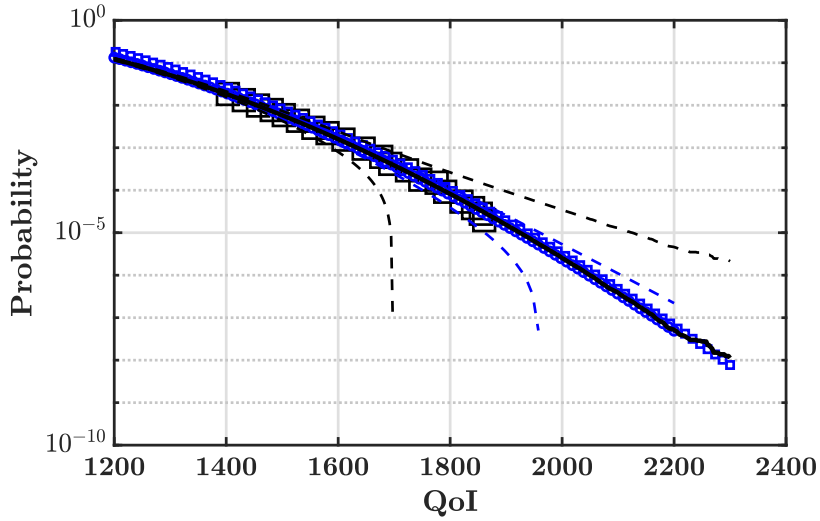

Figure 6.3: Complementary of the cumulative density function (CDF) of the QoI. Probabilities are obtained with brute force calculation (—), the ISP method with time-dependent weight based on R_{1356} (○), and R_{1737} (□) and $M = 2500$ particles. Uncertainty of the estimator computed with the ISP algorithm using R_{1356} for the time-dependent weight is shown (--) along with the theoretical Monte-Carlo uncertainty that would be obtained with $M = 2500$ realizations (--). The computed probabilities provided in Ref. [16] are also provided for reference (□). Plots correspond to the Lorenz 96 case with 32 degrees of freedom.

The performances of the importance splitting algorithms with fixed and time-dependent weights are further investigated in Fig. 6.4, where the variance of the probability estimator is plotted in terms of the computational gain compared to a naive Monte-Carlo simulation. More precisely, the computational gain G is defined as the number of brute force simulations required to achieve the same variance as the ISP, divided by the number of particles M used for the ISP:

$$G = \frac{p - p^2}{M\sigma_{ISP}^2}, \tag{6.6}$$

where p is the probability of the rare event, and σ_{ISP}^2 is the variance of the

importance sampling estimator.

For both the fixed weight and time-dependent weighting factor, significant computational savings can be obtained, especially for low-probability events. The target probability corresponding to $Q(T_f) = 1356$ and $Q(T_f) = 1737$ are indicated as the vertical black lines. Interestingly, the importance splitting algorithm does not provide computational gains at these levels, which means that the final distribution of Q is not centered around the target levels. Therefore, the choice of the weights according to the rationale of Eq. 6.4 does not guarantee computational efficiency at the level targeted. As expected, when the cloning is more aggressive, the computational gain increases more steeply as the probability decreases. This is observed for both the fixed and time-dependent weights. The main difference between fixed and time-dependent weighting is apparent when targeting higher values of the QoI. The fixed weight only provides computational gain for probabilities lower than 10^{-6} and is consistently outperformed by the time-dependent weight algorithm. This result can be explained by the fact that the fixed weight method discards many trajectories too quickly. The average pruning ratio taken across the 10^5 realizations of the ISP for the fixed and time-dependent weighting factors are shown in Fig. 6.4 for both target levels, and indicate a consistently larger pruning ratio for the fixed weight method. At lower target levels, while the pruning ratio is larger, the computational gains between the fixed and time-dependent weighting factors are almost the same. It is likely that even a small number of additional trajectories that are not pruned can have a disproportionate effect on the performance of the estimator. This further emphasizes the importance of the weighting method for this algorithm. Additional cases are run with 64 and 1024 degrees of freedom instead of 32 to evaluate the effect the dimensionality of the problem of the findings. The results (shown in Appendix C.1) suggest that the above findings hold for higher number of dimensions as well.

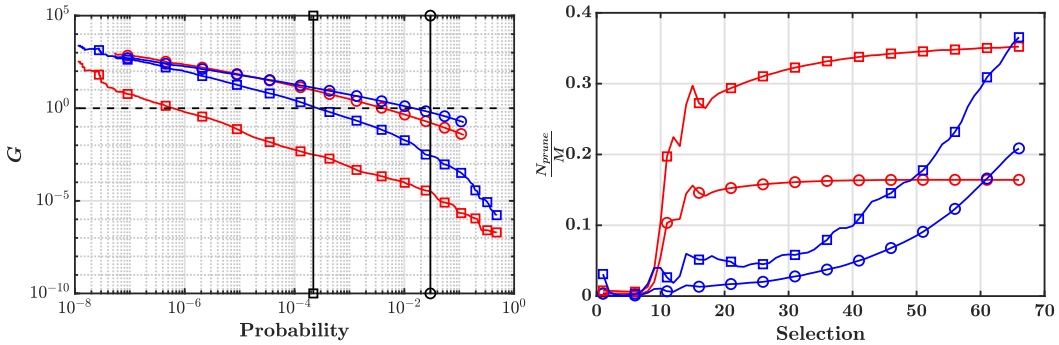

Figure 6.4: Left: computational gain expressed in terms of Eq. 6.6 when targeting the level 1356 with fixed weight (⊖) and time-dependent weight (⊖); when targeting the level 1737 with fixed weight (⊟) and time-dependent weight (⊟). The vertical line with ⊖ denotes the probability corresponding to the level 1356, and with ⊟ denotes the probability corresponding to the level 1737. Right: pruning ratio when targeting the level 1356 with fixed weight (⊖) and time-dependent weight (⊖); when targeting the level 1737 with fixed weight (⊟) and time-dependent weight (⊟). Plots correspond to the Lorenz 96 case with 32 degrees of freedom.

6.3 Self-similarity approach for estimating the path to a rare event

In the previous section, it was found that knowing the mean path to a rare event can significantly improve the statistics of the probability estimators, especially to estimate low probabilities. However, to obtain the rare mean path, the approach used in Sec. 6.2.3 required to observe many rare events in the first place, which defeats the purpose of the procedure. Instead, it is preferable to estimate the path to a rare event using a different method. In this section, a brief review of the available methods is provided in order to convey the point that simpler procedures are needed. For this purpose, the self-similarity based approach is introduced here. The method is tested using both a priori calculations and a posteriori analysis.

As mentioned in Sec. 6.2, it has been widely recognized that the knowledge of the average or most likely path leading to a rare event is advantageous in computing the probability of this event. In computational chemistry, transition paths are typically

obtained through an optimal sequence of trials and errors, also referred to as the shooting method [201]. Another approach well-suited for noise-driven rare events consists of finding the optimal time history of external forcing that can drive the system to a rare event. This optimum can be obtained by solving a minimization problem [51, 198] or by directly solving a partial differential equation (PDE) [202] for this instanton. However, such methods can create numerical issues for deterministic chaotic systems that evolve over long periods of time [205]. In this work, a simpler approach is developed, motivated by the observation that there exists self-similarity in the paths that lead to rare events for the system investigated.

6.3.1 A priori analysis

Using the brute force Monte-Carlo simulation for the Lorenz 96 case with 32 degrees of freedom (discussed in Sec. 6.2.3 with 8×10^8 trajectories), the rare mean path to many target levels can be accurately estimated. Several thresholds levels are selected between 1500 and 2000 and are separated by a constant step of size 25. The rare mean paths obtained are plotted in Fig. 6.5.

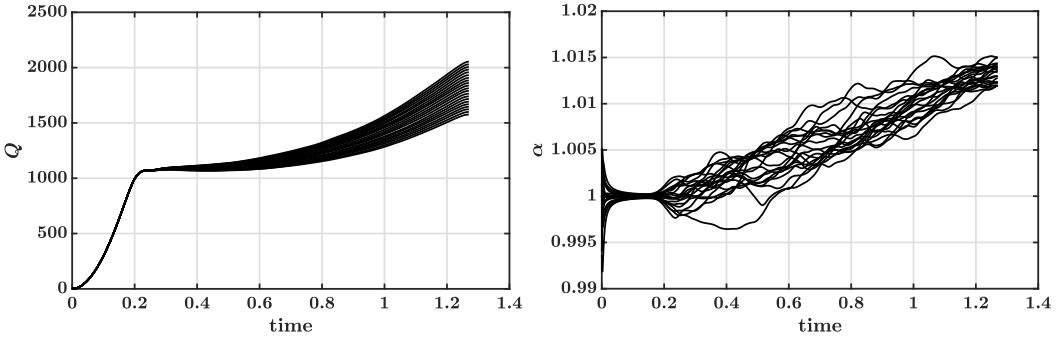

Figure 6.5: Left: rare mean path exceeding thresholds ranging from 1500 to 2000 and separated by a stepsize of 25. Right: self-similarity factor α computed from successive rare mean path (see Eq. 6.7). Plots correspond to the Lorenz 96 case with 32 degrees of freedom.

It can first be observed that the path leading to each one of the thresholds are surprisingly similar to one another. In other words, the paths that leads to rare

events share characteristics. This feature is termed *self-similarity*, which provides an approach to estimating the path leading to a rare event without necessarily observing it. The simplest model that can be formulated would consist in assuming that the path leading to a higher threshold for the QoI is simply shifted up by a certain ratio. More formally, given $a_1 < ... < a_m$ such that $a_{i+1} - a_i$ is constant and defining $R_i(t) = \langle Q(t) \mid Q(T_f) > a_i \rangle$,

$$\forall i \in [1, m], \frac{R_{i+1}(t)}{R_i(t)} = \alpha(t), \tag{6.7}$$

where α is independent of i. Here, α can be understood as a self-similarity factor that relates the rare mean paths separated by a step size of $a_{i+1} - a_i$ for the final value of the observable. In Fig. 6.5, this model is a priori tested by plotting the value of α. Indeed, the ratio α appears almost independent of the threshold considered which is in itself surprising given the simplicity of the model. It should be noted that many other models could be formulated and could involve the value of the QoI rescaled by its mean, or a more elaborate factor that depends on the response of the system to perturbation (Lyapunov exponents). Note that the same features are found with the Lorenz 96 system using 64 and 1024 degrees of freedom (Appendix C.1).

6.3.2 A posteriori analysis

To test the effectiveness of the self-similarity approach, an a posteriori analysis is conducted for the Lorenz 96 case with 32 degrees of freedom. A Monte-Carlo calculation with $M = 2500$ samples is conducted, where M is also the number of particles used in the importance splitting algorithm. Note that it is not unreasonable to expect a Monte-Carlo calculation to be run with M particles even for other purposes than of estimating the rare mean path. For example, a user of the ISP would typically run randomly sampled simulations in order to cross validate the output of the ISP, at least for the highest probability obtained with the ISP. Furthermore, the value of

the weighting factor requires estimating the first and second moments of the QoI, for which randomly sampled simulations would have to be run. Additionally, given that the probability estimate from the ISP is subject to some variance, it is preferable to run the ISP multiple times. The computational cost of the rare event path estimation is therefore of the same order of magnitude as other sanity checks that the user needs to run in general.

From the 2500 brute force calculations, the mean trajectory to threshold ranging from 1225 to 1325 are directly computed (based on definition in Eq. 6.5), in steps of $\Delta a = 25$, leading to at least 70 trajectories per threshold. The path $R_{1737}(t)$ to the threshold $Q(T_f) = 1737$ is then simply estimated as

$$\forall t \in [0, T_f],\ R_a(t) = \alpha_{ave}(t)^{\frac{a-b}{\Delta a}}\ R_b(t), \tag{6.8}$$

where R_a is the path to the target level (here, $a = 1737$), b is the largest level directly sampled from the M random samples (here, $b = 1325$), $\alpha_{ave}(t) = \langle \frac{R_{i+1}(t)}{R_i(t)} \rangle$. From here, the time-dependent weight $C(t)$ can be constructed according to Eq. 6.4. However, the extrapolation procedure incurs numerical errors that can be amplified in regions where $\sigma_Q^2(t)$ is close to 0. In practice, the absolute value of the weighting factor can be extremely large in these regions and lead to unreasonable pruning ratio. Instead, the weighting factor can be regularized by recognizing that the particle selection should be more and more aggressive close to T_f. In other terms, $|C(t)|$ should be an increasing function of time. Since the variance of the observable is expected to be large at T_f (the perturbations have had sufficient time to amplify), the numerical error at the latest time is least pronounced. Therefore, $C(t)$ can be enforced to be an increasing function of time in the following manner: starting from the value of C at the final time, step backwards from t to the previous timestep $t - \Delta t$. If $C(t - \Delta t) > C(t)$ then $C(t - \Delta t) = C(t)$; otherwise, do nothing. Then keep stepping backwards (compare $C(t - \Delta t)$ and $C(t - 2\Delta t)$). This procedure can then lead to a

step-like function for $C(t)$ which will be reflected in the pruning ratio (Fig. 6.6).

Figure 6.6 shows the extrapolated path towards the desired threshold is compared with path obtain from brute-force Monte Carlo computation. The extrapolation procedure does incur inaccuracies, but overall follows the correct trend. The ISP algorithm is then run with $M = 2500$ particles, with the weights $C(t)$ obtained from the extrapolated mean path. The ISP is executed 10^5 times in order to obtain good statistical convergence of the estimator. As can be seen in Fig. 6.6, the computational gain obtained with the a posteriori test is slightly lower than by using a brute force calculation to compute the rare mean path. This is because the rare mean path estimated using the self-similarity model is subject to inaccuracies, which lead pruning more observations than needed (See Fig. 6.6 right). However, the a posteriori test still outperforms the method with the fixed weighting factor, across all probabilities. By examining the pruning ratio, it appears that fewer samples are pruned when using the self-similarity approach as compared to the fixed weight method. The pruning ratio exhibits a series of steps that are due to the correction of numerical errors in the extrapolation. The same procedure appears to hold for a 64-dimensional and 1024-dimensional system (Appendix C.1).

6.4 Applicability to other systems

In Sec. 6.2 it was shown that the knowledge of the rare mean path could improve the convergence properties of the ISP algorithm. In Sec. 6.3, it was found that a simple approach could be used to estimate the rare mean path from less rare mean paths, and was demonstrated in the case of the Lorenz 96 case. In this section, it is examined whether the observations made in Sec. 6.3 are applicable for problems more representative of turbulent flows, which is the motivation behind this work. An a priori analysis similar to the one conducted in Sec. 6.3 is conducted for two different dynamical systems.

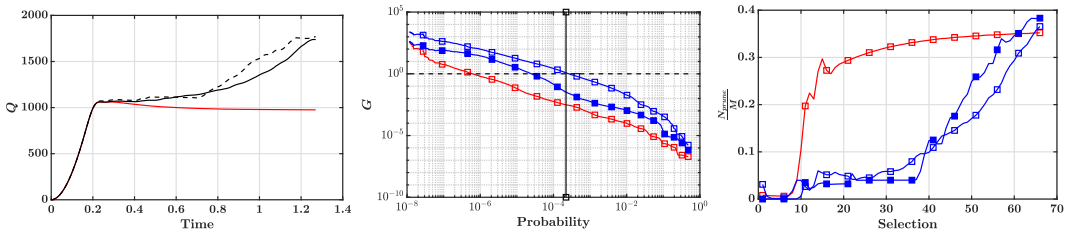

Figure 6.6: Left: rare mean path R_{1737} obtained from brute force computation (—), from the self-similarity approximation (- -) and ensemble average time history of the observable (—). Middle: computational gain computed as Eq. 6.6 when targeting the level 1737 with the fixed weight (⊟), the time-dependent weight obtained from the brute force calculation (⊟), the time-dependent weight obtained from the self-similarity approximation ■. Right: pruning ratio obtained when targeting the level 1737 with fixed weight (⊟) and time-dependent weight obtained from brute force calculation (⊟) and the time-dependent weight obtained from the self-similarity approximation (■). Plots correspond to the Lorenz 96 case with 32 degrees of freedom.

6.4.1 Kuramoto-Sivashinsky Equation (KSE)

The 1D Kuramoto-Sivashinsky [135, 136] equation is often used as a surrogate for the spatiotemporal chaos seen in turbulent flows. In this work, the formulation with with unit viscosity coefficient is used:

$$\forall t \in [0, T_f], \frac{\partial u}{\partial t} + \nabla^4 u + \nabla^2 u + \nabla u^2 = 0, \tag{6.9}$$

where u is defined on the domain $[0, 32\pi]$ and $u(t=0) = cos(x/16) \cdot (1 + sin(x/16))$, and $T_f = 150$ time units. The equations are integrated in time using the ETDRK4 scheme [137] with a fixed timestep of 0.25 time units. The equations are solved in Fourier space using $N = 128$ modes. Here, $\boldsymbol{\xi}$ is defined as the discrete version of u in physical space, i.e., $\boldsymbol{\xi} \in \mathbb{R}^{128}$ and the function q that defines the QoI is defined as

$$Q(t) = \frac{1}{N} \sum_{i=1}^{N} \xi_i^2. \tag{6.10}$$

Figure 6.7 shows the evolution of the QoI for different initial conditions, and exhibits variations representative of a chaotic system. The event probability is then defined as $P(Q(T_f) > a)$. The probabilities corresponding to different thresholds are shown in Fig. 6.7 (right) and were obtained by running 8×10^8 trajectories.

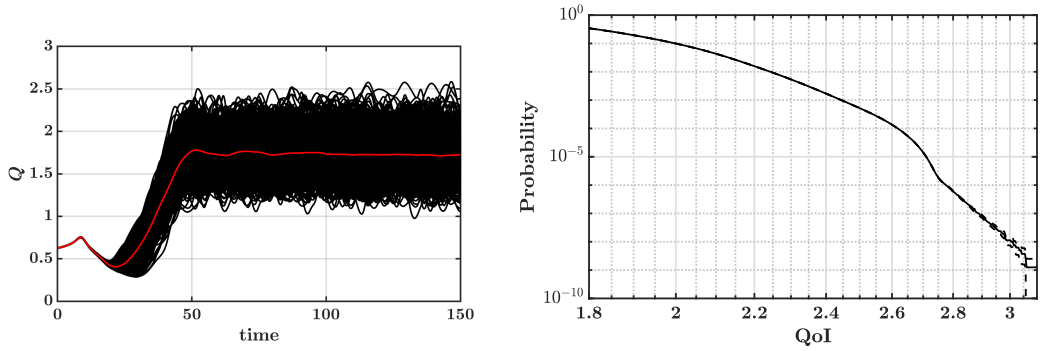

Figure 6.7: Left: instantaneous values of the observable $Q(t)$ plotted over time (—). Ensemble average of Q (—). Right: complementary of the cumulative density function (CDF) of the QoI. Probabilities are obtained with brute force calculation (—) plotted along with the theoretical Monte-Carlo uncertainty (--). Plots correspond to the KSE case.

The rare mean path for thresholds ranging from 2.2 to 2.7 (thresholds for which at least 1000 trajectories can be obtained) and separated by a constant step of 0.05 are shown in Fig. 6.8 (left). It can be observed that the rare mean path follow the same functional at first (red lines), which suggest that the self-similarity approach holds initially. However, the rarest mean paths gradually deviate from the initial functional and would not be reasonably estimated using the self-similarity approach. In Fig. 6.8 (right), the self-similarity factor $\alpha(t)$ is plotted. The self-similarity approximation is reasonably accurate at early to intermediate times, but shows more variability at later times. Overall, these observations suggest that the self-similarity approach could be useful for short term predictions. Nevertheless, the rare mean paths do not significantly differ from one another, and it is still reasonable to expect the less rare mean paths to be informative of the rarer mean path.

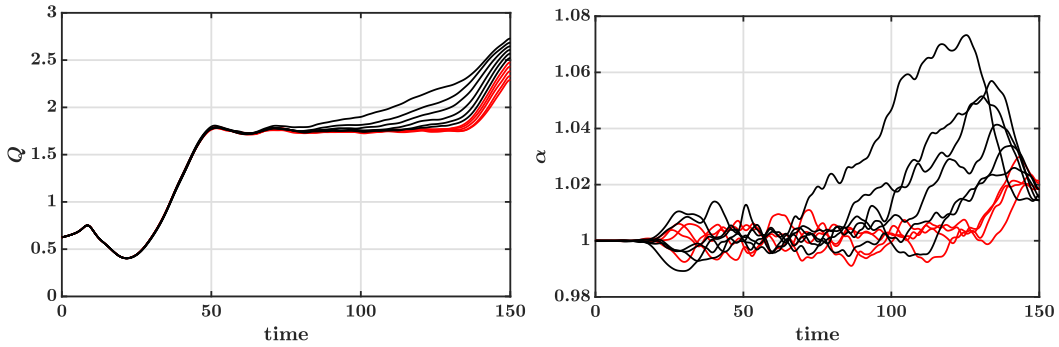

Figure 6.8: Left: rare mean path exceeding thresholds ranging from 2.2 to 2.7 and separated by a stepsize of 0.05. Right: self-similarity factor α computed from successive rare mean path (see Eq. 6.7). Plots correspond to the KSE case.

6.4.2 High-altitude relight in aircraft engines

In aircraft engines operating at high altitude, there is a finite possibility of the flame blowing out, which will lead to loss of propulsion. For this reason, the ability to relight the combustor within short times is crucial for safety (and necessary to obtain certification). During the relight procedure, a spark source is repeatedly used to inject high enthalpy gases into a combustor that is fueled but is at low temperature. While some of these sparks can lead to ignition, propagation of the flame kernel, and eventual stabilization of the gas turbine, the chaotic flow inside the combustor introduces a source of uncertainty. The goal then is to estimate the probability of ignition given a set of operating conditions.

A canonical flow configuration that replicates this ignition process was experimentally studied by [206] and the a corresponding simulation is shown in Fig. 6.9, based on the modeling study of [3]. Here, the spark is injected from the base of the flow (marked igniter in the figure). The kernel then traverses into the region that contains the fuel-air mixture and convecting in a turbulent flow. Subsequent mixing and chemical reactions lead to either a successful or failed ignition event. The forward model is deterministic in nature, similar to other examples studied in the current work. The

main sources of uncertainty are the discharge efficiency of the spark igniter and the initial turbulence state in the system. It was determined that the turbulence effect is dominant over igniter efficiency for the range of conditions considered. To quantify ignition, the volume of the kernel at a particular time is used to mark the outcome of the spark injection. More precisely, the observable Q is the volume of burnt products, and the rare event is defined in terms of the final volume of the ignition kernel, such that $P(Q(T_f) < a)$ needs to be estimated.

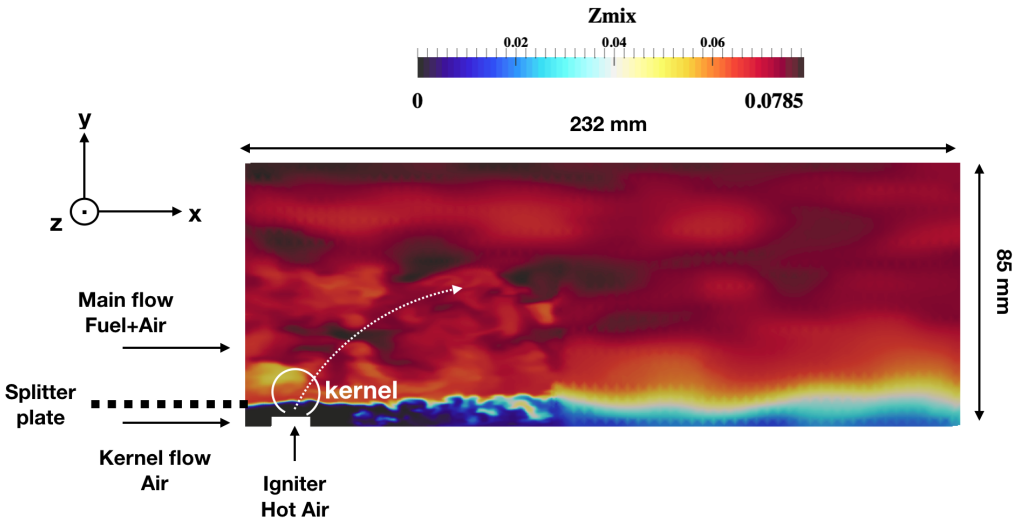

Figure 6.9: Schematic of the ignition configuration simulated. The contour of an initial mixture fraction field at the spanwise mid-plane of the configuration is shown. At the initial time, a hot kernel is ejected from the bottom and mixes with surrounding fuel after it emerges. The trajectory of a spark kernel is sketched by the dashed white line.

Details of the simulation procedure and operating conditions are provided in [207]. Briefly, each simulation of a sparking event is conducted using the large eddy simulation (LES) procedure, with an initial flow field that is sampled from a well-developed homogeneous flow. A total of 541 calculations are conducted among which 235 led to ignition success. Note that the number of simulations conducted is much lower than for the other cases since the system contains approximately 10^7 degrees of freedom.

The results of the calculations are shown in Fig. 6.10. The volume of the kernel

appears to grow exponentially, driven by the Arrhenius-type reaction chemistry that leads to ignition. As can be seen, all the calculations follow an exponential-like path. However, some ignition events result in weaker flames than others and are therefore more susceptible to be extinguished at later times. The CDF of the volume of the ignition kernel is shown in Fig. 6.10 (right) and can only be reasonably estimated for probabilities larger than 10^{-2}, due to the small sample set used.

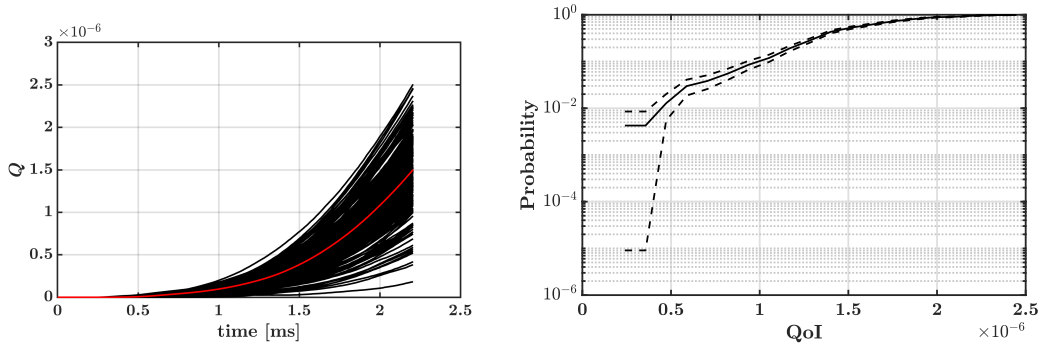

Figure 6.10: Left: instantaneous values of the observable $Q(t)$ plotted over time (—). Ensemble average of Q (—). Right: cumulative density function (CDF) of the QoI. Probabilities are obtained with brute force calculations (—) plotted along with the theoretical Monte-Carlo uncertainty (- -). Plots correspond to the high-altitude relight case.

In Fig. 6.11, the self-similarity approach is tested using a sequence of thresholds ranging from $a = 1.4$ cm^3 to $a = 1.2$ cm^3 with steps of 0.05 cm^3. Note that the plots are only shown after 0.5 ms as the kernel volumes are too small before that time and produce numerical errors when ratios are computed. The rare mean path follows a self-similar structure, which indicates that extreme events can be estimated from the less-rare mean paths. Figure 6.11 tests the self-similarity approach outlined in Sec. 6.3. At early times, the similarity factor shows large variations, but quickly reaches a nearly constant value in the range of $0.94 - 0.96$. The initial variability can be safely removed from the pruning process if the weighting factor is enforced to be a monotonically increasing function of time. At later times, the values of α are close for the different threshold values, indicating that the self-similarity assumption holds

for this system as well.

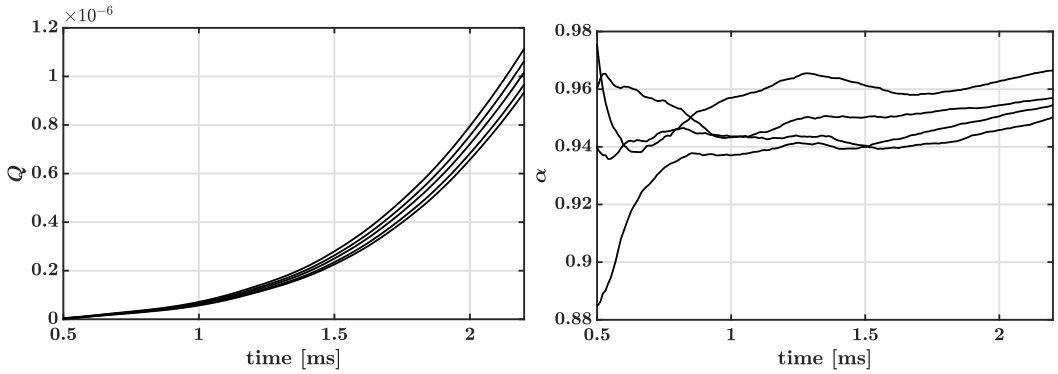

Figure 6.11: Left: rare mean path exceeding thresholds ranging from 1.4 cm^3 to 1.2 cm^3 and separated by a stepsize of 0.05 cm^3. Right: self-similarity factor α computed from successive rare mean path (see Eq. 6.7). Plots correspond to the high-altitude relight case.

6.5 Summary and conclusions

Based on prior work of Wouters et al. [16], the computational advantage obtained by estimating the mean path to a rare event was demonstrated. It was shown that such a path estimation consistently reduces the variance of the probability estimator, especially when the goal is to compute very low probabilities.

Analysis of paths for events at increasingly rare QoIs shows that there exists a self-similarity in these paths that could be exploited to reduce computational cost. In particular, the path followed by a less rare event was found to have a form that is similar to that of a more rare event. An algorithm that exploits this characteristic was constructed and tested a priori and a posteriori for the Lorenz 96 case. It was shown to successfully outperform the importance splitting algorithm that uses a constant weighting factor.

The existence of this self-similarity structure was studied in more complex cases. Two cases, namely the KSE and a high-altitude relight problem, were considered. In the KSE-based system, it was shown that self-similarity holds for a range of rare

event probabilities, but can lead to errors when used for events with very low probability. The high-altitude relight problem showed that the self-similarity factor varies initially, but converges to a nearly constant value with time. Both these results demonstrate that the self-similarity approach is valid for deterministic problems, and can be extended to more complex systems.

For future work, the self-similarity validity needs to be tested a posteriori for practical problems, such as the high-altitude relight configuration. This step is not necessarily straightforward as cloning a deterministic simulation requires that the individual trajectory is perturbed without affecting the rare event probability. In the case of a Lorenz 96 problem, a simple random cloning strategy could be used. For turbulent flows, where the spatial coherence of perturbations matter, a more detailed perturbation method is required. Another path for improvement would be to revisit the self-similarity model formulated in Sec. 6.3. At the moment, a rudimentary model that exploits the self-similarity property for the rare mean path was formulated. More elaborate models could be formulated to be more suited for different systems and to be more resilient to numerical errors. While it was shown that the present approach could be implemented with low computational overhead, it could be advantageous to leverage multi-fidelity approaches to learn the rare mean path, in the same vein as Ref. [194]. Finally, throughout this work, no distinction is made between the observable and the QoI. It could be advantageous to derive a method allowing to pick an observable for which self-similarity properties are more pronounced.

CHAPTER VII

Conclusions and Future Directions

7.1 Summary

The objective of the dissertation was to lay out the foundations of extreme events predictions in the context of turbulent combustion. This goal is fundamentally different from other aspects of turbulent combustion research and required to adopt a comprehensive approach. The core research questions at stake were defined, and technical routes to tackle them were explored. Some of the questions are left open for future research, and this thesis attempted to provide as many guidelines as possible to approach these. The rest of the section summarizes chapter by chapter the advances presented in this work.

Chapter I:

In this chapter, the goal was to develop a framework for approaching the problem of extreme event prediction in turbulent combustion.

1. The mathematical definition of extreme events and rare events was provided and resembled that given in other scientific fields, such as geophysics. To guide future research efforts, a causality-based classification of extreme events is formulated for the first time and is illustrated using examples drawn from turbulent combustion applications. Type I events are fully controllable by input parameters. Type II events are driven by uncertainty. Type III events are related to

the long-term dynamics of the system (its attractor). For each type of event, examples related to turbulent combustion are provided.

2. While Type I events (controllable extreme events) have been the focus of most studies, Type II and III are still poorly understood. In particular, the predictive questions that pertain to Type II and III events are different from traditional challenges tackled by the combustion community. The following five predictive questions are explicitly listed for the first time and can form the basis of future research for extreme event prediction: 1) predict when the next extreme event occurs; 2) estimate the statistical properties of the extreme event; 3) predict extreme events before having observed them; 4) provide bounds on QoI; 5) explain the mechanism through which an extreme event occurs. The contribution of the thesis are limited to questions 1), 2), and 5). Further developments are required to tackle questions 3) and 4).

Chapter II:

Extreme events are defined by a peculiar dynamical process: an excursion away from the normal behavior. To capture or even understand this process, it is necessary to characterize the dynamical behavior of the system. This chapter introduces the concept of Lyapunov analysis as a tool that can characterize the dynamics of turbulent combustion problems. This chapter motivates the use of the Lyapunov analysis but does not introduce new mathematical concepts.

1. The classification of extreme events is interpreted from a dynamical system point of view. In particular, the phase-space behavior of each type of events is described.

2. The mathematical definition of the Lyapunov analysis is reviewed. It can provide a global description of the dynamics (independent of the location in phase

space) through the Lyapunov exponents (LE). It can also provide a local description of the dynamics (dependent on the location in phase space) through the Lyapunov vectors. Here, the importance of the backward Lyapunov vectors is highlighted as it can describe how a perturbation is gradually amplified.

3. It is shown that the Lyapunov analysis and its derivatives have potential applications for all five predictive questions listed earlier. In this thesis, the Lyapunov analysis is only used for reduced-order modeling and understanding the process through which an extreme event might occur.

Chapter III:

In this chapter, the numerical properties of the Lyapunov analysis are investigated. Only a few applications of the Lyapunov analysis to fluid dynamics problems can be found in the literature, and basic convergence questions still needed to be answered.

1. It is explained how the state vector can be constructed when the Lyapunov analysis is conducted with low Mach solvers. This is the first time that this description is provided.

2. The convergence of the LEs with spatial and temporal discretization is difficult to show in general because LEs are affected by both discretization and statistical errors. It is recognized that the statistical errors can be eliminated for laminar flows. A convergence procedure is proposed and derived from the link between the LEs and the temporal eigenvalues of the Orr-Sommerfeld analysis.

3. Using a series of numerical tests, the convergence properties of the LEs with spatial and temporal discretization are clearly obtained for the first time. It appears that the LEs converge at the same rate as the spatial discretization order, while the temporal discretization only has an effect for large timesteps. The reason behind this convergence property is undefined at the moment.

4. The convergence properties found for the laminar flow appeared to hold for turbulent one dimensional and three-dimensional flows. This observation allows using the Lyapunov analysis on a discretized domain in order to characterize the dynamics of the "true" continuous problem.

Chapter IV:

The Lyapunov analysis is conducted for a statistically stationary homogeneous isotropic turbulent flow (HIT). The goal of the section is to gain fundamental insight on the complexity of dynamics of turbulent flows and on the process through which perturbations amplify.

1. For the first time, enough number of LEs are computed in a HIT flow to directly estimate the attractor dimension of the flow field. It appeared that the attractor dimension is several orders of magnitude lower than the number of degrees of freedom required to resolve the flow field. This result suggests that severely coarse-grained models that capture the dynamics of the flow can be derived. The scaling properties of the attractor dimension are also obtained as a function of the Kolmogorov length scale η. It is found that the Kaplan-Yorke dimension scales as $(\frac{L}{\eta})^{2.8}$, where L is the domain size, which is close to other theoretical estimates.

2. By analyzing the structure of the backward Lyapunov vectors, it is found that perturbations amplify where enstrophy is large, but not where kinetic energy is large. Physically, this result can be interpreted by recognizing that the flow direction constantly changes in regions of large enstrophy, which could allow small perturbations to accumulate over time.

3. The structure of the response of the flow field to perturbations is also correlated with the enstrophy field. It is unclear at the moment why would the evolution of perturbation be correlated with enstrophy of the underlying flow field. However,

it provides guidelines for reduced order models that would aim at capturing the emergence of extreme events.

Chapter V:

The Lyapunov analysis is then used with two turbulent partially premixed flames that have been extensively studied in the past. Both flames are subject to large amounts of strain that can lead to intermittent extinctions. This is the first application of the Lyapunov analysis to a turbulent combustion problem.

1. It was found that using the classical algorithm to compute the Lyapunov exponents could lead to numerical problems with the turbulent flames investigated. If the initial perturbation is too small, the perturbation size could experience large amplitude changes which would pollute the value of the LE. It was found that by either increasing the perturbation size or waiting for a few timesteps before recording the perturbation magnitude, this problem could be bypassed.

2. By computing the first 300 LEs, a lower bound of the Kaplan Yorke dimension was obtained and is several orders of magnitude lower than the number of degrees of freedom required to run a direct numerical simulation.

3. The perturbations appeared to amplify in regions of extinction and reignition. This is observation can be explained by the fact that the flow field experiences significant changes at these locations, since the time derivative of the density is large. It is also found that perturbations do not grow where the reaction rate is large. This observation remains unexplained at the moment.

4. For such a complex problem, direct numerical simulation is not affordable. Therefore, large eddy simulations (LES) had to be conducted. It is shown that in this case, no convergence can be obtained for the LEs. Nevertheless, the Lyapunov vectors showed similar features between a coarse and fine large eddy

simulations. This observation suggests that the description of the Lyapunov vectors obtained with LES could hold at finer resolutions.

Chapter VI:

This chapter treats the problem of estimating the statistics of extreme and rare events. The challenge lies in accelerating the observation of rare events. This is done here using an importance splitting genealogical algorithm that creates copies of the system that are deemed likely to reach a rare state. Selecting the copies that are likely to lead to a rare event can be accelerated if the path to the rare event can be inferred.

1. It is shown with an a priori analysis on the Lorenz 96 problem that trajectories of observable that lead to a rare event can be similar to trajectories that lead to less rare events. This observation is not mathematically guaranteed but appeared to be satisfied with the observable and systems chosen. At the moment, it is unclear what are the mathematical requirements for the governing equation and the observable that ensure the self-similarity property.

2. Using this observation, it is possible to formulate a self-similarity-based model that approximates the path to rare events using the path to less rare events. The method is tested a posteriori and leads to increased efficiency of the probability estimator of the genealogical algorithm.

3. The model is tested a priori on other problems relevant for turbulent combustion. It appears that the self-similarity property holds but that the model should be refined to be valid in general.

7.2 Future challenges and recommendations

Given that studying extreme events provides a new approach for gaining insight into complex systems, there is a need for a research strategy moving forward. Below,

some essential pathways are identified to start a discussion on this important topic.

7.2.1 Develop low-fidelity tools that capture extreme events

In the present work, detailed simulations were used to gain an understanding of the dynamical behavior of the system. However, predicting that an extreme event will occur in a real system should not require to resolve all the dynamics of the system. Therefore, there exists a crucial need to develop low-fidelity models of turbulent combustion that still allow capturing extreme events and the correct response of the system to perturbations. Note that these models do not need to represent all the dynamics of the system, but the most important ones that eventually lead to an extreme event. Thus, the development of low-fidelity models that can capture extreme events goes hand in hand with a better understanding of the process through which these events occur. For thermoacoustic instabilities, the advent of flame describing functions (FDF) and flame transfer functions (FTF) [208] is a valuable effort in this direction. For other types of extreme events, it is not clear how to accurately design low-fidelity models. The most straightforward techniques, such as decreasing the mesh cell count, were found to affect to some extent the dynamics of the system even when the statistics are correctly captured (see Chap. V).

In particular, developing methods that can follow individual realizations rather than statistical measures is essential. In this context, approaches based on manifolds may be useful [158, 209, 210]. Other approaches, such as reduced-order modeling (ROM), could be used to construct representations that specifically target extreme events. When developing such models, quantifying the uncertainty introduced by model reduction becomes important [211]. Further, current approaches to model validation may not be viable when dealing with such extreme event statistics. For instance, Chap. IV showed that well-established methods for simulating homogeneous isotropic turbulence, which is the most canonical of turbulent flows, do not capture

the dynamics consistently. In the context of pre-classifying anomalous events, fast algorithms that can operate in the phase-space of the observables is necessary. Recently, there has been a focus on techniques such as convolution neural networks with application to turbulent combustion [212], which can classify trajectories in real-time.

7.2.2 Develop rare events tools for turbulent combustion

While there exists a large number of tools to probe different aspects of rare and extreme events (Ref. [90]), their direct utilization in the field of turbulent combustion is not straightforward. Many of these tools have been developed for low-dimensional or non-physical problems, and cannot be extended to practical systems at all. Chapter VI provides an illustration of this problem. Cloning particles in the Lorenz 96 system could be simply done by introducing random perturbations. However, random perturbations would have little to no effect in a turbulent flow problem. Appropriate cloning methods with spatial and temporal coherence are required for importance splitting tools to be used in the context of turbulent combustion. Other techniques assume constraints non-suited for the problems of interest, such as incompressibility [213, 214]. Hence, there exists a wide range of opportunities to develop tools for combustion applications.

Note that in this context, turbulent combustion can also serve as a prototype for high-dimensional complex systems where rare and extreme events are central to design choices. Techniques developed for turbulent combustion could well be useful in a wide variety of fields.

Part of developing such computational frameworks also involves identifying validation experiments and configurations. A significant source of interest in combustion physics is due to the presence of a diverse set of experimental tools that can probe different aspects of physics. However, such tools are often limited to capturing statistical measures such as averages and variances. Establishing experimental techniques

for rare events is essential. Given that a direct approach to recreating such events is practically intractable, innovative approaches to reproducing the causal mechanisms or measurements that expose the phase space characteristics of the flow would be indispensable.

7.2.3 Model the triggers of extreme events

Among the triggers of extreme events provided in Chap. I, it was shown that external perturbations could make the system strongly deviate from normal conditions. In order to model the response of the system to such perturbations, it is necessary first to model these external variations. While there have been attempts to provide more detailed boundary conditions to high-fidelity combustion tools [215, 216], modeling triggering events requires more information on the nature of such processes. For instance, in the high-altitude relight problem (see Chap. I), the ignitor that provides the necessary high enthalpy ignition source may itself exhibit considerable variability. The level of detail and quantification of related uncertainties is a significant modeling challenge.

However, there is a more subtle notion involved here. Currently, combustion models are developed based on the flow physics present inside the combustor. When external variations can introduce large changes to this flow structure, it becomes necessary for models to be sensitive to such perturbations. In this context, models that are regime agnostic [174, 217, 218] or those that can adapt to different operating conditions [219–222] are more suitable. In some cases, the flow regime itself can be changed. For instance, in the deflagration-to-detonation transition, the flow field is initially subsonic but can become supersonic after the transition. Hence, not only is the modeling of external perturbations important but also is the ability of the combustion models to respond to these changes.

7.2.4 Research focus on phase space structure

The approach to modeling in turbulent combustion has followed the statistical path not only because it is useful but also because it provides an intuitive description of the extreme complexity in flow physics. In particular, the concept of filtering or statistical averaging delineates the terms in the governing equation that require modeling. However, data-driven tools have embraced dynamical systems or phase-space driven approach, whereby the treatment of the modeling problem as a description of the structure of the phase space is most straightforward. As machine learning and data-driven approaches are integrated into modeling, there is a need to rethink the notion of statistical modeling.

In particular, many tools for probing extreme events could be significantly improved through a priori knowledge about the structure of phase space. For instance, being able to infer the local phase-space structure (dimension, volume, and orientation of the stable manifolds, for instance) can vastly accelerate the search for extreme events. It would also be useful in creating biased sampling approaches (see Chap. VI). Even information on the dimension of the attractor derived in Chap. IV and Chap. V, has not been explored for many canonical closed flows.

7.3 Outlook

Extreme events analysis can be a powerful approach to improve design techniques. By understanding the failure of a combustor from a computational standpoint, it would be possible to develop less conservative designs and improve the efficiency of industrial devices. With further development, it could even be possible to anticipate failure before observing it, thereby decreasing the cost of design. Furthermore, extreme event analysis can help to derive reduced order models that could be used to anticipate a failure not only during the design phase but also in real-time operations.

With the emergence of the internet of things, reduced-order models obtained from the extreme event analysis could be used to make decisions regarding the maintenance of the device, for example. These perspectives are exciting opportunities for detailed computations, which could have a practical impact on industrial problems. As illustrated in this work, these perspectives require an evolution of the numerical tools used in the field of turbulent combustion.

Other fields of engineering and science, most notably weather forecasting, have embraced extreme events modeling as a prime analysis approach. This effort has dramatically helped modeling activities and has provided valuable insights that are not obtainable from just analyzing the average behavior of systems. More importantly, there appear to be many commonalities in how such extreme events arise, through what can be broadly classified as emergent behavior due to the synchronization of different elements of the system. Fields that have established a rich history of extreme event analysis can serve as a starting point for the mutation of numerical tools.

Perhaps a greater challenge will be changing the design mindset in the propulsion industry. What can be learned from the extreme event analysis should be valuable enough to justify an investment in new computational tools. Therefore, the benefit of these tools needs to be illustrated in practical problems. Not only this requires numerical tools that can handle high-dimensional and multi-physics problems, but it would require an appropriate configuration to examine. For this purpose, experiments geared towards extreme event analysis and datasets of failures in industrial combustors are essential.

List of publications:

- **Ensemble-LES Analysis of Perturbation Response of Turbulent Partially-Premixed Flames**, Malik Hassanaly, V. Raman, *Proceedings of the Combustion Institute*, Vol. 37, Issue 2, pp.2249-2257, 2019.

- **Numerical convergence of the Lyapunov spectrum computed using low Mach number solvers**, Malik Hassanaly, V. Raman, *Journal of Computational Physics*, Vol. 386, pp.467-485, 2019.

- **Lyapunov spectrum of forced homogeneous isotropic turbulent flows**, Malik Hassanaly, V. Raman, *Submitted*, 2019.

- **A self-similarity principle for the computation of rare event probability**, Malik Hassanaly, V. Raman, *In preparation*, 2019.

- **Computational Tools for Data-Poor Problems in Turbulent Combustion**, Malik Hassanaly, V. Raman, *In preparation*, 2019.

- **A minimally-dissipative low-Mach number solver for complex reacting flows in OpenFOAM**, Malik Hassanaly, H. Koo, C. F. Lietz, S. T. Chong, V. Raman, *Computers and Fluids*, Vol. 162, pp.11-25, 2018.

- **Emerging Trends in Numerical Simulations of Combustion Systems**, V. Raman, Malik Hassanaly, *Proceedings of the Combustion Institute*, Vol. 37, Issue 2, pp.2073-2089, 2019.

- **Large Eddy Simulation of Pressure and Dilution Jet Effects on Soot Formation in a Model Aircraft Swirl Combustor**, S. T. Chong, Malik Hassanaly, H. Koo, M. E. Mueller, V. Raman, K. P. Geigle, *Combustion and Flame*, Vol. 192, pp.452-472, 2018.

- **Large Eddy Simulation of Soot Formation in a Model Gas Turbine Combustor**, H. Koo, Malik Hassanaly, V. Raman, M. E. Mueller, K. P. Geigle, *Journal of Engineering for Gas Turbines and Power*, Vol. 139, Issue 3, pp.031503, 2017.

- **Experimental data-based reduced-order model for analysis and prediction of flame transition in gas turbine combustors**, S. Barwey, Malik Hassanaly, V. Raman, *Combustion Theory and Modelling*, 2019.

- **A Comprehensive Modeling Procedure for Estimating Statistical Properties of Forced Ignition**, Y. Tang, Malik Hassanaly, V. Raman, B. Sforzo, J. Seitzman, *Combustion and Flame*, Vol 206, pp.158-176, 2019.

- **Numerical Simulation of Lean Premixed High Swirl Flame Flashback** Y. Tang, Malik Hassanaly, V. Raman, *In preparation.*

- **Data-Driven Analysis of Transition for Multimodal Cavitation**, S. Barwey, H. Ganesh, Malik Hassanaly, D. Knister, V. Raman, S. Ceccio, E. Johnsen, *In preparation.*

List of conference proceedings:

- **Reduced Description of Dynamical Systems by Approximate Inertial Manifolds**, M. Akram, Malik Hassanaly, V. Raman, *57th AIAA Aerospace Sciences Meeting*, 2019.

- **Perturbation Dynamics in Turbulent Flames**, Malik Hassanaly, V. Raman, *55th AIAA Aerospace Sciences Meeting*, 2017.

- **Classification and Simulation of Anomalous Events in Turbulent Combustion**, Malik Hassanaly, S. Voelkel, V. Raman, *10th Mediterranean Combustion Symposium*, 2017.

- **Numerical simulation of forced ignition of Jet-fuel/air using large eddy simulation (LES) and a tabulation-based ignition model**, Y. Tang, Malik Hassanaly, V. Raman, B. Sforzo, J. Seitzman, *57th AIAA Aerospace Sciences Meeting*, 2019.

- **Detailed Kinetics Based Modeling of Jet Fuel Ignition in Turbulent Stratified Flows**, Y. Tang, Malik Hassanaly, V. Raman, B. Sforzo, J. Seitzman, *ASME Turbo Expo*, 2018.

- **Turbulent Mixing and Combustion of Supercritical Jets**, S. T. Chong, Y. Tang, Malik Hassanaly, V. Raman *55th AIAA Aerospace Sciences Meeting*, 2017.

- **Large eddy simulation of flame stabilization in a multi-jet burner using a non-adiabatic flamelet approach**, Y. Tang, Malik Hassanaly, H. Koo, V. Raman, Large eddy simulation of flame stabilization in a multi-jet burner using a non-adiabatic flamelet approach *54th AIAA Aerospace Sciences Meeting*, 2016.

- **Influence of Fuel Stratification on Turbulent Flame Propagation**, Malik Hassanaly, V. Raman, H. Koo, M. B. Colket, *53rd AIAA Aerospace Sciences Meeting*, 2015.

- **Large Eddy Simulation of Flame Flashback in Swirling Premixed CH4/H2-Air Flames** , C. F. Lietz, Malik Hassanaly, V. Raman, *53rd AIAA Aerospace Sciences Meeting*, 2015.

- **Large Eddy Simulation of premixed flame flashback in a turbulent channel**, C. F. Lietz, Malik Hassanaly, V. Raman, H. Kolla, J. Chen, A. Gruber, *52nd AIAA Aerospace Sciences Meeting*, 2014.

APPENDICES

APPENDIX A

Lyapunov analysis of homogeneous isotropic turbulence (HIT)

A.1 Enforcement of mass conservation in linearly forced turbulence

While implementing the LE algorithm, it was discovered that the numerical algorithm for the advancement of the governing equations has to strictly enforce the incompressibility constraint. In methods that use vorticity-based equations [223], this property is implicitly ensured. In the explicit time-marching scheme used here, it was found that an enforcement procedure needs to be incorporated. These details are provided here for the sake of completeness.

In spectral space, Eq. 4.2.2 takes the following form

$$\forall \boldsymbol{\kappa}, \quad \frac{\partial}{\partial t}\widehat{u}_i(\boldsymbol{\kappa},t) \; + \; \nu\kappa^2\widehat{u}_i(\boldsymbol{\kappa},t) \quad = \quad -j\kappa_i\widehat{p}(\boldsymbol{\kappa},t) \; - \; \widehat{(\frac{\partial u_i u_k}{\partial x_k})}_{\boldsymbol{\kappa}} \; + \; A\widehat{u}_i(\boldsymbol{\kappa},t). \quad \text{(A.1)}$$

The incompressibility condition ($j\boldsymbol{\kappa}\cdot\widehat{\boldsymbol{u}}(\boldsymbol{\kappa},t)=0$) is used to determine the pressure as a function of the non-linear term. Let $NL_i \equiv -\widehat{(\frac{\partial u_i u_k}{\partial x_k})}_{\boldsymbol{\kappa}}$, then the full momentum

equation becomes

$$\frac{\partial}{\partial t}\widehat{u}_i(\boldsymbol{\kappa},t) + \nu\kappa^2\widehat{u}_i(\boldsymbol{\kappa},t) - A\widehat{u}_i(\boldsymbol{\kappa},t) = -\kappa_i\frac{\boldsymbol{NL}\cdot\boldsymbol{\kappa}}{\kappa^2} + NL_i. \tag{A.2}$$

In prior works [149, 150], constraining the pressure to be a function of the non-linear convective term is deemed sufficient to enforce incompressibility. In fact, in their seminal paper on spectral methods for turbulent flows, [149] mention that the flow field remains incompressible if its initial divergence is exactly equal to zero. However, machine precision errors always prevent the incompressibility condition to be exactly satisfied. If no other treatment is applied, it is shown in this section that this can lead to instabilities for simulations run over long times.

These machine precision errors manifest in two different ways: a) some of the modes grow exponentially; b) the error in the validity of incompressibility constraint increases with time.

A.1.1 Exponentially growing modes: the linear modes

Consider the wavenumber $\boldsymbol{\kappa} = (\kappa_x, \kappa_y, \kappa_z) = (a, 0, 0)$, where $a \neq 0$. In an exactly incompressible field, $\boldsymbol{\kappa}\cdot\widehat{\boldsymbol{u}} = 0$. Here, this means that $\widehat{u_x} = 0$. However, incompressibility is only numerically enforced through the value of the pressure and the momentum equation is still solved for this mode.

In this particular case, the right hand side of Eq. A.2 in the direction x is equal to $-NL_x + NL_x = 0$

Therefore, the Galerkin projection of the Navier Stokes equation becomes

$$\frac{\partial}{\partial t}\widehat{u_x}(\boldsymbol{\kappa},t) = (A - \nu a^2).\widehat{u_x}(\boldsymbol{\kappa},t) \tag{A.3}$$

Likewise, for the wavenumbers $(0, a, 0)$ and $(0, 0, a)$, the non-linear term and the pressure term exactly cancel respectively in the direction y and z. These modes are

called *linear modes*, due to the linear evolution equations, in the rest of this appendix.

For the linear modes, if $A > \nu a^2$, and if the wavenumber coefficient $\widehat{u}_i(\boldsymbol{\kappa}, t)$ is initially not exactly equal to 0, then the wavenumber coefficients diverge.

Note that in order to sustain turbulence in the domain, it is desired that $A > \nu a^2$, at least for $a = 1$

- If $A = \nu$, then the modes with wavenumber $|\kappa| = 1$ are only subject to convection and pressure term, while the other ones are subject to a reduced but positive viscosity. The velocity fluctuations monotonically decrease except for the linear modes which remain constant. In the end, all the wavenumber coefficients are equal to zero except for the ones corresponding to $|\kappa| = 1$ for which the coefficients are equal to their initial values.

- If $A < \nu$, all the modes in the domain decay since they are subject to a reduced but positive viscosity and no forcing at all. Therefore, the turbulence decays for all the modes.

A.1.2 Exponentially growing divergence

One solution to the issue with the linear modes is to not apply forcing selectively to these modes so that they decay to zero with time and do not influence the simulation results. It is demonstrated here that this approach leads to inconsistencies in enforcing a divergence-free flow field.

The divergence constraint in spectral space can be written as

$$\boldsymbol{\kappa} \cdot \widehat{\boldsymbol{u}}(\boldsymbol{\kappa}) = 0. \tag{A.4}$$

Here, the goal is to evaluate the stability properties of the divergence of each spectral mode. To do so, one can write the transport equation of the divergence by taking the divergence of the momentum equation but without canceling the terms of

the form $\boldsymbol{\kappa} \cdot \widehat{\boldsymbol{u}}$.

Let $B = j\boldsymbol{\kappa} \cdot \widehat{\boldsymbol{u}}$, then

$$\frac{dB}{dt} + \nu\boldsymbol{\kappa}^2 B = |\boldsymbol{\kappa}|^2 p + j\boldsymbol{NL} \cdot \boldsymbol{\kappa} + AB. \tag{A.5}$$

In the numerical procedure, the first and second terms of the right-hand side are constructed such that they cancel each other, leading to

$$\frac{dB}{dt} = (A - \nu\boldsymbol{\kappa}^2)B. \tag{A.6}$$

Again, if $A - \nu\kappa^2 > 0$ then any initial numerical error in divergence can exponentially amplify. It is, in practice, impossible to avoid such errors. Note that Eq. A.6 is true for all the wavenumbers.

A.1.3 Additional correction

The numerical issues are addressed using a two-step correction procedure. First, the set of Fourier coefficients are projected on to a divergence-free space after each time-step. Let $\widehat{\boldsymbol{u}}$ be the mode obtained at the end of the timestep, with $\boldsymbol{\kappa} \cdot \widehat{\boldsymbol{u}}(\boldsymbol{\kappa}) = B$. Let $\widehat{\boldsymbol{u_p}}(\boldsymbol{\kappa})$ be the projection of this mode onto the divergence-free space, and is defined as

$$\widehat{\boldsymbol{u_p}}(\boldsymbol{\kappa}) = \widehat{\boldsymbol{u}}(\boldsymbol{\kappa}) + j\frac{\boldsymbol{\kappa}}{|\boldsymbol{\kappa}|^2}B \tag{A.7}$$

Note that this correction does not affect the flow field if it is already incompressible. In spectral space, this correction is straightforward to impose and has a negligible impact on the computing time.

Second, the turbulent forcing field is also projected onto a divergence-free space. Eq. A.6 becomes

$$\frac{\partial B}{\partial t} = -\nu\boldsymbol{\kappa}^2 B, \tag{A.8}$$

and the divergence of all the modes tends to zero. The projection of the forcing term can be achieved similar to that of the turbulent flow field. Note that forcing schemes that are not based on the velocity field (for example, [162]) also use this extra-correction step.

A.2 Uncertainty estimates of attractor dimension and scaling

Since the negative LEs are not available for the highest Reynolds number case (Case 4), the dimension needs to be estimated based on certain assumptions. From Fig. 4.2, it can be reasonably inferred that the shape of the spectrum is similar across different Reynolds number. Further, it is approximated using a power law form as $a(i-1)^{\alpha} + \lambda_1$, where i is the LE index. The value of a is chosen such that the fit passes through a certain λ_i. For the finest resolution, i is chosen to be 49, which is the largest index available. For the other cases, i is chosen such that λ_i/λ_1 is the same as for the highest Re_λ. As a result, the fit is parameterized using only one variable: α.

In Fig. A.1, the parameter α is plotted for the three lowest Re_λ cases. Based on this result, α is extrapolated linearly with respect to the Re_λ. For this purpose, the slope is estimated using any two combinations of the three available points, and the extrapolation is done starting from any of the three available points. Nine possible values for α are obtained. All of these values are used to fit the first 49 LE of largest Re_λ case. Finally, the average of all these possible dimensions is taken to be the best dimension estimate. The uncertainty estimate is obtained from the maximal and the minimal dimensions obtained using all the possible α.

At this stage, an estimate of the attractor dimension for Cases 1, 2, 3 and 4 along with an uncertainty estimate has been obtained. In addition, an uncertainty estimate for the mean turbulent quantities (here, the Kolmogorov length scale η) can

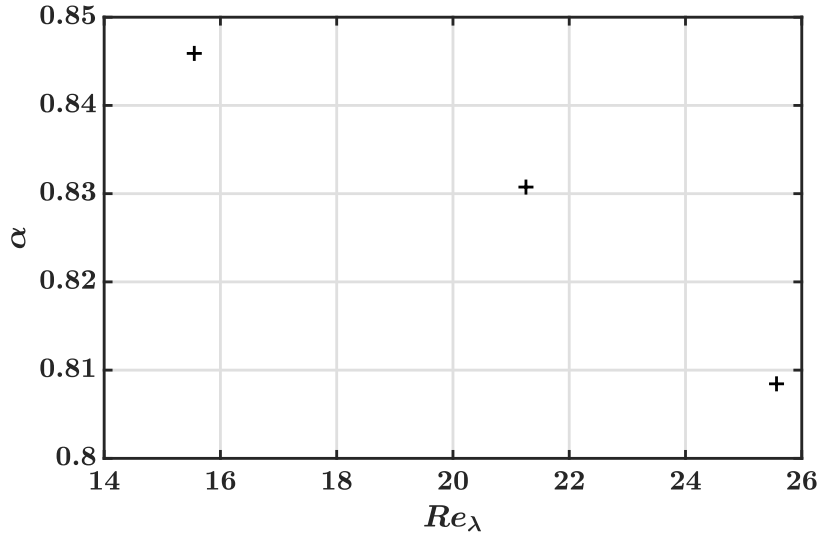

Figure A.1: Value of α obtained from the fit applied to the LE computed with Case 1, 2 and 3.

be obtained using the method outlined in Ref. [141]. Given these dimension estimates for the four Reynolds numbers, the goal is to determine the scaling of the dimension as a function of $\frac{L}{\eta}$, where $L = 2\pi$. In other terms, one wants to fit a curve of the form ax^b through the data points, get an estimate as well as an uncertainty estimate for b. To do so, an approach similar to the one used in Appendix A.2 is used. Different possible scalings are generated and are used to obtain an uncertainty estimate.

Schematically, the points that are used to compute the scaling are arranged in a manner illustrated by Fig. A.2. The x-axis represents the $\frac{L}{\eta}$ and the y-axis represent the estimated dimension. For each Cases 1-4, an uncertainty estimate for both axes is available. In Fig. A.2, the data of only two cases (for simplification) through which a fit goes are schematically shown. Given the estimates, many different fits are possible. For each Case, one can consider that one fit intersect any of the five points indicated in Fig. A.2 (represented by the dashed lines), which implies that there are then 5^4 possible fits for the data.

All of these fits are generated here, resulting in 5^4 possible values for b. At each data point, if a fit uses any point different than the point 5 shown in Fig. A.2, it is

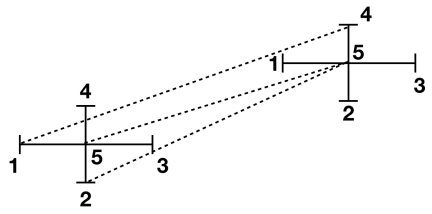

Figure A.2: Schematic of the uncertainty estimation method for the attractor dimension scaling. For each case, 5 points are considered using the uncertainty estimate of the dimension. The horizontal error bar represents the statistical error for the value of the average $\frac{L}{\eta}$, the vertical error bar contains the statistical uncertainty and the extrapolation uncertainty used to compute the dimension. The dashed lines represent examples of the fits considered.

attributed a lower weight equal to the ratio $\frac{e^{-1/2}}{e^0}$. The lowest possible weight for a fit is then $\frac{e^{-2}}{e^0} \approx 0.135$. The estimate for b and for its uncertainty estimate are obtained as a weighted average of the b and b^2 values generated by each fit. In the end, this procedure leads to the scaling $b = 2.8 \pm 0.095$.

A.3 Consequences of the energy spectrum of the GSV on the energy spectrum of the CLV

From Fig. 4.12, the energy spectra of the GSVs do not change much based on the index. This feature is used to relate the energy spectra of the GSVs to that of the CLVs. In particular, it is shown that the first few CLVs cannot be localized in Fourier space. Let $\boldsymbol{\phi}_i$ be the i-th CLV and $\boldsymbol{g}_i$ be the i-th GSV, then the CLV can be expressed as [73]:

$$\forall \boldsymbol{x},\ \boldsymbol{\phi}_j(\boldsymbol{x}) = \sum_{i=1}^{j} a_{i,j} \boldsymbol{g}_i(\boldsymbol{x}), \tag{A.9}$$

where $\boldsymbol{x}$ denotes the physical space location and $a_{i,j} \in \mathbb{R}$. For ease of notation, the physical space location $\boldsymbol{x}$ is dropped from the notation. Since $\boldsymbol{\phi}_j$ are normalized,

$$\sum_{i=1}^{j} a_{i,j}^2 = 1. \tag{A.10}$$

Equation. A.9 can be rewritten using the Galerkin projection onto the Fourier modes as

$$\forall \boldsymbol{\kappa},\ \widehat{\boldsymbol{\phi}}_j(\boldsymbol{\kappa}) = \sum_{i=1}^{j} a_i \widehat{\boldsymbol{g}}_i(\boldsymbol{\kappa}), \tag{A.11}$$

where κ is a three dimensional wavenumber, $\widehat{\boldsymbol{\phi}}_j(\boldsymbol{\kappa})$ and $\widehat{\boldsymbol{g}}_i(\boldsymbol{\kappa}) \in \mathbb{C}^3$ are the Fourier amplitudes of the mode $\boldsymbol{\kappa}$.

Let $K_0 \in \mathbb{R}$. The goal is to find a relation between the energy at the wavenumber K_0 for the j-th CLV, which is defined as

$$E_{\boldsymbol{\phi}_j}(K_0) = \sum_{\substack{\boldsymbol{\kappa} \\ |\boldsymbol{\kappa}|=K_0}} \widehat{\boldsymbol{\phi}_j}(\boldsymbol{\kappa})^* \cdot \widehat{\boldsymbol{\phi}_j}(\boldsymbol{\kappa}), \tag{A.12}$$

where $\cdot^*$ denotes the complex conjugate. Using Eq. A.11,

$$E_{\boldsymbol{\phi}_j}(K_0) = \sum_{i=1}^{j} a_{i,j}^2 E_{\boldsymbol{g}_i}(K_0) + \sum_{\substack{\boldsymbol{\kappa} \\ |\boldsymbol{\kappa}|=K_0}} \sum_{\substack{k,l \le j \\ k \neq l}} a_{k,j} a_{l,j} (\widehat{\boldsymbol{g}}_k(\boldsymbol{\kappa})^* \cdot \widehat{\boldsymbol{g}}_l(\boldsymbol{\kappa}) + \widehat{\boldsymbol{g}}_l(\boldsymbol{\kappa})^* \cdot \widehat{\boldsymbol{g}}_k(\boldsymbol{\kappa})). \tag{A.13}$$

Due the fact that the energy spectra of the GSV are relatively independent of the index, Eq. A.10 can be used to write

$$E_{\boldsymbol{\phi}_j}(K_0) \approx E_{GSV}(K_0) + 2 \sum_{k,l,\ k \neq l} a_{k,j} a_{l,j} E_{corr,kl}(K_0), \tag{A.14}$$

where $E_{GSV}(K_0)$ is the energy of the GSV for Fourier modes of amplitude K_0, and

$E_{corr,kl}(K_0) = \frac{1}{2}\sum_{\boldsymbol{\kappa}|\boldsymbol{\kappa}|=K_0}(\widehat{\boldsymbol{g}}_k(\boldsymbol{\kappa})^* \cdot \widehat{\boldsymbol{g}}_l(\boldsymbol{\kappa}) + \widehat{\boldsymbol{g}}_l(\boldsymbol{\kappa})^* \cdot \widehat{\boldsymbol{g}}_k(\boldsymbol{\kappa}))$

The second term of the right-hand side of Eq. A.14 is what distinguishes the energy spectrum of the GSVs from the spectrum of the CLVs. Note that this term is real but not necessarily positive. This term can be estimated from the database generated in the present study. In Fig. A.3, the ratio $\frac{|E_{corr,kl}(\boldsymbol{\kappa})|}{E_{GSV}(\boldsymbol{\kappa})}$ is plotted against $\boldsymbol{\kappa}$ for all combinations of GSVs from 1 through 19 indices. For all of these combinations, the ratio can be reasonably estimated to be equal to 0.5 for all the wavenumber amplitudes.

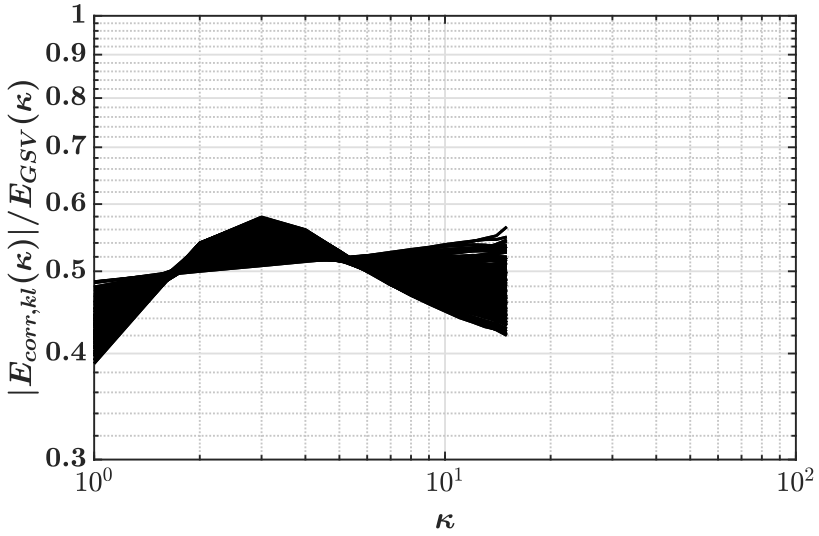

Figure A.3: Ratio $\frac{|E_{corr,kl}(\boldsymbol{\kappa})|}{E_{GSV}(\boldsymbol{\kappa})}$ plotted for Case 1 and the first 19 pairs of LVs, plotted against the wavenumber amplitude.

Further, to bound the CLV spectrum, bounds on the product of coefficients $a_{k,j}a_{l,j}$ are needed. To do so, it can be recognized that the possible $a_{p,j}$ are the points located on the j-sphere (hypersphere of dimension j) of radius 1 which leads to

$$\forall p, q,\ |a_{p,j}a_{q,j}| = |cos\gamma_p cos\gamma_q \prod_{k=1}^{p-1} sin\gamma_k \prod_{l=1}^{q-1} sin\gamma_l|, \tag{A.15}$$

where $\gamma_i \in [0, \pi]$ if $i \leq j-2$ and $\gamma_{j-1} \in [0, 2\pi]$. By recognizing that $|a_{p,j}a_{q,j}|$ either

contains a product of the form $|cos\gamma_p sin\gamma_p|$ or $|cos\gamma_q sin\gamma_q|$,

$$\forall p, q, \ |a_{p,j} a_{q,j}| \leq 0.5 \tag{A.16}$$

Using the triangle inequality, one can then obtain bounds for the energy spectrum of $\boldsymbol{\phi}_j$:

$$max(E_{GSV}(K_0) - \frac{1}{2}\binom{j}{2} E_{GSV}(K_0), 0) \lesssim E_{\boldsymbol{\phi}_j}(K_0) \lesssim E_{GSV}(K_0) + \frac{1}{2}\binom{j}{2} E_{GSV}(K_0). \tag{A.17}$$

Note that the bounds increase in range as the index of the CLV increases. As a result, these bounds are useful only for the first few CLVs. For example, the bounds for the second CLV can be obtained as $0.5E_{GSV}(K_0) \lesssim E_{\boldsymbol{\phi}_2}(K_0) \lesssim 1.5E_{GSV}(K_0)$. These bounds are shown in Fig. A.4, and follow the shape of the GSV spectrum. As a result, it can be guaranteed that the first few CLVs are not localized in Fourier space.

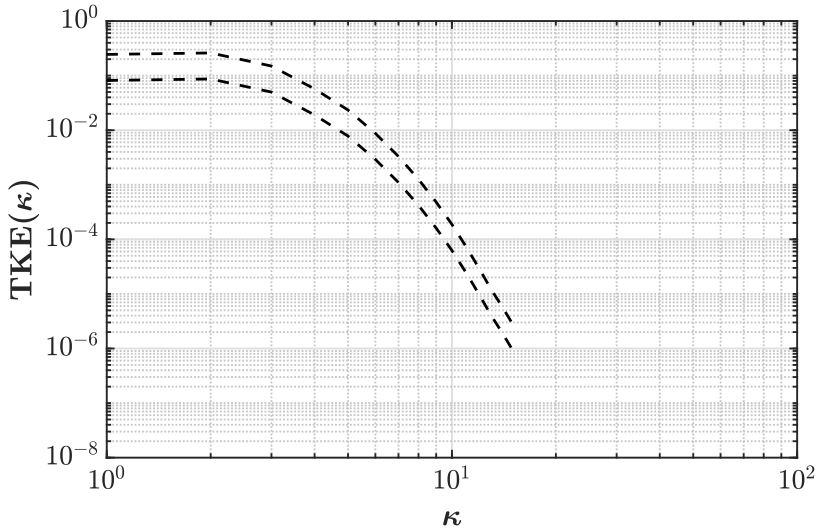

Figure A.4: Estimated bounds for the energy spectrum of the second CLV.

A.4 Influence of the forcing scheme on the structure of the Lyapunov vectors

In this appendix, the correlations and conditional averages of $\delta\boldsymbol{\xi}^2$ with different turbulent quantities that were obtained for the Case 5, 6, 7 which (different forcing schemes) are shown.

A.4.1 Case 5

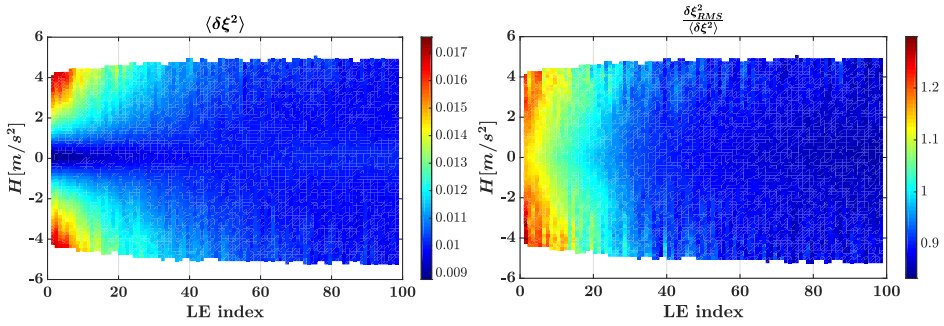

Figure A.5: Left: conditional average of $\delta\boldsymbol{\xi}^2$ at different helicity values H, for each LV. Right: conditional RMS of $\delta\boldsymbol{\xi}^2$ at different helicity values H, for each LV, rescaled by the conditional average of $\delta\boldsymbol{\xi}^2$. Plots are generated with the data from Case 5.

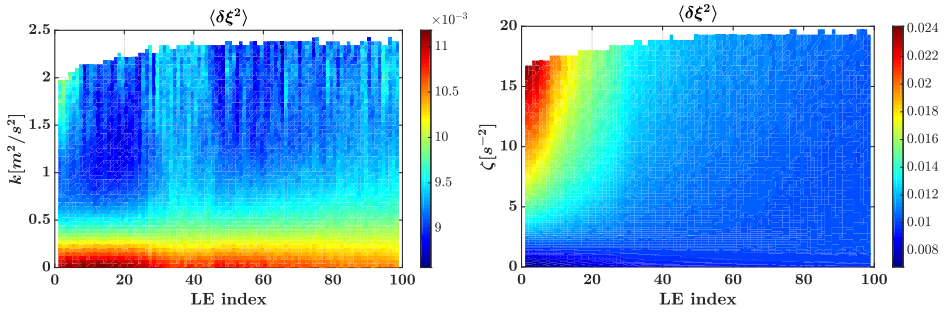

Figure A.6: Left: conditional average of $\delta\boldsymbol{\xi}^2$ at different turbulent kinetic energy values k, for each LV. Right: conditional average of $\delta\boldsymbol{\xi}^2$ at different enstrophy values ζ, for each LV. Plots are generated with the data from Case 5.

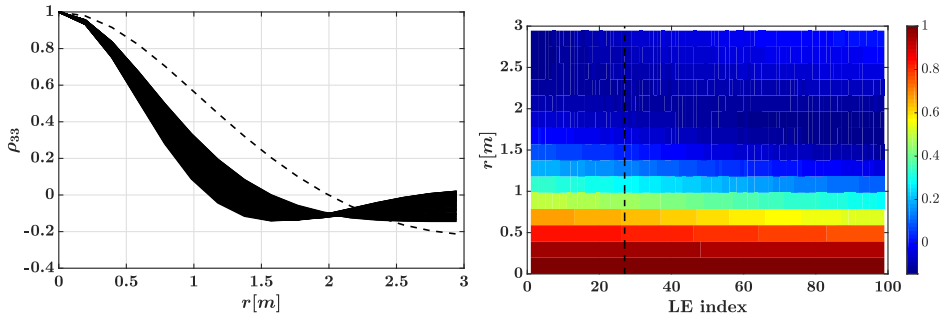

Figure A.7: Left: spatial correlation $\rho_{33}(r)$ of the LVs (—) and of the underlying flow-field (- -). Right: spatial correlation $\rho_{33}(r)$ of the LVs plotted against the LE index and the distance. Plots are generated with the data of Case 5.

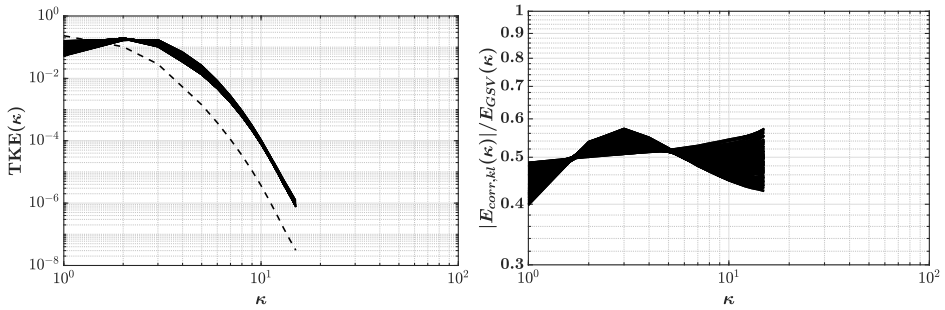

Figure A.8: Left: time-averaged energy spectrum of the computed LVs (—). Time-averaged energy spectrum of the underlying flow field (- -). Right: ratio $\frac{|E_{corr,kl}(\boldsymbol{\kappa})|}{E_{GSV}(\boldsymbol{\kappa})}$ plotted for the first 19 pairs of LVs, plotted against the wavenumber amplitude. Plots are generated with the data of Case 5.

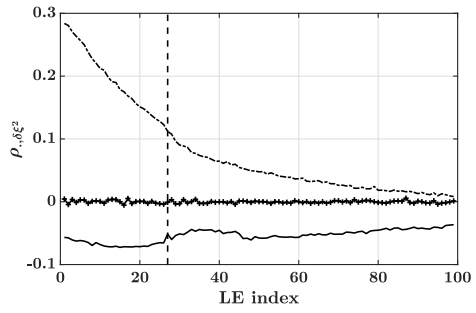

Figure A.9: Field correlation of $\delta\boldsymbol{\xi}^2$ and ζ (···), $\delta\boldsymbol{\xi}^2$ and H (+), $\delta\boldsymbol{\xi}^2$ and k (—). The curves are plotted alongside the index where the LS crosses zero (- -). Plot generated with the data of Case 5.

A.4.2 Case 6

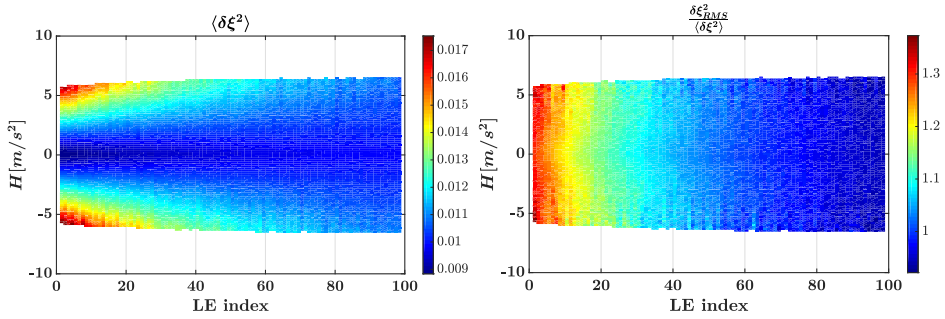

Figure A.10: Left: conditional average of $\delta\boldsymbol{\xi}^2$ at different helicity values H, for each LV. Right: conditional RMS of $\delta\boldsymbol{\xi}^2$ at different helicity values H, for each LV, rescaled by the conditional average of $\delta\boldsymbol{\xi}^2$. Plots are generated with the data from Case 6.

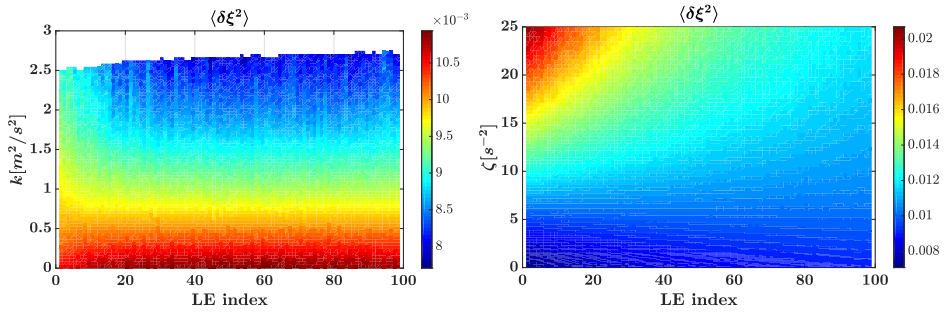

Figure A.11: Left: conditional average of $\delta\boldsymbol{\xi}^2$ at different turbulent kinetic energy values k, for each LV. Right: conditional average of $\delta\boldsymbol{\xi}^2$ at different enstrophy values ζ, for each LV. Plots are generated with the data from Case 6.

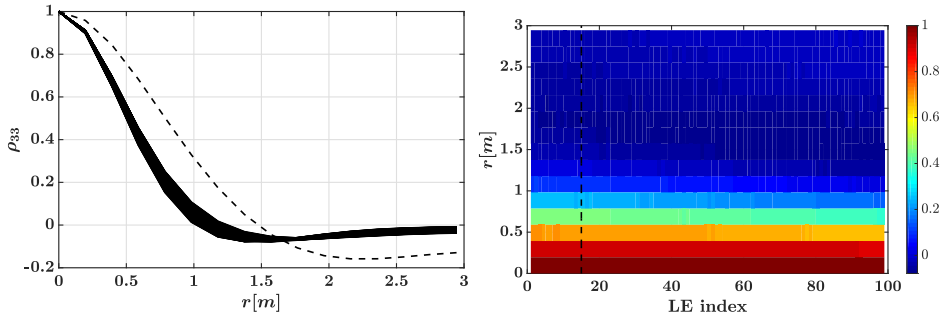

Figure A.12: Left: spatial correlation $\rho_{33}(r)$ of the LVs (—) and of the underlying flow-field (--). Right: spatial correlation $\rho_{33}(r)$ of the LVs plotted against the LE index and the distance. Plots are generated with the data of Case 6.

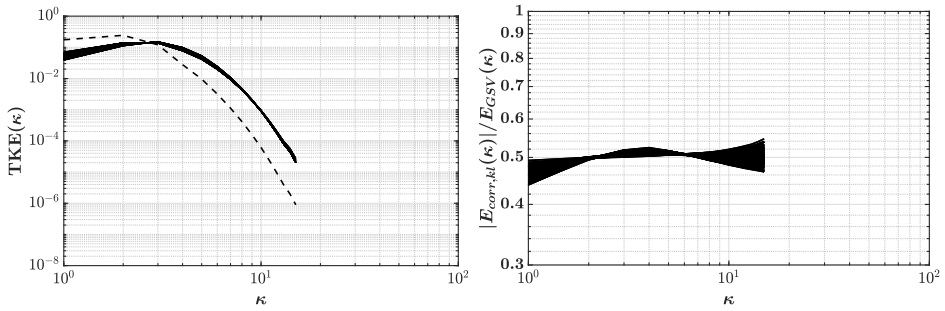

Figure A.13: Left: time-averaged energy spectrum of the computed LVs (—). Time-averaged energy spectrum of the underlying flow field (- -). Right: ratio $\frac{|E_{corr,kl}(\boldsymbol{\kappa})|}{E_{GSV}(\boldsymbol{\kappa})}$ plotted for the first 19 pairs of LVs, plotted against the wavenumber amplitude. Plots are generated with the data of Case 6.

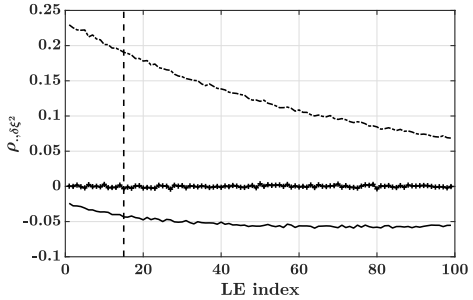

Figure A.14: Field correlation of $\delta\boldsymbol{\xi}^2$ and ζ (···), $\delta\boldsymbol{\xi}^2$ and H (+), $\delta\boldsymbol{\xi}^2$ and k (—). The curves are plotted alongside the index where the LS crosses zero (- -). Plot generated with the data of Case 6.

A.4.3 Case 7

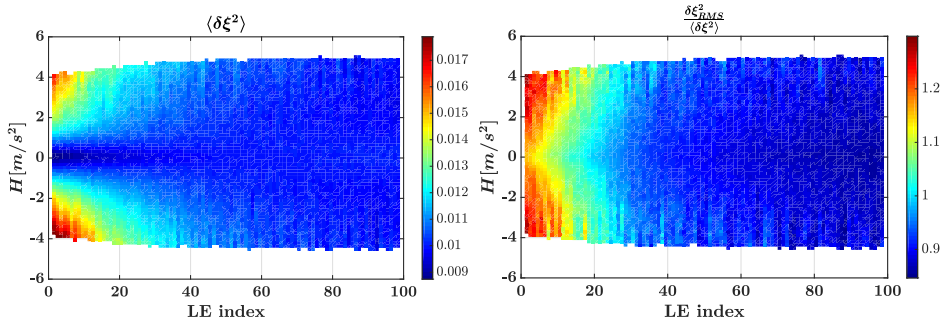

Figure A.15: Left: conditional average of $\delta\boldsymbol{\xi}^2$ at different helicity values H, for each LV. Right: conditional RMS of $\delta\boldsymbol{\xi}^2$ at different helicity values H, for each LV, rescaled by the conditional average of $\delta\boldsymbol{\xi}^2$. Plots are generated with the data from Case 7.

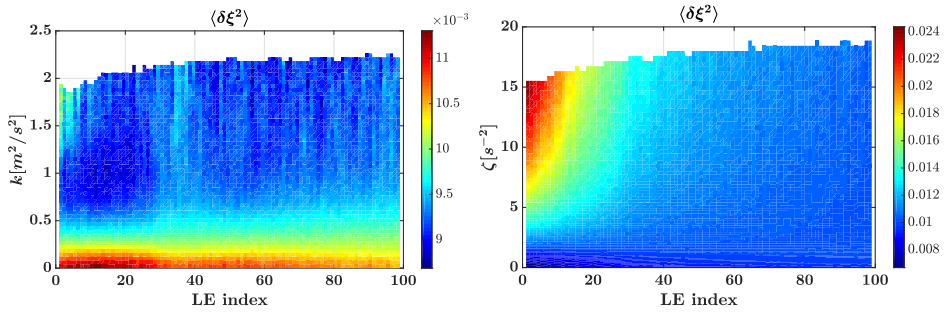

Figure A.16: Left: conditional average of $\delta\boldsymbol{\xi}^2$ at different turbulent kinetic energy values k, for each LV. Right: conditional average of $\delta\boldsymbol{\xi}^2$ at different enstrophy values ζ, for each LV. Plots are generated with the data from Case 7.

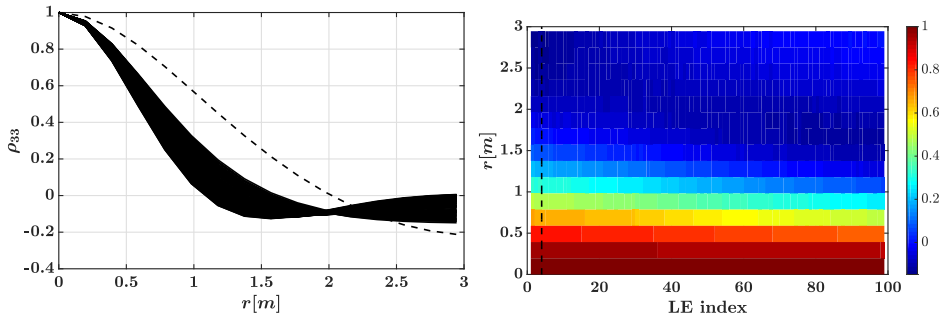

Figure A.17: Left: spatial correlation $\rho_{33}(r)$ of the LVs (—) and of the underlying flow-field (--). Right: spatial correlation $\rho_{33}(r)$ of the LVs plotted against the LE index and the distance. Plots are generated with the data of Case 7.

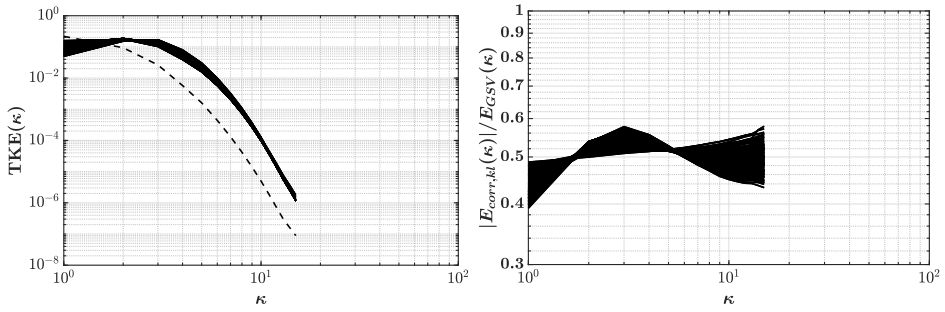

Figure A.18: Left: time-averaged energy spectrum of the computed LVs (—). Time-averaged energy spectrum of the underlying flow field (- -). Right: ratio $\frac{|E_{corr,kl}(\boldsymbol{\kappa})|}{E_{GSV}(\boldsymbol{\kappa})}$ plotted for the first 19 pairs of LVs, plotted against the wavenumber amplitude. Plots are generated with the data of Case 7.

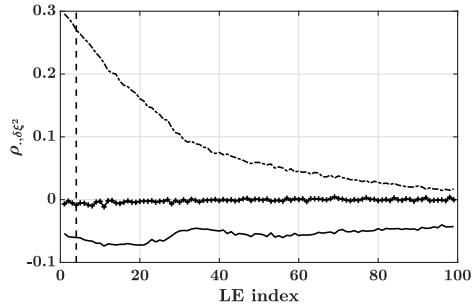

Figure A.19: Field correlation of $\delta\boldsymbol{\xi}^2$ and ζ (···), $\delta\boldsymbol{\xi}^2$ and H (+), $\delta\boldsymbol{\xi}^2$ and k (—). The curves are plotted alongside the index where the LS crosses zero (- -). Plot generated with the data of Case 7.

APPENDIX B

Lyapunov spectrum of a partially premixed jet flame

B.1 Convective and absolute instabilities

When perturbations are applied on a fluid systems, they can amplify and be convected with the local flow velocity. The amplification is referred to as *absolute instability* and the convection as *convective instability*. In general both phenomenon occur, and there is no practical fluid systems purely convectively unstable or absolutely unstable. When computing the expansion rate of a perturbation, one does not examine the magnitude of a perturbation at a local point in space, but instead considers a spatial integration of the perturbation magnitude, thereby not discarding perturbations that have been convected. If one considers closed or periodic systems, no matter how the perturbation is convected, it will always be in the domain. However, in the case of open domains, the perturbation can exit the domain which would prevent one from recording it as part of the LE calculation procedure. The Lyapunov analysis of an open system through Algo. 3.1, including the present turbulent jet flame, is in general not possible.

Several studies in the past have indicated that jets with large density ratio are more subject to absolute instabilities than convective instabilities [224, 225]. To ensure that the jet studied here is more absolutely unstable than convectively unstable, the computed LVs were averaged over time, and their average is shown in Fig. B.1. Since this average is mostly localized upstream, it suggest that only a negligible part of the perturbation are convected out of the domain, and the perturbation are mostly amplified in the shear layer of the jet.

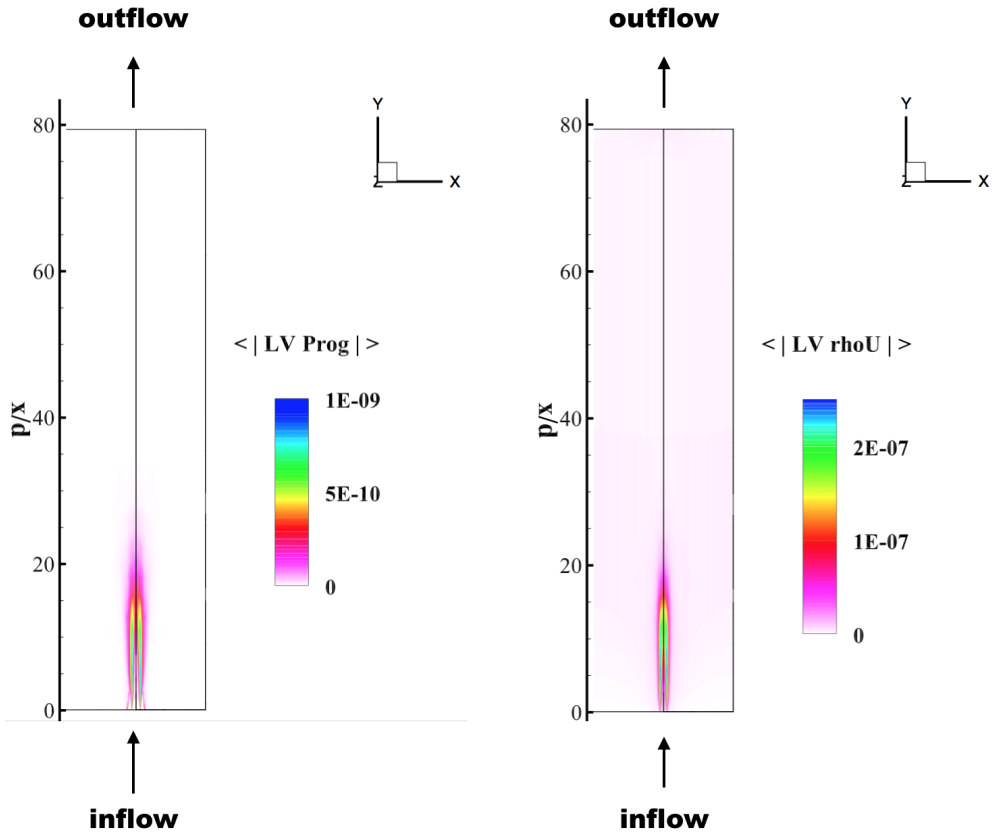

Figure B.1: Contour of the time averaged components of the first LV for progress variable (left) and axial momentum (right).

APPENDIX C

Statistical analysis of extreme events

C.1 Validation of algorithm for higher-dimensional problems

In this section, the Lorenz 96 system is investigated in 64 dimensions and 1024 dimensions to determine whether the features found at 32 dimensions hold with increase in dimensionality. The QoI is defined in the same manner as the levels chosen for the 32-dimensional case (Eq. 6.3). The numerical integration and the timestep size are the same as for the 32-dimensional case. Figure C.1 shows the instantaneous evolution of the QoI for 1000 realizations, along with the ensemble average QoI, for the 64 and 1024-dimensional case.

The target levels chosen for the 64 and 1024-dimensional cases are located two and four standard deviations away from the mean (similar to the choices made for the 32 dimensional case). The target levels chosen are 1244 and 1512 for the 64-dimensional case; 1042 and 1109 for the 1024-dimensional case. The number of particles is $M = 2500$. All the ISP simulations are run 10^5 times in order to ensure convergence of the statistics of the probability estimator. In Fig. C.2 (for the 64-dimensional case) and Fig. C.3 (for the 1024-dimensional case), it can be seen that the estimators obtained

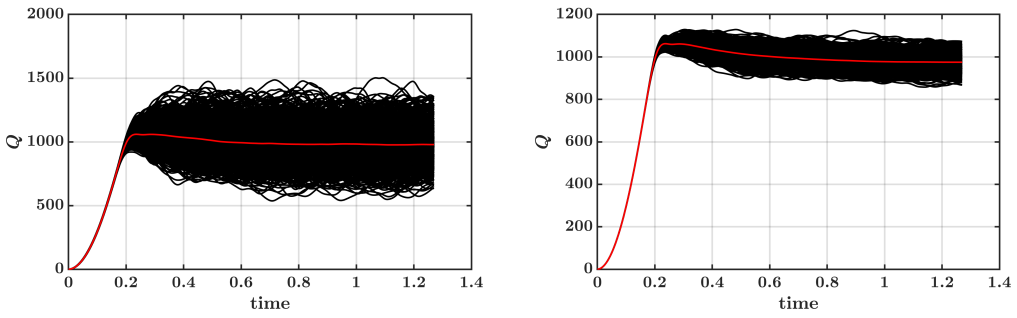

Figure C.1: Instantaneous values of the observable $Q(t)$ plotted over time (—). Ensemble average of Q (—). Left: Lorenz 96 case with 64 degrees of freedom. Right: Lorenz 96 case with 1024 degrees of freedom.

are still unbiased (left plots) and provide a consistent improvement compared to the fixed weight methods (middle plots). This improvement can again be linked to the smaller pruning ratio induced by the time-dependent weighting factor.

The self-similarity approach is tested a priori for the 64-dimensional case by sampling 8×10^8 realizations and computing the rare mean path exceeding levels ranging from 1400 to 1650 and separated by a constant step size of 25. For the 1024-dimensional case, 2×10^8 realizations are run and rare mean paths exceeding levels ranging from 1060 to 1110 and separated by a constant step size of 5 are shown. The results of the a priori analysis are shown in Fig. C.4 (for the 64-dimensional case) and Fig. C.5 (for the 1024-dimensional case). Similar to the results obtained in Sec. 6.3.1, there is a self-similar structure to these paths. The self-similarity model proposed in Sec. 6.3.1 is tested, and shows an equally valid level of agreement.

Finally, the self-similar model is tested a posteriori. Using a brute force calculation run with 2500 realizations, the paths leading to QoI ranging from 1100 to 1225 separated by a step size of 25 are obtained for the 64-dimensional case. Paths leading to QoI ranging from 990 to 1050 separated by a step size of 10 are obtained for the 1024-dimensional case. The rare mean path exceeding the thresholds 1512 (for the 64-dimensional case) and 1109 (for the 1024-dimensional case) are then estimated,

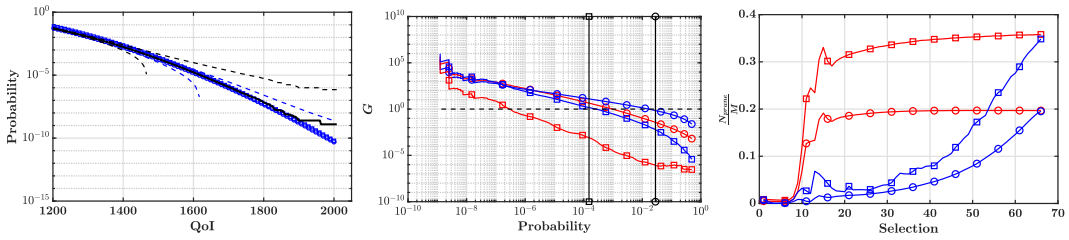

Figure C.2: Left: complementary of the cumulative density function (CDF) of the QoI. Probabilities are obtained with brute force calculation (—), the ISP method with time-dependent weight based on R_{1244} (○), and R_{1512} (□) and $M = 2500$ particles. Uncertainty of the estimator computed with the ISP algorithm using R_{1244} for the time-dependent weight is shown (- -) along with the theoretical Monte-Carlo uncertainty that would be obtained with $M = 2500$ realizations (- -). Middle: computational gain computed as Eq. 6.6 when targeting the level 1512 with the fixed weight (⊟), the time-dependent weight obtained from the brute force calculation (⊟), the time-dependent weight obtained from the self-similarity approximation ■. Right: pruning ratio obtained when targeting the level 1512 with fixed weight (⊟) and time-dependent weight obtained from brute force calculation (⊟) and the time-dependent weight obtained from the self-similarity approximation (■). Plots correspond to the Lorenz 96 problem with 64 degrees of freedom.

similar to the procedure outlined in Sec. 6.3.2. Figure C.6 (64-dimensional case) and Fig.C.7 (1024-dimensional case) show that the self-similarity approach provides a reasonable approximation of the rare mean path. The self-similarity procedure is able to provide almost the same computational efficiency as the a priori procedure, while consistently outperforming the fixed weight method.

Finally, the performance of the ISP algorithm is compared between the 32, 64 and 1024-dimensional cases. For each case, the computational gain of the a posteriori analysis, obtained by targeting a level located four standard deviations away from the mean is plotted in Fig. C.8. It can be seen that the performance does not degrade as the number of dimension increases. This observation suggests that the ISP method used here could be useful for very large-dimensional problems such as turbulent flows.

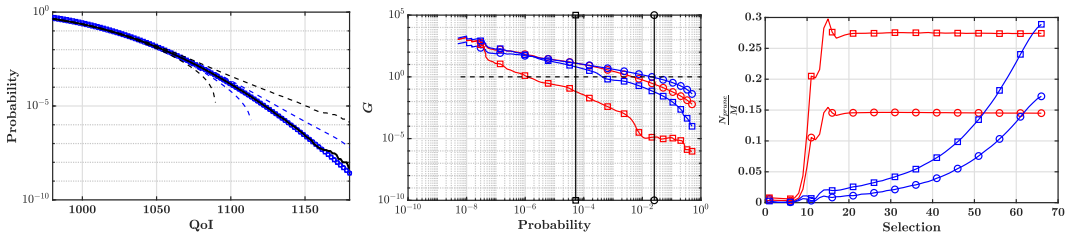

Figure C.3: Left: complementary of the cumulative density function (CDF) of the QoI. Probabilities are obtained with brute force calculation (—), the ISP method with time-dependent weight based on R_{1042} (○), and R_{1109} (□) and $M = 2500$ particles. Uncertainty of the estimator computed with the ISP algorithm using R_{1042} for the time-dependent weight is shown (- -) along with the theoretical Monte-Carlo uncertainty that would be obtained with $M = 2500$ realizations (- -). Middle: computational gain computed as Eq. 6.6 when targeting the level 1109 with the fixed weight (-□-), the time-dependent weight obtained from the brute force calculation (-□-), the time-dependent weight obtained from the self-similarity approximation -■-. Right: pruning ratio obtained when targeting the level 1109 with fixed weight (-□-) and time-dependent weight obtained from brute force calculation (-□-) and the time-dependent weight obtained from the self-similarity approximation (-■-). Plots correspond to the Lorenz 96 problem with 1024 degrees of freedom.

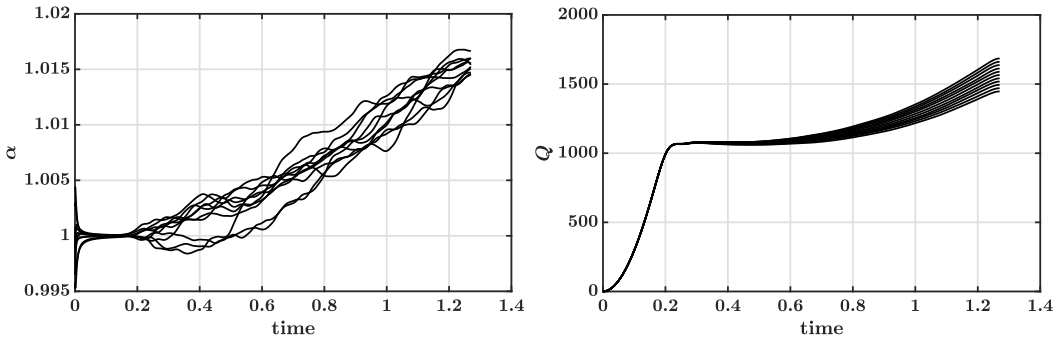

Figure C.4: Left: rare mean path exceeding thresholds ranging from 1400 to 1650 and separated by a stepsize of 25. Right: self-similarity factor α computed from successive rare mean path (see Eq. 6.7). Plots correspond to the Lorenz 96 case with 64 degrees of freedom.

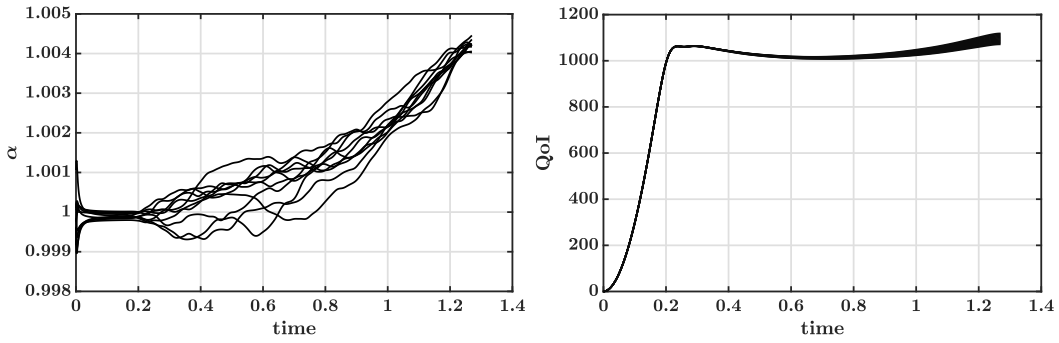

Figure C.5: Left: rare mean path exceeding thresholds ranging from 1060 to 1110 and separated by a stepsize of 5. Right: self-similarity factor α computed from successive rare mean path (see Eq. 6.7). Plots correspond to the Lorenz 96 case with 1024 degrees of freedom.

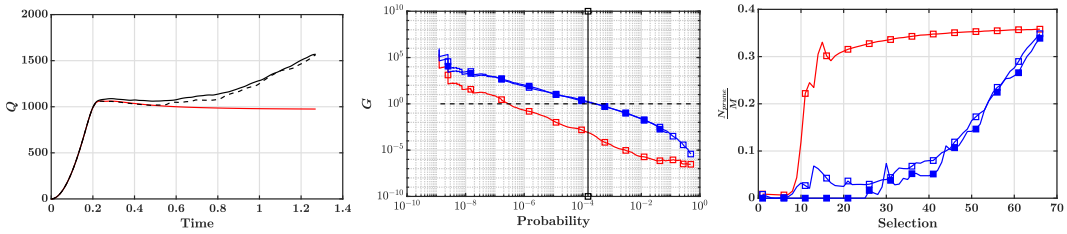

Figure C.6: Left: rare mean path R_{1512} obtained from brute force computation (—), from the self-similarity approximation (- -) and ensemble average time history of the observable (—). Middle: computational gain computed as Eq. 6.6 when targeting the level 1512 with the fixed weight (⊟), the time-dependent weight obtained from the brute force calculation (⊟), the time-dependent weight obtained from the self-similarity approximation ■. Right: pruning ratio obtained when targeting the level 1512 with fixed weight (⊟) and time-dependent weight obtained from brute force calculation (⊟) and the time-dependent weight obtained from the self-similarity approximation (■). Plots correspond to the Lorenz 96 case with 64 degrees of freedom.

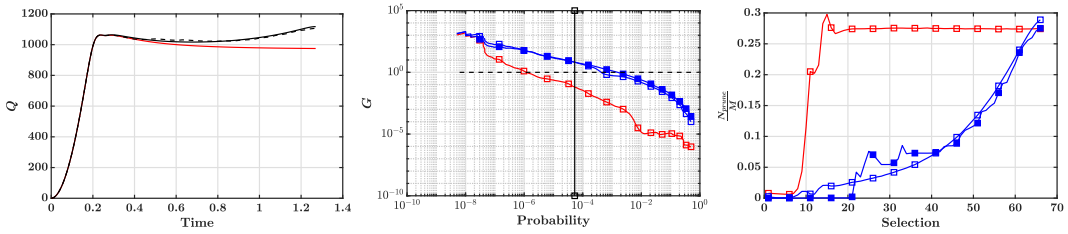

Figure C.7: Left: rare mean path R_{1109} obtained from brute force computation (—), from the self-similarity approximation (- -) and ensemble average time history of the observable (—). Middle: computational gain computed as Eq. 6.6 when targeting the level 1109 with the fixed weight (⊟), the time-dependent weight obtained from the brute force calculation (⊟), the time-dependent weight obtained from the self-similarity approximation ■. Right: pruning ratio obtained when targeting the level 1109 with fixed weight (⊟) and time-dependent weight obtained from brute force calculation (⊟) and the time-dependent weight obtained from the self-similarity approximation (■). Plots correspond to the Lorenz 96 case with 1024 degrees of freedom.

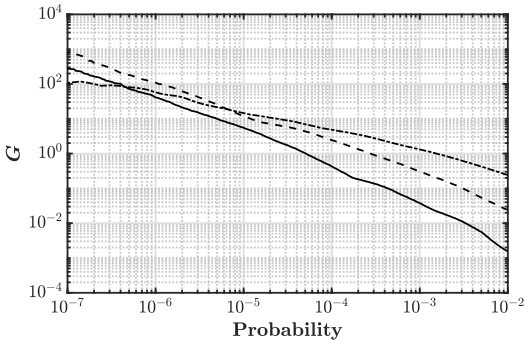

Figure C.8: Computational gain computed as Eq. 6.6 when targeting the level located four standard deviations away from the mean for the 32-dimensional case (—), the 64-dimensional case (- -) and the 1024-dimensional case (···).

BIBLIOGRAPHY

BIBLIOGRAPHY

[1] "https://en.wikipedia.org/wiki/Jet_engine#/media/File:Jet_engine.svg," .

[2] Tang, Y., Hassanaly, M., Raman, V., Sforzo, B., Wei, S., and Seitzman, J. M., "Simulation of gas turbine ignition using Large eddy simulation approach," *ASME Turbo Expo 2018*, No. GT2018-76216, 2018.

[3] Tang, Y., Hassanaly, M., Raman, V., Sforzo, B., and Seitzman, J., "A comprehensive modeling procedure for estimating statistical properties of forced ignition," *Combustion and Flame*, Vol. 206, 2019, pp. 158–176.

[4] Lietz, C., Hassanaly, M., and Raman, V., "Large Eddy Simulation of Flame Flashback in Swirling Premixed CH4/H2-Air Flames," *53rd AIAA Aerospace Science Meeting*, No. AIAA 2015-0844, 2015.

[5] Wei, S., Sforzo, B., and Seitzman, J., "High-Speed Imaging of Forced Ignition Kernels in Nonuniform Jet Fuel/Air Mixtures," *Journal of Engineering for Gas Turbines and Power*, Vol. 140, No. 7, 2018, pp. 071503.

[6] An, Q., Kwong, W. Y., Geraedts, B. D., and Steinberg, A. M., "Coupled dynamics of lift-off and precessing vortex core formation in swirl flames," *Combustion and Flame*, Vol. 168, 2016, pp. 228–239.

[7] Barwey, S., Hassanaly, M., An, Q., Raman, V., and Steinberg, A., "Experimental Data Based Reduced Order Model for Predicting Flame Transition in Gas Turbine Combustors," *Submitted*.

[8] Koo, H., Hassanaly, M., Raman, V., Mueller, M. E., and Geigle, K. P., "Large-eddy simulation of soot formation in a model gas turbine combustor," *Journal of Engineering for Gas Turbines and Power*, Vol. 139, No. 3, 2017, pp. 031503.

[9] Guiberti, T., Zimmer, L., Durox, D., and Schuller, T., "Experimental analysis of V-to M-shape transition of premixed CH4/H2/air swirling flames," *ASME Turbo Expo 2013: Turbine Technical Conference and Exposition*, American Society of Mechanical Engineers, 2013, pp. V01AT04A063–V01AT04A063.

[10] Seo, S., *Parametric study of lean premixed combustion instability in a pressurized model gas turbine combustor.*, Ph.D. thesis, The Pennsylvania State University, 2000.

[11] Chiu, H.-H. and Huang, J.-S., "Multiple-state phenomena and hysteresis of a combusting isolated droplet," *Atomization and Sprays*, Vol. 6, No. 1, 1996.

[12] Popov, P. P., Sideris, A., and Sirignano, W. A., "Low-Probability Events Leading to Rocket Engine Combustion Instability," *AIAA Journal*, Vol. 55, No. 3, 2017, pp. 919–929.

[13] Tailleur, J. and Kurchan, J., "Probing rare physical trajectories with Lyapunov weighted dynamics," *Nature Physics*, Vol. 3, 2007, pp. 203–207.

[14] Carroll, P. L. and Blanquart, G., "A proposed modification to Lundgren's physical space velocity forcing method for isotropic turbulence," *Physics of Fluids*, Vol. 25, No. 10, 2013, pp. 105114.

[15] Barlow, R. S. and Frank, J. H., "Effects of turbulence on species mass fractions in methane/air jet flames," *Symposium (International) on Combustion*, Vol. 27, Elsevier, 1998, pp. 1087–1095.

[16] Wouters, J. and Bouchet, F., "Rare event computation in deterministic chaotic systems using genealogical particle analysis," *Journal of Physics A: Mathematical and Theoretical*, Vol. 49, 2016, pp. 374002.

[17] Read, R. W., *Experimental investigations into high-altitude relight of a gas turbine*, Ph.D. thesis, University of Cambridge, 2008.

[18] Dooley, K. A., "Continuous plasma ignition system," 1996, US Patent 5,587,630.

[19] Board, N. T. S., "DCA18MA142 SWA1380 INVESTIGATIVE UPDATE," Tech. rep., 2018.

[20] Administration, F. A., "Turbine engine power-loss and instability ain extreme conditions of rain and hail," 2000, Advisory Circular 33.78-1.

[21] Lefebvre, A. H., *Gas turbine combustion*, CRC press, 1998.

[22] Descamps, C., Bouallou, C., and Kanniche, M., "Efficiency of an Integrated Gasification Combined Cycle (IGCC) power plant including CO2 removal," *Energy*, Vol. 33, No. 6, 2008, pp. 874–881.

[23] Taamallah, S., Vogiatzaki, K., Alzahrani, F., Mokheimer, E., Habib, M., and Ghoniem, A., "Fuel flexibility, stability and emissions in premixed hydrogen-rich gas turbine combustion: Technology, fundamentals, and numerical simulations," *Applied energy*, Vol. 154, 2015, pp. 1020–1047.

[24] Ebi, D. and Clemens, N. T., "Experimental investigation of upstream flame propagation during boundary layer flashback of swirl flames," *Combustion and Flame*, Vol. 168, 2016, pp. 39–52.

[25] Onorato, M., Osborne, A. R., and Serio, M., "Extreme wave events in directional, random oceanic sea states," *Physics of Fluids*, Vol. 14, No. 4, 2002, pp. L25–L28.

[26] Solli, D. R., Ropers, C., Koonath, P., and Jalali, B., "Optical rogue waves," *Nature*, Vol. 450, No. 7172, 2007, pp. 1054.

[27] Hubert, P., Tessier, Y., Lovejoy, S., Schertzer, D., Schmitt, F., Ladoy, P., Carbonnel, J., Violette, S., and Desurosne, I., "Multifractals and extreme rainfall events," *Geophysical Research Letters*, Vol. 20, No. 10, 1993, pp. 931–934.

[28] Ragone, F., Wouters, J., and Bouchet, F., "Computation of extreme heat waves in climate models using a large deviation algorithm," *Proceedings of the National Academy of Sciences*, Vol. 115, No. 1, 2018, pp. 24–29.

[29] Krause, S. M., Börries, S., and Bornholdt, S., "Econophysics of adaptive power markets: When a market does not dampen fluctuations but amplifies them," *Physical Review E*, Vol. 92, No. 1, 2015, pp. 012815.

[30] Sornette, D., "Predictability of catastrophic events: Material rupture, earthquakes, turbulence, financial crashes, and human birth," *Proceedings of the National Academy of Sciences*, Vol. 99, No. suppl 1, 2002, pp. 2522–2529.

[31] Filimonov, V. and Sornette, D., "Quantifying reflexivity in financial markets: Toward a prediction of flash crashes," *Physical Review E*, Vol. 85, No. 5, 2012, pp. 056108.

[32] Collins, J. A., *Failure of materials in mechanical design: analysis, prediction, prevention*, John Wiley & Sons, 1993.

[33] Ghil, M., Yiou, P., Hallegatte, S., Malamud, B., Naveau, P., Soloviev, A., Friederichs, P., Keilis-Borok, V., Kondrashov, D., Kossobokov, V., et al., "Extreme events: dynamics, statistics and prediction," *Nonlinear Processes in Geophysics*, Vol. 18, No. 3, 2011, pp. 295–350.

[34] Yeung, P., Zhai, X., and Sreenivasan, K. R., "Extreme events in computational turbulence," *Proceedings of the National Academy of Sciences*, Vol. 112, No. 41, 2015, pp. 12633–12638.

[35] Wagner, J. L., Yuceil, K. B., Valdivia, A., Clemens, N. T., and Dolling, D. S., "PIV measurements of the unstart proces in a supersonic inlet/isolator," *38th Fluid Dynamics Conference and Exhibit*, No. 2008-3849, 2008.

[36] Sforzo, B., Kim, J., Jagoda, J., and Seitzman, J., "Ignition probability in a stratified turbulent flow with a sunken fire igniter," *Journal of Engineering for Gas Turbines and Power*, Vol. 137, No. 1, 2015, pp. 011502.

[37] Tang, Y., Hassanaly, M., Raman, V., Sforzo, B., and Seitzman, J. M., "Numerical simulation of forced ignition of Jet-fuel/air using large eddy simulation (LES) and a tabulation-based ignition," *AIAA Scitech 2019 Forum*, 2019, p. 2242.

[38] Oberleithner, K., Stöhr, M., Im, S. H., Arndt, C. M., and Steinberg, A. M., "Formation and flame-induced suppression of the precessing vortex core in a swirl combustor: experiments and linear stability analysis," *Combustion and Flame*, Vol. 162, No. 8, 2015, pp. 3100–3114.

[39] Eckmann, J.-P. and Ruelle, D., "Ergodic theory of chaos and strange attractors," *Review of Moderm Physics*, Vol. 57, 1985, pp. 617–656.

[40] Chong, S. T., Hassanaly, M., Koo, H., Mueller, M. E., Raman, V., and Geigle, K.-P., "Large eddy simulation of pressure and dilution-jet effects on soot formation in a model aircraft swirl combustor," *Combustion and Flame*, Vol. 192, 2018, pp. 452–472.

[41] Raman, V. and Fox, R. O., "Modeling of fine-particle formation in turbulent flames," *Annual Review of Fluid Mechanics*, Vol. 48, 2016, pp. 159–190.

[42] Geigle, K. P., Hadef, R., and Meier, W., "Soot formation and flame characterization of an aero-engine model combustor burning ethylene at elevated pressure," *Journal of Engineering for Gas Turbines and Power*, Vol. 136, No. 2, 2014, pp. 021505.

[43] Candel, S., Durox, D., Schuller, T., Bourgouin, J.-F., and Moeck, J. P., "Dynamics of swirling flames," *Annual review of fluid mechanics*, Vol. 46, 2014, pp. 147–173.

[44] Chterev, I., Foley, C. W., Foti, D., Kostka, S., Caswell, A. W., Jiang, N., Lynch, A., Noble, D. R., Menon, S., Seitzman, J. M., and Lieuwen, T., "Flame and flow topologies in an annular swirling flow," *Combustion Science and Technology*, Vol. 186, No. 8, 2014, pp. 1041–1074.

[45] Huang, Y. and Yang, V., "Bifurcation of flame structure in a lean-premixed swirl-stabilized combustor: transition from stable to unstable flame," *Combustion and Flame*, Vol. 136, No. 3, 2004, pp. 383–389.

[46] Bouchet, F. and Venaille, A., "Statistical mechanics of two-dimensional and geophysical flows," *Physics reports*, Vol. 515, No. 5, 2012, pp. 227–295.

[47] Gotoda, H., Nikimoto, H., Miyano, T., and Tachibana, S., "Dynamic properties of combustion instability in a lean premixed gas-turbine combustor," *Chaos: An Interdisciplinary Journal of Nonlinear Science*, Vol. 21, No. 1, 2011, pp. 013124.

[48] Poinsot, T., "Prediction and control of combustion instabilities in real engines," *Proceedings of the Combustion Institute*, Vol. 36, No. 1, 2017, pp. 1–28.

[49] Juniper, M. P. and Sujith, R., "Sensitivity and nonlinearity of thermoacoustic oscillations," *Annual Review of Fluid Mechanics*, Vol. 50, 2018, pp. 661–689.

[50] Huang, Y. and Yang, V., "Dynamics and stability of lean-premixed swirl-stabilized combustion," *Progress in energy and combustion science*, Vol. 35, No. 4, 2009, pp. 293–364.

[51] Zhang, B., Marzouk, Y., Min, B.-Y., and Sahai, T., "Rare Event Simulation of a Rotorcraft System," *2018 AIAA Non-Deterministic Approaches Conference*, 2018, p. 1181.

[52] Raman, V. and Hassanaly, M., "Emerging Trends in Numerical Simulations of Combustion Systems," *Proceedings of the Combustion Institute*, Vol. 37, 2019, pp. 2073–2089.

[53] Milnor, J., "On the concept of attractor," *The theory of chaotic attractors*, Springer, 1985, pp. 243–264.

[54] Eckmann, J.-P. and Ruelle, D., "Ergodic-Theory of Chaos and Strange Attractors," *Review of Modern Physics*, Vol. 57, 1985, pp. 617–656.

[55] Zandonade, P. S., Langford, J. A., and Moser, R. D., "Finite-volume optimal large-eddy simulation of isotropic turbulence," *Physics of fluids*, Vol. 16, No. 7, 2004, pp. 2255–2271.

[56] Langford, J. A. and Moser, R. D., "Optimal LES formulations for isotropic turbulence," *Journal of Fluid Mechanics*, Vol. 398, 1999, pp. 321.

[57] Pope, S. B., "Self-conditioned fields for large-eddy simulations of turbulent flows," *Journal of Fluid Mechanics*, Vol. 652, 2010, pp. 139–169.

[58] Berkooz, G., "An observation on probability density equations, or, when do simulations reproduce statistics?" *Nonlinearity*, Vol. 7, No. 2, 1994, pp. 313.

[59] "Turbulent Non-Premixed Flame Workshop, https://tnfworkshop.org," 2018.

[60] "International Sooting Flame Workshop, https://www.adelaide.edu.au/cet/isfworkshop," 2018.

[61] Smagorinsky, J., "General Circulation Experiments with the Primitive Equations: I. The Basic Equations." *Monthly Weather Review*, Vol. 91, 1963, pp. 99–164.

[62] Métais, O. and Lesieur, M., "Statistical predictability of decaying turbulence," *Journal of the Atmospheric Sciences*, Vol. 43, 1986, pp. 857–870.

[63] Molteni, F., Buizza, R., Palmer, T. N., and Petroliagis, T., "The ECMWF ensemble prediction system: Methodology and validation," *Quarterly journal of the royal meteorological society*, Vol. 122, No. 529, 1996, pp. 73–119.

[64] Kalnay, *Atmospheric Modeling, Data Assimilation and Predictability*, Cambridge University Press, 2003.

[65] Gruber, A., Chen, J. H., Valiev, D., and Law, C. K., "Direct numerical simulation of premixed flame boundary layer flashback in turbulent channel flow," *Journal of Fluid Mechanics*, Vol. 709, 2012, pp. 516–542.

[66] Lietz, C., Hassanaly, M., Raman, V., Kolla, H., Chen, J., and Gruber, A., "LES of Premixed Flame Flashback in a Turbulent Channel," *52nd AIAA Aerospace Science Meeting*, No. AIAA 2014-0824, 2014.

[67] Poincaré, H., "Sur le problème des trois corps et les équations de la dynamique," *Acta mathematica*, Vol. 13, No. 1, 1890, pp. A3–A270.

[68] Mañé, R., *Ergodic Theory and Differentiable Dynamics*, Springer-Verlag, 1987.

[69] Ott, E., *Chaos in dynamical systems*, Cambridge university press, 2002.

[70] Lyapunov, A. M., "The general problem of the stability of motion," *International journal of control*, Vol. 55, No. 3, 1992, pp. 531–534.

[71] Oseledets, V. I., "A multiplicative ergodic theorem. Characteristic Ljapunov, exponents of dynamical systems," *Trudy Moskovskogo Matematicheskogo Obshchestva*, Vol. 19, 1968, pp. 179–210.

[72] Ruelle, D., "Ergodic theory of differentiable dynamical systems," *Publications Mathématiques de l'Institut des Hautes Études Scientifiques*, Vol. 50, No. 1, 1979, pp. 27–58.

[73] Ginelli, F., Chaté, H., Livi, R., and Politi, A., "Covariant lyapunov vectors," *Journal of Physics A: Mathematical and Theoretical*, Vol. 46, No. 25, 2013, pp. 254005.

[74] Galanti, B. and Tsinober, A., "Is turbulence ergodic?" *Physics Letters A*, Vol. 330, No. 3-4, 2004, pp. 173–180.

[75] Lapeyre, G., "Characterization of finite-time Lyapunov exponents and vectors in two-dimensional turbulence," *Chaos: An Interdisciplinary Journal of Nonlinear Science*, Vol. 12, No. 3, 2002, pp. 688–698.

[76] Haller, G. and Yuan, G., "Lagrangian coherent structures and mixing in two-dimensional turbulence," *Physica D: Nonlinear Phenomena*, Vol. 147, No. 3-4, 2000, pp. 352–370.

[77] Coulliette, C., Lekien, F., Paduan, J. D., Haller, G., and Marsden, J. E., "Optimal pollution mitigation in Monterey Bay based on coastal radar data and nonlinear dynamics," *Environmental science & technology*, Vol. 41, No. 18, 2007, pp. 6562–6572.

[78] Cencini, M. and Vulpiani, A., "Finite size Lyapunov exponent: review on applications," *Journal of Physics A: Mathematical and Theoretical*, Vol. 46, No. 25, 2013, pp. 254019.

[79] Karrasch, D. and Haller, G., "Do finite-size Lyapunov exponents detect coherent structures?" *Chaos: An Interdisciplinary Journal of Nonlinear Science*, Vol. 23, No. 4, 2013, pp. 043126.

[80] Haller, G. and Sapsis, T., "Lagrangian coherent structures and the smallest finite-time Lyapunov exponent," *Chaos: An Interdisciplinary Journal of Nonlinear Science*, Vol. 21, No. 2, 2011, pp. 023115.

[81] Finn, J. and Apte, S. V., "Integrated computation of finite-time Lyapunov exponent fields during direct numerical simulation of unsteady flows," *Chaos: An Interdisciplinary Journal of Nonlinear Science*, Vol. 23, No. 1, 2013, pp. 013145.

[82] Amon, C. H., Guzmán, A. M., and Morel, B., "Lagrangian chaos, Eulerian chaos, and mixing enhancement in converging–diverging channel flows," *Physics of Fluids*, Vol. 8, No. 5, 1996, pp. 1192–1206.

[83] Legras, B. and Vautard, R., "A guide to Liapunov vectors," *Proceedings 1995 ECMWF seminar on predictability*, Vol. 1, Citeseer, 1996, pp. 143–156.

[84] Yang, H.-l. and Radons, G., "Comparison between covariant and orthogonal Lyapunov vectors," *Physical Review E*, Vol. 82, No. 4, 2010, pp. 046204.

[85] Ginelli, F., Poggi, P., Turchi, A., Chaté, H., Livi, R., and Politi, A., "Characterizing dynamics with covariant Lyapunov vectors," *Physical Review Letters*, Vol. 99, No. 13, 2007, pp. 130601.

[86] Buizza, R. and Palmer, T. N., "The Singular-Vector Structure of the Atmospheric Global Circulation," *Journal of the Atmospheric Sciences*, Vol. 52, 1995, pp. 1434–1456.

[87] Reynolds, C. A. and Errico, R. M., "Convergence of singular vectors toward Lyapunov vectors," *Monthly weather review*, Vol. 127, No. 10, 1999, pp. 2309–2323.

[88] Vastano, J. A. and Moser, R. D., "Short-time Lyapunov exponent analysis and the transition to chaos in Taylor-Couette flow," *Journal of Fluid Mechanics*, Vol. 233, 1991, pp. 83–118.

[89] Inubushi, M., Takehiro, S.-i., and Yamada, M., "Regeneration cycle and the covariant Lyapunov vectors in a minimal wall turbulence," *Physical Review E*, Vol. 92, No. 2, 2015, pp. 023022.

[90] Hassanaly, M. and Raman, V., "Computational Tools for Data-poor Problems in Turbulent Combustion," *AIAA Scitech 2019 Forum*, 2019, p. 0998.

[91] Kaplan, J. L. and Yorke, J. A., "Chaotic behavior of multidimensional difference equations," *Functional Differential equations and approximation of fixed points*, Springer, 1979, pp. 204–227.

[92] Clark, S. P., "Estimating the fractal dimension of chaotic time series," *Lincoln Laboratory Journal*, Vol. 3, No. 1, 1990.

[93] Constantin, P. and Foias, C., "Global Lyapunov Exponents, Kaplan-Yorke Formulas and the Dimension of the Attractors for 2D Navier-Stokes Equations," *Communications on pure and applied mathematics*, Vol. 38, No. 1, 1985, pp. 1–27.

[94] Tran, C. V., "The number of degrees of freedom of three-dimensional Navier–Stokes turbulence," *Physics of Fluids*, Vol. 21, No. 12, 2009, pp. 125103.

[95] Ott, E., "Attractor dimensions," *Scholarpedia*, Vol. 3, No. 3, 2008, pp. 2110, revision #91015.

[96] Xu, M. and Paul, M. R., "Chaotic Rayleigh-Bénard convection with finite sidewalls," *Physical Review E*, Vol. 98, No. 1, 2018, pp. 012201.

[97] Cousins, W. and Sapsis, T. P., "Reduced-order precursors of rare events in unidirectional nonlinear water waves," *Journal of Fluid Mechanics*, Vol. 790, 2016, pp. 368–388.

[98] Babaee, H. and Sapsis, T. P., "A minimization principle for the description of modes associated with finite-time instabilities," *Proc. R. Soc. A*, Vol. 472, No. 2186, 2016, pp. 20150779.

[99] Farazmand, M. and Sapsis, T. P., "Dynamical indicators for the prediction of bursting phenomena in high-dimensional systems," *Physical Review E*, Vol. 94, No. 3, 2016, pp. 032212.

[100] Blanchard, A. and Sapsis, T., "Analytical description of optimally time-dependent modes for reduced-order modeling of transient instabilities," SIAM Journal on Applied Dynamical Systems.

[101] Farazmand, M. and Sapsis, T. P., "A variational approach to probing extreme events in turbulent dynamical systems," *Science Advances*, Vol. 3, No. 9, 2017, pp. e1701533.

[102] Blonigan, P. J., Farazmand, M., and Sapsis, T. P., "Are extreme dissipation events predictable in turbulent fluid flows?" *arXiv preprint arXiv:1807.10263*, 2018.

[103] Kaiser, E., Noack, B. R., Cordier, L., Spohn, A., Segond, M., Abel, M., Daviller, G., Östh, J., Krajnović, S., and Niven, R. K., "Cluster-based reduced-order modelling of a mixing layer," *Journal of Fluid Mechanics*, Vol. 754, 2014, pp. 365–414.

[104] Rao, C., Ray, A., Sarkar, S., and Yasar, M., "Review and comparative evaluation of symbolic dynamic filtering for detection of anomaly patterns," *Signal, Image and Video Processing*, Vol. 3, No. 2, 2009, pp. 101–114.

[105] Karnatak, R., Kantz, H., and Bialonski, S., "Early warning signal for interior crises in excitable systems," *Physical Review E*, Vol. 96, No. 4, 2017, pp. 042211.

[106] Hassanaly, M. and Raman, V., "Numerical convergence of the Lyapunov spectrum computed using low Mach number solvers," *Journal of Computational Physics*, Vol. 386, 2019, pp. 467–485.

[107] Benettin, G., Galgani, L., Giorgilli, A., and Strelcyn, J.-M., "Lyapunov characteristic exponents for smooth dynamical systems; A method for computing all of them. Part 1: Theory," *Meccanica*, Vol. 15, 1980, pp. 21–30.

[108] Benettin, G., Galgani, L., Giorgilli, A., and Strelcyn, J.-M., "Lyapunov characteristic exponents for smooth dynamical systems and for Hamiltonian systems; A method for computing all of them. Part 2: Numerical application," *Meccanica*, Vol. 15, 1980, pp. 21–30.

[109] Shimada, I. and Nagashima, T., "A numerical approach to ergodic problem of dissipative dynamical systems," *Progress of theoretical physics*, Vol. 61, No. 6, 1979, pp. 1605–1616.

[110] Ding, R. and Li, J., "Nonlinear finite-time Lyapunov exponent and predictability," *Physics Letters A*, Vol. 364, No. 5, 2007, pp. 396–400.

[111] Björck, Å., "Numerics of gram-schmidt orthogonalization," *Linear Algebra and Its Applications*, Vol. 197, 1994, pp. 297–316.

[112] Schmidt, E., "Über die Auflösung linearer Gleichungen mit unendlich vielen Unbekannten," *Rendiconti del Circolo Matematico di Palermo (1884-1940)*, Vol. 25, No. 1, 1908, pp. 53–77.

[113] Wolf, A., Swift, J. B., Swinney, H. L., and Vastano, J. A., "Determining Lyapunov exponents from a time series," *Physica D: Nonlinear Phenomena*, Vol. 16, No. 3, 1985, pp. 285–317.

[114] Ershov, S. V. and Potapov, A. B., "On the concept of stationary Lyapunov basis," *Physica D: Nonlinear Phenomena*, Vol. 118, No. 3-4, 1998, pp. 167–198.

[115] Wolfe, C. L. and Samelson, R. M., "An efficient method for recovering Lyapunov vectors from singular vectors," *Tellus*, Vol. 59A, 2007, pp. 355–366.

[116] Harlow, F. H. and Welch, J. E., "Numerical calculation of time-dependent viscous incompressible flow of fluid with free surface," *Physics of Fluids*, Vol. 8, 1965, pp. 2182–2189.

[117] Hassanaly, M., Koo, H., Lietz, C. F., Chong, S. T., and Raman, V., "A minimally-dissipative low-Mach number solver for complex reacting flows in OpenFOAM," *Computer and Fluids*, Vol. 162, 2018, pp. 11–25.

[118] Desjardins, O., Blanquart, G., Balarac, G., and Pitsch, H., "High order conservative finite difference scheme for variable density low Mach number turbulent flows," *Journal of Computational Physics*, Vol. 227, No. 15, 2008, pp. 7125–7159.

[119] Shunn, L., Ham, F., and Moin, P., "Verification of variable-density flow solvers using manufactured solutions," *Journal of Computational Physics*, Vol. 231, 2012, pp. 3801–3827.

[120] Kim, J. and Moin, P., "Application of a fractional-step method to incompressible Navier-Stokes equations," *Journal of Computational Physics*, Vol. 59, No. 2, 1985, pp. 308–323.

[121] Pitsch, H., "Large-Eddy Simulation of Turbulent Combustion," *Annual Review of Fluid Mechanics*, Vol. 38, 2006, pp. 453–482.

[122] Pierce, C. D., *Progress-variable approach for large-eddy simulation of turbulence combustion*, Ph.D. thesis, Stanford University, 2001.

[123] De Charentenay, J., Thévenin, D., and Zamuner, B., "Comparison of direct numerical simulations of turbulent flames using compressible or low-Mach number formulations," *International journal for numerical methods in fluids*, Vol. 39, No. 6, 2002, pp. 497–515.

[124] Keefe, L., Moin, P., and Kim, J., "The dimension of attractors underlying periodic turbulent Poiseuille flow," *Journal of Fluid Mechanics*, Vol. 242, 1992, pp. 1–29.

[125] Giraud, L., Langou, J., and Rozloznik, M., "The loss of orthogonality in the Gram-Schmidt orthogonalization process," *Computers & Mathematics with Applications*, Vol. 50, No. 7, 2005, pp. 1069–1075.

[126] Fernandez, P. and Wang, Q., "Lyapunov spectrum of the separated flow around the NACA 0012 airfoil and its dependence on numerical discretization," *Journal of Computational Physics*, Vol. 350, 2017, pp. 453–469.

[127] Kim, D. and Choi, H., "A Second-Order Time-Accurate Finite Volume Method for Unsteady Incompressible Flow on Hybrid Unstructured Grids," *Journal of Computational Physics*, Vol. 162, 2000, pp. 411–428.

[128] Grosch, C. E. and Salwen, H., "The continuous spectrum of the Orr-Sommerfeld equation. Part 1. The spectrum and the eigenfunctions," *Journal of Fluid Mechanics*, Vol. 87, No. 1, 1978, pp. 33–54.

[129] Schmid, P. J. and Henningson, D. S., *Stability and Transition in Shear Flows*, Springer, 2001.

[130] Orszag, S. A., "Accurate solution of the OrrSommerfeld stability equation," *Journal of Fluid Mechanics*, Vol. 50, 1971, pp. 689–703.

[131] Dongarra, J., Straughan, B., and Walker, D., "Chebyshev tau-QZ algorithm methods for calculating spectra of hydrodynamic stability problems," *Applied Numerical Mathematics*, Vol. 22, No. 4, 1996, pp. 399–434.

[132] Orr, W. M., "The stability or instability of the steady motions of a perfect liquid and of a viscous liquid. Part II: A viscous liquid," *Proceedings of the Royal Irish Academy. Section A: Mathematical and Physical Sciences*, Vol. 27, JSTOR, 1907, pp. 69–138.

[133] Sommerfeld, A., "Ein beitrag zur hydrodynamischen erklaerung der turbulenten fluessigkeitsbewegungen," *Atti del*, Vol. 4, 1908, pp. 116–124.

[134] Kravchenko, A. G. and Moin, P., "On the Effect of Numerical Errors in Large Eddy Simulations of Turbulent Flows," *Journal of Computational Physics*, Vol. 131, 1997, pp. 310–322.

[135] Kuramoto, Y. and Tsuzuki, T., "Persistent propagation of concentration waves in dissipative media far from thermal equilibrium," *Progress of theoretical physics*, Vol. 55, No. 2, 1976, pp. 356–369.

[136] Sivashinsky, G. I., "Nonlinear analysis of hydrodynamic instability in laminar flamesI. Derivation of basic equations," *Acta astronautica*, Vol. 4, No. 11-12, 1977, pp. 1177–1206.

[137] Kassam, A.-K. and Trefethen, L. N., "Fourth-order time-stepping for stiff PDEs," *SIAM Journal of Scientific Computing*, Vol. 26, 2005, pp. 1214–1233.

[138] Cox, S. M. and Matthews, P. C., "Exponential time differencing for stiff systems," *Journal of Computational Physics*, Vol. 176, No. 2, 2002, pp. 430–455.

[139] Ding, X., Chaté, H., Cvitanović, P., Siminos, E., and Takeuchi, K., "Estimating the dimension of an inertial manifold from unstable periodic orbits," *Physical review letters*, Vol. 117, No. 2, 2016, pp. 024101.

[140] Mohan, P., Fitzsimmons, N., and Moser, R. D., "Scaling of Lyapunov exponents in homogeneous isotropic turbulence," *Physical Review Fluids*, Vol. 2, No. 11, 2017, pp. 114606.

[141] Oliver, T. A., Malaya, N., Ulerich, R., and Moser, R. D., "Estimating uncertainties in statistics computed from direct numerical simulation," *Physics of Fluids*, Vol. 26, 2014, pp. 035101.

[142] Rosales, C. and Meneveau, C., "Linear forcing in numerical simulations of isotropic turbulence: Physical space implementations and convergence properties," *Physics of Fluids*, Vol. 17, 2005.

[143] Pope, S. B., *Turbulent Flows*, Cambridge University Press, 2000.

[144] van Meel, J. A. and Posch, H. A., "Lyapunov instability of rough hard-disk fluids," *Physical Review E*, Vol. 80, No. 1, 2009, pp. 016206.

[145] Karimi, A. and Paul, M. R., "Extensive chaos in the Lorenz-96 model," *Chaos: An Interdisciplinary Journal of Nonlinear Science*, Vol. 20, No. 4, 2010, pp. 043105.

[146] Hassanaly, M. and Raman, V., "Lyapunov spectrum of forced homogeneous isotropic turbulent flows," Submitted.

[147] Yang, H.-l., Takeuchi, K. A., Ginelli, F., Chaté, H., and Radons, G., "Hyperbolicity and the effective dimension of spatially extended dissipative systems," *Physical review letters*, Vol. 102, No. 7, 2009, pp. 074102.

[148] Eckmann, J.-P., Forster, C., Posch, H. A., and Zabey, E., "Lyapunov modes in hard-disk systems," *Journal of statistical physics*, Vol. 118, No. 5-6, 2005, pp. 813–847.

[149] Orszag, S. A. and Patterson Jr, G., "Numerical simulation of three-dimensional homogeneous isotropic turbulence," *Physical Review Letters*, Vol. 28, No. 2, 1972, pp. 76.

[150] Moin, P. and Mahesh, K., "Direct numerical simulation: a tool in turbulence research," *Annual review of fluid mechanics*, Vol. 30, No. 1, 1998, pp. 539–578.

[151] Lundgren, T. S., "Linearly forced isotropic turbulence," *CTR Annual Research Briefs*, Center for Turbulence Research, CTR, Stanford University, 2003, pp. 461–473.

[152] Constantin, P., Foias, C., Manley, O. P., and Temam, R., "Determining modes and fractal dimension of turbulent flows," *Journal of Fluid Mechanics*, Vol. 150, 1985, pp. 427–440.

[153] Xu, M. and Paul, M. R., "Covariant Lyapunov vectors of chaotic Rayleigh-Bénard convection," *Physical Review E*, Vol. 93, No. 6, 2016, pp. 062208.

[154] Inubushi, M., Kobayashi, M. U., Takehiro, S.-i., and Yamada, M., "Covariant Lyapunov analysis of chaotic Kolmogorov flows," *Physical Review E*, Vol. 85, No. 1, 2012, pp. 016331.

[155] Bosetti, H. and Posch, H. A., "Orthogonal versus covariant Lyapunov vectors for rough hard disc systems," *Journal of Physics A: Mathematical and Theoretical*, Vol. 46, No. 25, 2013, pp. 254011.

[156] Ruelle, D., "Microscopic fluctuations and turbulence," *Physics Letters A*, Vol. 72, No. 2, 1979, pp. 81–82.

[157] Foias, C., Sell, G. R., and Temam, R., "Inertial manifolds for nonlinear evolutionary equations," *Journal of differential equations*, Vol. 73, No. 2, 1988, pp. 309–353.

[158] Akram, M., Hassanaly, M., and Raman, V., "Reduced Description of Dynamical Systems by Approximate Inertial Manifolds," *57th AIAA Aerospace Sciences Meeting*, 2019.

[159] Landau, L. D. Lifshitz, E. M., *Fluid Mechanics*, Pergamon Press, 1987.

[160] Gibbon, J. D. and Titi, E., "Attractor dimension and small length scale estimates for the three-dimensional Navier-Stokes equations," *Nonlinearity*, Vol. 10, No. 1, 1997, pp. 109.

[161] Siggia, E. D. and Patterson, G., "Intermittency effects in a numerical simulation of stationary three-dimensional turbulence," *Journal of Fluid Mechanics*, Vol. 86, No. 3, 1978, pp. 567–592.

[162] Eswaran, V. and Pope, S. B., "Direct Numerical Simulations of the Turbulent Mixing of a Passive Scalar," *Physics of Fluids*, Vol. 31, 1988, pp. 506.

[163] Ghosal, S., Lund, T. S., Moin, P., and Akselvoll, K., "A Dynamic Localization Model for Large-Eddy Simulation of Turbulent Flows," *Journal of Fluid Mechanics*, Vol. 286, 1995, pp. 229–255.

[164] Palmore Jr, J. A. and Desjardins, O., "Technique for forcing high Reynolds number isotropic turbulence in physical space," *Physical Review Fluids*, Vol. 3, No. 3, 2018, pp. 034605.

[165] Sullivan, N. P., Mahalingam, S., and Kerr, R. M., "Deterministic forcing of homogeneous, isotropic turbulence," *Physics of Fluids*, Vol. 6, No. 4, 1994, pp. 1612–1614.

[166] Laffargue, T., Tailleur, J., and Van Wijland, F., "Lyapunov exponents of stochastic systems–from micro to macro," *Journal of Statistical Mechanics: Theory and Experiment*, Vol. 2016, No. 3, 2016, pp. 034001.

[167] Forster, C., Hirschl, R., Posch, H. A., and Hoover, W. G., "Perturbed phase-space dynamics of hard-disk fluids," *Physica D: Nonlinear Phenomena*, Vol. 187, No. 1-4, 2004, pp. 294–310.

[168] Egolf, D. A., Melnikov, I. V., Pesch, W., and Ecke, R. E., "Mechanisms of extensive spatiotemporal chaos in Rayleigh–Bénard convection," *Nature*, Vol. 404, No. 6779, 2000, pp. 733.

[169] Morriss, G., "Localization properties of covariant Lyapunov vectors for quasi-one-dimensional hard disks," *Physical Review E*, Vol. 85, No. 5, 2012, pp. 056219.

[170] Taniguchi, T. and Morriss, G. P., "Localized behavior in the Lyapunov vectors for quasi-one-dimensional many-hard-disk systems," *Physical Review E*, Vol. 68, No. 4, 2003, pp. 046203.

[171] Hassanaly, M. and Raman, V., "Ensemble-LES analysis of perturbation response of turbulent partially-premixed flames," *Proceedings of the Combustion Institute*, Vol. 37, No. 2, 2019, pp. 2249–2257.

[172] Merci, B., Roekaerts, D., Peeters, T. W. J., and Dick, E., "The impact of the turbulence model and inlet boundary conditions on calculation results for reacting flows," *Proceedings of the Fifth International Workshop on Measurement and Computation of Turbulent Non-premixed Flames*, Delft, The Netherlands, 2000, pp. 226–227.

[173] *Sixth International Workshop on Measurement and Computation of Turbulent Non-premixed Flames*, Sapporo, Japan, 2002.

[174] Raman, V. and Pitsch, H., "A consistent LES/filtered-density function formulation for the simulation of turbulent flames with detailed chemistry," *Proceedings of the Combustion Institute*, Vol. 31, 2006, pp. 1711–1719.

[175] Pitsch, H. and Steiner, H., "Large-Eddy Simulation of a Turbulent Piloted Methane/Air Diffusion Flame (Sandia Flame D)," *Physics of Fluids*, Vol. 12, No. 10, 2000, pp. 2541–2554.

[176] Kempf, A., Lindstedt, R. P., and Janicka, J., "Large-Eddy Simulation of Bluff-Body Stabilized Nonpremixed Flame," *Combustion and Flame*, Vol. 144, No. 1-2, 2006, pp. 170–189.

[177] Wang, H. and Pope, S. B., "Lagrangian investigation of local extinction, reignition and auto-ignition in turbulent flames," *Combustion Theory and Modelling*, Vol. 12, No. 5, 2008, pp. 857–882.

[178] *Fourth International Workshop on Measurement and Computation of Turbulent Non-premixed Flames*, Darmstadt, Germany, 1999.

[179] Pierce, C. D. and Moin, P., "Progress-variable approach for large-eddy simulation of non-premixed turbulent combustion," *Journal of Fluid Mechanics*, Vol. 504, 2004, pp. 73–97.

[180] Pitsch, H., "A C++ Computer Program for 0-D and 1-D Laminar Flame Calculations," RWTH Aachen.

[181] Bowman, C. T., Hanson, R. K., Davidson, D. F., and *et al.*, "Gri-Mech 2.11," http://www.me.berkeley.edu/gri_mech/, 1995.

[182] Kaul, C. M., Raman, V., Knudsen, E., Richardson, E. S., and Chen, J. H., "Large eddy simulation of a lifted ethylene flame using a dynamic nonequilibrium model for subfilter scalar variance and dissipation rate," *Proceedings of the Combustion Institute*, Vol. 34, No. 1, 2013, pp. 1289–1297.

[183] Jaravel, T., Riber, E., Cuenot, B., and Pepiot, P., "Prediction of flame structure and pollutant formation of Sandia flame D using Large Eddy Simulation with direct integration of chemical kinetics," *Combustion and Flame*, Vol. 188, 2018, pp. 180–198.

[184] Xu, J. and Pope, S. B., "PDF calculations of turbulent nonpremixed flames with local extinction," *Combustion and Flame*, Vol. 123, No. 3, 2000, pp. 281–307.

[185] Hassanaly, M. and Raman, V., "A self-similarity principle for the computation of rare event probability," Submitted.

[186] Hassanaly, M., Voelkel, S., and Raman, V., "Classification and Simulation of Anomalous Events in Turbulent Combustion," *Proceedings of the 10th Mediterranean Combustion Symposium*, 2017.

[187] Sornette, D., Johansen, A., and Bouchaud, J.-P., "Stock market crashes, precursors and replicas," *Journal de Physique I*, Vol. 6, No. 1, 1996, pp. 167–175.

[188] Weinan, E., Ren, W., and Vanden-Eijnden, E., "Simplified and improved string method for computing the minimum energy paths in barrier-crossing events," *Journal of Chemical Physics*, Vol. 126, No. 16, 2007, pp. 164103.

[189] Frei, C. and Schär, C., "Detection probability of trends in rare events: Theory and application to heavy precipitation in the Alpine region," *Journal of Climate*, Vol. 14, No. 7, 2001, pp. 1568–1584.

[190] Kim, J., Bucklew, J. A., and Dobson, I., "Splitting method for speedy simulation of cascading blackouts," *IEEE Transactions on Power Systems*, Vol. 28, No. 3, 2013, pp. 3010–3017.

[191] Siegmund, D., "Importance sampling in the Monte Carlo study of sequential tests," *The Annals of Statistics*, 1976, pp. 673–684.

[192] Morio, J., Balesdent, M., Jacquemart, D., and Vergé, C., "A survey of rare event simulation methods for static input–output models," *Simulation Modelling Practice and Theory*, Vol. 49, 2014, pp. 287–304.

[193] De Boer, P.-T., Kroese, D. P., Mannor, S., and Rubinstein, R. Y., "A tutorial on the cross-entropy method," *Annals of operations research*, Vol. 134, No. 1, 2005, pp. 19–67.

[194] Peherstorfer, B., Cui, T., Marzouk, Y., and Willcox, K., "Multifidelity importance sampling," *Computer Methods in Applied Mechanics and Engineering*, Vol. 300, 2016, pp. 490–509.

[195] Cérou, F. and Guyader, A., "Adaptive Multilevel Splitting for Rare Event Analysis," *Stochastic Analysis and Applications*, Vol. 25, 2007, pp. 417–443.

[196] Bouchet, F., Rolland, J., and Simonnet, E., "Rare event algorithm links transitions in turbulent flows with activated nucleations," *Physical review letters*, Vol. 122, No. 7, 2019, pp. 074502.

[197] Teo, I., Mayne, C. G., Schulten, K., and Lelivre, T., "Adaptive multilevel splitting method for molecular dynamics calculation of benzamidine-trypsin dissociation time," *Journal of chemical theory and computation*, Vol. 12, No. 6, 2016, pp. 2983–2989.

[198] Laurie, J. and Bouchet, F., "Computation of rare transitions in the barotropic quasi-geostrophic equations," *New Journal of Physics*, Vol. 17, No. 1, 2015, pp. 015009.

[199] Lestang, T., Ragone, F., Bréhier, C.-E., Herbert, C., and Bouchet, F., "Computing return times or return periods with rare event algorithms," *Journal of Statistical Mechanics: Theory and Experiment*, Vol. 2018, No. 4, 2018, pp. 043213.

[200] Del Moral, P., Garnier, J., et al., "Genealogical particle analysis of rare events," *The Annals of Applied Probability*, Vol. 15, No. 4, 2005, pp. 2496–2534.

[201] Dellago, C., Bolhuis, P. G., and Geissler, P. L., "Transition path sampling," *Advances in chemical physics*, Vol. 123, 2002, pp. 1–78.

[202] Grafke, T., Grauer, R., and Schäfer, T., "The instanton method and its numerical implementation in fluid mechanics," *Journal of Physics A: Mathematical and Theoretical*, Vol. 48, No. 33, 2015, pp. 333001.

[203] Lorenz, E. N., "Predictability: A problem partly solved," *Proc. Seminar on predictability*, Vol. 1, 1996.

[204] Nemoto, T., Bouchet, F., Jack, R. L., and Lecomte, V., "Population-dynamics method with a multicanonical feedback control," *Physical Review E*, Vol. 93, No. 6, 2016, pp. 062123.

[205] Souza, A., "Instantons as a Means to Probe Chaotic Attractors," Tech. rep., WHOI, 2015.

[206] Sforzo, B., H., D., Wei, S., and Setzman, J., "Liquid Fuel Composition Effects on Forced, Nonpremixed Ignition," *Journal of Engineering for Gas Turbines and Power*, Vol. 139, 2017, pp. 031509.

[207] Hassanaly, M., Tang, Y., Barwey, S., and Raman, V., "Analysis of the effect of turbulence on aircraft engine ignition," *Proceedings of the 11th Mediterranean Combustion Symposium*, 2019.

[208] Poinsot, T., "Prediction and control of combustion instabilities in real engines," *Proceedings of the Combustion Institute*, Vol. 36, 2017, pp. 1–28.

[209] Temam, R., "Induced trajectories and approximate inertial manifolds," *ESAIM: Mathematical Modelling and Numerical Analysis*, Vol. 23, No. 3, 1989, pp. 541–561.

[210] Lu, F., Lin, K. K., and Chorin, A. J., "Data-based stochastic model reduction for the Kuramoto–Sivashinsky equation," *Physica D: Nonlinear Phenomena*, Vol. 340, 2017, pp. 46–57.

[211] Mueller, M. E. and Raman, V., "Model form uncertainty quantification in turbulent combustion simulations: Peer models," *Combustion and Flame*, Vol. 187, 2018, pp. 137–146.

[212] Akintayo, A., Lore, K. G., Sarkar, S., and Sarkar, S., "Early detection of combustion instabilities using deep convolutional selective autoencoders on hi-speed flame video," *arXiv preprint arXiv:1603.07839*, 2016.

[213] Lin, Z., Thiffeault, J.-L., and Doering, C. R., "Optimal stirring strategies for passive scalar mixing," *Journal of Fluid Mechanics*, Vol. 675, 2011, pp. 465–476.

[214] Tobasco, I. and Doering, C. R., "Optimal wall-to-wall transport by incompressible flows," *Physical review letters*, Vol. 118, No. 26, 2017, pp. 264502.

[215] Schlüter, J. U., Pitsch, H., and Moin, P., "Large-eddy simulation inflow conditions for coupling with Reynolds-averaged flow solvers," *AIAA journal*, Vol. 42, No. 3, 2004, pp. 478–484.

[216] Klein, M., Sadiki, A., and Janicka, J., "A digital filter based generation of inflow data for spatially developing direct numerical or large eddy simulations," *Journal of computational Physics*, Vol. 186, No. 2, 2003, pp. 652–665.

[217] Haworth, D., "Progress in probability density function methods for turbulent reacting flows," *Progress in Energy and combustion Science*, Vol. 36, No. 2, 2010, pp. 168–259.

[218] Pope, S. B., "A Monte Carlo method for the PDF equations of turbulent reactive flow," *Combustion Science and Technology*, 1981.

[219] Nguyen, P.-D., Vervisch, L., Subramanian, V., and Domingo, P., "Multidimensional flamelet-generated manifolds for partially premixed combustion," *Combustion and Flame*, Vol. 157, No. 1, 2010, pp. 43–61.

[220] Fiorina, B., "Accounting for complex chemistry in the simulations of future turbulent combustion systems," *57th AIAA Aerospace Sciences Meeting*, 2019.

[221] Ihme, M., "Requirements Towards Predictive Simulations of Turbulent Combustion," *57th AIAA Aerospace Sciences Meeting*, 2019.

[222] Mueller, M. E., "A Computationally Efficient Turnkey Approach to Turbulent Combustion Modeling: From Elusive Fantasy to Impending Reality," *57th AIAA Aerospace Sciences Meeting*, 2019.

[223] Kim, J., Moin, P., and Moser, R. D., "Turbulence Statistics in Fully Developed Channel Flow at low Reynolds Number," *Journal of Fluid Mechanics*, Vol. 177, 1987, pp. 133–166.

[224] Huerre, P. and Monkewitz, P. A., "Local and global instabilities in spatially developing flows," *Annual review of fluid mechanics*, Vol. 22, No. 1, 1990, pp. 473–537.

[225] Sreenivasan, K. R., Raghu, S., and Kyle, D., "Absolute instability in variable density round jets," *Experiments in Fluids*, Vol. 7, No. 5, 1989, pp. 309–317.